REPORT DOCUMENTATION PAGE

AFRL-SR-AR-TR-04-

0312

1. REPORT DATE (DD-MM-YYYY) 062004	2. REPORT TYPE Final	3. DATES COVERED (From - To) Nov 2000 - Nov 2003

4. TITLE AND SUBTITLE
Synthetic Jet Actuation - Modeling, Actuator Development and Application to Separation Control

5a. CONTRACT NUMBER

5b. GRANT NUMBER
F49620-01-1-0012

5c. PROGRAM ELEMENT NUMBER

6. AUTHOR(S)
Dr. Othon K. Rediniotis

5d. PROJECT NUMBER

5e. TASK NUMBER

5f. WORK UNIT NUMBER

7. PERFORMING ORGANIZATION NAME(S) AND ADDRESS(ES)
Texas Engineering Experiment Station
Texas A&M University
College Station Texas   77843-3141

8. PERFORMING ORGANIZATION REPORT NUMBER

9. SPONSORING/MONITORING AGENCY NAME(S) AND ADDRESS(ES)
USAF/AFRL
AFOSR
801 N. Randolph Street
Arlington VA   22203

10. SPONSOR/MONITOR'S ACRONYM(S)
AFOSR

11. SPONSOR/MONITOR'S REPORT NUMBER(S)

12. DISTRIBUTION/AVAILABILITY STATEMENT
Distribution Statement A. Approved for public release; distribution is unlimite

20040625 138

13. SUPPLEMENTARY NOTES

14. ABSTRACT
This work presents an investigation of synthetic jet actuation for separation control over wings/airfoils, in steady and unsteady flows, the development of high-power, compact synthetic jet actuators (SJA) for flow separation control, the modeling and control of such actuators and the modeling and control of the resulting SJA-controlled aerodynamics and wing/airfoil, respectively. The developed actuator is compact enough to fit in the interior of a NACA0015 profiled wing with a chord of 0.375 m. Test bench experiments showed that the multi-piston actuator array was capable of producing exit velocities of up to 90 m/s for an actuator frequency of 130 Hz. The actuator was placed in a NACA 0015 wing and tested in a wind tunnel. An experimental investigation into the effects of a synthetic jet actuator on the performance of the wing, in steady flow, is described. Emphasis is placed on the capabilities of the actuator to control the separation of the flow over the wing at high angles of attack. The investigation included the use of force balance measurements, on-surface flow visualization with oil and tufts, off-surface flow visualizations with smoke, surface pressure distribution measurements and wake surveys.

15. SUBJECT TERMS

16. SECURITY CLASSIFICATION OF:			17. LIMITATION OF ABSTRACT	18. NUMBER OF PAGES	19a. NAME OF RESPONSIBLE PERSON
a. REPORT U	b. ABSTRACT U	c. THIS PAGE U	UU	140	19b. TELEPHONE NUMBER (Include area code)

Standard Form 298 (Rev. 8/98)
Prescribed by ANSI Std. Z39.18

SYNTHETIC JET ACTUATION – MODELING, ACTUATOR DEVELOPMENT AND APPLICATION TO SEPARATION CONTROL

Final Project Report

Submitted by

Othon K. Rediniotis
Aerospace Engineering Department
Texas A&M University
College Station, Texas 77843-3141

to the

TABLE OF CONTENTS

ABSTRACT

This work presents an investigation of synthetic jet actuation for separation control over wings/airfoils, in steady and unsteady flows, the development of high-power, compact synthetic jet actuators (SJA) for flow separation control, the modeling and control of such actuators and the modeling and control of the resulting SJA-controlled aerodynamics and wing/airfoil, respectively.

The developed actuator is compact enough to fit in the interior of a NACA0015 profiled wing with a chord of 0.375 m. Test bench experiments showed that the multi-piston actuator array was capable of producing exit velocities of up to 90 m/s for an actuator frequency of 130 Hz. The actuator was placed in a NACA 0015 wing and tested in a wind tunnel. An experimental investigation into the effects of a synthetic jet actuator on the performance of the wing, in steady flow, is described. Emphasis is placed on the capabilities of the actuator to control the separation of the flow over the wing at high angles of attack. The investigation included the use of force balance measurements, on-surface flow visualization with oil and tufts, off-surface flow visualizations with smoke, surface pressure distribution measurements and wake surveys. In addition to flow separation control data, results corresponding to hot wire measurements at the exit of the slot, are also presented and are used for the characterization of the flowfield generated by the synthetic jet actuators. Most of the tests were performed at a freestream velocity of 35 m/s, corresponding to a Reynolds number of 8.96×10^5. The angle of attack was varied from –2.0 to 29 degrees. At angles of attack lower than 10 degrees the actuator tends to increase the lift curve slope as the actuation frequency is increased. At higher angles of attack, the SJA extends the range of angle of attack for which the wing may be operated without stalling. The use of the actuator causes an 80% increase in the value of maximum lift coefficient, and the angle at which stall occurs is increased from 12 to 18 degrees (for the Reynolds number range of the test). The drag on the wing is decreased as a consequence of SJA actuation. This was verified with the force balance measurements and by analysis of the wake surveys. For angles of attack larger than 18 degrees, once massive stall has occurred over the wing, the operation of the SJA still provides a small amount of lift augmentation. At angles of attack larger than 25 degrees, a large frequency of actuation is required to produce any noticeable effects.

An experimental investigation was then undertaken to evaluate the effectiveness of a Synthetic Jet Actuator (SJA) for flow control on a ramping airfoil. A NACA 0015 profiled wing was pitched up at various rates with concomitant surface pressure acquisition. The developed self-contained synthetic jet actuator was positioned in the interior of the wing. Synthetic jet actuation parameters included actuator frequency, exit width and rate of change of the exit width. The behavior of the surface pressures is investigated as well as their integrated properties. The data suggests that the effect of the SJA is to delay the onset of the dynamic stall vortex formation to higher incidence, and in some cases, for the parameters and incidence range investigated, suppress it totally. However, in the instances when formed, the synthetic jet appears to increase the loading induced by the stall vortex. At low ramp rates, the synthetic jet forcing causes the formation of a stall vortex where the unforced data showed a pseudo-static stall type behavior. Hot wire anemometer surveys of the jet exit showed that compressibility effects would manifest for small slot exit areas, and increased with frequency. Variation of the SJA driving frequency showed the ability to control the flow from massively separated to fully attached at 25 degrees instantaneous angle of attack.

Then, a low speed wind tunnel investigation was conducted to determine the effects of Synthetic Jet Actuators (SJAs) on a sinusoidally pitching wing. During the dynamic motion, pressures were recorded around the wing using a high-speed pressure scanner connected to thirty-two tappings. Integration of these pressures yielded instantaneous lift and pitching moment. The motion consisted of a 12.5 deg excursion around a 12.5 deg mean. Pitch frequencies of 0.2Hz to 2.0Hz were evaluated. The data showed that during the upstroke, at low pitch frequencies, the SJA delayed stall. As the frequency increased, the effect of the SJA compared to the unforced case diminished as the dynamic motion itself delayed the onset of stall. During the downstroke, the SJA caused a more rapid flow re-attachment, resulting in considerably smaller hysteresis loops. For the highest pitch frequency evaluated, the hysterisis loop was eliminated.

Subsequently, we developed a model of the developed SJA, for control purposes. The actuator motor was supplied with an input voltage profile generated by dSPACE. This input consists of

superimposed sinusoidal and square signals of different frequencies, so that all the dynamic modes of the motor are excited for correct model identification. This experimental data is fed to an Observer Kalman Identification Algorithm (OKID), which lead to the identified "pseudo-linear" model with 'Voltage' as the input and 'SJA Motor Frequency' as the output. Then we discuss the modeling of the SJA fluid mechanics, i.e. the development of an actuator model that accepts as its input the actuator frequency and outputs the actuator velocity at its exit. The combination of the two models above yield a complete model for the actuator dynamics/fluid mechanics.

Finally, we discuss the on-going efforts in designing the control laws for hingeless wing control via synthetic jet actuation. We particularly discuss the control methodologies to generate a desired pitching moment at a particular angle of attack. The main challenge in designing the control methods for the SJA wing is the unknown input-output mapping of the wing aerodynamics. In the present investigation, we use a non-parametric approach to model the unknown wing dynamics and aerodynamics. Further, this model was then utilized to design control laws for set point tracking of the angle of attack. We present the formulation of two different control laws for synthetic jet actuation pitch control. The first formulation involves the design of a PID controller for set point tracking that is easy to implement and useful in gaining sufficient insight into the control related issues. The second formulation involves the design of model-error control synthesis based controller that could resolve the limitations faced with the PID controller.

1. INTRODUCTION

General

For the case of wall-bounded flows, the separation of the boundary layer is associated with large energy losses, and in most applications adversely affects the aerodynamic loads in the form of lift loss and drag increase. Therefore, there is a strong incentive to delay or manipulate the occurrence of flow separation. For example, if the separation of the boundary layer formed over a bluff body is delayed, the pressure drag is greatly reduced; also separation delay will permit the operation of an airfoil/wing at higher angles of attack. Furthermore, the delay or elimination of separation can increase the pressure recovery in a diffuser. On the other hand, in some cases separation is beneficial, as is the case of delta wings, which possess high-lift capabilities as a direct result of flow separation and the formation of two leading edge vortices. In view of the above, separation control is of great importance to most of the systems involving fluid flow, such as air, land or underwater vehicles, turbomachines, diffusers, etc.

Flow Separation

Prandtl (1904), founder of the boundary layer theory, explained the physical phenomenon of separation in the following way: Consider the velocity profile of a two-dimensional or axially symmetric boundary layer upstream of a point of separation where the pressure gradient is continuous and adverse (see Figure 1.1). Within the thin boundary layer of thickness δ, the viscous effects produce a strong velocity gradient du/dy, which prevails near the wall (u is the streamwise velocity component and y is the distance normal to the wall). The no slip condition imposed at the wall causes the velocity at the wall to be zero, increasing rapidly with distance y until it gradually approaches the value of U_e, which is the inviscid flow velocity at the outer edge of the boundary layer. Compared to the freestream, the retarded flow in the boundary layer suffers a greater deceleration, and since the energy (momentum) of the flow close to the wall is small, the ability of the flow to move forward and overcome the adverse pressure gradient becomes limited. In terms of energy principles, the kinetic energy gained by the fluid at the expense of potential energy in the favorable pressure gradient region is depleted by viscous effects within the boundary layer. The small amount of energy left in the flow is expended further downstream in order to overcome the pressure rise as well as the viscous friction, and hence the fluid is eventually brought to rest. Due to the fact that the main stream itself is decelerating, it cannot reenergize the fluid in the boundary layer. Thus when the surface streamline reaches a point on the wall in which $\partial u/\partial y\,|_{y=0} = 0$ (or zero shear stress position), it begins to break away from the wall and the flow separates from the surface. The surface streamline nearest to the wall leaves the body at this point and the boundary layer is said to separate (Maskell 1955). The zero stress condition implies that the wall friction (τ_w) changes at this point from a positive value to a negative value. If τ_w is negative, then $\partial u/\partial y$ is also negative, which implies that the velocity of the fluid near the wall is negative, hence there is a flow reversal downstream of the separation point. At separation, the rotational flow region next to the wall suddenly thickens, the normal velocity component increases, and the boundary layer approximations are no longer valid.
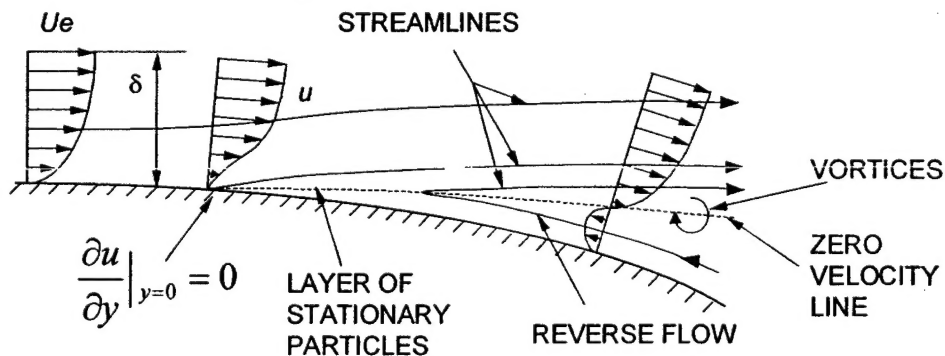

Figure 1.1: Schematic of the velocity profile near a separation point.

Due to the large energy losses, which are associated with boundary layer separation, the performance of many practical devices is often limited by the separation location. For example, if separation is postponed the pressure drag of a bluff body is decreased, the circulation and hence the lift of an airfoil at a high angle of attack is enhanced, and the pressure recovery in a diffuser is improved. The strong effect that flow separation has over the aerodynamic properties of wings and other lift producing devices has been the driving force behind the great amount of theoretical and experimental research that has been produced for the purpose of understanding and harnessing such a phenomenon. Many efforts have been made in the past few decades in establishing a firm analytical foundation for steady, two-dimensional separation. In contrast, the theoretical or numerical analysis of three-dimensional or unsteady separation is considerably less developed, and progress to date in these areas has depended significantly on experimental work.

The breakthrough in unsteady separation research was achieved by Moore, Rott and Sears during the 1950's. Prior to their work, it was believed that steady and unsteady separations had the same characteristics; namely, the point of vanishing wall shear, the termination of the boundary layer, and the beginning of the wake or bubble of separated fluid. Rott (1956), while analyzing the unsteady flow in the vicinity of a stagnation point, noted that the point of vanishing wall shear did not coincide with the point of boundary layer detachment. In the same year, Sears (1956) made an assumption that the unsteady separation point was characterized by the simultaneous vanishing of the shear and of the velocity at a point within the boundary layer as seen by an observer in a coordinate system convected with the separation velocity. Two years later, Moore (1958), while investigating a steady flow over a moving wall, arrived at a model analogous to that for unsteady separation. He stated, "for a slowly moving wall separation occurs when, at some point in the boundary layer, the profile velocity and shear simultaneously vanish". A detailed review of both steady and unsteady separation phenomena may be found in Gad-el-Hak (2000).

Flow Separation Control

Many researchers have developed and tested methods of separation control in a variety of applications. Chang (1976) presents an extensive review of flow separation techniques prior to 1976. Gad-el-Hak and Bushnell (1991) provide a comprehensive review on the research in the area of separation control previous to the year 1991. Typically the separation control techniques may be grouped in two categories: passive and active techniques. Most of the techniques, developed for passive separation control, may be found in the review by Gad-el-Hak and Bushnell (1991). Some of the parameters affecting the selection of a separation control technique include, but are not limited to: weight of system, power consumption (active type), power density, parasitic drag of device, size, reliability, cost and efficiency.

Separation control techniques have been based on many principles, some of which will be mentioned in the following paragraphs. Due to the fact that separation occurs because the low energy flow in the boundary layer close to the surface is unable to overcome an adverse pressure gradient, one way of delaying separation has been the modification of the velocity profile in the boundary layer in order to make it as full as possible or reduce the steepness of the adverse pressure gradient by streamlining the surface. Also, another method of delaying separation is the use of auxiliary devices (vortex generators, turbulators, etc) that enhance the mixing in the shear layer, which increases the turbulence level and hence, the energy of the fluid in the neighborhood of the wall. The modification and or control of the viscosity near the wall by heat addition in the case of liquids or heat transfer from the fluid to the wall in the case of gases has also been shown to work in delaying separation.

Another method of modifying the curvature of the velocity profile close to the wall has been to apply suction in order to remove the low energy fluid from the boundary layer through slots or orifices on the surface. Prandtl (1904) pioneered the work in this area of separation control. In his first experiments he applied flow suction through a spanwise slot on one side of a circular cylinder, showing that the boundary layer remained attached to the suction side of the cylinder for a longer part of its surface. Many other researchers have since applied suction as a separation control tool (see reviews by Chang, 1976 and Gad-el-Hak, 2000).

The use of moving boundaries, which utilize the no-slip condition at the surface in order to energize the fluid close to the wall, has also been explored in the past. For example, rotating cylinders have been used to delay separation at the leading and trailing edges of airfoils and control surfaces as well as at flap junctures (Johnson et al. 1975, Mokhtarian and Modi 1988, Modi et al.1989, Alvarez –Calderon 1964).

Additional energy may be supplied to the near-wall fluid by injecting a foreign fluid in the vicinity of the wall (blowing). This additional momentum may be provided by an external source or by locally redirecting the fluid into the wall region. Passive techniques do not require additional power but have an associated drag penalty. Passive blowing through leading edge slats and trailing edge flaps are commonly used in aircraft wings (Smith 1975, Lin et al. 1992). Although the amount of blowing that they provide is limited by the pressure differentials produced by the wings themselves, their effects on the lift and drag characteristics are dramatic. The effects of leading edge slats and trailing edge flaps may be further enhanced by using auxiliary power such as high pressure air bled of from the engine compressor (internally blown slats and flaps) or directly deflecting the exhaust jet flow from the engine (externally blown flap, upper surface blowing, etc). Goodmanson and Gratzer (1973, 1974) provide a comprehensive description of some of these augmented devices.

As mentioned above the momentum of the boundary layer may be enhanced by means of injection of a fluid into the near wall vicinity. This fluid may be injected parallel to the surface (tangential blowing) in order to directly increase the momentum of the boundary layer or may be injected perpendicular to the wall (normal blowing) in order to increase the mixing rate in the shear layer. There is a great amount of literature that is readily available in the area of steady blowing. Gad-el-Hak (2000) provides an extensive review of this area.

The use of tangential jet blowing over highly curved surfaces has proved to be a very effective way of augmenting aerodynamic and hydrodynamic forces without the need of moving surfaces. This type of flow control is often referred to as circulation control. Developments in this area (Englar, 1975) show its significance for helicopters and "vertical and/or short take-off and landing" (V/STOL) aircraft. Englar (2000) presents and discusses a large variety of proven uses of the circulation control concept for boundary layer control as well as for augmentation/modification of the aerodynamic characteristics of aircraft and other fluid handling machines. The circulation control concept is based on the "Coanda Effect", named after the Romanian inventor Henri Coanda. Figure 1.2 illustrates the "coanda effect" principles under which circulation control is achieved. For this case, a jet exits a slot and follows the curved surface as an inviscid fluid would, until the balance between the pressure gradient normal to the surface and the centrifugal force exerted on the flow is destroyed by the separation of the thickening boundary layer. The fact that the flow remains attached to a great portion of the curved surface proves that this type of blowing is an effective method of boundary layer separation control.

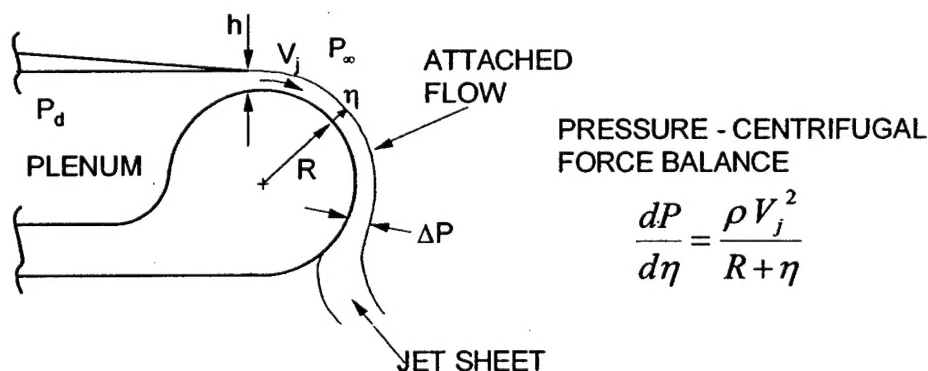$$\frac{dP}{d\eta} = \frac{\rho V_j^2}{R+\eta}$$

Figure 1.2: Illustration of the Coanda Effect

In recent years, the use of pulsed jets emanating from the surface has also shown to have benefits as separation control devices (McManus et al. 1996, McManus and Magil 1997). These pulsed jets have

7

the ability to produce a large amount of vorticity and to enhance the momentum transport within the boundary layer, thus achieving fairly good stall suppression.

Other active methods of controlling boundary layer separation and re-attachment include acoustic excitations (Huang et al. 1987, Hsiao et al. 1990), periodic forcing of the velocity field by means of an oscillating flap or wire (Koga et al. 1984, Bar-Sever 1989), as well as many other techniques that will not be discussed herein. The publications by Lachman (1961) and Chang (1976) and the reviews by Gad-el-Hak (1990) and Gad-el-Hak and Bushnell (1991) provide extensive information and further references on this exciting topic.

As presented above, the techniques for flow separation control by suction and blowing are based on different principles. Suction removes low-energy fluid from the near-wall area thus entraining higher energy fluid from the upper layers of the boundary layer. On the other hand, blowing adds energy to the near wall-fluid by either direct injection of high-energy fluid into the boundary layer (tangential blowing) or by enhancing the mixing of the flow within the shear layer. In spite of the differences between these two types of control, there is yet an additional form of flow separation control that has been widely used and combines oscillatory blowing. The use of oscillatory blowing and suction has proven to be more effective that just steady blowing or steady suction. One variation of the oscillatory blowing and suction technique is the use of the so called zero-mass-flux actuators.

Synthetic Jet Actuators (SJAs)

In the recent years the development of the so-called "synthetic jet" or "zero mass flux" devices and their potential for flow control, especially separation control, mixing enhancement and fluidic thrust vectoring, has received a great amount of attention from the fluid dynamics community. This type of systems mostly involves small-scale, low-energy, typically high-frequency actuators, whose operation is based on the concentrated input of energy at high receptivity regions of the flowfield. They take advantage of the physical flow evolution processes to amplify the applied disturbance, which stands apart from the traditional brut force macro-scale control. Moreover, in terms of practical implementation, they offer significant benefits over oscillatory blowing techniques from an existing air supply. The latter technique requires supply lines that deliver the air from the supply source to the location of flow control. Even in fixed wing configurations, this increases the complexity, cost and weight of the overall system. In rotary wing flow control applications, for example rotating blade stall in helicopters (Greenblatt et al., 1998), the situation is further complicated by the need to transfer, via pneumatic connections, the air from a supply source that resides in the fixed fuselage frame to the rotating frame of the blade; a practical impossibility. In contrast, a synthetic jet actuator (SJA) can be a stand-alone unit installed at the location where the flow control is needed, requiring very little communication with hardware away from that site. In this case, the communication is mostly in the form of electrical power and signals. Furthermore, the SJA could be integrated with flow sensors, control circuitry and control algorithms that can all reside in the vicinity of the flow control site, further reducing the system's need to communicate with remote hardware.

Current research of synthetic jet actuation includes investigation of the performance of this technology for modifying the lift, drag and flight control characteristics of unconventional airfoils as well as flow separation over bluff bodies (Amitay et al., 1998; Smith et al., 1998; Seifert et al., 1993; Seifert and Pack, 1999a). This technology could lead to elimination, reduction or manipulation of steady and unsteady flow separation over a wing/blade, via active flow control and in a "hingeless" manner (no conventional moving control surfaces). A result of this technology can be the active modification of the pressure distribution over an aerodynamic surface, leading to "dynamic virtual shaping". Flow separation manipulation (not just separation delay) could open new horizons in vehicle control and presents an exciting alternative over conventional control surfaces, since: (a) it can alter the aerodynamic loading over a larger wing/blade area, providing higher control authority and (b) could eliminate leading-edge or trailing-edge moving surfaces. It becomes more and more evident that, at least in the design of military aircraft, one of the most important design criteria is vehicle low observability; to the point that the aircraft geometry design is largely based on radar signature considerations with little input from aerodynamics. One might even say that the aerodynamics is put into the design after the vehicle geometry has been

8

determined. Therefore, hingeless flow control will allow the optimization of the aerodynamics without disrupting the physical outside geometry of the vehicle and therefore, to a large extent, its radar signature.

The existing literature presents very promising applications of the synthetic jet technology to flow separation under both, laboratory and real flight conditions (Greenblatt and Wygnaski, 1998, Greenblatt et al., 1998, Seifert and Pack, 1999b, Pack and Seifert, 2000 and Seifert and Pack, 2000). In the recent years a large amount of numerical computations and simulations has been produced in the area of flow separation control over lifting surfaces via synthetic jet actuators (Donovan et al., 1998, Hassan and Munts, 2000, He and Kral, 2000, and He et al., 2001). Another application of synthetic jet technology is the control of the aerodynamic performance of lifting surfaces through fluidic modifications of their apparent aerodynamic shape (Amitay et al., 1998, Honohan et al., 2000, Parekh and Glezer, 2000). Jet vectoring has also become an area of flow control that can receive benefits from the application of synthetic jet actuators (Smith and Glezer, 1997, Smith et al., 1999 and Pack and Seifert, 1999). This area is of extreme importance in the development of jet engine exhaust systems as well as in the area of control surface augmentation.

In most efforts in the existing literature, the synthetic jet actuators (SJA) are either powered piezoelectrically (Rathnasingham and Breuer, 1997; Seifert et al., 1998) or are powered from external hardware. For example, in Greenblatt and Wygnaski (1998), as well as in Seifert and Pack (1999a and 1999b), the mechanism used to generate the pressure oscillations necessary for the zero-mass-flux flow control was a hardware-intensive pneumatic mechanism, with most of the hardware residing outside the test section. For the previous cases, the pressure oscillations were generated outside the test section and the model, and were then directed into the model through plumbing. Similarly, McCormick (2000), presented an acoustic based method to produce the synthetic jet, in which most of the hardware was also outside of the test section.

For most air and water vehicle applications, the SJAs will need to be compact in order to be housed inside the control surface of the body whose aerodynamic/hydrodynamic characteristics they are trying to modify. On the other hand, piezoceramic-based synthetic jet actuators, which can be small enough to be housed inside the control surface, exhibit performance deterioration when operating at frequencies away from the actuator resonance frequencies, have limited maximum amplitudes and generally quickly deteriorate at off-design conditions. There is an explicit need for the development of compact, high-power synthetic jet actuators that can meet the size, weight, efficiency and power density requirements of full-scale flow control applications. The present work addresses these needs, via development and characterization of compact, high power synthetic jet actuators, and demonstration of the developed technology in representative flow control problems.

The author and his colleagues have developed several models for DC motor-driven synthetic jet actuators (Rao et al., 2000), which have advantages over piezoelectric actuators. One of these is that the amplitude of oscillation can be on the order of millimeters, and the frequency of operation is variable. These motor driven actuators have been used to control or completely eliminate separation over an airfoil even in the post-stall regime. For these actuators, the driving motor has to supply enough power to overcome both the fluid pressure forces and the inertial forces of the moving parts of the actuator.

It has been shown (Seifert et al., 1996), that there exists an optimum frequency at which the separation control by means of oscillatory blowing is optimal, therefore the ability of being able to control the frequency of operation of the actuator without degrading its performance is of great importance. Hence the use of the compact DC motor powered synthetic jet actuators, with a variable frequency and large amplitudes of oscillation is evident. Gilarranz and Rediniotis (2001a) showed that they could delay the separation over a NACA 0015 wing operating at a high angle of attack with a DC motor powered synthetic jet actuator that fits entirely inside the wing.

Kral et al., (1997) presented a numerical simulation of the flowfield generated by a circular synthetic jet actuator treating the orifice of the actuator as a suction/blowing boundary condition. On the other hand, Rizzetta et al., (1999) presented a numerical simulation of the flowfield generated by a slotted piezoelectrically driven synthetic jet actuator. This last simulation included the analysis of the flowfield inside the cavity of the actuator. In their report, Rizzetta et al. investigate the effects of the geometry of the cavity over the performance of the actuator. Also, Müller et al., (2000) present an analysis of the

9

optimal geometry for micro-machined acoustic resonators that can be utilized for the optimization of the actuator cavity.

There have been a several publications presenting experimental characterizations of synthetic jet actuators. In the work of Rathnasingham and Breuer (1997) the average resulting flowfield produced by a synthetic jet with a circular orifice was examined using hotwire anemometry. On the other hand, Gilarranz et al. (1998) performed experimental measurements on a synthetic jet using a high-frame-rate particle image velocimetry system (PIV) obtaining simultaneous measurements of the instantaneous flowfield generated by these devices at many points within a 2-D plane. Smith and Glezer (1998) performed experimental investigations on the flowfield produced by a rectangular synthetic jet. Mallison et al. (2001) performed an experimental and numerical study of synthetic jet flows, in which they used a circular orifice jet. For both of these last studies, phase averaged hot-wire anemometry results were presented.

It is very important to realize the versatility of SJAs in producing a range of different flow patterns, depending on the SJA geometric and operational parameters. To illustrate this versatility of SJAs we offer the following example. Gilarranz et al. (1998) and Gilarranz (1998) showed that by just varying the actuator's Strouhal number, $St = (fd)/V$ (based on the actuator frequency (f), the maximum velocity at the SJA exit orifice/slot (V) and the orifice's characteristic lengthscale (d)), the flow generated by the actuator could vary from a jet-like to a sink-like flow pattern. This is illustrated in figures 1.3 and 1.4. These plots represent instantaneous flowfields collected via Particle Image Velocimetry (PIV), in the actuator orifice vicinity of an axisymmetric SJA. The actuator orifice is at the top middle of each plot. The two cases examined here, have St values that are different by an order of magnitude (0.2 and 2, for figures 1.3 and 1.4, respectively), while the Re numbers have been kept almost the same. Two distinctly different flowfields are produced.

For St=0.2 (figure 1.3) and for the specific time instant captured, a vortex ring has been completely developed, has detached from the orifice and is convected downstream with the jet. The early stages of the suction cycle are obvious. It is seen that although the suction cycle has begun, and the flow adjacent to the orifice is being ingested into the orifice, the flow further away from the orifice still maintains a jet-like pattern with high axial momentum. The formation of a saddle point is obvious on the jet axis and separates the jet flow (below it) from the suction flow (above it). The formation of a saddle point has significant implications, especially in terms of the possibilities it offers in achieving "virtual boundary shaping". Moreover, this type of flow pattern can be used to control flow separation by energizing the boundary layer. The oscillatory jet adds momentum to the boundary layer in two ways. During the suction part of the cycle, it draws the low momentum fluid in the boundary layer inside the cavity, thereby bringing the higher momentum fluid, at the boundary layer edge, near the surface. On the other hand, during the blowing part of the cycle, it adds the same fluid with higher momentum to the flow. By properly shaping the SJA orifice/slot in a curved, or "Coanda" configuration, this momentum can be delivered almost tangentially to the surface. Therefore, the actuator not only produces momentum itself, but also enhances the boundary layer's ability to overcome adverse pressure gradients through the mixing it induces of the low momentum fluid near the surface with the high momentum external flow. This mixing is further enhanced by the unsteady nature of the SJA excitation. The effectiveness of this mixing process relates to the high receptivity of the shear layer emanating from the point of separation. Appropriate selection of the SJA oscillation frequency, excites the shear layer and promotes the development of its natural instability, which leads to the formation of large vortical coherent structures. These flow structures in turn promote boundary layer mixing and, hence, momentum exchange between the outer and inner parts of the boundary layer.
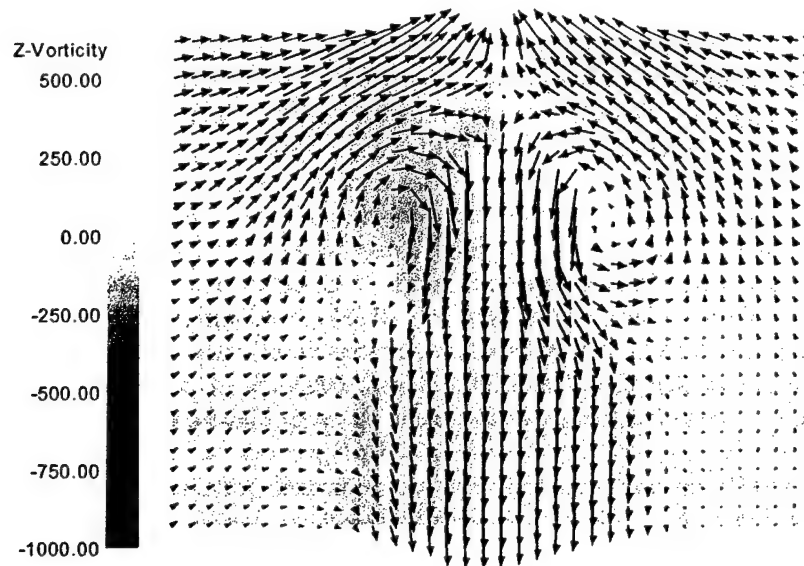
Figure 1.3: Instantaneous synthetic jet flowfield for St = 0.2

For St=2 a totally different flow pattern is produced, as shown in figure 1.4. It may be seen from this figure that for these operating conditions, during the suction cycle, the whole flowfield shown is affected by the actuator, while on the other hand, during the blowing cycle, only the areas adjacent to the orifice are affected, a behavior exactly opposite to that observed in the St=0.2 case. The flowfield for these operating conditions resembles a net suction flow. This fact can be even visually confirmed by plain observation of the visualized flowfield with the naked eye. This clearly contrasts the flowfield generated in the St=0.2 case. This different flow behavior at significantly different St numbers should be expected if one recalls the physical meaning of the Strouhal number, as the ratio of unsteady effects over inertial effects. At high Strouhal numbers, the unsteadiness is too high for the fluid mass to follow. In this case, the unsteadiness cannot "penetrate" the body of fluid that is unwilling to follow the constant change. With some tuning of the Strouhal number, this type of flowfield can nicely lend itself to transition control applications. As we have shown in our work, finer tuning of the Strouhal number can lead to a "breathing" flow pattern, in which, neither blowing nor suction dominates the flowfield. As seen in Joshi et al. (1997), this is exactly the type of boundary excitation needed to control the growth of natural instabilities that ultimately lead to turbulent transition.

A similar explanation for these two distinctly different flow patterns could be given by viewing the Strouhal number as the ratio between convection and oscillation time scales of the fluid particles in the exit orifice; if the oscillation time scales are large, convective instabilities can develop, which lead to the formation of a vortex and the jet-like profile. A fundamentally similar explanation is also presented in McCormick (2000), based on Ingard's Acoustic Streaming Criterion (Ingard, 1953).

Finally, in view of the fact that most of the applications presented above have dealt with the use of synthetic jet actuators for control of external flows, the reader may be misguided to think that they are only applicable to these types of flow. This is by no means the intention of the author. In fact, the flow control capabilities of synthetic jet actuators, make them ideally fit for turbomachinery applications and for control of internal flows. One example of their applicability to areas that are of interest to the turbomachinery research community is the work of McCormick (2000). In this study, he used a synthetic jet actuator to enhance the pressure recovery of a 2-D diffuser ($\theta = 20°$) whose operation under normal conditions (without actuation) was very close to the fully developed 2-D stall regime as defined by the Kline chart. In fact, the actuator produced a pressure recovery, which even outperformed the one generated by the optimal diffuser angle ($\theta = 13°$). Also of interest is the capability of the SJAs to delay the flow separation over airfoils/blades and generally curved or flat surfaces at high angles of attack. This potential can also be exploited by the turbomachinery research and manufacturing community for several applications.
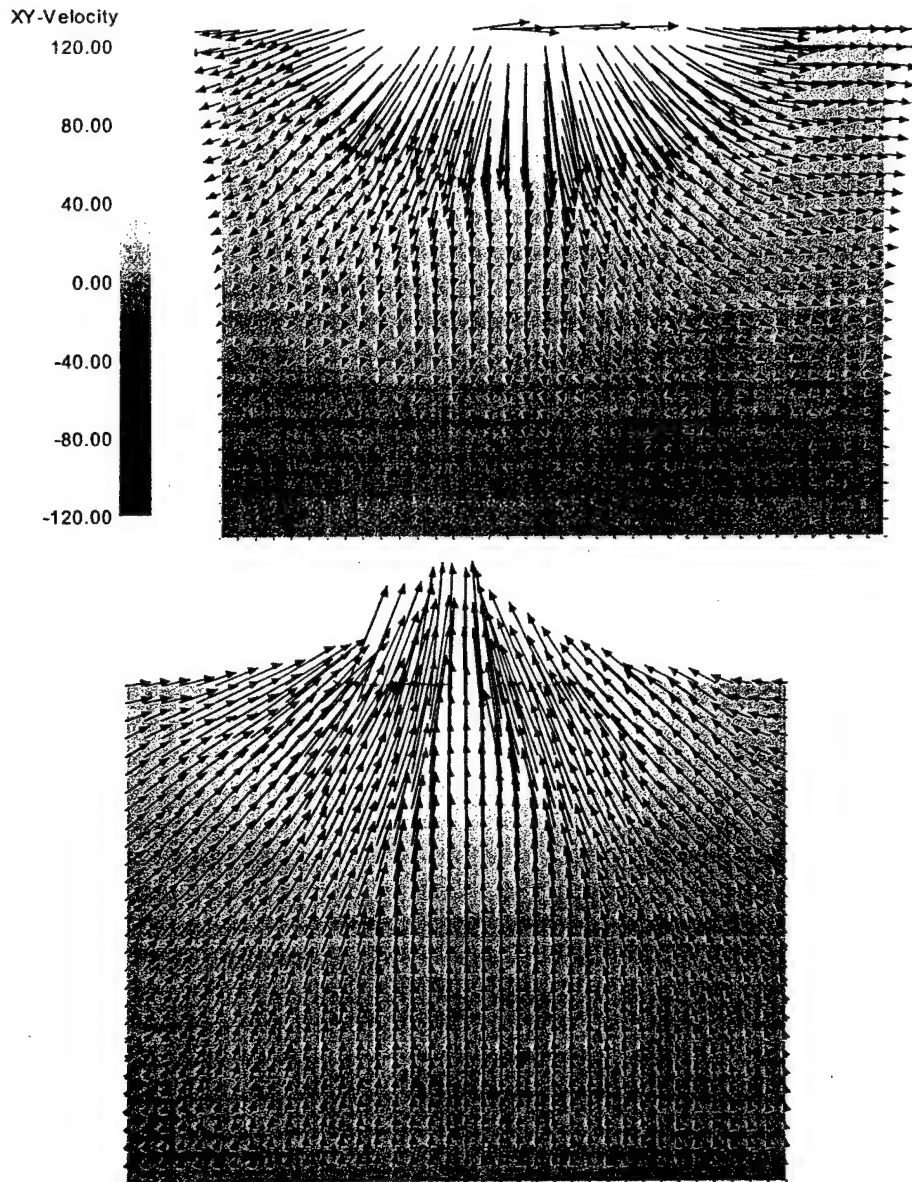
11

Figure 1.4: Instantaneous synthetic jet flowfield for St = 2. Blowing cycle (top), suction cycle (bottom).

The use of inlet guide vanes (IGV) produces an increase in the performance of a stage for the design flow conditions, but often produces a limitation in the operating range of the machine. This has been overcome partially by the use of variable geometry IGVs. The flow manipulation capability (flow vectoring) of SJAs can be used in combination with either stationary or variable geometry IGVs in order to increase the operating range of the machine at which the performance is optimal. SJAs can also be mounted on the aerodynamic surfaces of vaned diffusers in centrifugal compressors or pumps. For this case, their ability to delay the flow separation (at off-design conditions) is of great importance as it extends the operating range of the machine and enhances the pressure recovery of the diffuser leading to higher efficiencies.

Yet another application of SJA's is in the pressure recovery exhaust systems of combined cycle power plants. For this case, higher pressure recovery means a lower pressure at the turbine outlet plane. The work of Sultanian et al. (1999) shows the separation of the flowfield from the struts at off design conditions in an annular diffuser passage (with struts). This separation is due to the high levels of swirl

12

angle of the flow, which cause the flow to separate producing a large pressure drop. It is mentioned that for a gas turbine exhaust system most of the total pressure loss is associated with secondary flows in the stalled regions, hence a mechanism to reduce this stall can dramatically lower the pressure drop and increase the pressure recovery of the system. As mentioned above, the SJAs are particularly effective for this application. SJAs may also be used on the stator blades of turbomachines to increase their range of operation by delaying and/or eliminating flow separation and stall at off-design conditions. Finally, other applications may include the enhancement of heat transfer of blades and flow mixing control in turbomachinery combustion systems. For this last application, control of flow mixing has many benefits, which include a possible reduction in the size of combustors, higher combustion efficiencies, increase in the life of combustors as well as a marked favorable impact on the amount of pollutants generated during the combustion process.

In recent years, there has been a certain amount of research performed in the use of synthetic jets for flow mixing control. Ritchie and Seitzman (2000) performed experiments in which they controlled fuel-air mixing by means of an array of synthetic jets placed in the periphery of two coaxial jets. Also, Davis and Glezer (2000) showed the ability of a synthetic jet array to manipulate large and small-scale structures in coaxial jets, which led to an enhancement of the mixing process within the jets.

Preliminary results by Bae et al. (2000) suggest that synthetic jet actuators may also be used in turbomachinery applications for control of the tip clearance flows in compressor cascades.

2. DEVELOPMENT OF SYNTHETIC JET ACTUATORS

General

      This section will present the principles of operation of a synthetic jet actuator. Parameters developed by the research community used to quantify if an actuator has the capability of controlling flow separation for a certain configuration will be discussed. Development of compact, high-power synthetic jet actuators will be detailed.

Principle of Operation of Synthetic Jet Actuators

      The principle of operation of a synthetic jet actuator is illustrated in figure 2.1, which presents a cross-sectional view of a sample axisymmetric actuator. The actuator consists of a closed cavity in which one of the ends is covered by an oscillating piston. A rigid wall with a small orifice covers the other end. This orifice is the only communication of the cavity with the external flow to be controlled by the actuator. The oscillation of the piston produces a fluctuation of the pressure field in the cavity and at the orifice, causing it to periodically act as a source or a sink. The result of this is a net jet emanating from the orifice, i.e. net momentum flux. So, although there is no net mass flux addition, a jet is formed (hence the term "synthetic").

      Several ways to produce synthetic jets have been developed. For example, for piezoelectrically driven actuators, a flexible membrane is used instead of a piston. For this case piezoelectric ceramics are used to excite the natural frequency of the flexible membrane, driving it to resonance. The deflection of the membrane causes a pressure fluctuation inside the cavity similar to the one produced by the piston described above. The use of a membrane driven at its resonance frequency has some inherent drawbacks, one of which is the deterioration of the actuator performance when it is driven at frequencies which are not close to the resonant frequency of the membrane. Also the limited maximum amplitude of oscillation of the membrane requires the orifice exit to be small to obtain large exit velocities, this in turn, causes compressibility effects in the actuator to be large, increasing the energy losses within the actuator. Another way of producing a synthetic jet actuator is to have a fixed volume closed cavity with an orifice and directly supplying the desired pressure fluctuation pneumatically through plumbing. This method requires the development of a complex plumbing system with vacuum and high-pressure lines and high-speed valves, which increases the complexity of the actuator and complicates the packaging of the actuator into a wing or other surface to be controlled.
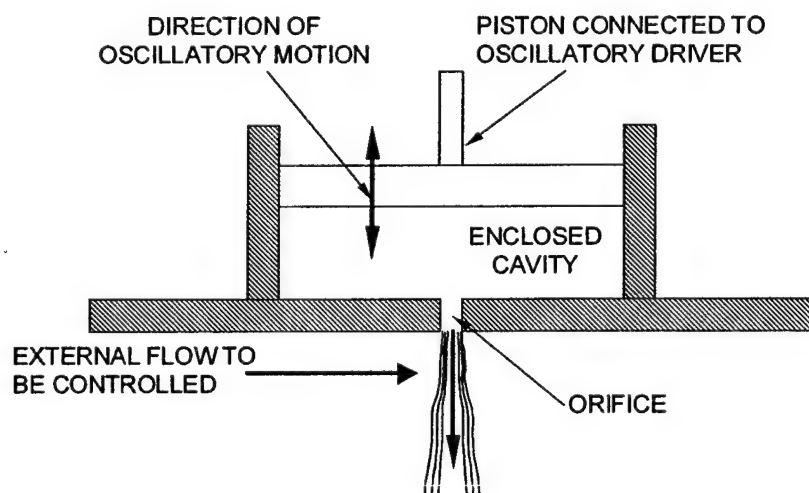
Figure 2.1: Schematic showing principle of operation of synthetic jet actuators.

      Several modeling techniques have been proposed in order to simulate the behavior of synthetic jet actuators and theoretically characterize the flowfields that they produce (Rizzeta et al., 1999, Rao et al., 2000, Müller et al., 2000 and McCormick, 2000). Due to the complexity of the flowfield generated by the synthetic jet actuators, most of the models have had to be "calibrated" in order to match the theoretical

14

predictions with the experimental measurements, and a simple analytical model is still elusive. The author and his colleagues are currently working on the modeling of the synthetic jet actuators proposed for this work, however the model is not yet available. Nevertheless, a simple way to estimate the exit velocity of the flow within the actuator is to use the continuity equation for an incompressible flow. Consider an actuator like the one shown in figure 2.2. The movement of the piston of area Ap, causes a change in the volume (Vr) of the cavity, which leads to a flow through the orifice of area Ao. The movement of the piston is defined by its velocity Up(t), while the velocity of the flow (Uo) is determined using the equation of continuity and assuming an incompressible flow (Panton, 1996).
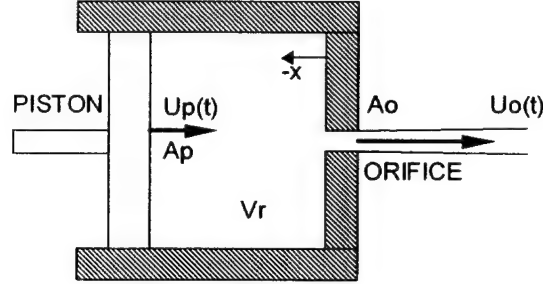
Figure 2.2: Schematic of a synthetic jet actuator for demonstration of the use of the continuity equation for incompressible flow.

For the case shown in figure 2.2, the equation of continuity may be written as:

$$\frac{d(\rho Vr)}{dt} = -\rho\, Uo\, Ao \qquad (2.1)$$

were ρ is the density of the fluid inside the cavity.

Assuming incompressible flow (ρ = constant), equation 2.1 may be written as:

$$\frac{d(Vr)}{dt} = -Uo\, Ao \qquad (2.2)$$

in view that the area of the piston remains constant as the piston moves, the change in volume (Vr) may be represented as

$$\frac{d(Vr)}{dt} = -Ap\, Up \qquad (2.3)$$

which reduces equation 2.2 to the following expression,

$$Ap\, Up = Uo\, Ao \qquad (2.4)$$

As may be seen in equation 2.4, the exit velocity of the flow is defined by the velocity of the piston and the relation between the area of the piston and the area of the orifice.

If the piston is connected to a crankshaft, as in the case of the actuator that is proposed in this work and that will be introduced later, the piston will oscillate back and forth with a velocity given by:

$$Up = Xp\,\omega \sin(\omega t) \qquad (2.5)$$

where Xp is the 0-peak amplitude of the piston stroke and ω is the rotating frequency of the crankshaft in rad/s.

As will be shown later, the use of the equation of continuity for an incompressible flow works quite well for the estimation of the flow exit velocity when the dimensions of the slot are large enough that the compressibility effects within the actuator are negligible. When the slot is small, compressibility effects in the actuator cavity become large and the flow exit velocity may no longer be predicted by this expression.

Synthetic Jet Actuators for Flow Separation Control

As mentioned in the previous section, the use of synthetic jet actuators for control of flow separation over lifting surfaces at high angles of attack has received a great amount of attention in the recent years. It is widely accepted in the literature that for such applications, the optimal non-dimensional

15

frequency (or Strouhal number) must be on the order of 1 (Seifert et al., 1993). This non-dimensional frequency is defined as:

$$F^+ = f \frac{x_{te}}{U_\infty} \tag{2.6}$$

where, f is the actuator frequency, x_{te} is the distance from the actuator to the trailing edge of the airfoil and U_∞ is the value of the freestream velocity. Seifert and Pack (2000), show that in order to be effective, an actuator must produce one to four vortices over the controlled region at all times. This is achieved by operating the actuator at or close to a Strouhal number (F^+) value of unity.

Moreover, the literature indicates that jet momentum coefficients (Cµ) of at least 0.002 are necessary before any substantial effects on the flow can be observed. This coefficient is defined as the ratio between the momentum of the jet emanating from the actuator and the momentum of the freestream. It may be calculated either using the maximum velocity at the slot exit or by using the RMS value of the jet exit velocity. For the results presented here, the jet momentum coefficient was calculated using the maximum value of the velocity of the flow exiting the jet. The expression that defines the coefficient is then (Seifert et al., 1993):

$$C_\mu = \frac{(\rho h u^2)_{jet}}{(\rho C U^2)_\infty} \tag{2.7}$$

where, ρ is the fluid density, h is the width of the jet exit, u is the amplitude of the velocity at the jet exit, C is the reference or characteristic length (for example, in this case the chord length of the airfoil) and the subscript "∞" indicates "freestream".

As mentioned in the previous section, the application of synthetic jets to flow separation control is based on their ability to energize the boundary layer. For the case of synthetic jets equipped with tangential slot exits (see figure 2.3), the actuator adds momentum to the boundary layer in several ways. During the suction part of the cycle, it draws the low momentum fluid from the near wall region into the cavity, thereby bringing the higher momentum fluid, at the boundary layer edge closer to the wall. On the other hand, during the blowing part of the cycle, it adds the same fluid with higher momentum into the flow, almost tangentially to the surface. In addition to this mechanism to increase the momentum of the fluid within the boundary layer, the oscillatory nature of the flowfield generated by these actuators, promotes the mixing of the low momentum fluid near the wall with higher energy fluid close to the edge of the boundary layer (Amitay et al., 1998). The effectiveness of this mixing process is related to the high receptivity of the shear layer. Proper excitation of the shear layer promotes the development of its natural instability, which leads to the formation of large vortical structures. These flow structures promote boundary layer mixing and hence momentum exchange between the outer and inner parts of the boundary layer.
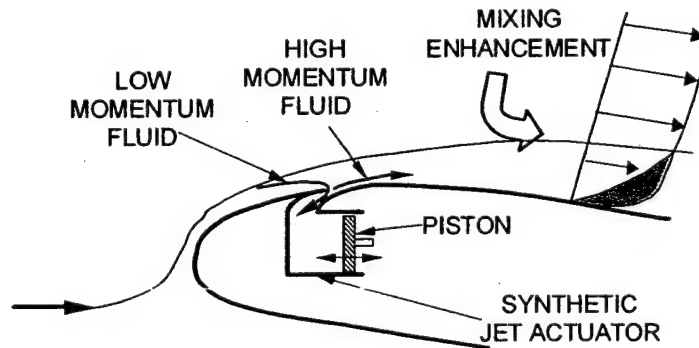
Figure 2.3: Principle of operation of synthetic jet actuators for flow separation control.

Design of High-Power Synthetic Jet Actuators

As mentioned previously, the work presented here addresses the need for compact, zero-mass-flux actuators that can be entirely housed inside a wing/blade. The development of compact, high-power synthetic jet actuators is presented in this section. These actuators do not share the limitations of often used piezoceramic-based synthetic jet actuators, which exhibit performance deterioration when operating at frequencies away from the actuator resonance frequencies and have limited maximum amplitudes.

To understand the limitations of piezoceramic actuators, consider the application of synthetic jet actuators to flow separation control over an airfoil. As mentioned above, the optimal non-dimensional actuation frequency, F^+, must be of the order of 1. Moreover, a jet momentum coefficient ($C\mu$) of at least 0.002 is also required. For practical separation control applications, in either fixed or rotary wing configurations, a typical freestream would, conservatively, be on the order of M=0.5, and x_{le} would be on the order of the wing/blade chord, which here it is assumed to be on the order of 0.6 m. Consider a representative wing/blade, as shown in figure 2.4. Given the fact that the spar cannot be structurally compromised, the entire synthetic jet actuator (SJA) assembly would have to be accommodated within the internal volume upstream of the spar. Therefore the width of the SJA driving membrane would be on the order of an average between the two dimensions of that internal volume, i.e. on the order of 0.07m. Using these values and equation 2.6, the optimal frequency is around 300 Hz. From equation 2.7 and for two jet exit width values, 1mm and 6mm (representing the low and high end of a typical width size spectrum, respectively), the following amplitudes of oscillation are obtained, using the continuity equation in the SJA chamber:

- h=0.001m: u =186 m/s, SJA membrane oscillation amplitude, A=1.5mm
- h=0.006m: u =76 m/s, SJA membrane oscillation amplitude, A=3.6mm
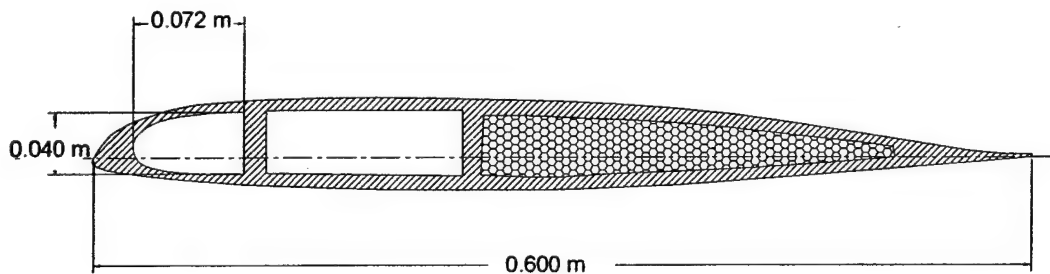
Figure 2.4: Schematic of representative wing/blade

As shown above, expected peak-to-peak strokes of the SJA membrane would be on the order of 3 mm at a frequency around 300Hz. These values are far from optimal for piezoelectric actuation. The required amplitudes are significantly larger than what piezoceramics are typically capable of and the required frequencies are lower than those at which piezoceramics have competitive power densities. In contrast, these numbers are ideal for rotary motor actuation. Compact electric motors exist, off-the-shelf, with optimal performance at around 18,000 rpm (or 300 Hz), measuring 25mm in diameter and 37mm in length, weighing 70 grams and with very competitive power densities (400 Watts per 70 grams, or 5.7KW/kgr).

The proposed principle of the SJA driving mechanism is well-developed, and has been extensively utilized in a variety of engines. It consists of a DC motor with its shaft connected eccentrically to a crank, which is in turn connected to the membrane/piston of the SJA. Due to the eccentricity, the rotary motion of the motor is translated to linear motion of the SJA membrane/piston. This design offers significant benefits over, for example, piezoceramic driving mechanisms:

- it can achieve membrane/piston oscillation amplitudes at least an order of magnitude higher.
- it eliminates the dependence of oscillation amplitude on the oscillation frequency, which plagues piezoceramic mechanisms.
- with available state-of-the-art, high power-density electric motors it can match and exceed the power densities of piezoceramic mechanisms.
- it requires significantly smaller driving voltages.

17

For the case of the proposed DC motor driven SJAs, electric motors drive a series of "off the shelf" small gasoline engines which are used as reciprocating compressors. The cylinder head of each of these engines is perforated and attached to a common plenum, which is closed on all sides except for a slot machined on one of the walls (see figure 2.5). The engines are synchronized, therefore the change in the cavity volume of the plenum is equal to the sum of the individual displacements of the pistons multiplied by the area of the pistons. The use of the available engine technology reduces the effort to manufacture pistons with no leakage, thus simplifying the design and construction of the SJA. Figure 2.6 shows some of the off-the-shelf components that were used in the construction of the actuators.

Single Piston Prototype

The first attempt to produce a DC motor driven SJA consisted of a single piston prototype. It was fabricated using spare parts from an O.S. Engines model number F.S. 52S four-stroke engine, with a displacement of 8.56 cubic centimeters (cc). The piston had a diameter of 23.0 mm with a stroke length of 20.6 mm. This engine was driven by a small DC electrical motor, with a maximum rated power of 325 W. This prototype is shown in figure 2.7. The chamber internal dimensions were $10.0 \times 25.4 \times 63.5$ mm^3, with an exit slot measuring 76.2×0.8 mm^2 or 76.2×1.6 mm^2. In other words, two different exit slot widths were tested (with the same chamber internal volume). These two configurations were tested in order to help the identification of the possible effects of slot dimensions on flow compressibility. The SJA was also equipped with a sensor that allowed the measurement of the operating frequency. As mentioned in the next section, exit flow velocity measurements were obtained for this prototype for a range of operating frequencies between 60 and 230 Hz. Results from these measurements will be shown in a later section. However, as it should be intuitively expected, compressibility effects are more pronounced for the narrow slot and for the higher oscillation frequencies.
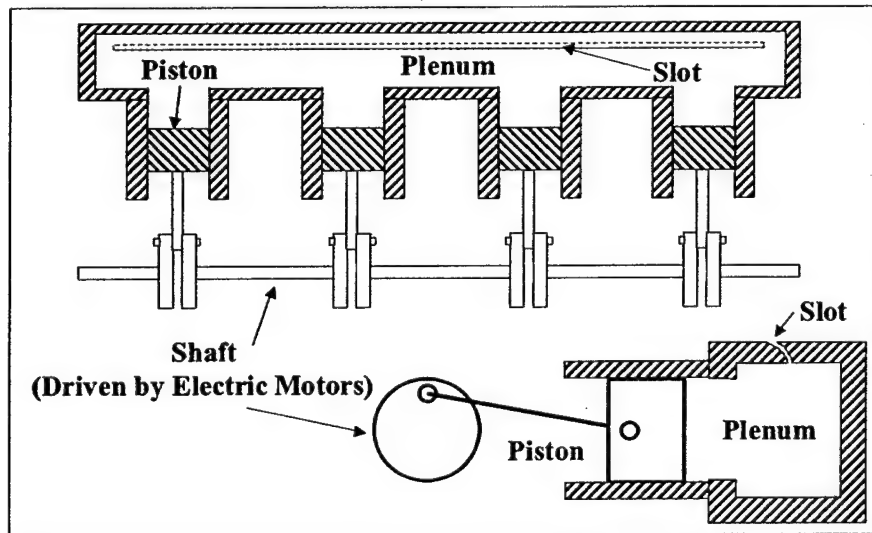
Figure 2.5: Schematic of DC motor driven synthetic jet actuator.

First Generation Synthetic Jet Actuator Array

Figure 2.8 shows the prototype first generation SJA array. As may be seen in the figure, it is composed of 4 reciprocating compressors (engines) which are driven by two DC motors. The geared shafts provide the required synchronization of the engines. Each engine had a displacement volume of 1.4 cc, with a peak-to-peak piston stroke of 12 mm, and a piston diameter of 12.5 mm. Each DC electric motor measured 50.8mm in length and 37 mm in diameter, had a maximum power of 100 W and weighed 0.2 kg. Compared to the second generation SJA array described later, this was a relatively low power, low maximum exit velocity array. It was first tested outside the wing and it yielded a maximum exit velocity of about 10 m/sec at a frequency of 200 Hz.
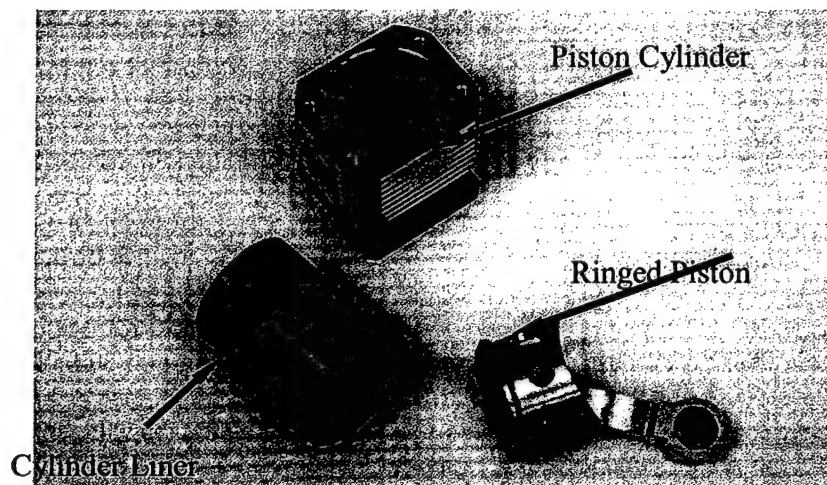
Figure 2.6: Off the shelf components used in the assembly of the synthetic jet actuator.

This setup was subsequently installed into a NACA 0015 wing with a chord length of 0.375 m, and a maximum thickness of 56.0 mm. The exit slot was placed at a distance of 43 mm from the leading edge on the upper half of the wing. The exit slot was machined so that it exits tangentially to the surface of the wing; it has a width of 0.8 mm and a length (spanwise) of 0.254 m. The wing with the SJA array is shown in figure 2.9. As may be seen in the figure, the entire actuator fits inside the cavity of the wing, making this SJA completely self-contained. To the authors' knowledge, besides the piezoelectrically driven actuators mentioned previously, this is one of the first non-piezoelectrically driven self-contained SJA. The tangential exit slot of the SJA may be seen on top of the wing.

The wing-SJA assembly was then tested in the 3'x4' Aerospace Engineering wind tunnel. The objective of this first generation SJA testing was to validate the flow separation principle and optimize SJA array parameters and slot location and dimensions. The installation of the wing in the test section and the experimental setup are shown in figure 2.10. Only flow visualization tests were performed at this phase. The smoke stream was introduced upstream of the wing and the flow patterns were recorded with a high-speed digital camera. Figure 2.11 presents the visualized flow over the wing, at an angle of attack of 20 degrees, without (top) and with (bottom) SJA actuation. The freestream velocity for these preliminary tests was 20 m/s, which corresponded to a Reynolds number of 5.9×10^5. Without SJA actuation, the flow separates very close to the leading edge and the wing is in the post-stall region. With SJA actuation, the flow remains attached over about 70% of the wing chord.

Second Generation High-Power Synthetic Jet Array

The knowledge gained from the first generation SJA array was used to develop a second generation, significantly more powerful array that could fit within the same wing. A schematic of the second generation array is shown in figure 2.12. It is composed of 6 reciprocating compressors (pistons) which are driven by two DC motors (Astro-Flight Model Cobalt 341). Each piston had a diameter of 27.7 mm and a peak-to-peak piston stroke of 22 mm, which generated a displacement volume of 13.26 cc. Each DC motor measured 69.8 mm in length and 41.1 mm in diameter, had a maximum power of 800 W and weighed 0.34 kg. As shown in figure 2.12, initially the motors were arranged in parallel to the camshaft in order to keep the span of the device smaller that the span of the wing internal cavity, however as mentioned in the next chapter, problems with the gears used in the driving mechanism (not shown in the figure), required the modification of this initial configuration. Compared to the first generation array, this was a significantly more powerful, high maximum exit velocity array. Figure 2.13 presents some of the details of a single engine cylinder and its interfacing to the crankshaft.
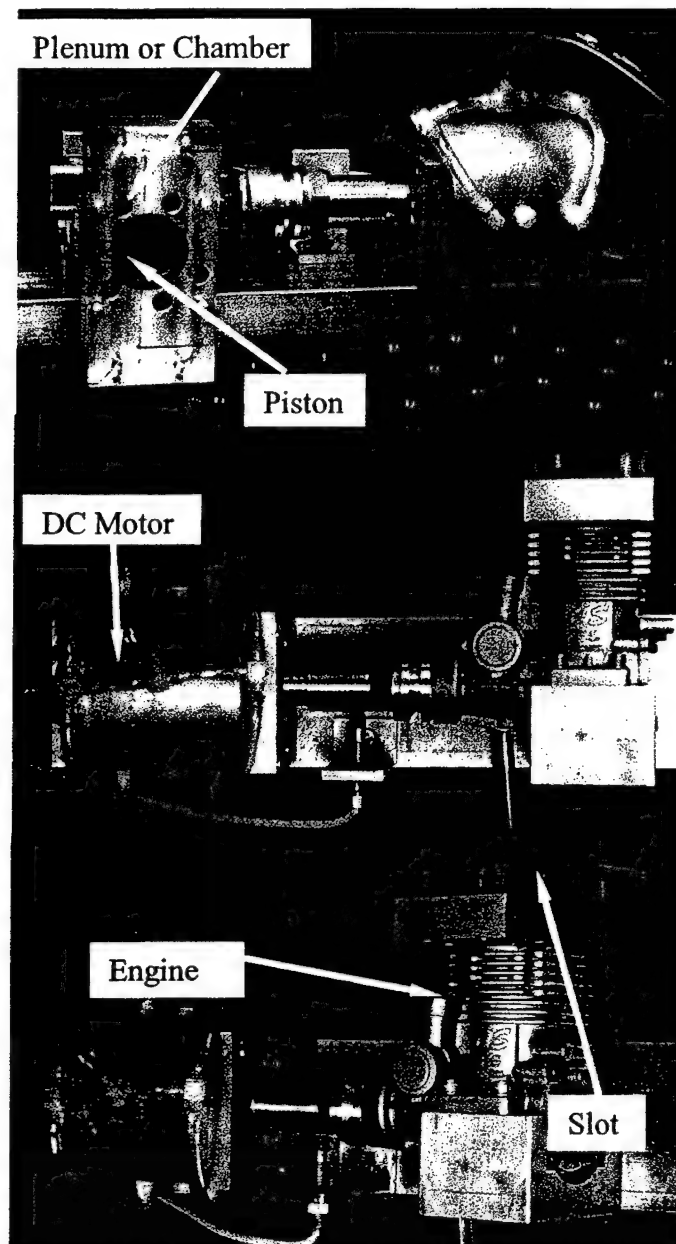
Figure 2.7: Single piston synthetic jet actuator prototype
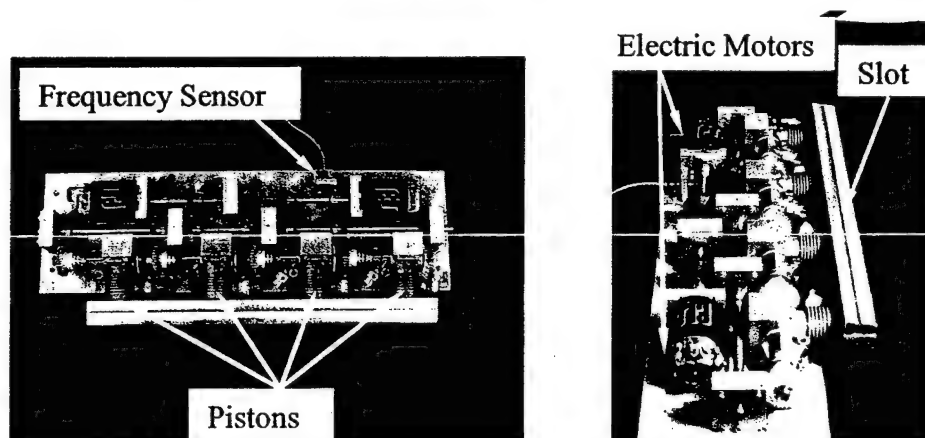
Figure 2.8: First generation synthetic jet actuator array.
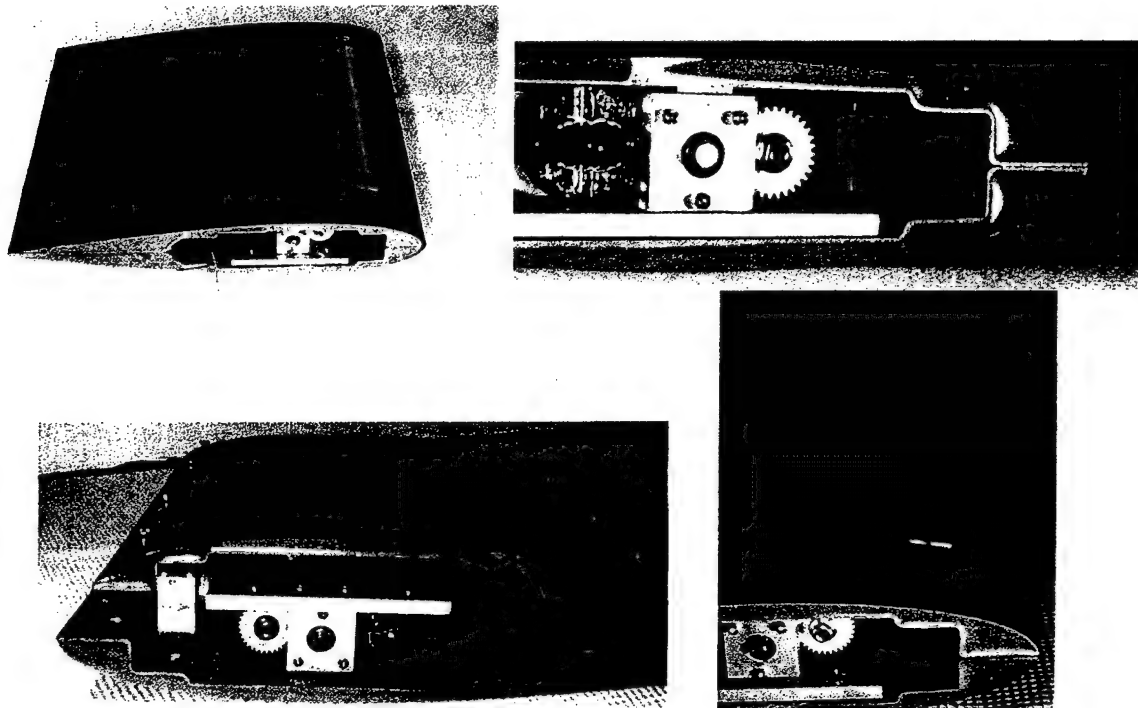
Figure 2.9: First generation synthetic jet actuator array installed in test wing
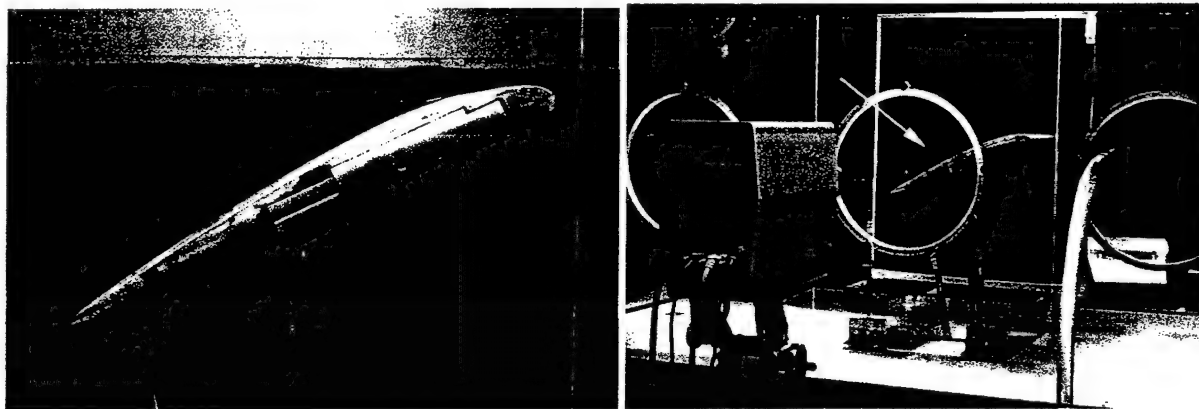
Figure 2.10: Preliminary test of first generation synthetic jet actuator array.

Figure 2.14 shows a schematic of the plenum cross-section illustrating the exit slot geometry and relative plenum internal volume. As may be seen in the figure, the exit slot is curved in order to permit the jet to exit tangentially to the surface of the wing (not shown in figure), taking advantage of the Coanda Effect. The value of the exit slot width was decided based on the following considerations. The maximum wind tunnel speed that could be achieved in the facility that would be used for the testing of this actuator was 45.0 m/sec. This, along with the given wing dimensions and a reduced frequency F^+ of 1, yielded a maximum needed frequency of 120 Hz. The SJA was designed to have a frequency range of 0 to 200 Hz, however due to limitations on the available power from the power supply, the maximum frequency of the actuator was 140 Hz. For the given engine stroke and displacement volume, and using the incompressible continuity equation mentioned in previous sections, the exit slot maximum velocity could be expressed as a function of frequency and exit slot width. From the above, figure 2.15 was generated, presenting the variation of the jet momentum coefficient $C\mu$ and its dependence on frequency and slot width for a given freestream velocity of 45 m/s. In order to avoid compressibility effects within the actuator chamber and

21

keeping in mind the required value of Cμ of at least 0.002 for an optimal frequency of 120 Hz, a slot width of 2 mm was selected.
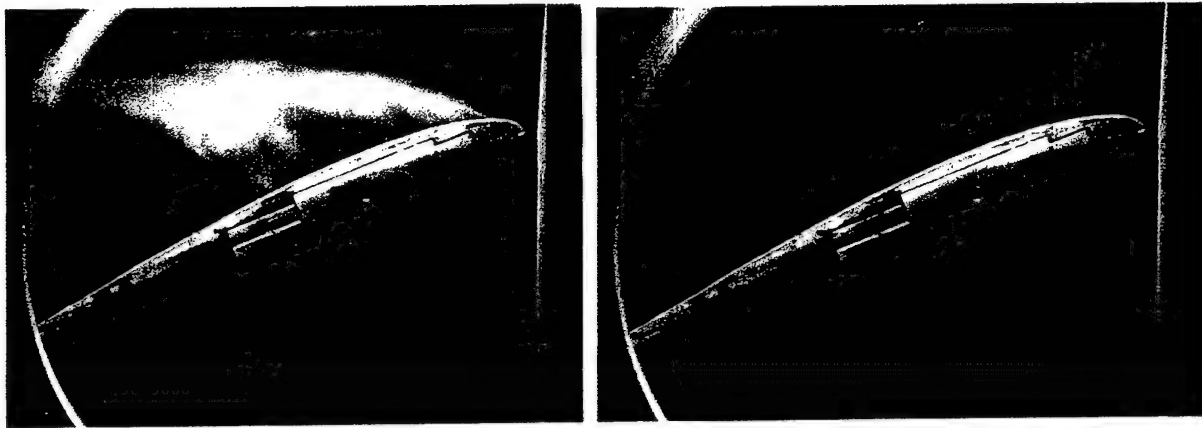
Figure 2.11: Preliminary flow visualization over wing, without (top) and with (bottom) actuation.
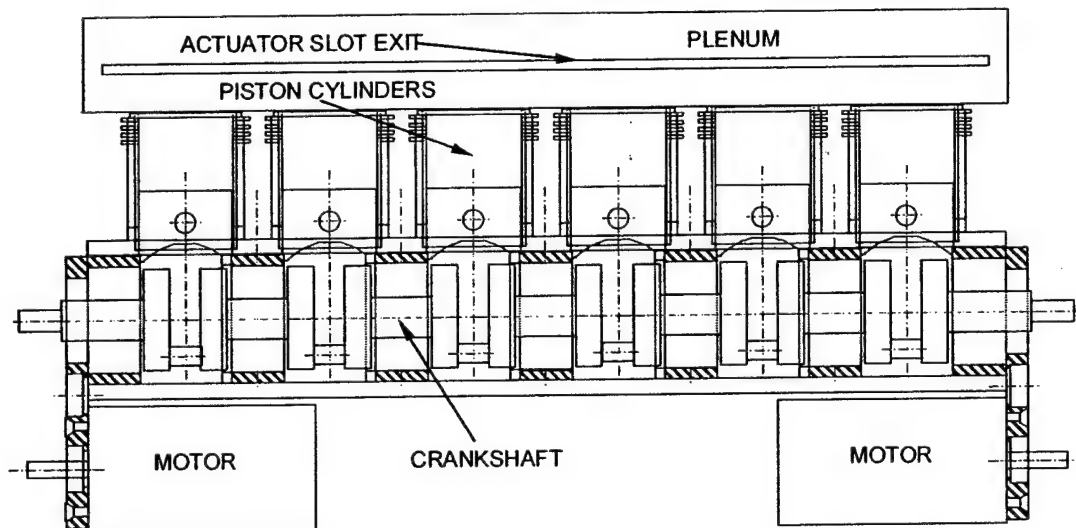
Figure 2.12: Schematic of second generation synthetic jet array.
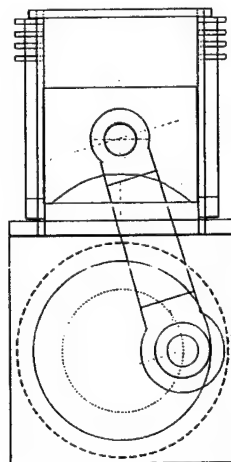
Figure 2.13: Schematic of piston–cylinder assembly and interfacing with crankshaft.

Figure 2.16 shows pictures of the second generation SJA array illustrating details on cylinder arrangement, slot geometry and cylinder phasing. It should be noted that the cylinders had to be properly phased in order to reduce array vibration The piston phasing typical of a six cylinder in-line engine was used for this actuator (de Silva, 1999). By referring to the bottom picture of figure 2.16 and numbering the cylinders from 1 to 6, starting from the left, the phasing was as follows: cylinders 1 and 6 at 240 degrees, cylinders 2 and 5 at 120 degrees and cylinders 3 and 4 at 0 degrees. The phasing of the pistons was achieved by proper phasing of the crankpins that connected to piston to the crankshaft as shown schematically in figure 2.17. It was found that the reduction in vibration severity from the unphased to the phased SJA operation was dramatic. This phasing in turn required the compartmentalization of the plenum, as it is obvious that if the plenum was not divided into six individual compartments, each one corresponding to each of the six cylinders, the engine phasing would result in zero net volume change during an operation cycle and thus no synthetic jet effect. The dimensions of each compartment are 6.35 x 24.1 x 44.7 mm^3.
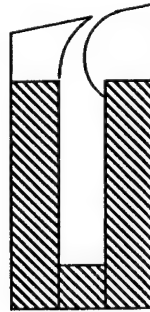
Figure 2.14: Plenum cross section showing exit slot geometry.
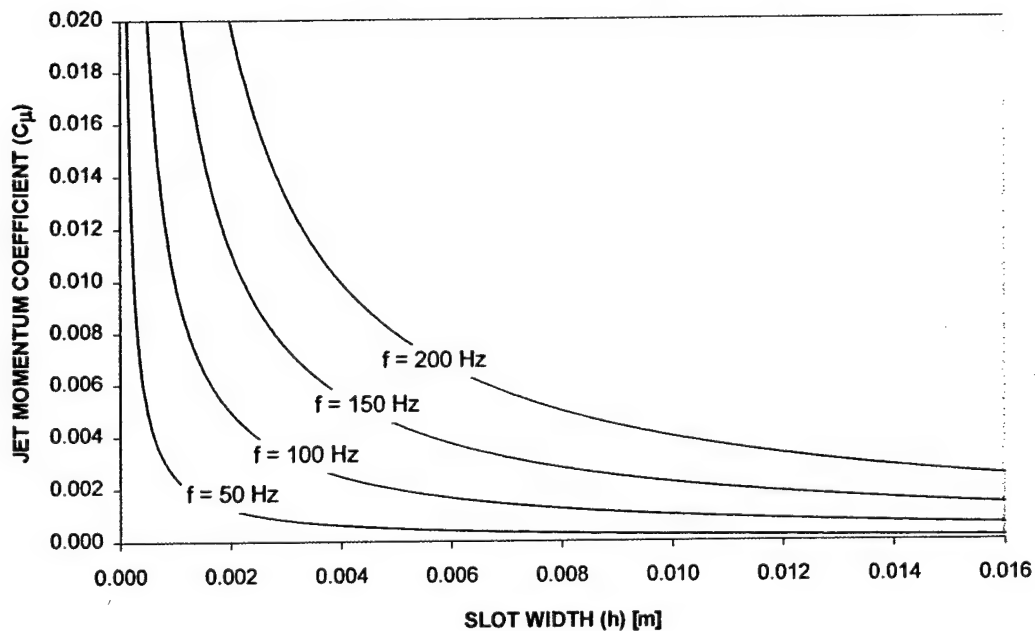
Figure 2.15: Dependence of Cμ on actuator frequency and slot width for $U_\infty = 45$ m/s.

The array was first tested outside the wing in order to document the maximum exit velocity as a function of frequency as well as investigate the effects of cylinder phasing and plenum compartmentalization to the flow. These tests will be described in the next section. However, it is important to state that initially, due to the difficulty of making walls to separate the flow within the jet exit, only the plenum for each individual piston was separated from each other (see figures 2.18 and 2.19). Preliminary results with this configuration showed that there were still strong interactions between

23

the jets generated by each piston, which were detrimental for the performance of the actuator (Gilarranz and Rediniotis, 2001b). This required the separating walls included in the plenum of the actuator to be extended up to the slot exit, as shown in figures 2.19 and 2.20. Tests performed on the actuator after these modifications showed that the extension of the wall actually was beneficial for the actuator performance. Subsequently the array was installed inside the wing and tested in the wind tunnel.

After the tests performed on the actuator without the wing were completed, it was installed in the test wing and extensive wind tunnel testing was performed. Details on the apparatus and procedure may be found in the next section.
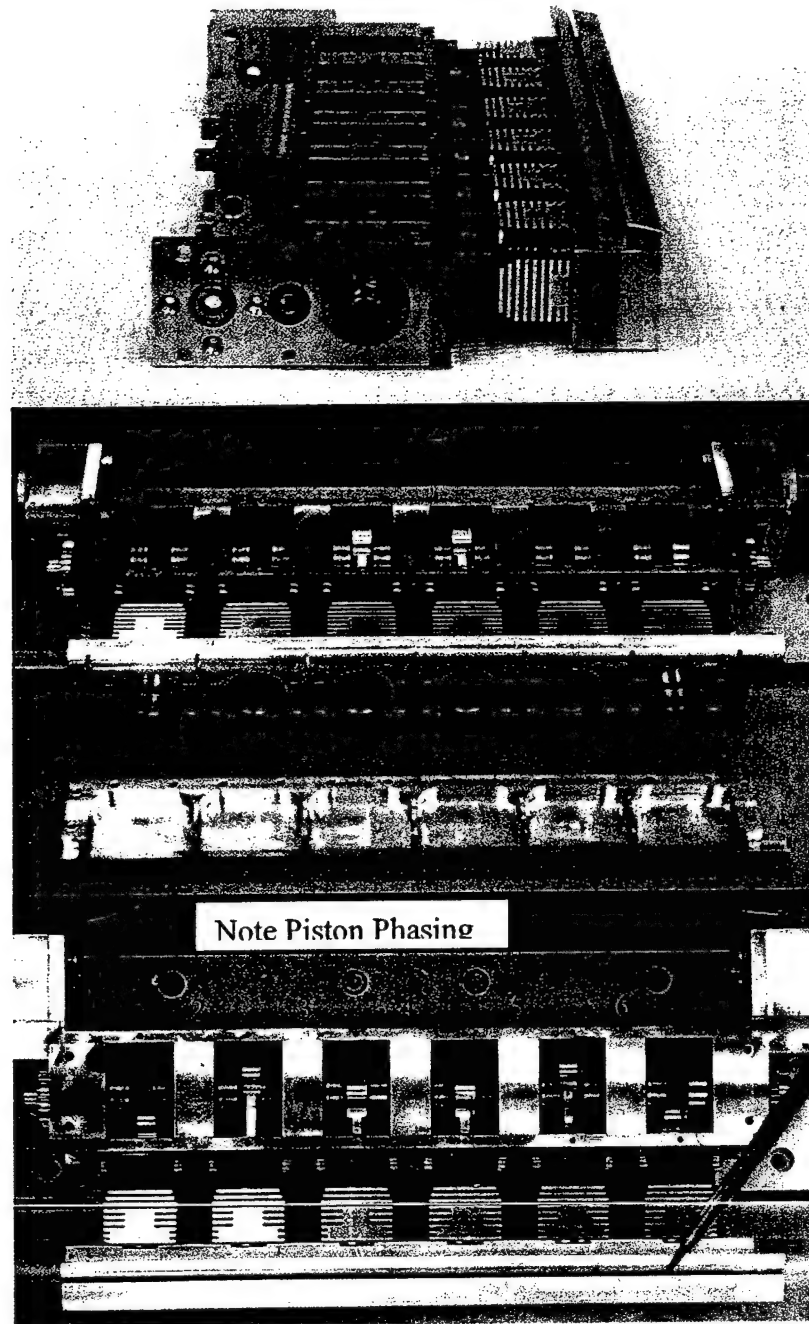
Figure 2.16: Second generation synthetic jet array.
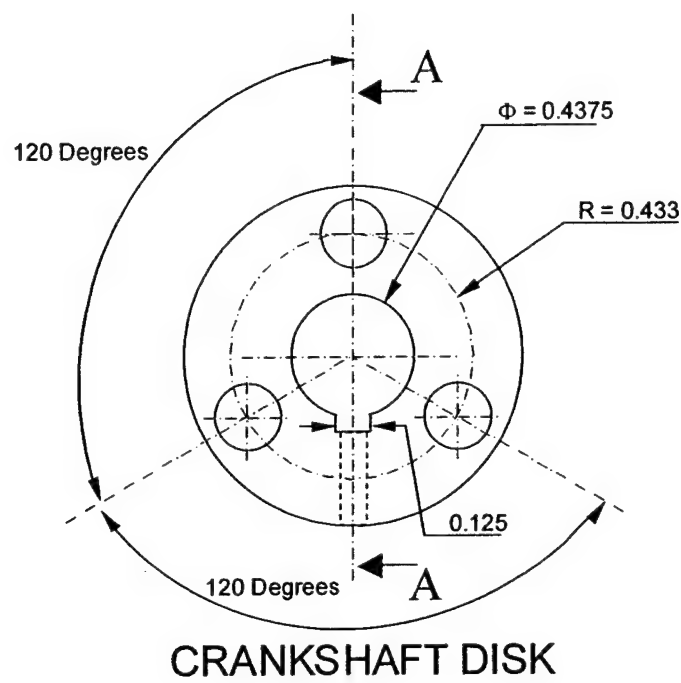
CRANKSHAFT DISK

Figure 2.17: Schematic of crankshaft disk, showing the three locations of the crankpins used to phase the pistons.

No separating walls in this region
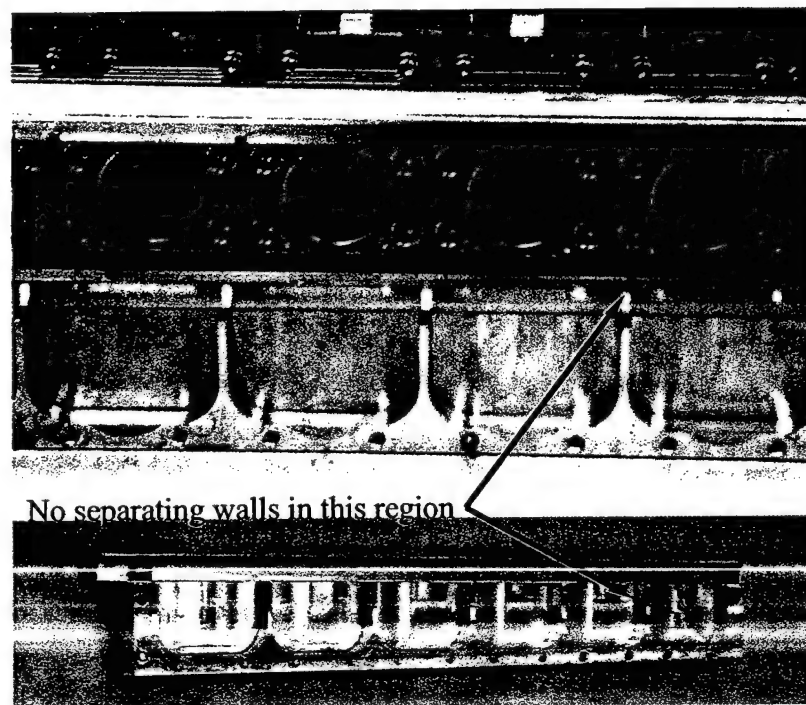
Figure 2.18: Initial configuration of plenum separating walls.
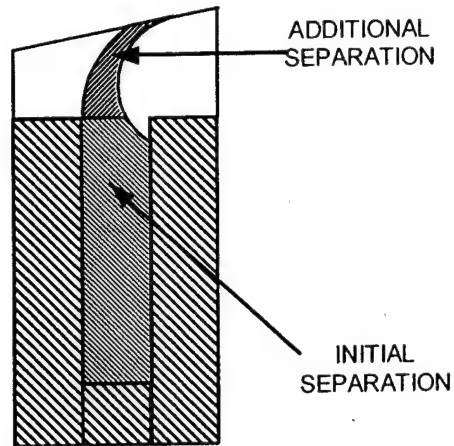
Figure 2.19: Schematic of plenum separation walls.
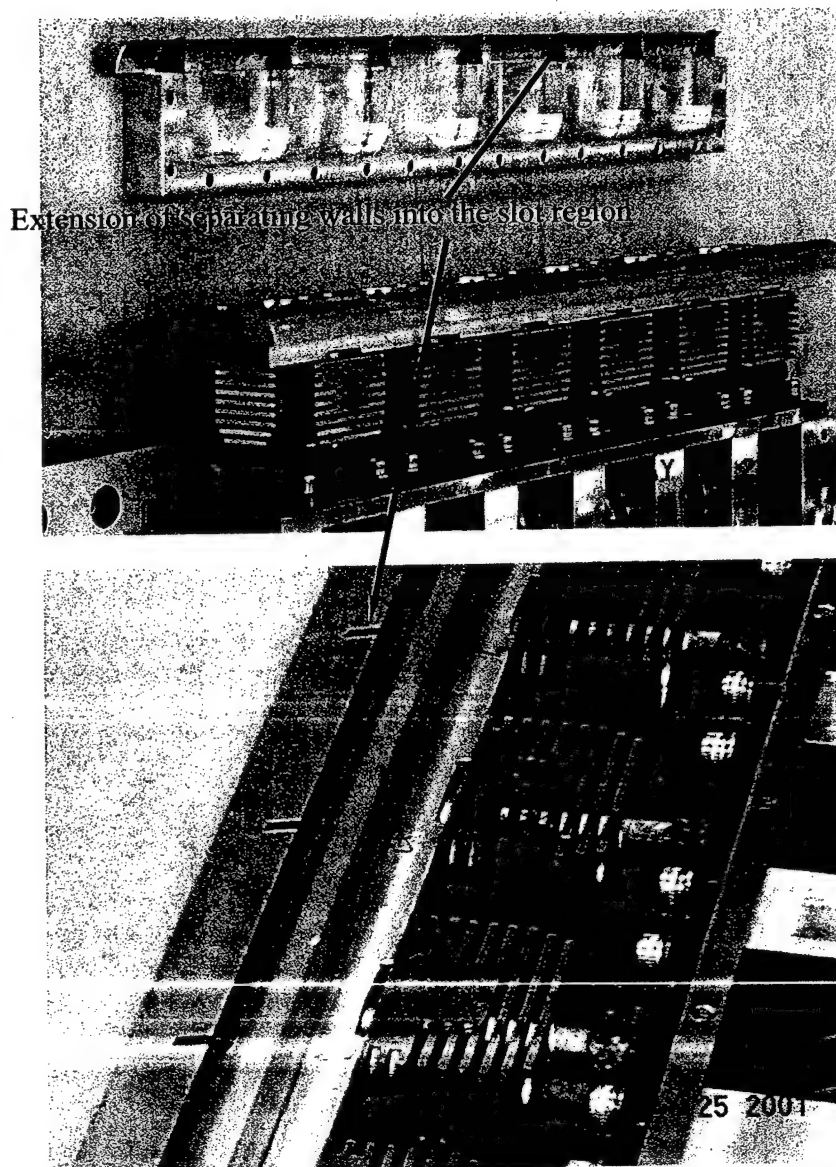
Figure 2.20: Final configuration of plenum separation walls.

3. EXPERIMENTAL SETUP AND PROCEDURES FOR ACTUATOR CHARACTERIZATION AND STEADY WIND TUNNEL TESTS

General

The performance of the synthetic jet actuator was evaluated using two different experimental setup configurations. The first configuration was designed to characterize the flowfield of the synthetic jet actuator. For this case, the tests involved the measurement of the instantaneous slot exit velocity of the actuator, both as a function of frequency for a fixed spatial position, or as a function of the spatial position for a certain operating frequency. These tests were performed with the actuator out of the wing and installed on a specially designed test bench. The second test configuration comprised wind tunnel testing of a model wing in which the actuator was installed, with the objective of evaluating the performance of the proposed actuator as a flow separation control device.

Bench Tests

In order to characterize the flowfield generated by the synthetic jet actuator, it was installed on a dedicated test bench. The test bench consisted of a 0.6 m x 0.9 m optical table (similar to the ones used for aligning laser optic elements) on which the actuator was mounted using a mounting plate. A three component traversing system was used to provide accurate placement of the measurement probes that were used during the tests. For the results reported, two types of measurement probes were used, a hot-wire anemometer and a fast response pressure probe. The data collected from the measurement probes were acquired using a P.C. equipped with a 16 bit A/D board. The traversing system was based on a Unidex 12 controller, which was connected to a data acquisition computer via a serial port. The accuracy of this system in position is within 0.01mm. Cooling air was provided to the electrical motors used to drive the actuators to extend the time period for which the actuators could be operated continuously at high frequency. The operating frequency of the actuator was measured using a Bently Nevada 3300 type proximity probe system connected to a frequency digital display. The proximity probe was placed in such a way that it sensed a coupling that was designed for this purpose and that was attached to the shaft of one of the electrical motors (see figure 3.1). The coupling had a notch machined into its surface, which caused a change in the output voltage of the probe every time the notch passed under the proximity probe. This periodic change in voltage was measured by a Fluke multimeter with a frequency sensing capability. This system was able to measure the frequency with an accuracy of 0.1 Hz. A Hewlett Packard 6269B DC power supply capable of providing 0-40 volts and 0-50 amperes was used to provide the required electrical power to the actuator.

Data Acquisition Code:

A data acquisition program was written in VisualBasic for this bench test application to acquire the instantaneous slot exit velocity data. The code required the input of:
- X, Y and Z initial positions to which the user wanted to move the measurement the probe .
- Calibration curves for the hot-wire probe and pressure transducer. This data was provided by the user in a file, which the program reads.
- Sample rate and number of samples per channel.
The acquired data included the signal from the proximity probe, the voltage output of the hot-wire sensor and the voltage output of the pressure transducer. Each data channel was sampled at the selected sample rate until the required number of samples were taken. The calibration curves were used to calculate the flow velocity at the specified frequency and position. For each measured data set, the data acquisition code also displays graphically the real time values of all parameters acquired by the code such that erroneous data can be instantly recognized. The program outputs to a monitor, and also stores all of the data to an output file.

The hot-wire system used to measure the slot exit velocity consisted of a TSI 1201 hot-wire probe interfaced with an A.A. Lab Systems Anemometer. The system was used in a constant temperature mode. A pressure probe was also used for the measurement of the slot exit velocity (see figure 3.2). This pressure probe was designed and assembled, following an analysis of the dynamic response

considerations for pressure-measuring instruments (Holman, 1994), using a 50 mm long stainless-steel hypodermic tube with an inner diameter of 0.25 mm. These dimensions provided a system with a behavior similar to a system with a critically damped dynamic response as may be seen in figures 3.3 and 3.4, which were generated experimentally by the author. Note that for frequencies of up to 400 Hz the amplification by the pneumatic system (which consists of the pressure transmitting tubing and pressure transducer cavity), of the measured pressure is within 2 percent of the actual value. The fast response pressure transducer used with the probe was an Endevco Model 8507C-2 with a range of ±213.8 kPa with a full-scale voltage output of 300 mV. The RSS accuracy of this transducer is 1.5 % of full scale, this includes the effects of non-linearity, repeatability and hysteresis. An Entran voltage amplifier (model IMV-15/10/100A-WW) with a gain of 100 is used to amplify the pressure transducer output signal, yielding the capability of resolving pressures down to 1 Pa.

Both measurement systems (hotwire and fast response pressure probe) were calibrated on a daily basis before any measurements were taken. The calibration was performed using a TSI 1125 probe calibrator while monitoring the chamber pressure with an Edwards Barocell pressure transducer.
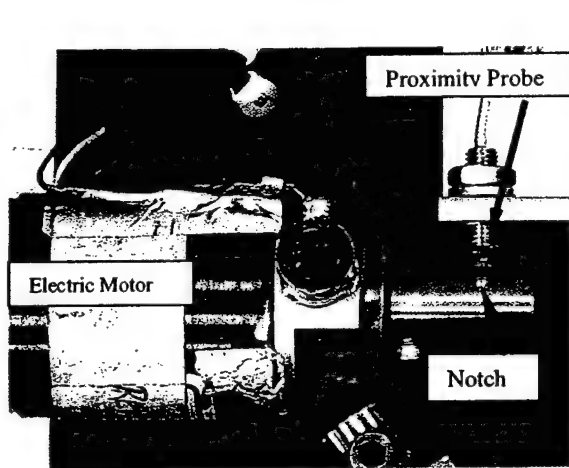
Figure 3.1: Location of proximity probe for frequency measurement.
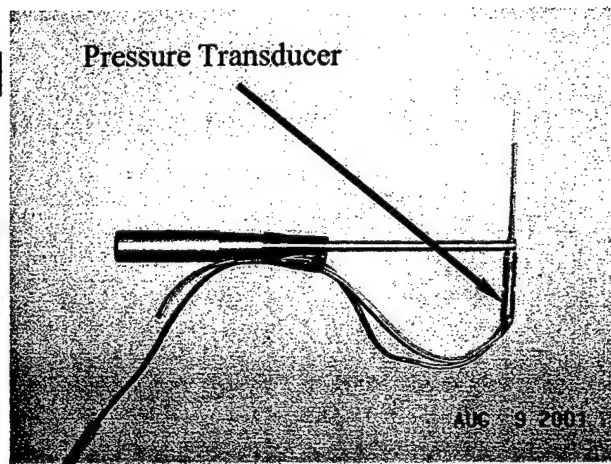
Figure 3.2: Fast response pressure probe.
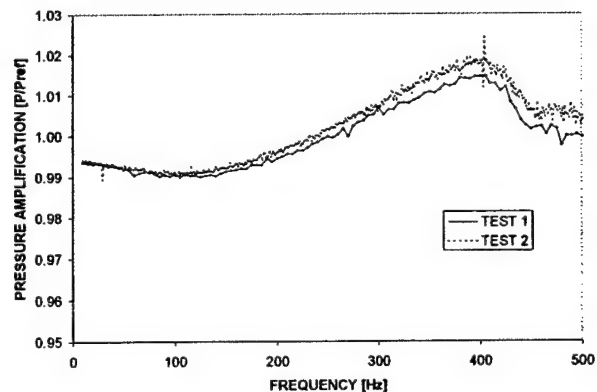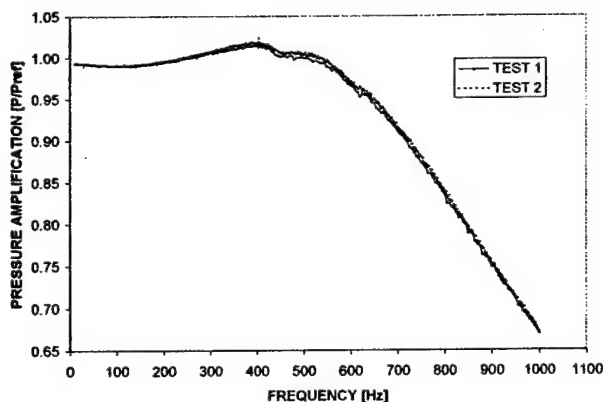
Figure 3.3: Dynamic response of fast response pressure probe, pressure amplification.
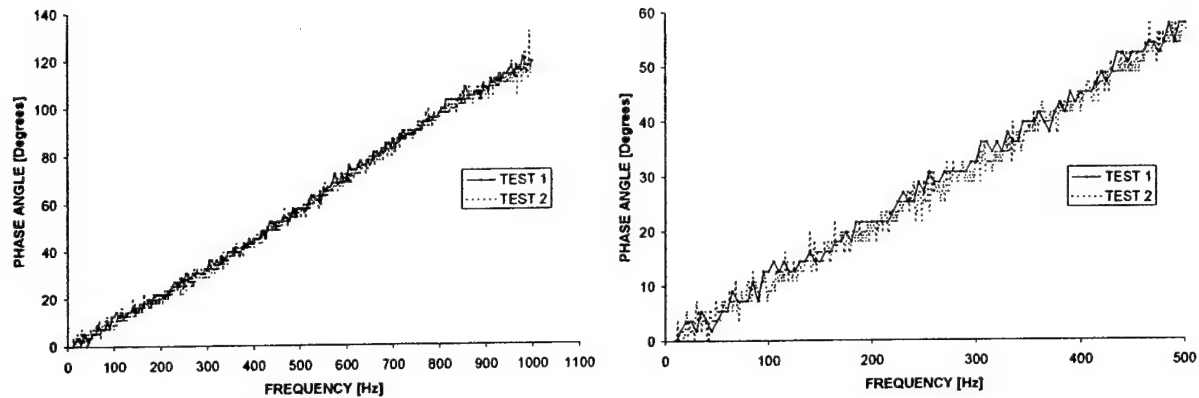
Figure 3.4: Dynamic response of fast response pressure probe, phase angle.

The bench tests involved two studies. The first types of tests consisted of the measurement of the instantaneous slot exit velocity at a fixed position for several values of actuator frequencies. The second type of tests consisted of measuring the slot exit velocity of the actuator at many spatial locations (by traversing the measuring probe) at a fixed actuator frequency. The measured data included the voltage signal from the proximity probe, the voltage output of the hot-wire sensor and the voltage output of the pressure transducer.

The first type of tests comprised of selecting the desired location at which the measurements were to be performed (typically at the slot centerline), and the range of velocities to test. After this the actuator was set to the selected operating velocity and the program would acquire the data. The program then prompted for a new velocity and after the change in velocity was acknowledged, the program would acquire the new set of data. Due to the large amount of data that was typically collected for each operating condition, the data corresponding to each data set was stored in a different file. This procedure was repeated until the data corresponding to all of the test conditions was obtained.

The second type of tests comprised selecting the desired actuator frequency at which the measurements were to be performed, and the spatial locations at which measurements would be taken. Typically, the measurements that were performed for this type of tests were performed close to the center of the slot exit (in the chordwise direction, see figure 3.5) and the measurement probe was traversed in the spanwise direction to cover the whole width of the actuator. After selecting the measurement locations, the actuator was set to the selected operating velocity and the program would proceed to move the probe to the desired locations and acquire the data. It is important to state that for this case the data acquisition was automated once the process started, that is the user only had to maintain the actuator frequency at a constant value and the code controlled the motion of the probe and sent it to each one of the required positions, waited for about 1 second and took the data. Due to the large amount of data that was typically collected for each spatial location, the data corresponding to each data set was stored in a different file.

Several synthetic jet actuator configurations were tested in the test bench described in the previous paragraphs, however in this work, the author will only include the information on the measurements performed on two of these configurations. The first configuration corresponds to the single piston actuator that was originally developed as a proof of concept technology demonstrator. The second configuration corresponds to the finalized version of the multi-piston synthetic jet actuator, which was then installed in a wing and tested in the wind tunnel.

Single Piston Actuator

The design specifications of this actuator were included in the previous chapters. The tests performed on this synthetic jet actuator were limited to the measurement of the exit slot velocity at its centerline as a function of actuator frequency. Two different slot exit geometries were tested. One of them corresponded to a 0.8 mm wide slot and the other one to a 1.6 mm wide slot. Details of this configuration may be found in the previous section. Data was taken in the range of frequencies between 60 and 230 Hz.

For these tests only hotwire data was recorded. Figure 3.6 shows details of the configuration used for these tests.

Multi-Piston Actuator

The design specifications of this actuator were presented in the previous chapter. This actuator was later installed inside the test wing for the aerodynamic tests that were performed in the wind tunnel. The tests conducted on this synthetic jet actuator comprised measurement of the slot exit velocity at the centerline of the actuator as a function of actuator frequency, as well as measurement of the exit velocity as a function of spanwise location for a given actuator frequency. Figure 3.7 shows details of the configuration of the experimental setup used for these tests. Figure 3.8 presents a schematic of the actual location of the measurement probes during the tests, as well as pictures of the actual setup.

For the case of the tests that measured exit velocity as a function of frequency, the measurement probe was usually placed at the centerline of the exit slot (both in the chordwise and spanwise position), and the frequency of the actuator was varied within the range of 30 to 130 Hz. Measurements were typically made at 10 Hz intervals.

For the case of the test that measured the exit velocity as a function of the spanwise location, the measurement probe was usually placed at the center of the slot exit (in the chordwise direction) and then it was traversed spanwise to cover the width of the whole actuator (six individual exit slots). Typically measurements were taken at ten spanwise locations for each exit slot, which totaled sixty spanwise positions per test.
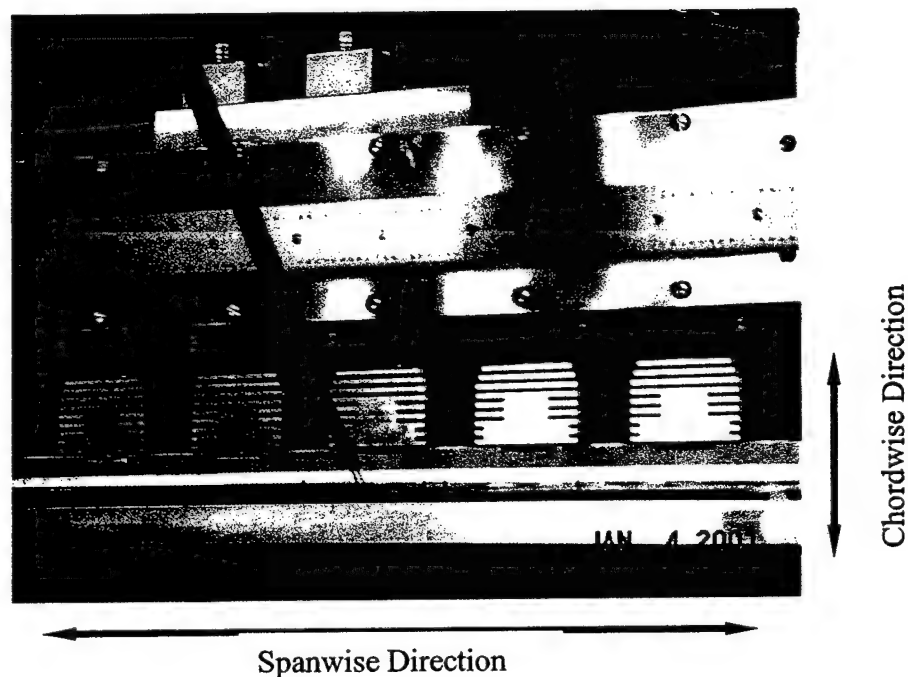
Figure 3.5: Definition of the probe directions of movement.
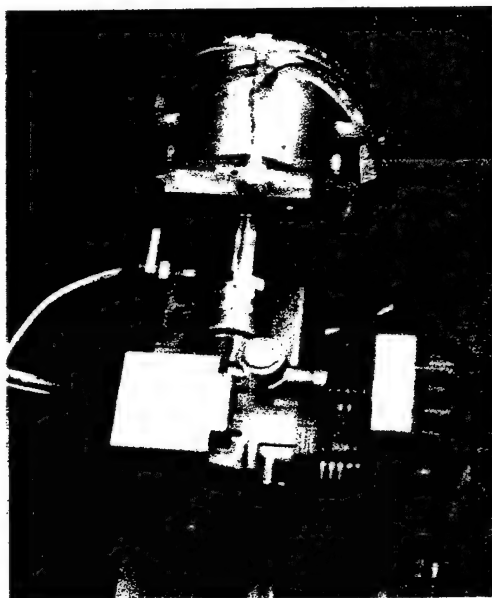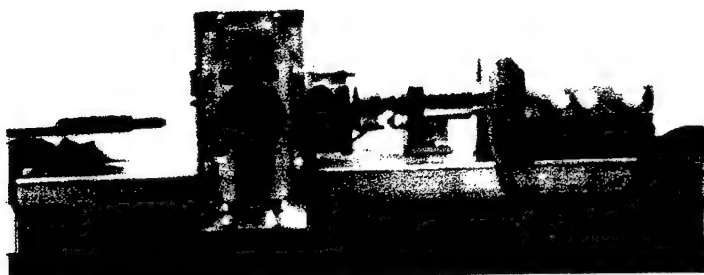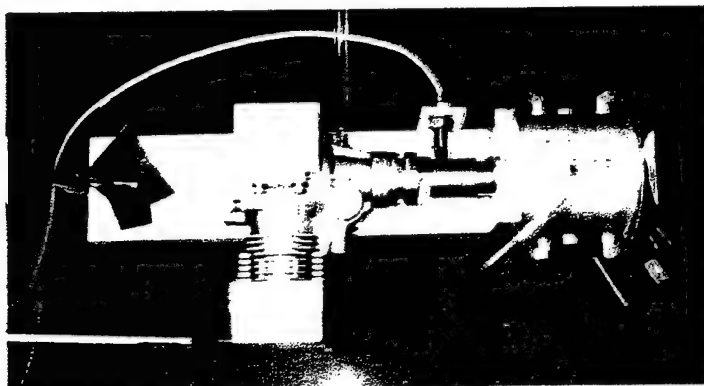
Figure 3.6: Experimental setup configuration for single piston actuator bench test.
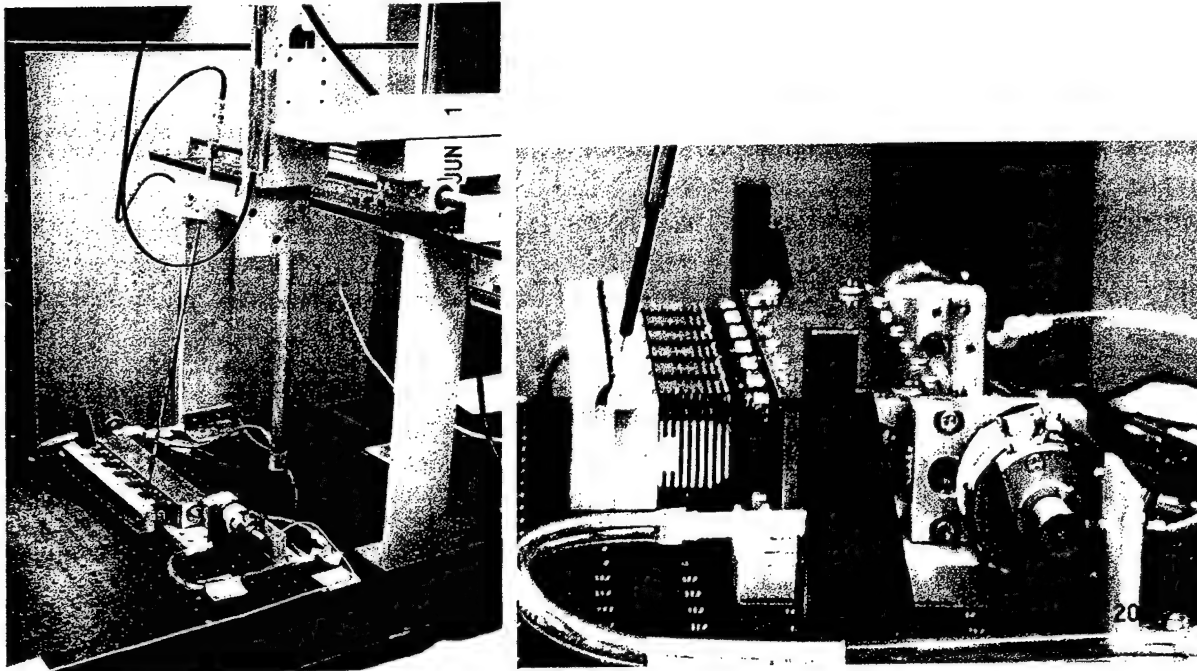
Figure 3.7: Experimental setup configuration for multi-piston actuator bench test.

Hotwire
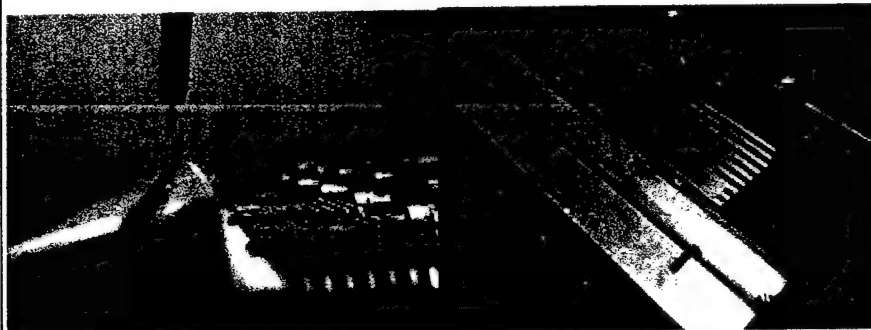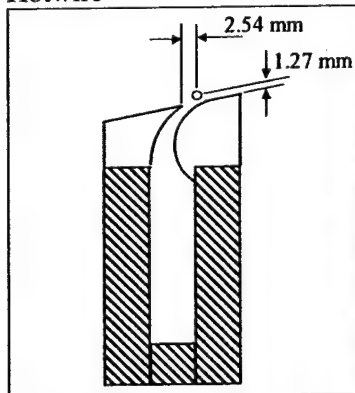
Fast Response Pressure Probe
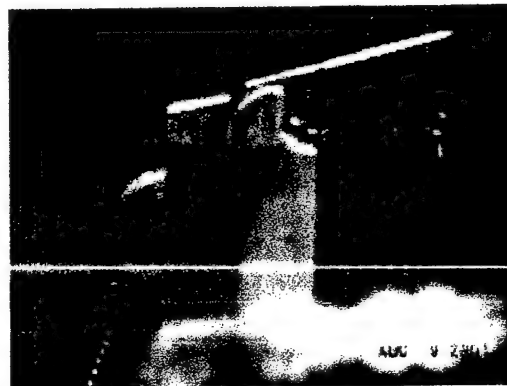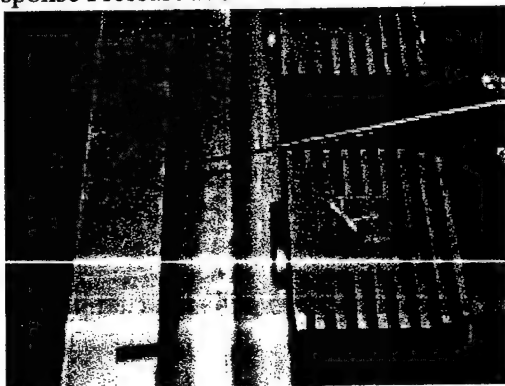
Figure 3.8: Position of measurement probes during bench tests.

Wind Tunnel Tests

In order to test the separation control capabilities and performance of the proposed actuator, if was placed into a wing with a cross-section profile based on a NACA 0015 airfoil and was tested in the 3'x4' wind tunnel at the Department of Aerospace Engineering at Texas A&M University.

Wind Tunnel Model

Figure 3.9 and table 3.1 show the geometric details of the wing used in the aerodynamic study. The wing was fabricated using Freeman Industries REPRO 95 aluminum filled epoxy. In order to provide easy access to the actuator and other instrumentation that was also going to be installed inside the wing, as well as to facilitate the fabrication process of the wing, it was fabricated in two halves (top and bottom) with a chamber to house the actuator and auxiliary instrumentation. It was found that the easiest way to make the wing was to fabricate a mold out of wood, which would provide the outer shape of the wing, that is the mold itself was a negative image of the wing that would later be produced by pouring the epoxy into the mold. This mold was made on a conventional milling machine and the author had to manually set the depth as a function of the coordinates of the chordwise position. A ¾ inch diameter ball tip end mill was used to machine the two halves of the wooden mold. Once the mold had been made in the milling machine, the author then proceeded to sand its internal surfaces in order to produce a smooth surface. This surface was then painted with wood sealant to provide an impermeable surface to prevent the liquid epoxy to be absorbed by the wood. After the two halves of the mold were finished, a separation wall was also made to put in between of the two halves of the mold in order to produce a wing in two parts. This separation wall included the wooden shape used to create the chamber inside the wing to house the actuator as well as the additional instrumentation that would be installed inside the wing. Figure 3.10 shows the two halves of the mold used to make the wing. Figure 3.11 shows the separation wall installed in between the two mold halves. Before the mold was assembled all of the internal walls of the mold and the separation wall were painted with a liquid wax and a mold release agent in order to facilitate the extraction of the finished wing halves after the epoxy had set.

Part of the aerodynamic tests performed of the wing, included the measurement of the effect of the synthetic jet actuator over the wing surface pressure distribution, hence the wing was equipped with 32 pressure taps distributed on the upper and bottom surfaces of the wing as shown in figure 3.12. Table 3.2 shows the nondimensional chordwise location of the pressure taps measured from the leading edge of the wing. The pressure taps were located close to the center of the wing in the spanwise direction and were slightly offset with respect to each other in order to reduce interference. The pressure taps had an orifice diameter of 0.7 mm which is small enough to avoid significant errors in the pressure measurements. The pressure ports were connected, via Tygon tubing, to a 32-channel ESP pressure scanner with a pressure range of ±5.0 kPa. The pressure scanner was also installed inside the wing. Figure 3.13 shows a picture of the internal details of the wing with the ESP pressure scanner and the synthetic jet actuator assembly.
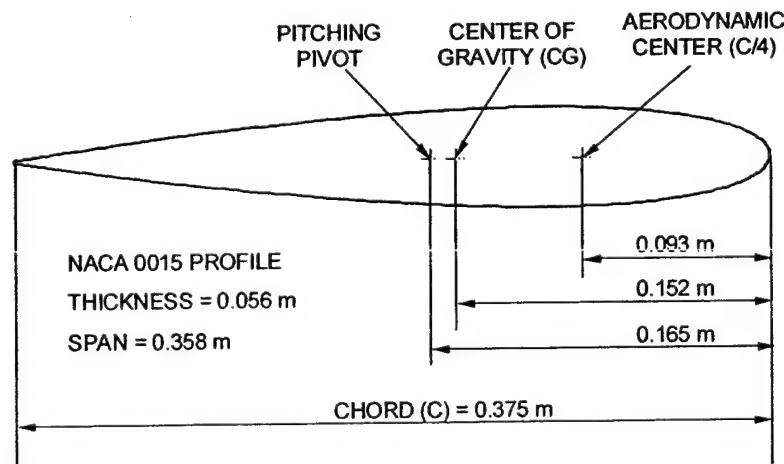

Figure 3.9: Wind tunnel model geometric details.

Table 3.1: Wind tunnel model geometric details. All distances measured from the leading edge of the wing

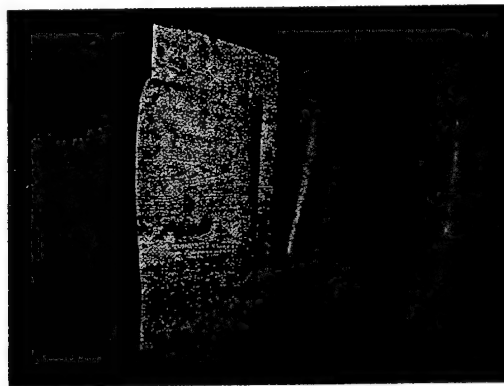| Parameter	Value [m]
Chord	0.375
Span	0.358
Maximum Thickness	0.056
Pivot Location	0.165
C.G. Location	0.152
Theoretical A.C. Location	0.093
Actuator Location	0.046

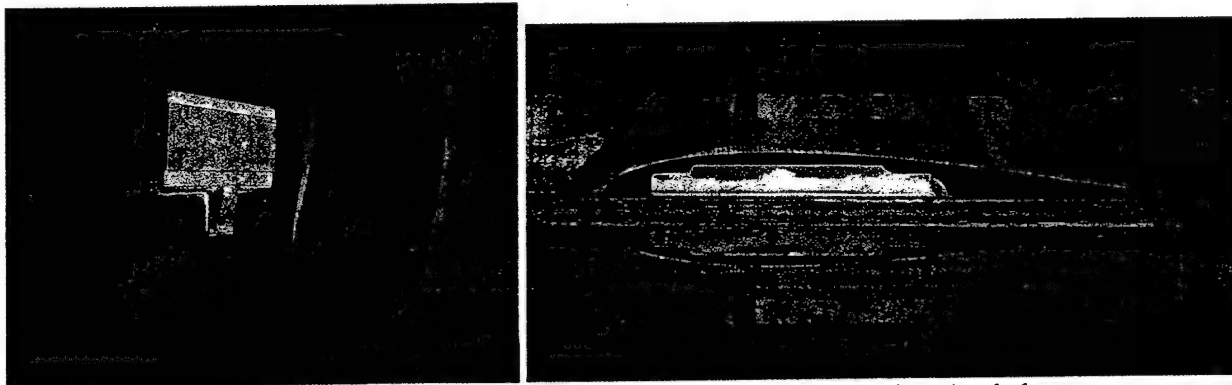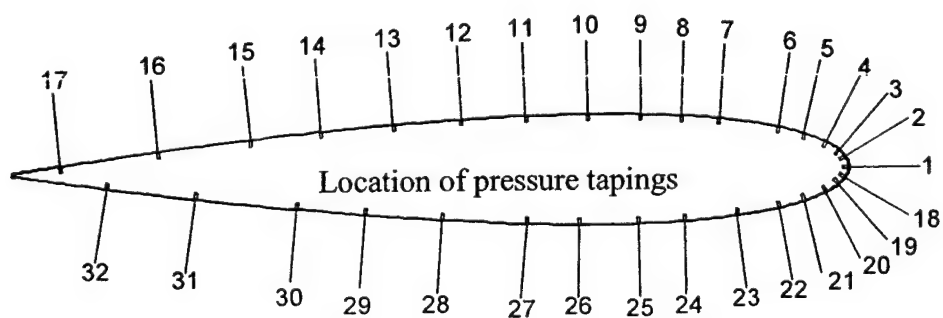Figure 3.10: Wooden molds used to cast the wing halves.

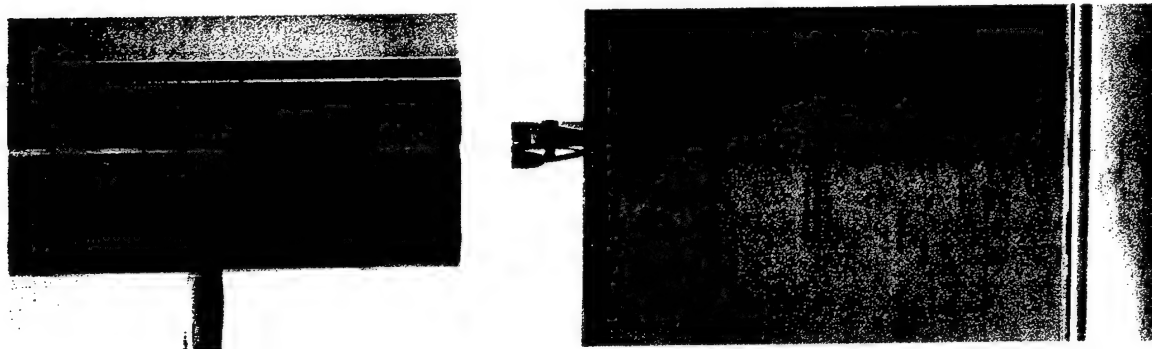Figure 3.11: Wooden molds and separation wall used to cast the wing halves.

Location of pressure tapings

Figure 3.12: Wind tunnel model surface pressure tapings.

Table 3.2: Pressure tap locations on wind tunnel model. All distances measured from the leading edge.

Top Surface		Bottom Surface	
Tap Number	Location (x/C)	Tap Number	Location (x/C)
1	0.000	18	0.003
2	0.003	19	0.014
3	0.012	20	0.027
4	0.027	21	0.051
5	0.054	22	0.083
6	0.085	23	0.136
7	0.156	24	0.197
8	0.200	25	0.254
9	0.251	26	0.325
10	0.315	26	0.386
11	0.386	28	0.488
12	0.464	29	0.580
13	0.546	30	0.661
14	0.631	31	0.780
15	0.715	32	0.888
16	0.824		
17	0.942		
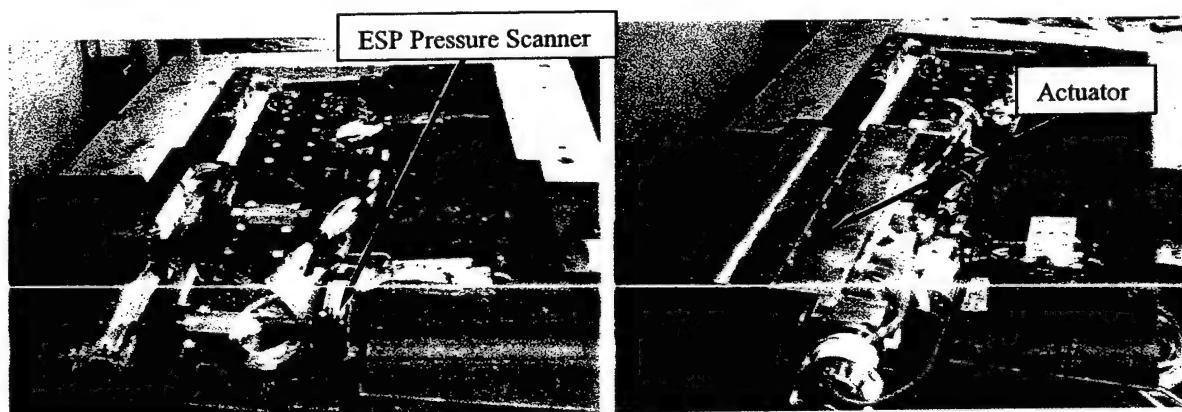
Figure 3.13: Internal assembly details of the wing showing ESP pressure scanner and synthetic jet actuator.

Due to manufacturing constraints and the size of the actuator that was designed for these tests, the maximum span of the wing was only 0.358 m. In order to enforce a two-dimensional flowfield over the wing, i.e. to eliminate the three-dimensional effects due to its finite span, the test wing was placed in-between two Plexiglas plates. These plates were used to prevent the high-pressure flow from the bottom surface of the wing (pressure side) to leak across the wing tips into the low-pressure flow on the upper surface of the wing (suction side).

The original SJA design had the DC motors used to power the actuators inside the wing, (see figure 3.14). Constant failure of the gears that transmitted the power from the motor to the actuator required modification of the design. It was decided that for the tests in this work, a direct drive mechanism would be sufficient. For this case, flexible couplings were used to transmit the power and the motors were placed in the same axis of rotation as the crankshaft of the actuator. This, however, required that the DC motors to partially extend beyond the sides of the actuator and consequently of the wing as may be seen in figures 3.15 and 3.16.

In the original design of the actuator, the connection used to support the wing in the wind tunnel was designed in such a way that the center of rotation of the wing during its pitching motion was at the DC motor axis of rotation for the original design, however when the design was changed to include a direct drive system, the motors were moved forward within the wing, hence the pivot center of the wing no longer coincided with the axis of rotation of the motors. This caused some difficulties due to the fact that the motors extended out of the wing and the Plexiglas side plates had to be installed to provide a two dimensional flowfield for the experiments. The fact that the wing did not rotate around the axis of the motors required that some rather large holes were machined in the Plexiglas walls in order to permit the wing to rotate freely without the motors making contact with the wall. In order to cover the large hole that was machined in the sideplates, two circular disks were attached to the sides of the wing as shown in figure 3.16. These disks had a diameter slightly smaller that the diameter of the hole machined in the sideplates and the center of the disk coincided with the center of rotation of the wing, hence as the wing rotated, the gap between the disk and the holes would be the same. This was required in order to be able to record accurate data from the pyramidal balance used to measure the aerodynamic forces on the wing.
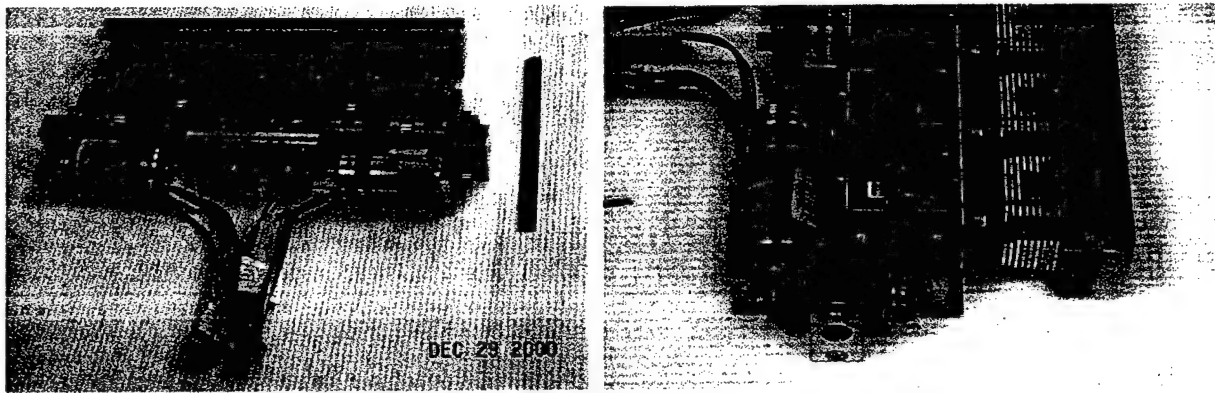
Figure 3.14: Original design of actuator with motors in a position that fit inside the wing.

The fact that the motors extended form the sides of the wing also required the motors to be shielded from the freestream in the wind tunnel. This was achieved by installing hollow cylinders attached to the Plexiglas side plates as shown in figure 3.17. Although special care was taken to make the gap between the Plexiglas disk mounted on the wing and the hole that was machined into the sideplates as small as possible, to prevent flow from leaking from the bottom surface of the wing (pressure side) to the top one (suction side), preliminary results suggested that the air was leaking through the gap, hence the gap was too large. The results also showed that the Plexiglas disk was making contact with the sideplates when the wing operated at high angles of attack due to deflection of the pyramidal balance when subjected to the aerodynamic loading. In view of these conflicting requirements and the fact that one of the primary objectives of this work was to obtain aerodynamic force measurements with the pyramidal

balance, it was decided to make the gap larger so that there was no contact. This required the development of a new way of keeping the flow from leaking from the pressure side to the suction side of the wing.

After analyzing several options, it was decided that the best solution to this problem was to attach additional sideplates directly to the wing. This would guarantee that there would be no leak and would permit the gap in the Plexiglas sideplates to be as large as necessary. Figure 3.18 shows the additional sideplates that were installed on the wing. They were made out of 1.5 mm thick aluminum sheet and were attached to the wing as shown. After installing these sideplates, preliminary testing of the wing, via force balance measurements, showed that there was no flow leaking from the pressure side to the suction side of the wing and the aerodynamic measurements showed that the gap between the circular disks of the wing and the hole machined in the Plexiglas sideplates was large enough so that there was no contact between these components. Figures 3.18 and 3.19 show the final configuration of the experimental setup that was utilized for the aerodynamic measurement tests. Figure 3.20: shows details of the electric motor cooling air connections as well as the electrical connections necessary to supply power to the synthetic jet actuator. It is important to state that special care was taken during the assembly and connection of all of the auxiliary equipment and cooling air hoses in order to minimize the transmission of any type of forces and moments to the pyramidal balance.
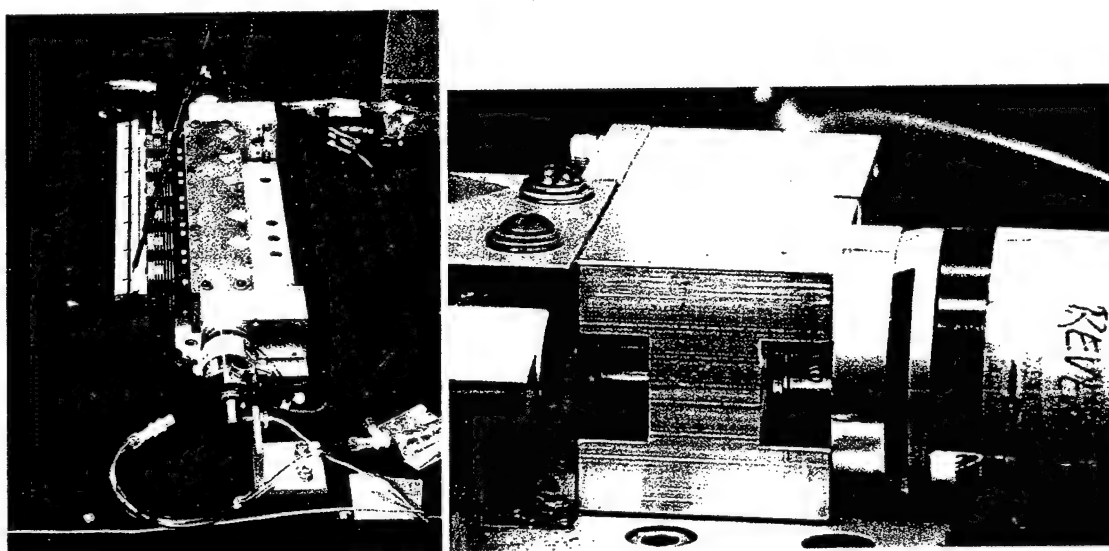
Figure 3.15: Revised actuator design with direct drive configuration.
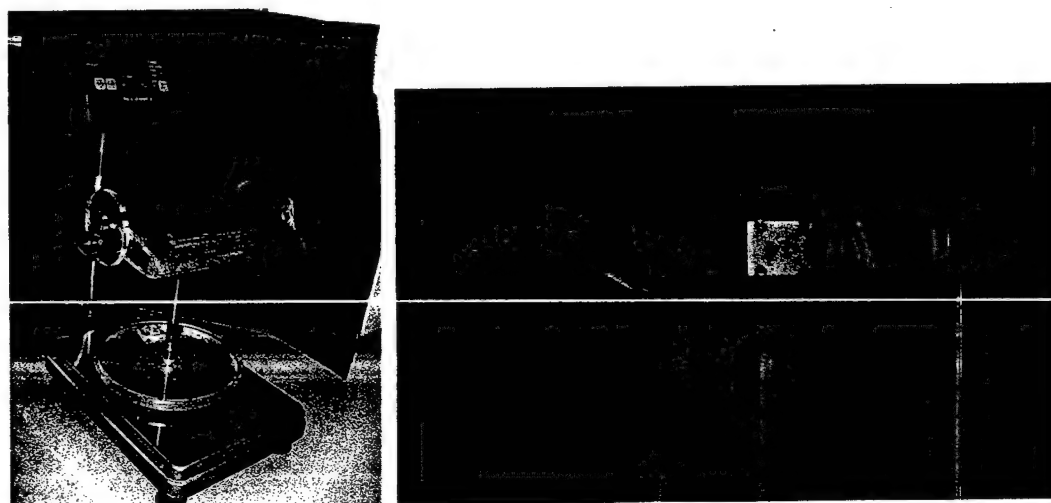
Figure 3.16: Circular disk installed on wing.

37
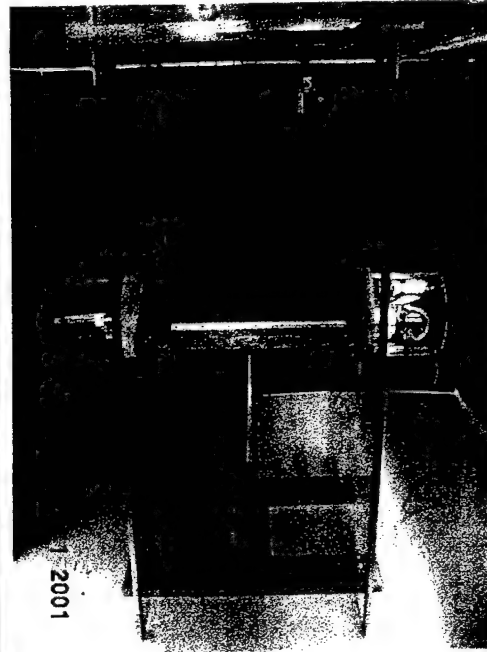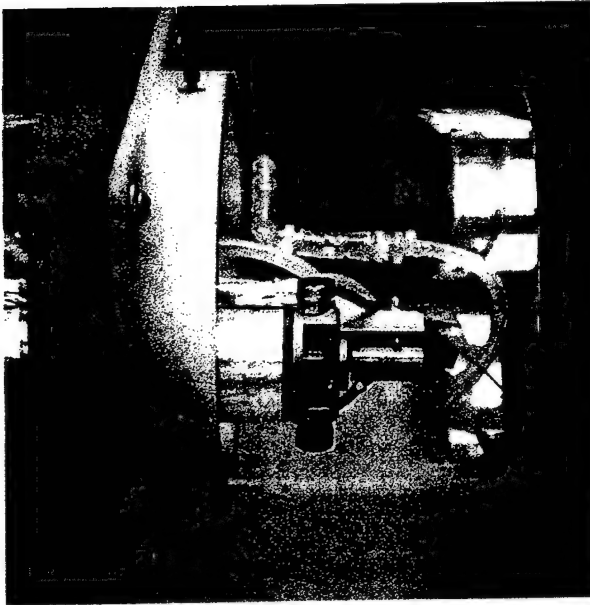
Figure 3.17: Side plates and motor covers.
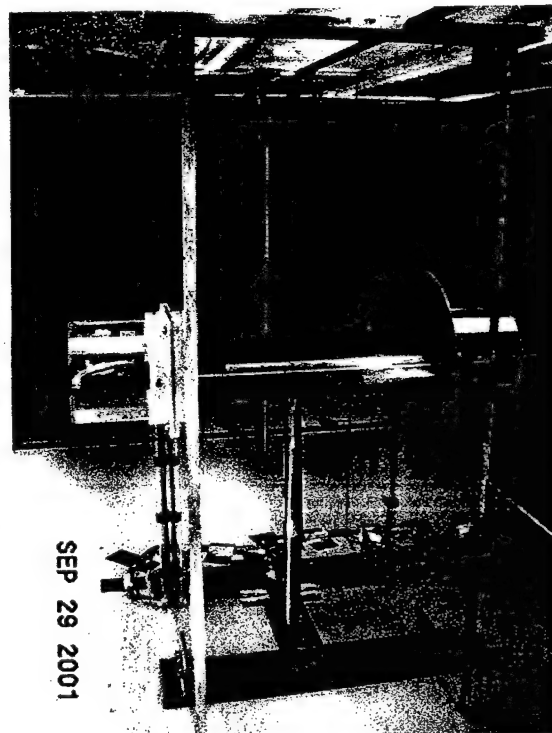
Figure 3.18: Location of additional aluminum sideplates

38
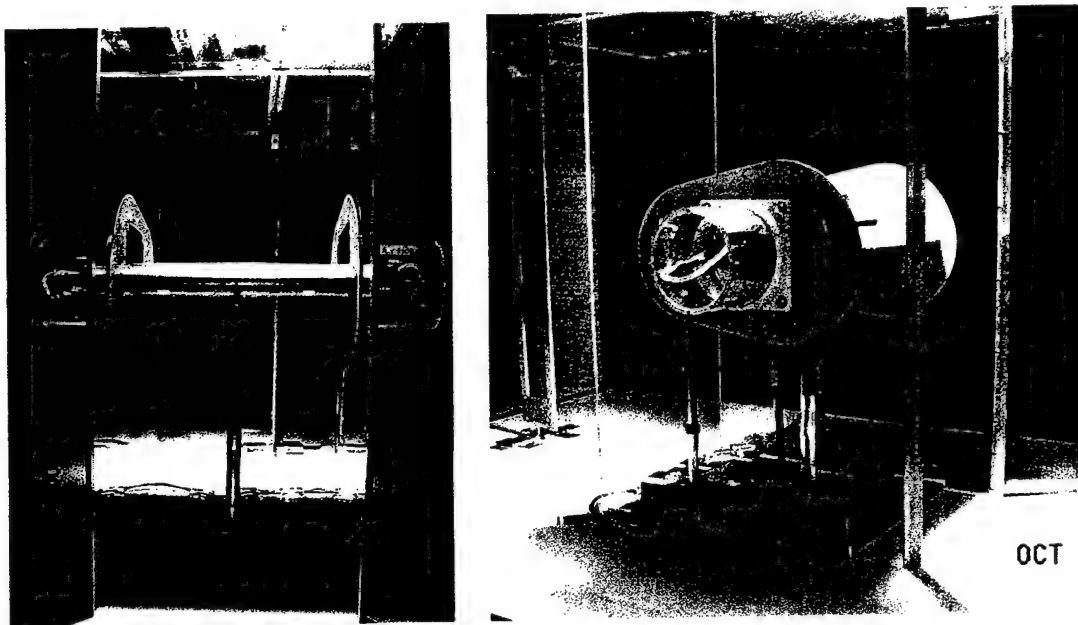
Figure 3.19: Final configuration of experimental setup used for wind tunnel measurements.
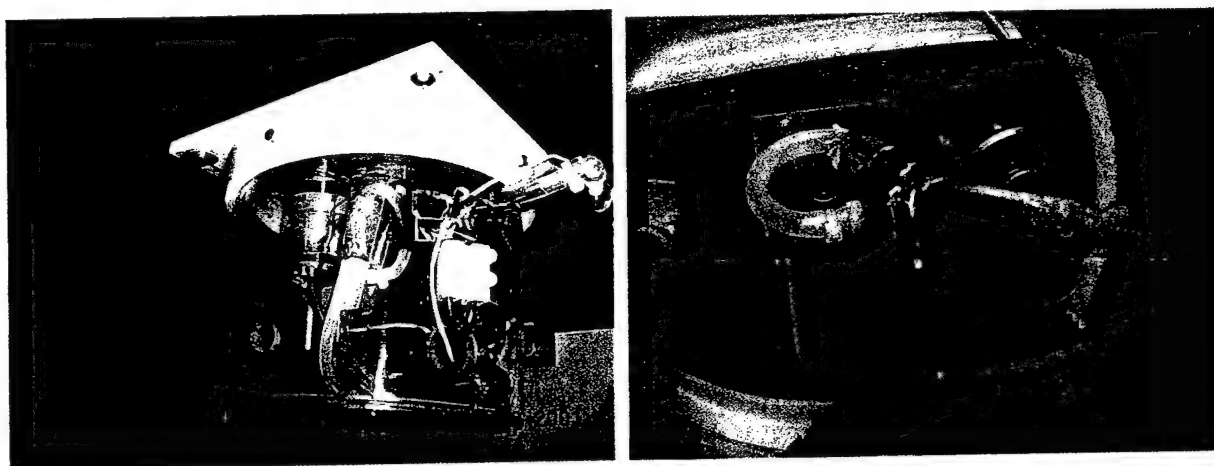
Figure 3.20: Details of cooling air hoses and electrical connections.

Experimental Facilities

The aerodynamic tests were performed at the Texas A&M University's 3' x 4' continuous wind tunnel at a freestream velocity (U) of 35 m/s, with a resulting Reynolds number based on the wing chord of Re = 8.9 x 10^5. Unless mentioned otherwise, the results presented correspond to the above-mentioned values. Although the wind tunnel is capable of operating at a maximum freestream velocity of 45 m/s (Re = 1.15 x 10^6), testing at a velocity higher that 35 m/s would overload one of the load cells (pitching moment) of the pyramidal balance, hence operation at higher speeds was kept to a minimum. The wind tunnel has a turbulence intensity of 0.3% at a freestream velocity of 35 m/s (Traub, 1999). This tunnel has an active cooling system, however at the time of the tests, the cooling system was damaged, hence the testing could not include any type of measurements that involved a long period of operation of the tunnel, such as multi-hole pressure probe surveys. The freestream velocity was determined using a wall mounted Pitot tube, manufactured by United Sensors, with a tip diameter of 3.175 mm. The supporting literature for this probe quotes accuracies within 1%, for pitch and yaw angles below ±10 deg (United Sensor, 1983). Differential pressure was measured using an Omega PX139 series pressure transducer with a range of ±2.0 kPa. The transducer has an output voltage range of 0.25 to 4.25 volts. The linearity and hysteresis

of the transducer is 1% of the full scale. This manometer can resolve pressures down to 1Pa. The output of the transducer was measured by an Omega I-Series temperature and process monitor with a voltage measurement resolution of 1μvolt. This monitor was interfaced with the wind tunnel data acquisition code via an Ethernet connection. Prior to testing, the output of the transducer/monitor pair was calibrated by generating a set of known pressures by means of a TSI model 1125 flow calibrator, and comparing the output of the transducer/monitor system with an Edwards Barocell pressure transducer, which was used as a standard. The range of the Barocell is 13.3 kPa, with an accuracy of 6.5 Pa.

Force Balance

A three component Aerolab pyramidal balance was used for force and moment determination. The balance measures two forces (lift and drag) as well as pitching moment. These components are measured directly by three strain gage load-cells. Due to the prohibitive cost of commercial calibration of this type of balance, a simplified calibration routine was developed. Conventional calibration of a 3 component balance requires the determination of the coefficients of a 3 by 9 matrix. The first order interactions are due to machining errors, gage location and variations in gage factor. The second order terms are due to balance deflection under loading. Thus for each component there are 3 first order interactions and 6 second order interactions. The standard calibration of a three-component balance requires the application of a very large amount of loading combinations per component (3 components in total), and requires specialized alignment fixtures and hundreds of man hours to implement. Rae and Pope (1999), present a simple procedure for the calibration of three component pyramidal balances. This procedure uses only the first order interactions between the loads and reduces the order of the calibration matrix to a 3 by 3 matrix. As the resulting calibration was limited to only the first order interactions, it was deemed vital to determine if the calibration was suitably accurate. Consequently, numerous proof loads were applied to the balance in pure as well as combined loads. From this, the accuracy of the balance was estimated at 0.5% of full scale for lift, drag and pitching moment. This is within the accuracy limit prescribed by Rae and Pope, and reinforced confidence in the simplified calibration routine. Through repeated data runs, repeatability of the balance for lift, drag and pitching moment was estimated to be $\Delta CL = 0.001$, $\Delta CD = 0.001$ and $\Delta Cm = 0.0008$.

Model pitch (angle of attack) was adjusted using a stepper motor with a 36:1 reduction gearbox, which was connected to a worm-gear mechanism. A high resolution optical encoder was connected to the input shaft of the gear box and its output was fed into the data acquisition program via a digital read out display with a RS232 output. Model angle of attack could be set to within 0.05 deg. Force balance data as well as wind tunnel dynamic pressure and temperature were acquired using a P.C. equipped with a 16 bit A/D board. Figure 3.21 shows a schematic diagram showing the configuration of the experimental setup for the force balance tests.
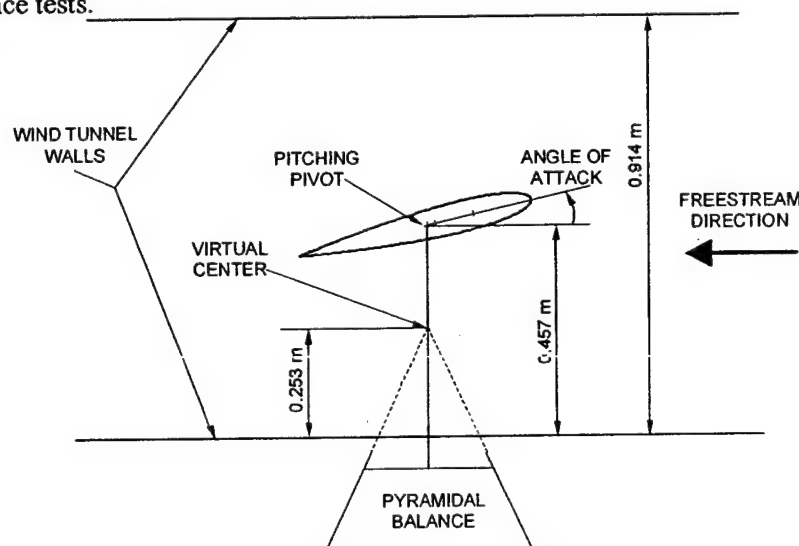

Figure 3.21: Schematic of wind tunnel experimental setup configuration for force balance testing.

Data Acquisition Code

A data acquisition program was written for this application to acquire the force balance data. The code was adapted from one originally written in QuickBasic for the 6-component pyramidal balance of the University of Witwatersrand, in Johannesburg, South Africa (Traub, 1992). The modified code, generated for the 3-component pyramidal balance used for these experiments, was written in VisualBasic. The code requires the input of:

- The mass of the model and mount.
- The model planform area, wing span and reference chord.
- The x and z location of the model and mount center of gravity.
- The x and z location of the user specified moment reference.

The program proceeds by recording the wind-off zeros. The tunnel speed is then subsequently set and the program enters the data acquisition phase. Each data channel is sampled 2000 times and averaged. The calibration matrix generated for the balance is then used to calculate the aerodynamic loads. Movement of the model center of gravity is taken into account. The data is then non-dimensionalized and converted from body to wind axis.

The results are then corrected for wind tunnel effects, which will be detailed later. The pressure transducer used to measure the tunnel dynamic pressure is manufactured by Omega, and resolve pressures to within 1Pa. For each measured data set, the data acquisition code also displays graphically real time lift, drag and pitching moment, in such a way that erroneous data can be instantly recognized. The program outputs to a monitor, and also stores all of the data to a user defined output file.

The force balance measurement part of the tests comprised pitching the model through a set angle of attack range from -2 to 29 degrees. Data was typically recorded at 2 degree intervals. In the vicinity of the maximum lift coefficient smaller α increments were used where necessary. Pitching moment was taken about 0.25 of the wing's chord. The wind tunnel tests were run at a free stream velocity of 35m/s, yielding a Reynolds number based on the wings chord of 8.9×10^5. Data was taken both with and without SJA actuation. The data taken with the actuator off provided a baseline for comparison. For the actuated case, data was taken with the actuator operating at frequencies of 60, 80, 100, 120 and 130 Hz.

Tare and Interference

The presence of the wind tunnel model support results in a tare drag, as well as interference between the support and the model, and the model and the support. Tare and interference was not measured for the results.

Flow Angularity

Rae and Pope (1999), present a method to determine the flow angularity, however due to the fact that the mounting mechanism of the wing does not permit it to be mounted in an inverted position, this method was not followed directly, instead, the author took force measurements for various runs and varied the pitch angle of the wing from −5 to 15 degrees. For these experiments, as the wing had a symmetric profile, the angle at which the lift coefficient curve intersected the coordinate axis (zero lift angle of attack) was taken to be the magnitude of the flow angularity. For this case the flow angularity was calculated to be 0.66 degrees at a freestream velocity of 35 m/s. This angularity includes effects due to balance and test section misalignment, tunnel flow angularity and possible asymmetry of airfoil halves.

Wind Tunnel Wall Effects

The constraining effect of wind tunnel walls are such that the model is effectively embedded in a flow field that is not representative of free air conditions. The corrections to account for these effects are typically broken up into those that affect dynamic pressure, and those that affect the effective model angle of attack. The model volume and wake cause an increase in the local free stream velocity, i.e. solid and wake blockage. Consequently all coefficients need to be corrected for these effects, which result in a slight decrease in the magnitude of the coefficients. Details on tunnel effects and appropriate corrections can be found in Rae and Pope (1999), which presents an excellent account of wind tunnel testing techniques and corrections. In this study, solid and wake blockage were corrected for using the method presented in the reference mentioned above.

41

Flow Visualization

Both on and off-surface flow visualization techniques were used. The on-surface visualization was accomplished using Titanium Dioxide suspended in a mixture of Kerosene, Linseed oil and Oleic acid. In addition to this method, tufts were also placed on the upper surface of the wing in order to provide a second means of surface flow measurements. Figure 3.22 shows the test wing with the tufts applied to the upper surface. For the case of off-surface flow visualization, smoke was injected upstream of the wing. All of the above mentioned tests were run in the 3' x 4' tunnel at a free stream velocity of 35m/s (Re = 8.9 x 10^5) at angles of attack (α) of 8, 12, 16, 18 and 20 degrees. All of the flow visualization tests were performed with and without operation of the synthetic jet actuator. For the case in which the actuator was not operated, during the surface flow visualization, the exit slot of the actuator was covered with electrical tape so that the Titanium Dioxide mixture did not enter the actuator plenum. For the case in which the actuator was used, it was operated at a frequency of 120 Hz. Video footage and digital still images were recorded during these tests and analyzed subsequently to determine the characteristics of the flowfield for the above-mentioned conditions.
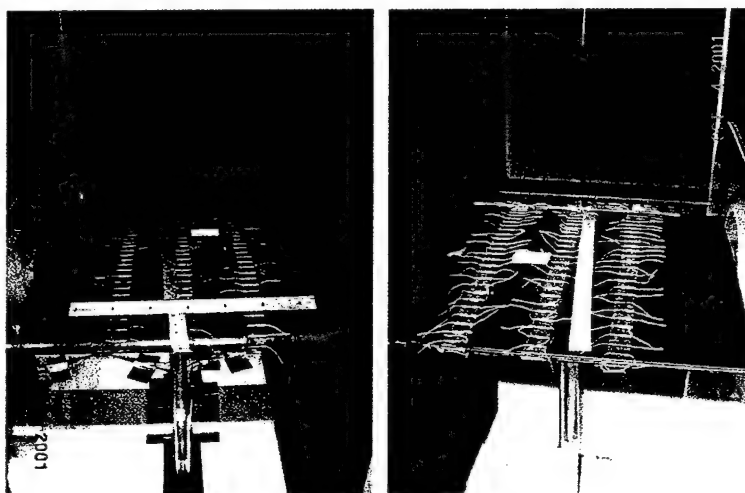
Figure 3.22: Tufts on upper surface of the wing.

Surface Pressure Measurement

Surface pressures were measured for an angle of attack (α) range from -2 to 29 degrees. Data was typically recorded at 2 degree intervals. In the vicinity of the maximum lift coefficient smaller α increments were used where necessary. The tests were run at a free stream velocity of 35m/s, yielding a Reynolds number based on the wings chord of 8.9 x 10^5. Data was taken both with and without actuation. The data taken with the actuator off provided a baseline for comparison. On the other hand, for the actuated case, data was taken with the actuator operating at frequencies of 60, 80, 100, 120 and 130 Hz. The surface pressures were evaluated using a 32 channel ESP pressure sensor with a measurement range of ±5.0KPa. Calibration of the ESP was checked by sequentially comparing a reference pressure imposed on each channel against the value measured by the Barocell pressure transducer described previously. Agreement between the Barocell and the ESP was generally within 1%. Prior to each test the ESP was zeroed to reduce drift. After completing a test, the ESP was again re-zeroed to ascertain if the zeroes had drifted significantly. The pressures measured by the ESP were digitized using a 12 bit A/D board.

Each time a data set was taken, the pressures at each location were sampled 200 times and averaged. After changing the operating conditions of the experiments (change of α or change in actuator frequency, etc.), data measurement was delayed for 5 seconds to allow the pressures to stabilize.

Wake Surveys

In order to better evaluate the performance of the proposed synthetic jet actuator as a flow separation control device, wake surveys were performed downstream of the wing by traversing a Pitot rake placed at a distance of x/C = 1.2 behind the trailing edge. The rake was fabricated with thirty two 1.5mm diameter (O.D.) tubes, spaced 25.4 mm apart, which were connected to a 32 channel ESP pressure sensor. Figure 3.23 shows details of the wake rake construction and installation. Figure 3.24 shows the position of the wake rake within the wind tunnel during the tests. Due to the fact that the separation between the tubes was rather large, a good resolution of the wake profile was obtained by traversing the rake vertically to nine positions for each operating condition. This yielded a vertical spatial resolution of 2.54 mm between the data points. Each time that the rake was moved, the data acquisition was stopped for 5 seconds to allow the pressures to stabilize. This time, in addition to the time it took the traversing mechanism to move the rake (about 1 second), resulted in the requirement of about one minute to measure the wake profile for each operating condition. For each location, the pressures were sampled 200 times and averaged. All of the wake measurements were performed at a Freestream velocity of 35 m/s yielding a Reynolds number of 8.9 x 10^5. Data was taken both with and without actuation. The data taken with the actuator off provided a baseline for comparison. On the other hand, for the actuated case, data was taken with the actuator operating at frequencies of 60, 80, 100, 120 and 130 Hz. The accuracy of the traversing system in positioning is within 0.03mm. As for the case of the surface pressure measurements, the pressures measured by the rake were evaluated using a 32 channel ESP pressure sensor with a measurement range of ±2.5KPa. The calibration for this ESP was also checked by sequentially comparing a reference pressure imposed on each channel against the value measured by the Barocell, with agreement within 1%. Prior to each test the ESP was zeroed to reduce drift. After completing a test, the ESP was again re-zeroed to ascertain if the zeroes had drifted significantly. The pressures measured by the ESP were digitized using a 12 bit A/D board.
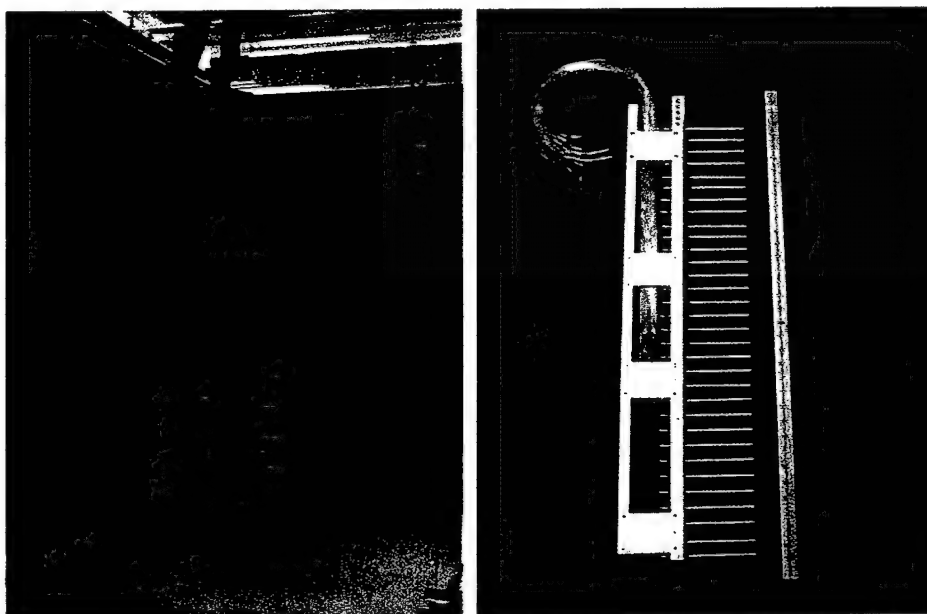
Figure 3.23: Details of wake rake construction and installation.
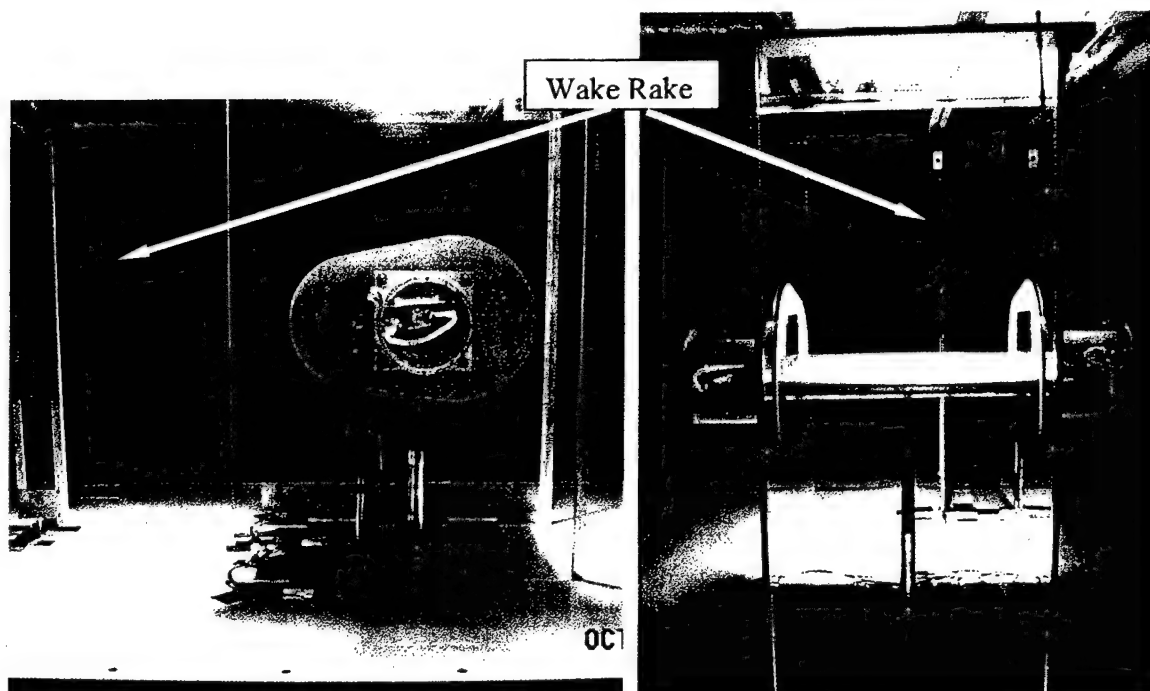
Figure 3. 24: Location of wake rake within the wind tunnel test section.

4. ACTUATOR CHARACTERIZATION AND STEADY WIND TUNNEL TEST RESULTS

This section contains a summary of the results acquired in the experimental investigation. The data is separated into bench test results (figures 4.1 to 4.7), force balance measurements (figures 4.8 – 4.21), on-surface flow visualization (figures 4.22 – 4.31), off-surface (smoke injection) flow visualization (figures 4.32 to 4.36), surface pressure measurements (figures 4.37 – 4.52) and wake surveys (figures 4.53 – 4.59).
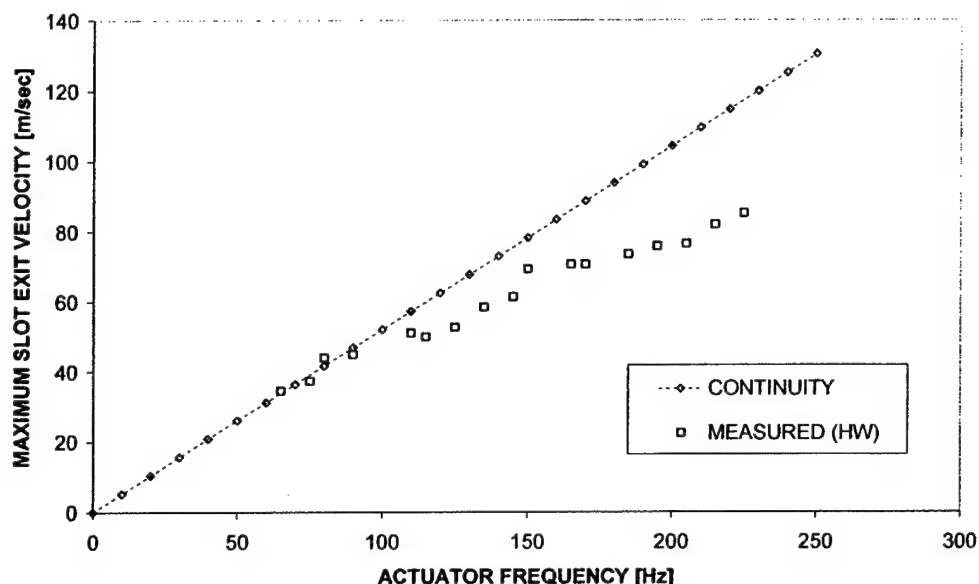
Figure 4.1: Maximum slot exit velocity as a function of actuator frequency for single piston prototype with a slot width of 0.8 mm. Comparison of hot-wire measurements and predictions using the continuity equation for incompressible flow.
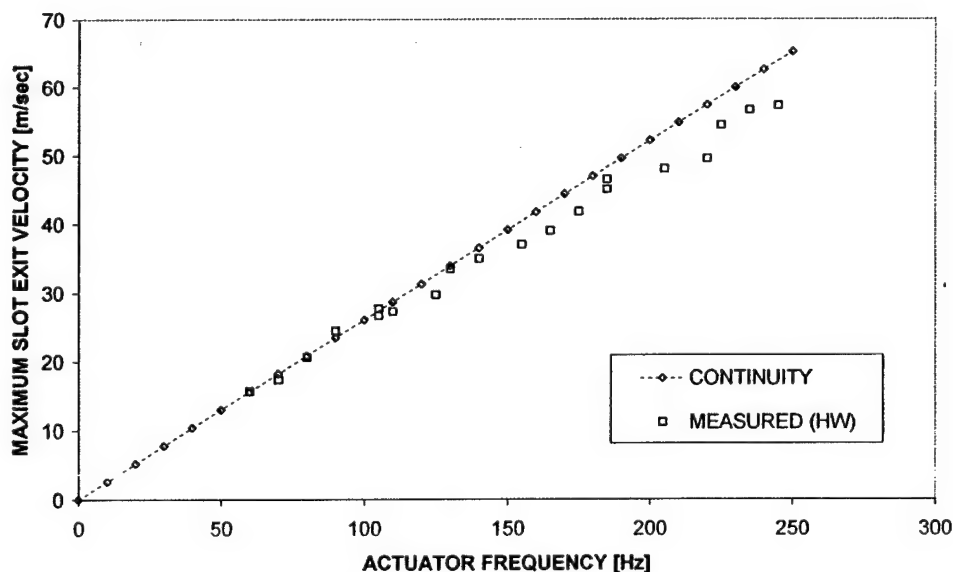
Figure 4.2: Maximum slot exit velocity as a function of actuator frequency for single piston prototype with a slot width of 1.6 mm. Comparison of hot-wire measurements and predictions using the continuity equation for incompressible flow.

45
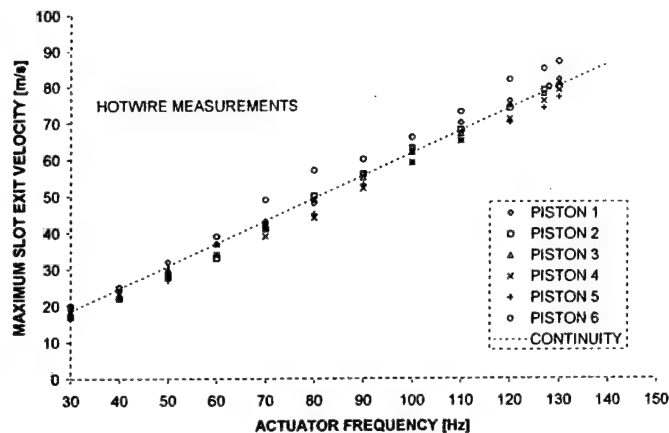
Figure 4.3: Maximum slot exit velocity as a function of actuator frequency. Comparison of hot-wire measurements and predictions using the continuity equation for incompressible flow.
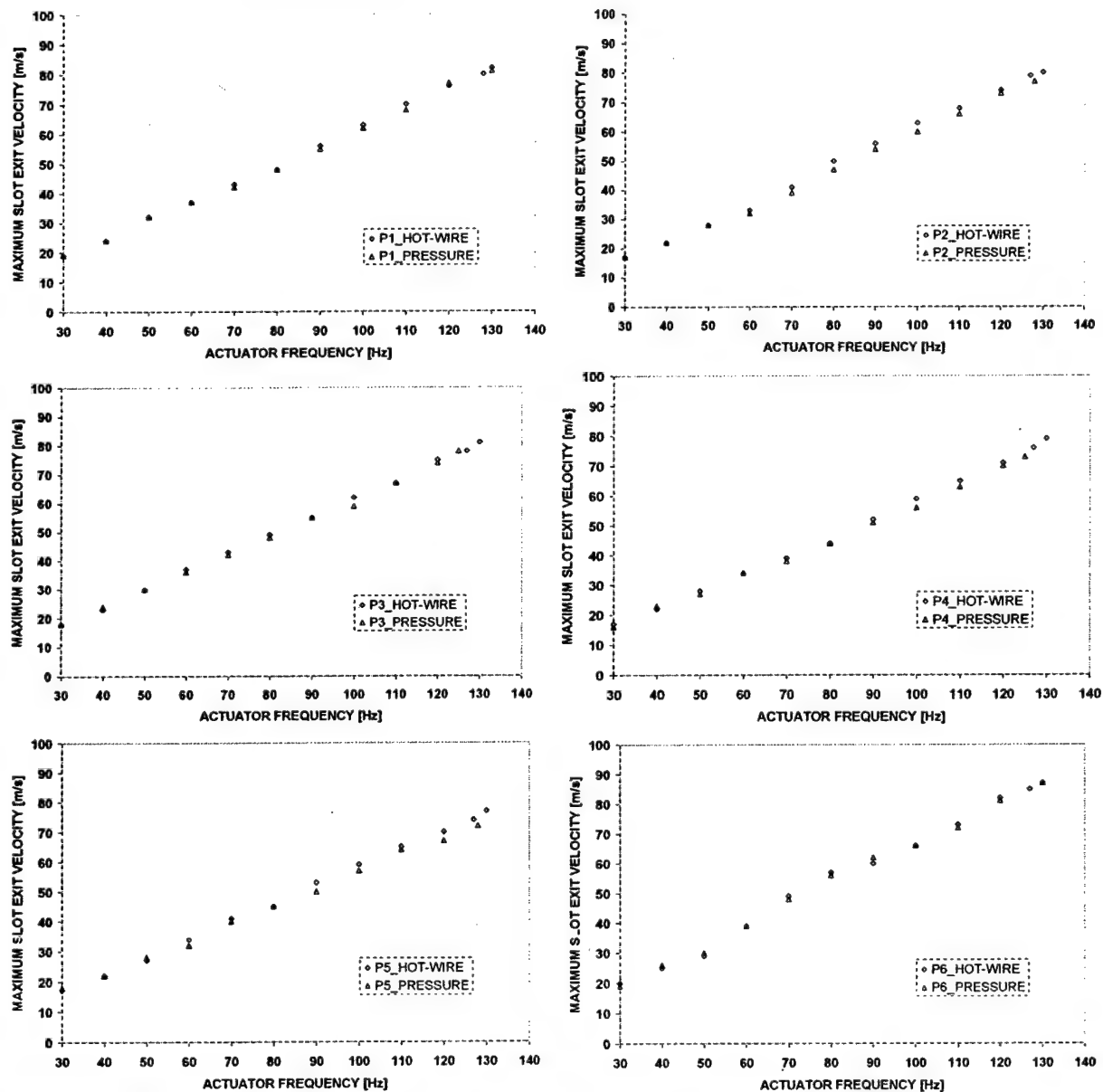
Figure 4.4: Maximum slot exit velocity as a function of actuator frequency. Comparison of hot-wire and fast-response pressure probe measurements for each piston.
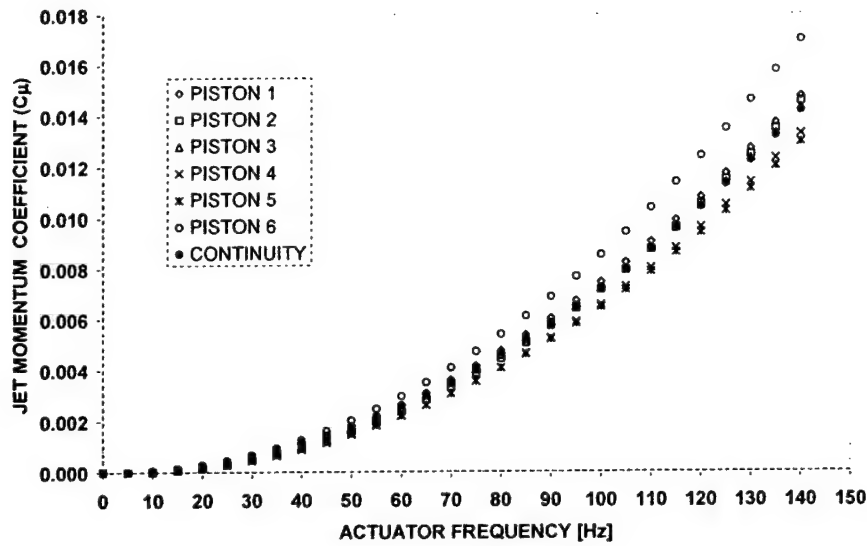
Figure 4.5: Jet momentum coefficient as a function of actuator frequency. Comparison of calculations based on hot-wire measurements for each piston and predictions using the continuity equation for incompressible flow.
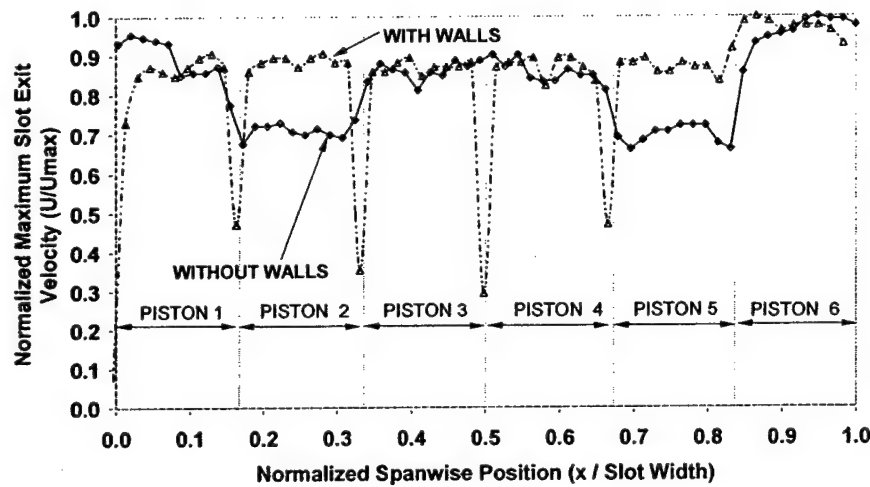
Figure 4.6: Effects of the extended actuator chamber separation walls over the spanwise distribution of the maximum jet exit velocity for an actuator frequency of 120 Hz.
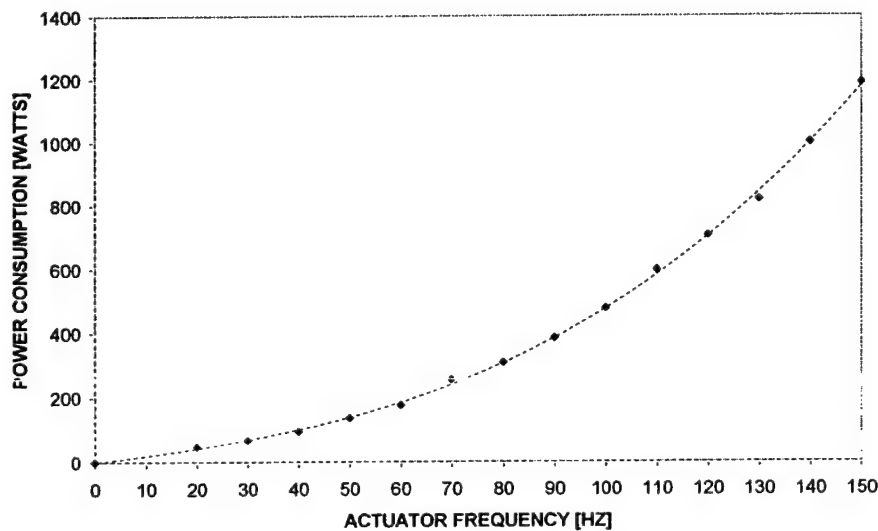
Figure 4.7: Power consumption of multi-piston synthetic jet actuator as a function of operating frequency.

47
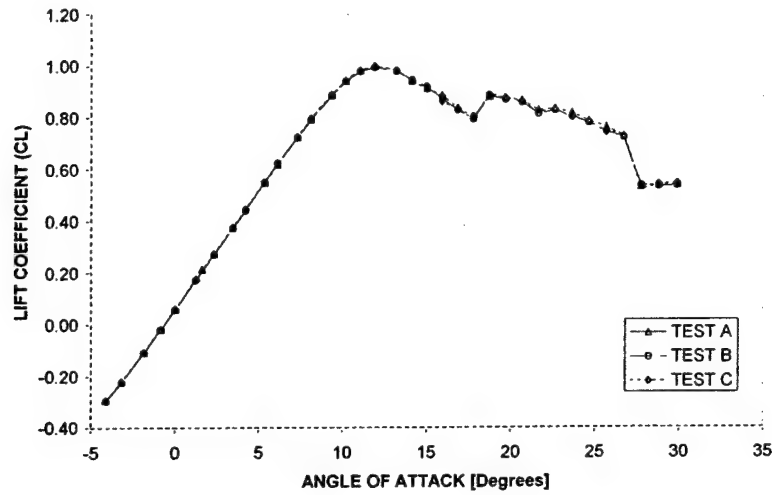
Figure 4.8: Repeated data runs for clean wing (no actuator). Lift coefficient (CL) vs. angle of attack (α).
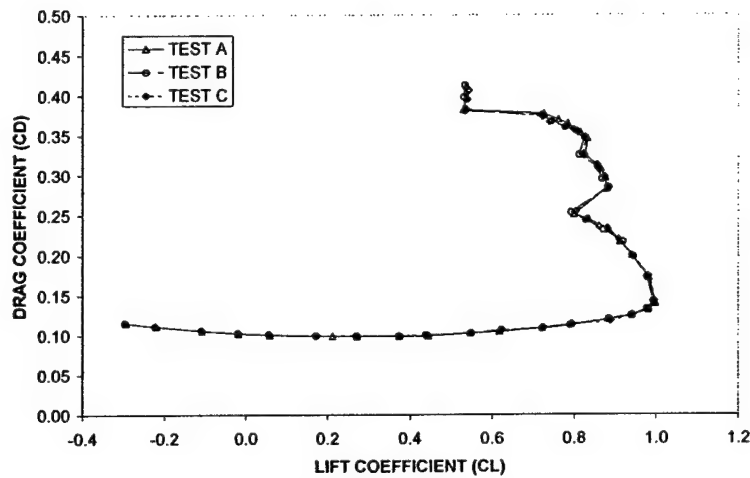
Figure 4.9: Repeated data runs for clean wing (no actuator). Drag coefficient (CD) vs. lift coefficient (CL).
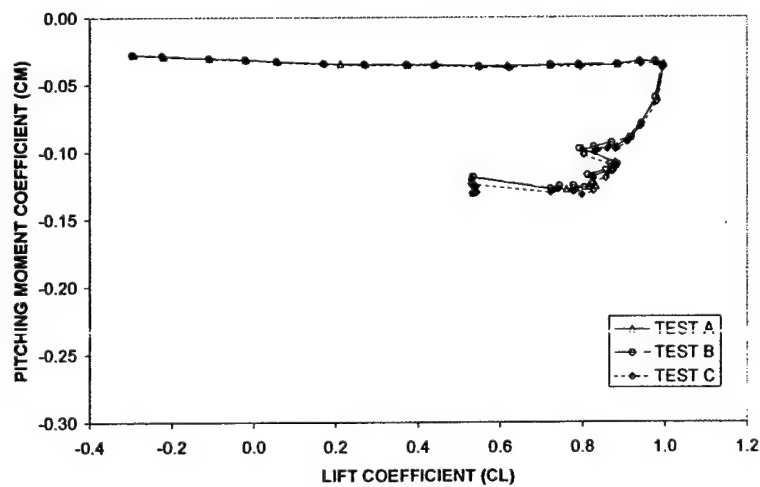
Figure 4.10: Repeated data runs for clean wing (no actuator). Pitching moment coefficient (CM) vs. lift coefficient (CL).

48
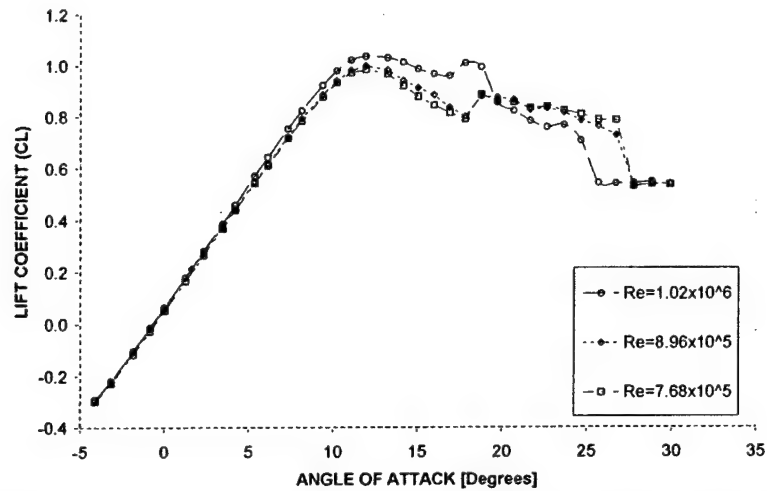
Figure 4.11: Effect of Reynolds number on aerodynamic performance of clean wing. Lift coefficient (CL) vs. angle of attack (α)..
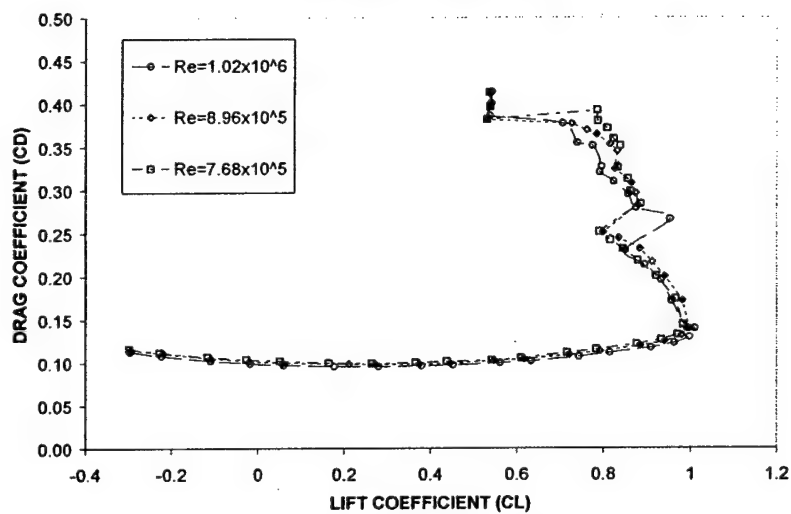
Figure 4.12: Effect of Reynolds number on aerodynamic performance of clean wing. Drag coefficient (CD) vs. lift coefficient (CL).
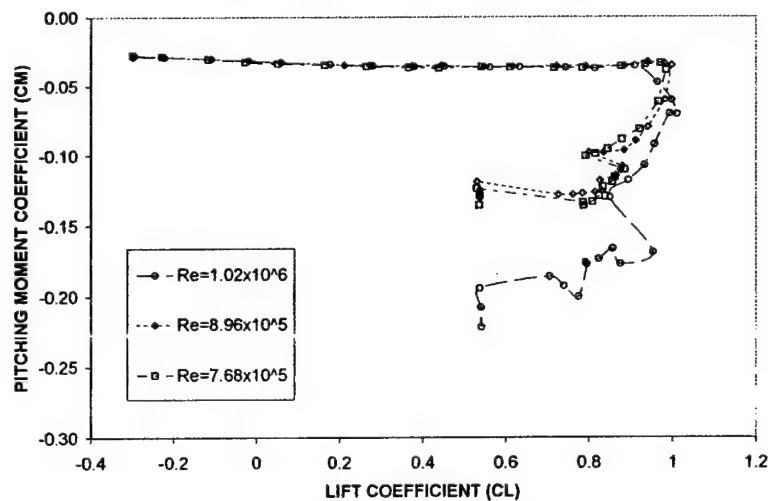
Figure 4.13: Effect of Reynolds number on aerodynamic performance of clean wing. Pitching moment coefficient (CM) vs. lift coefficient (CL).

49
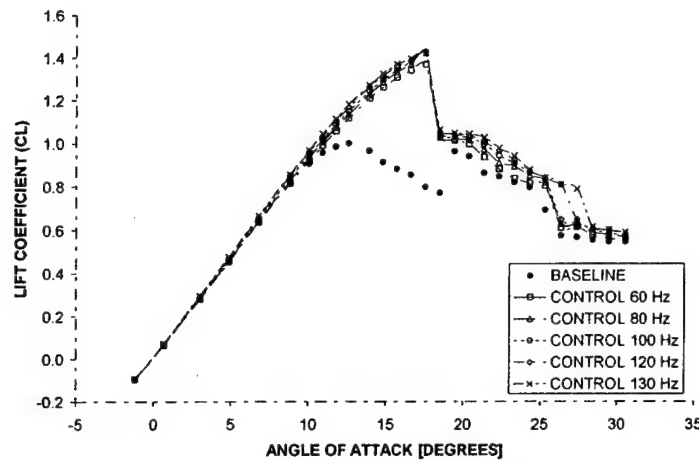
Figure 4.14: Effect of synthetic jet actuator on aerodynamic performance of test wing. Lift coefficient (CL) vs. angle of attack (α).
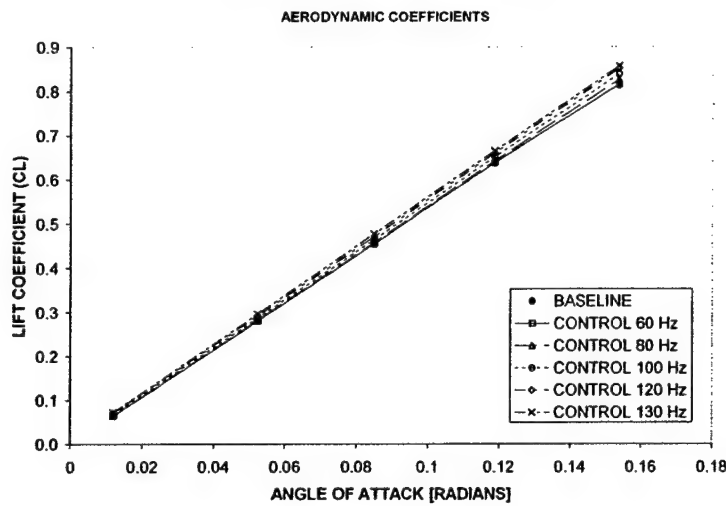
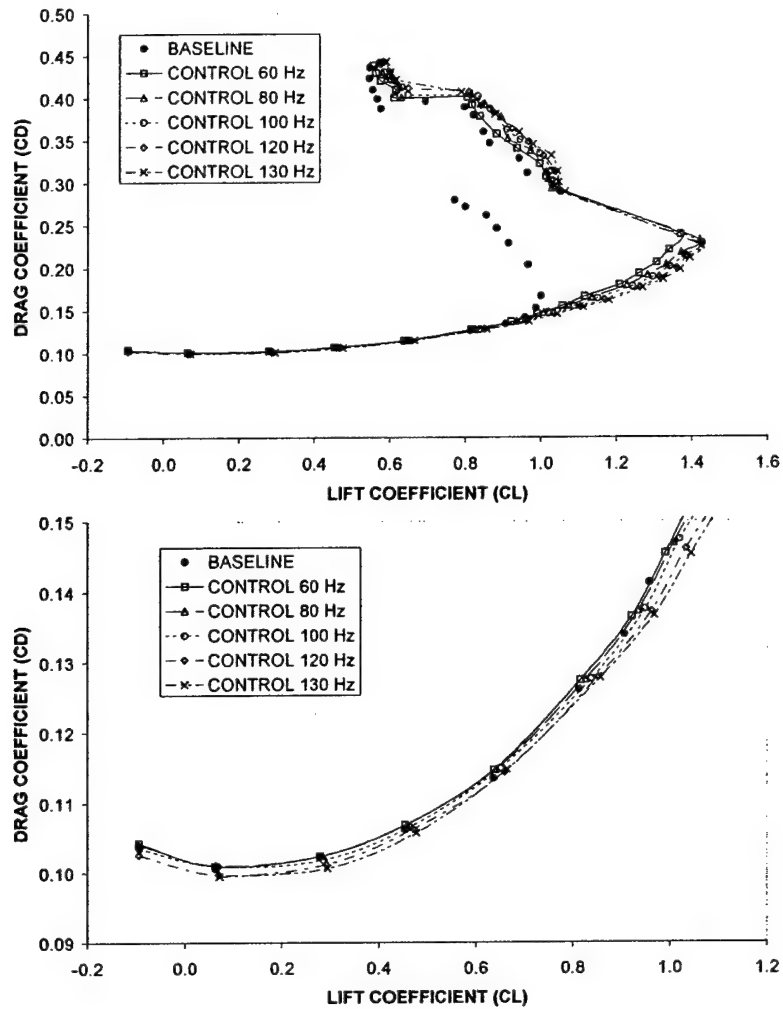Figure 4.15: Effect of synthetic jet actuator on aerodynamic performance of test wing. Close-up of lift coefficient (CL) vs. angle of attack (α).
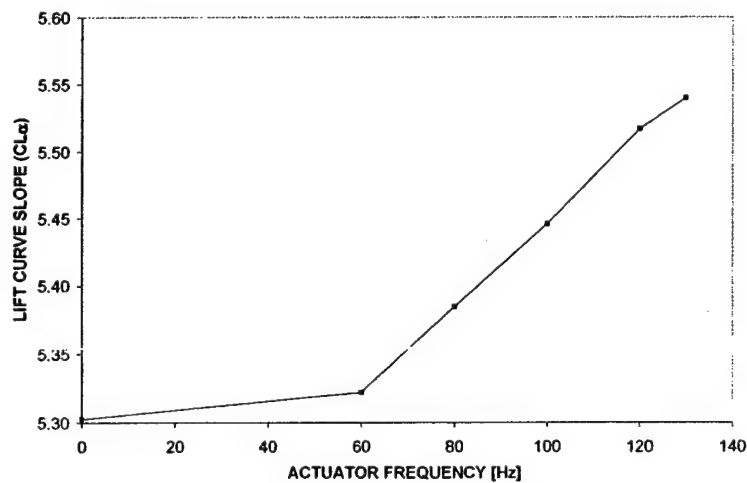
Figure 4.16: Effect of synthetic jet actuator on aerodynamic performance of test wing. Lift curve slope (CLα) vs. actuator frequency.

50
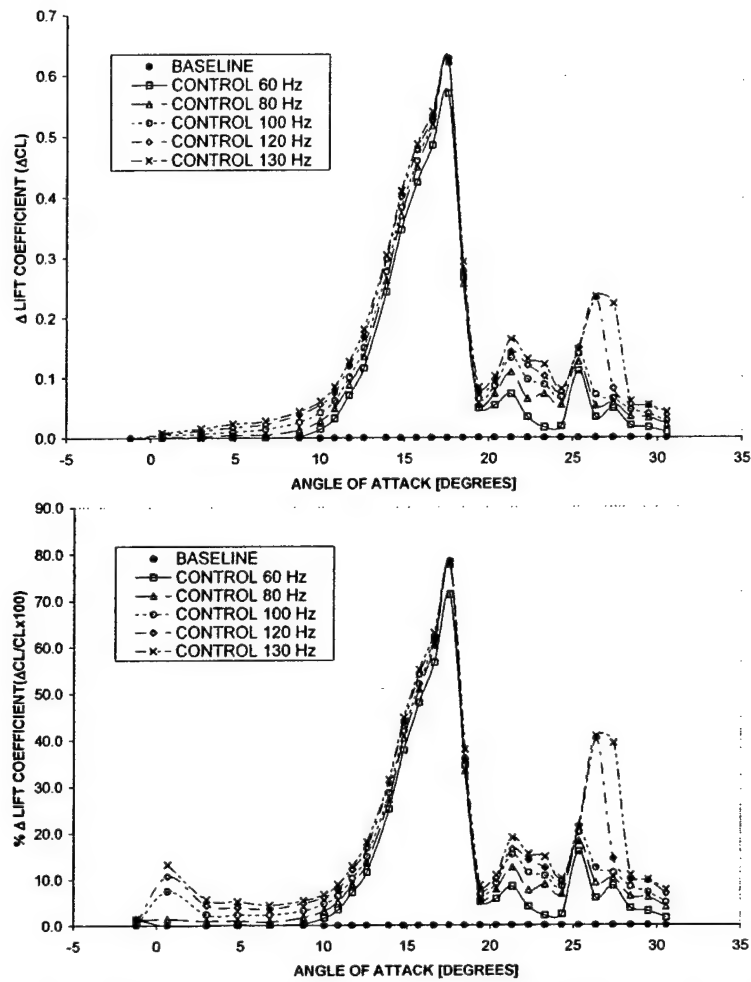
Figure 4.17: Effect of synthetic jet actuator on aerodynamic performance of test wing. Δ lift coefficient (ΔCL) vs. angle of attack (α).

Figure 4.18: Effect of synthetic jet actuator on aerodynamic performance of test wing. Maximum lift coefficient (CLmax) vs. actuator frequency.

51

Figure 4.19: Effect of synthetic jet actuator on aerodynamic performance of test wing. Drag coefficient (CD) vs. lift coefficient (CL).
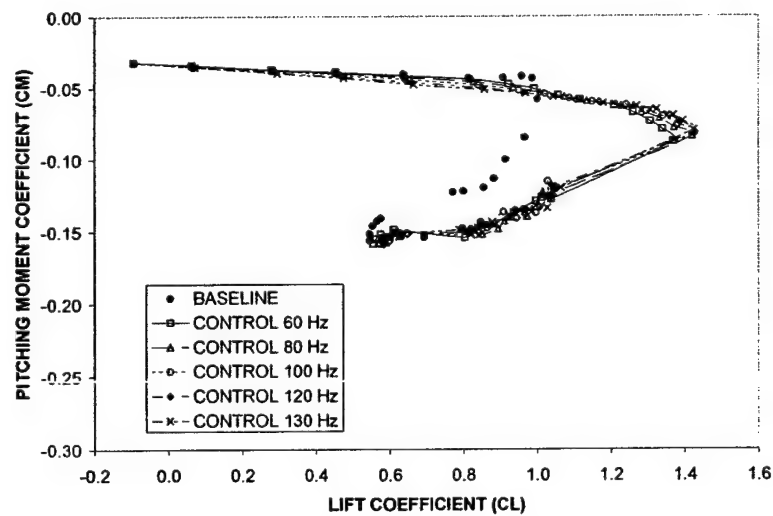
Figure 4.20: Effect of synthetic jet actuator on aerodynamic performance of test wing. Pitching moment coefficient (CM) vs. lift coefficient (CL).
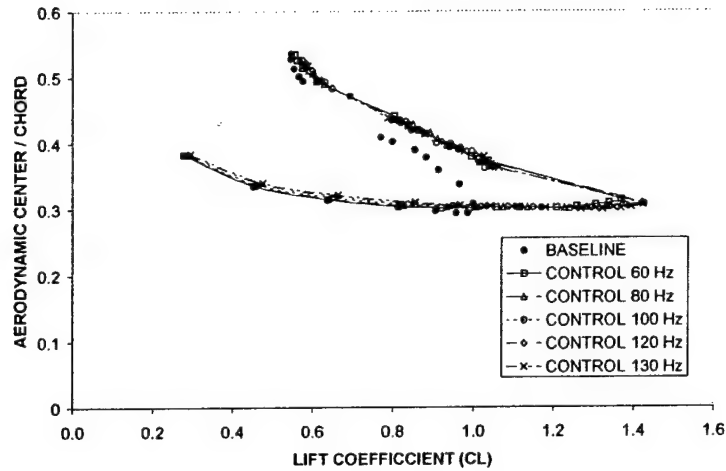
Figure 4.21: Effect of synthetic jet actuator on aerodynamic performance of test wing. Aerodynamic center location (AC) vs. lift coefficient (CL).
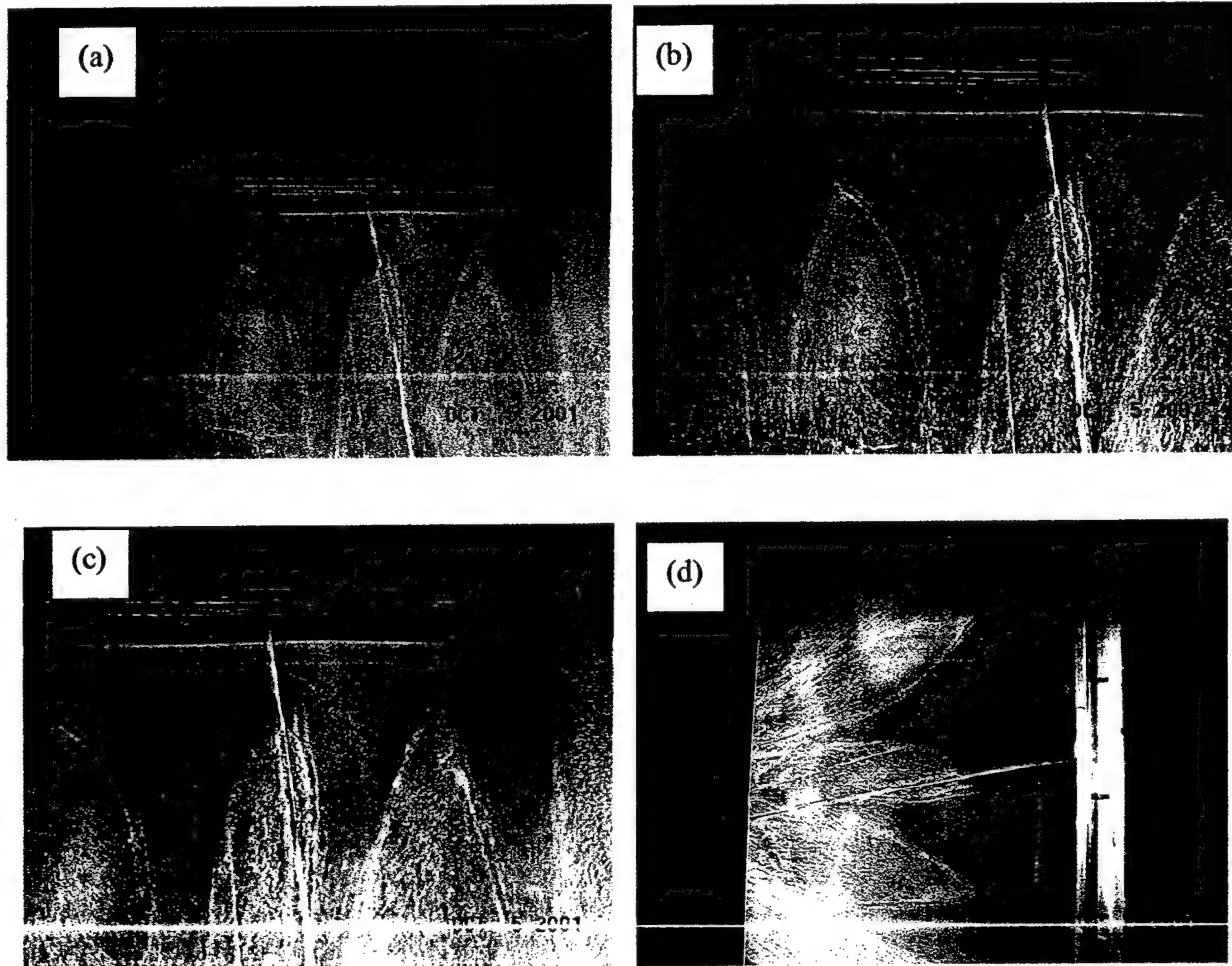

Figure 4.22: Oil surface flow visualization of test wing. Synthetic jet actuator operating at a frequency of 120 Hz. Wind tunnel off ($U_\infty = 0$ m/s). (a) Global view, (b) details of center piston region, (c) details of right side and (d) front view.
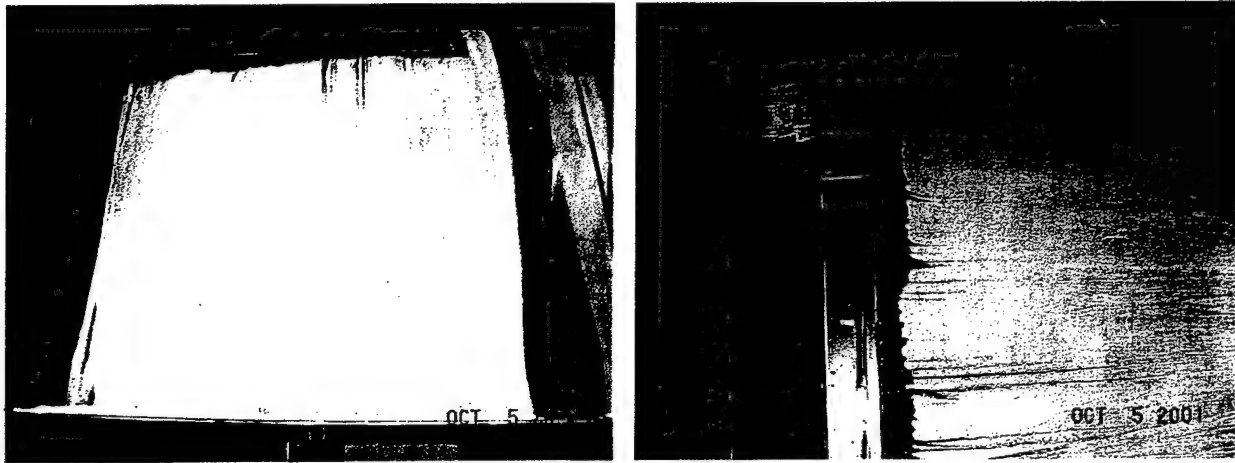
Figure 4.23: Oil surface flow visualization of test wing at $\alpha = 8$ degrees and $U_\infty = 35$ m/s. Flow is completely attached, hence SJA was not operated.
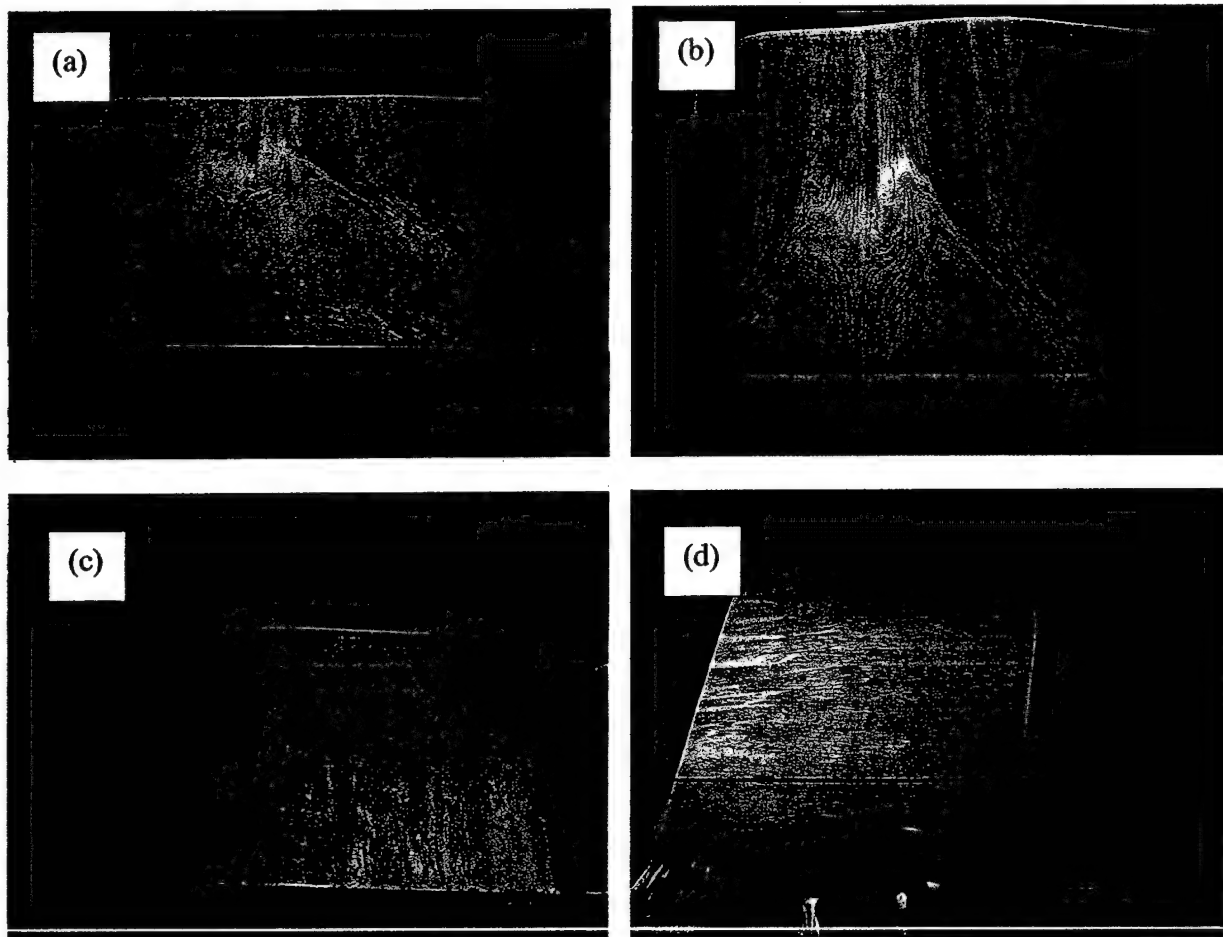

Figure 4.24: Oil surface flow visualization of test wing at $\alpha = 12$ degrees and $U_\infty = 35$ m/s. (a) and (b) correspond to no control, (c) and (d) correspond to control at 120 Hz.
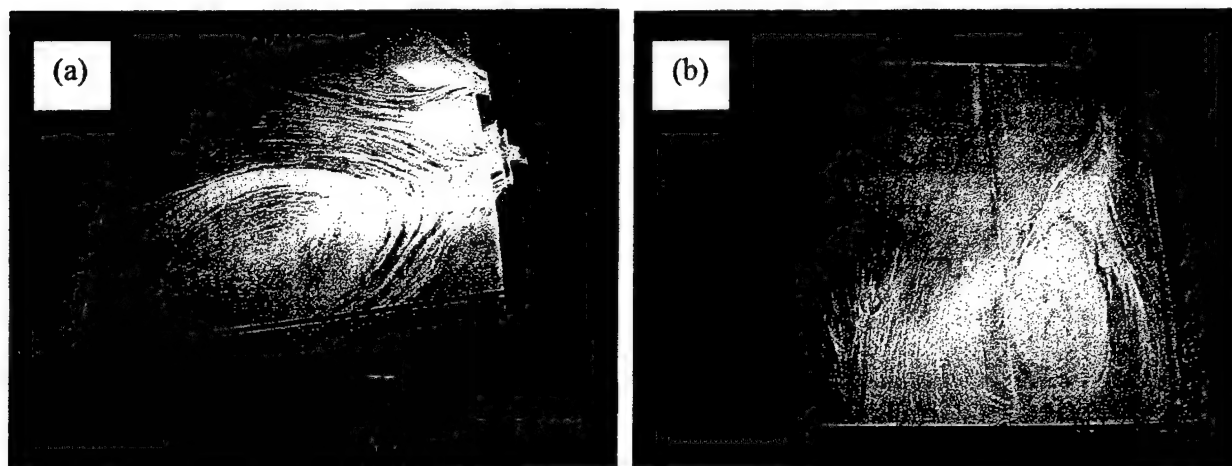
Figure 4.25: Oil surface flow visualization of test wing at α = 16 degrees and U_∞ = 35 m/s. (a) no control, (b) control at 120 Hz.
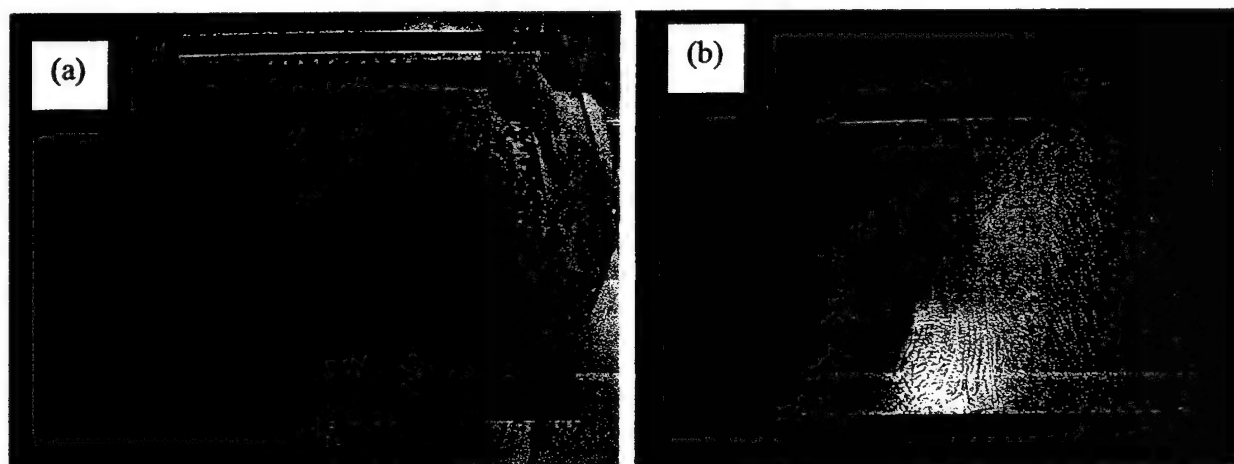

Figure 4.26: Oil surface flow visualization of test wing at α = 18 degrees and U_∞ = 35 m/s. (a) no control, (b) control at 120 Hz.
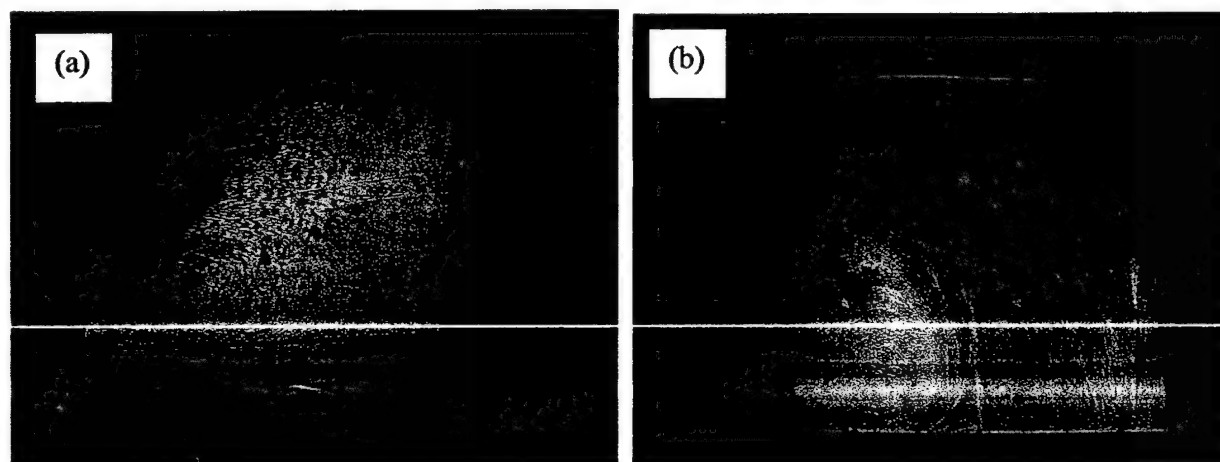

Figure 4.27: Oil surface flow visualization of test wing at α = 20 degrees and U_∞ = 35 m/s. (a) no control, (b) control at 120 Hz.
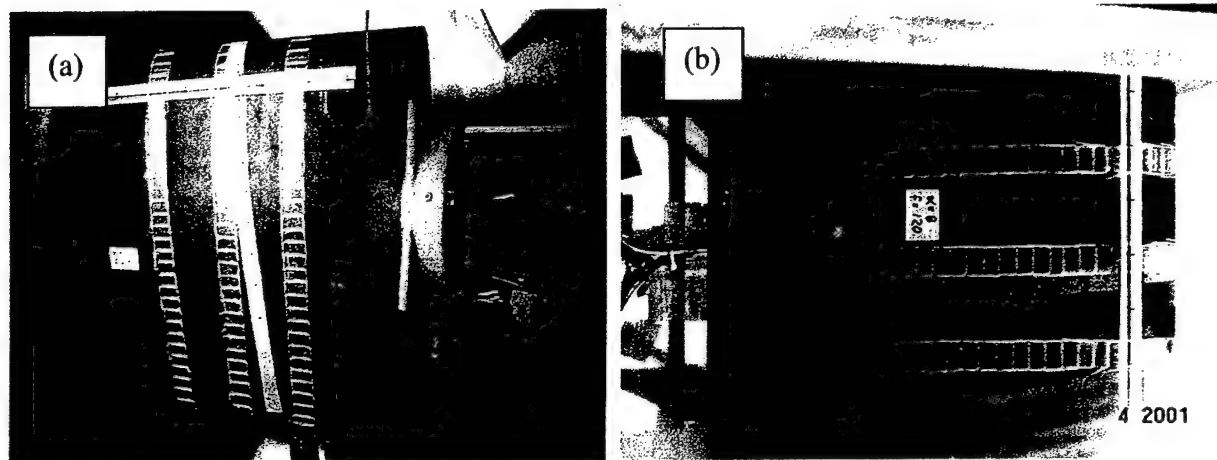
Figure 4.28: Tufts surface flow visualization of test wing at α = 8 degrees and U_∞ = 35 m/s. (a) no control, (b) control at 120 Hz.

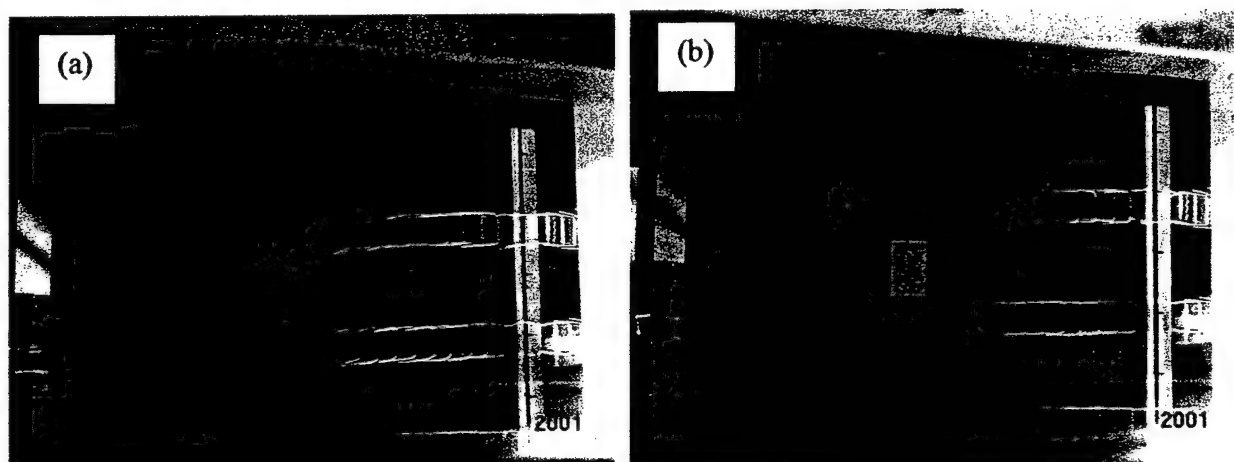

Figure 4.29: Tufts surface flow visualization of test wing at α = 12 degrees and U_∞ = 35 m/s. (a) no control, (b) control at 120 Hz.
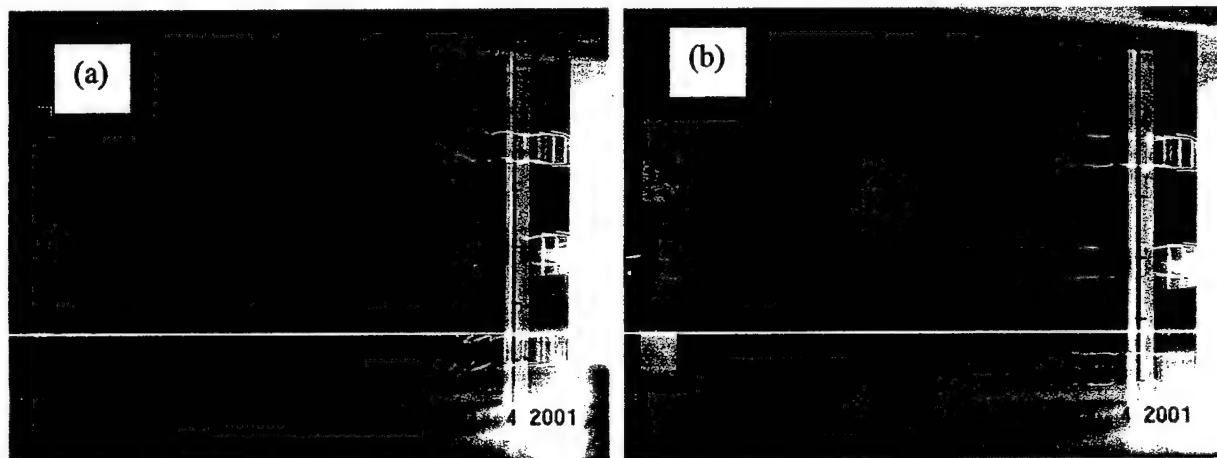

Figure 4.30: Tufts surface flow visualization of test wing at α = 16 degrees and U_∞ = 35 m/s. (a) no control, (b) control at 120 Hz.
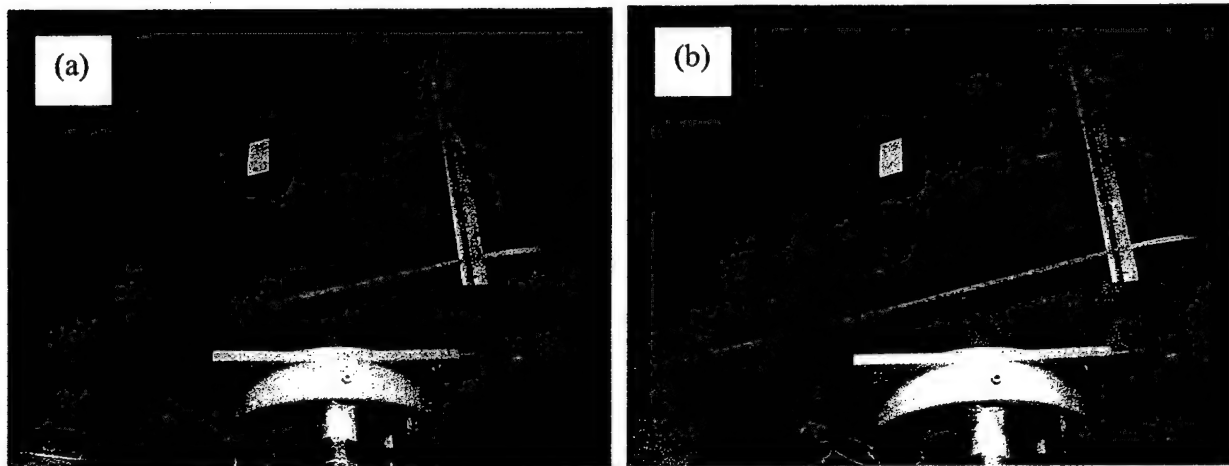
Figure 4.31: Tufts surface flow visualization of test wing at $\alpha = 18$ degrees and $U_\infty = 35$ m/s. (a) and (b) correspond to no control, (c) and (d) correspond to control at 120 Hz.

Figure 4.32: Smoke flow visualization of test wing at $\alpha = 8$ degrees and $U_\infty = 35$ m/s. (a) corresponds to no control and (b) corresponds to control at 120 Hz.

Figure 4.33: Smoke flow visualization of test wing at $\alpha = 12$ degrees and $U_\infty = 35$ m/s. (a) corresponds to no control and (b) corresponds to control at 120 Hz.

Figure 4.34: Smoke flow visualization of test wing at $\alpha = 16$ degrees and $U_\infty = 35$ m/s. (a) corresponds to no control and (b) corresponds to control at 120 Hz.
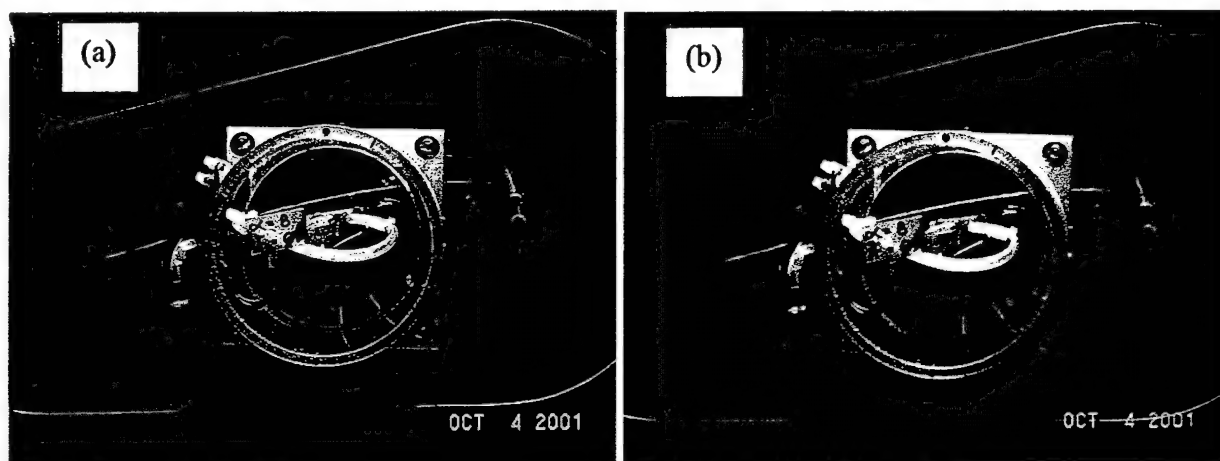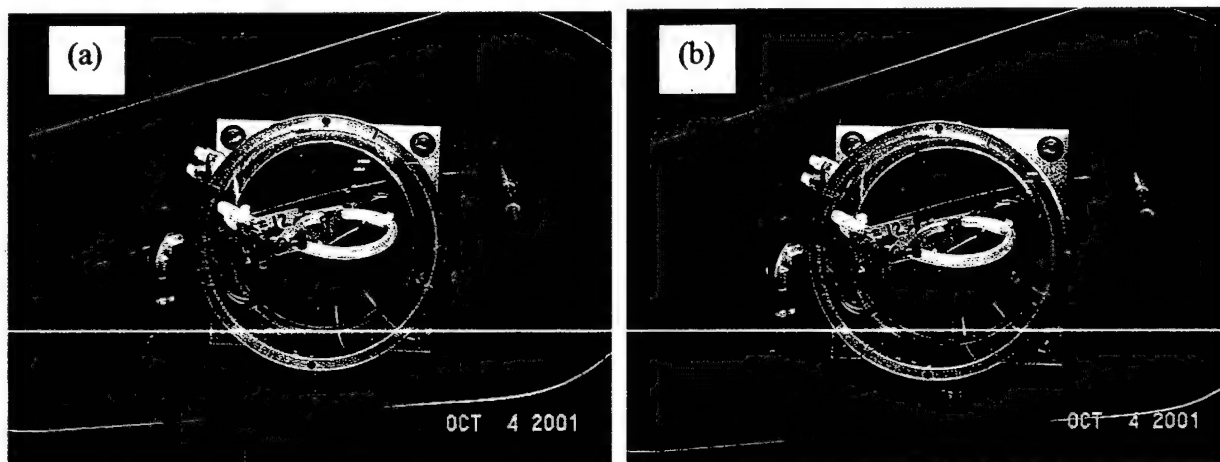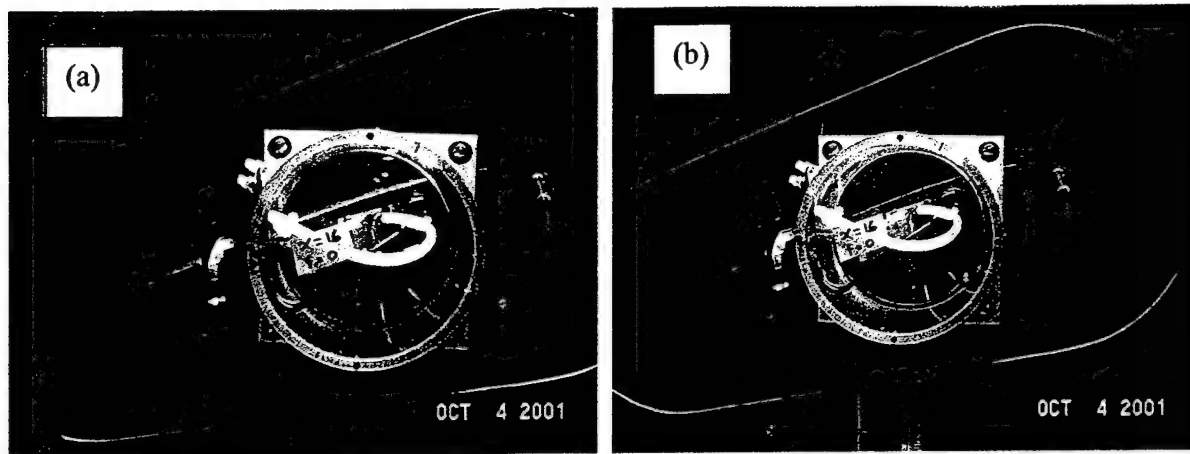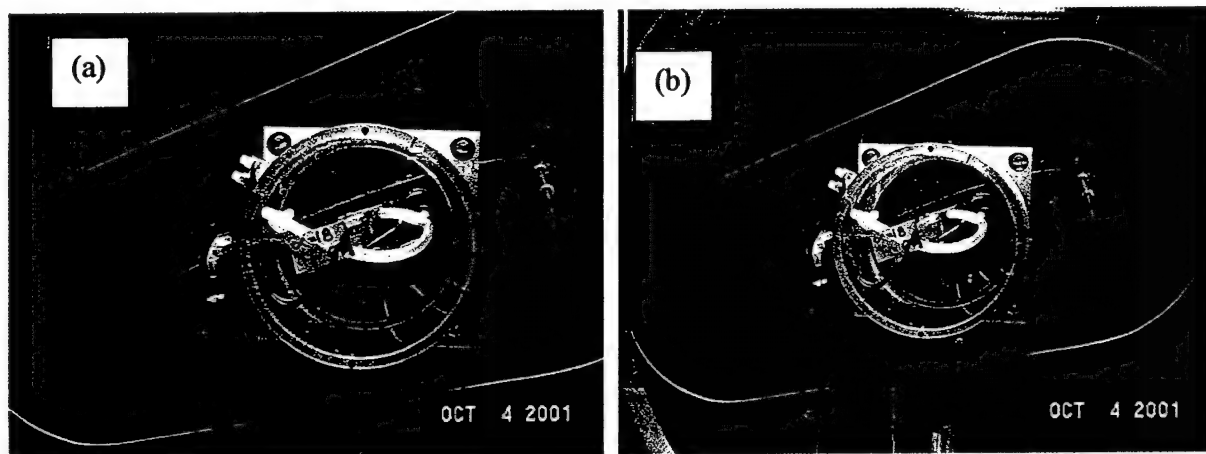

Figure 4.35: Smoke flow visualization of test wing at $\alpha = 18$ degrees and $U_\infty = 35$ m/s. (a) corresponds to no control and (b) corresponds to control at 120 Hz.
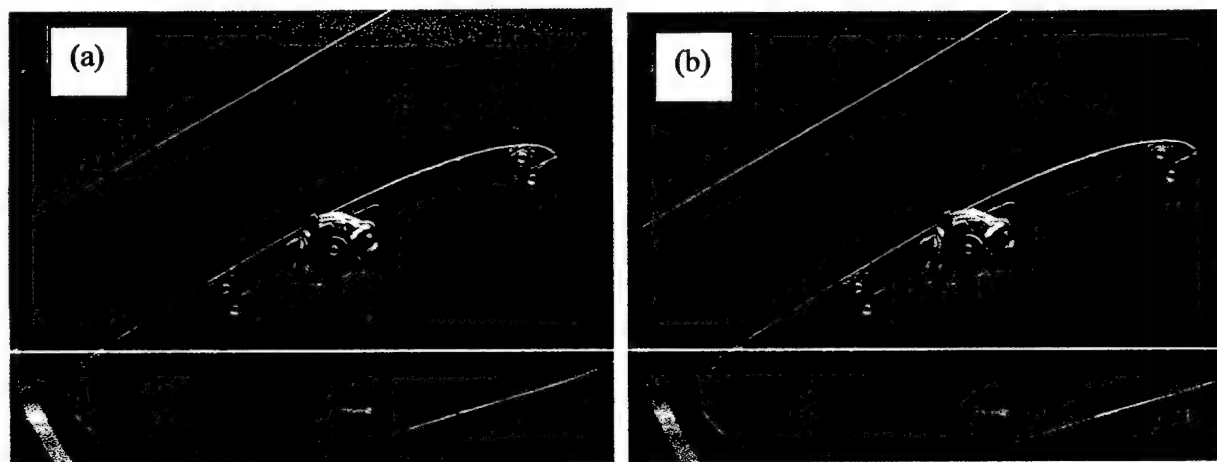
Figure 4.36: Preliminary smoke flow visualization of test wing at $\alpha = 25$ degrees and $U_\infty = 30$ m/s. (a) corresponds to no control and (b) corresponds to control at 120 Hz.

58

Figure 4.37: Surface static pressure distribution for $\alpha = -1.20$ degrees and $U_\infty = 35$ m/s.

Figure 4.38: Surface static pressure distribution for $\alpha = 0.60$ degrees and $U_\infty = 35$ m/s.

Figure 4.39: Surface static pressure distribution for $\alpha = 4.85$ degrees and $U_\infty = 35$ m/s.

Figure 4.40: Surface static pressure distribution for $\alpha = 6.75$ degrees and $U_\infty = 35$ m/s.

Figure 4.41: Surface static pressure distribution for $\alpha = 8.75$ degrees and $U_\infty = 35$ m/s.
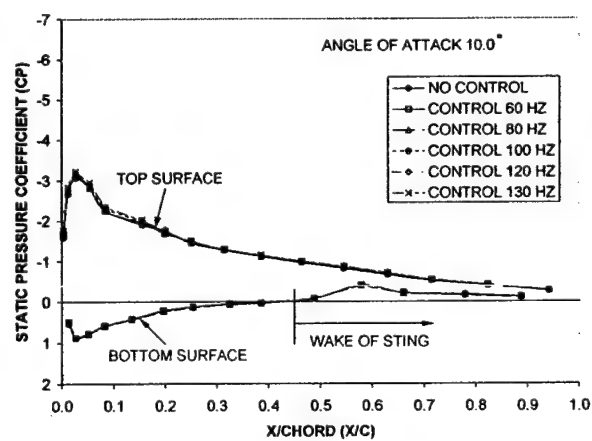
Figure 4.42: Surface static pressure distribution for $\alpha = 10.0$ degrees and $U_\infty = 35$ m/s.

59
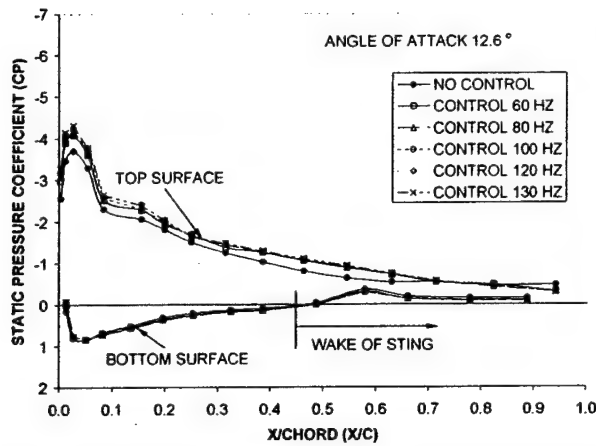
Figure 4.43: Surface static pressure distribution for α = 12.6 degrees and U_∞ = 35 m/s.
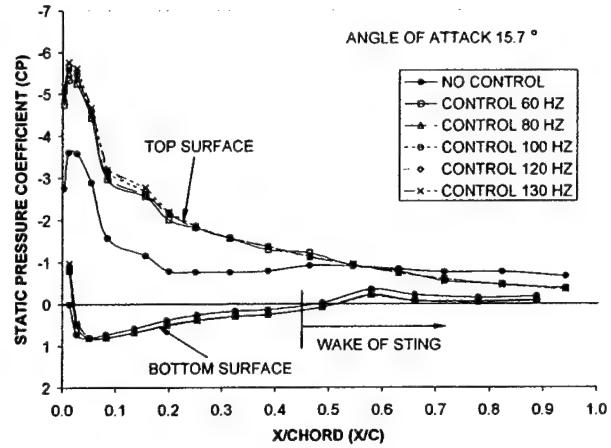
Figure 4.44: Surface static pressure distribution for α = 15.7 degrees and U_∞ = 35 m/s.
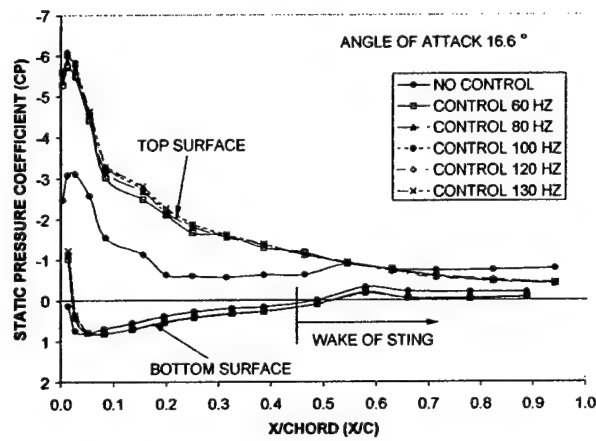
Figure 4.45: Surface static pressure distribution for α = 16.6 degrees and U_∞ = 35 m/s.
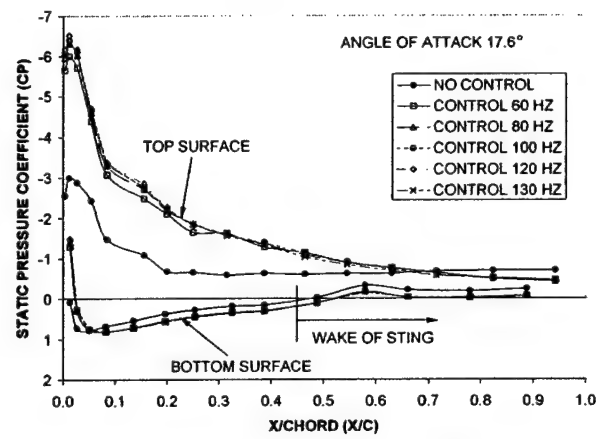
Figure 4.46: Surface static pressure distribution for α = 17.6 degrees and U_∞ = 35 m/s.
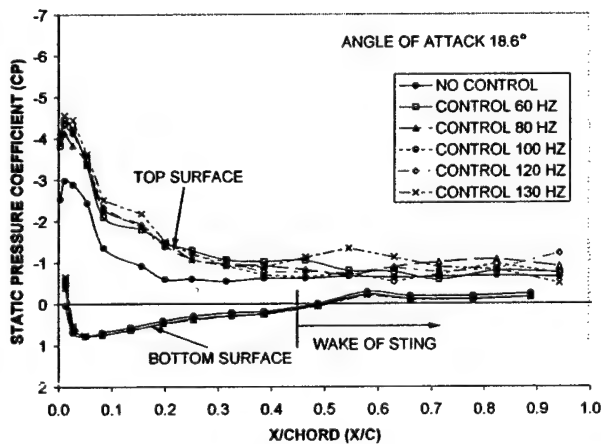
Figure 4.47: Surface static pressure distribution for α = 18.6 degrees and U_∞ = 35 m/s.
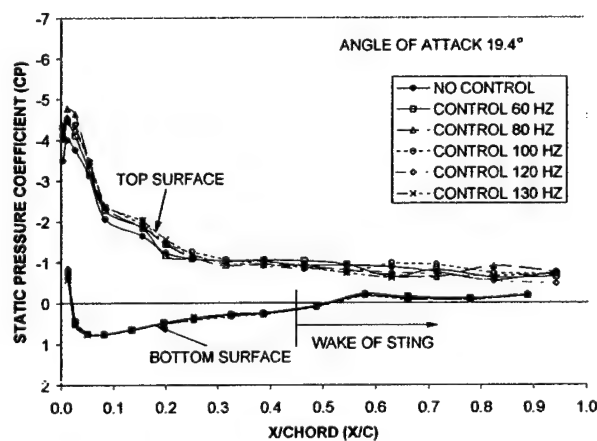
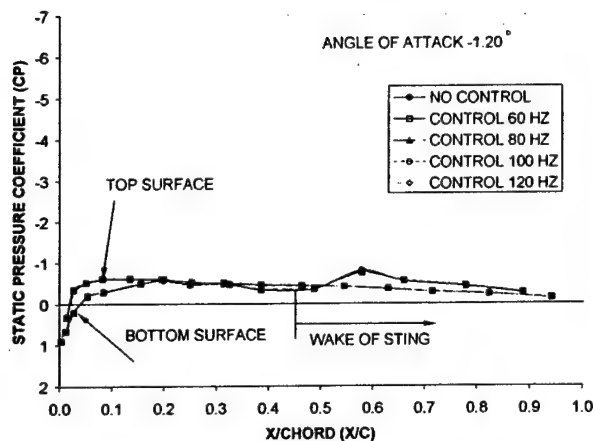Figure 4.48: Surface static pressure distribution for α = 19.4 degrees and U_∞ = 35 m/s.
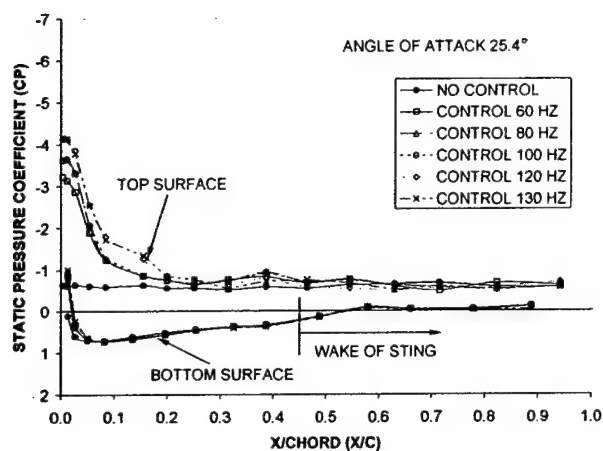
Figure 4.49: Surface static pressure distribution for $\alpha = 25.4$ degrees and $U_\infty = 35$ m/s.

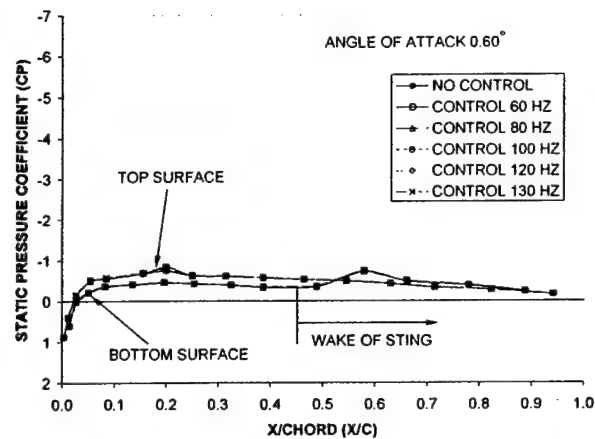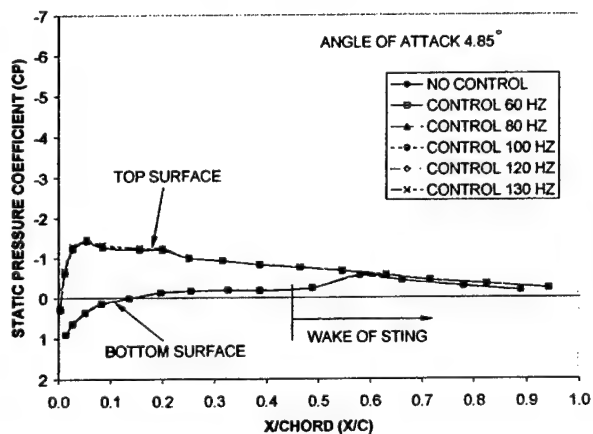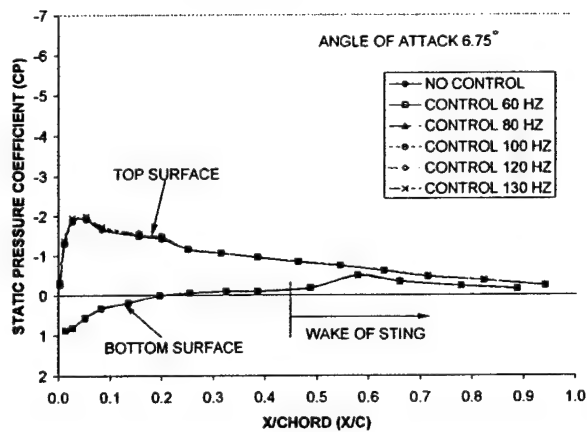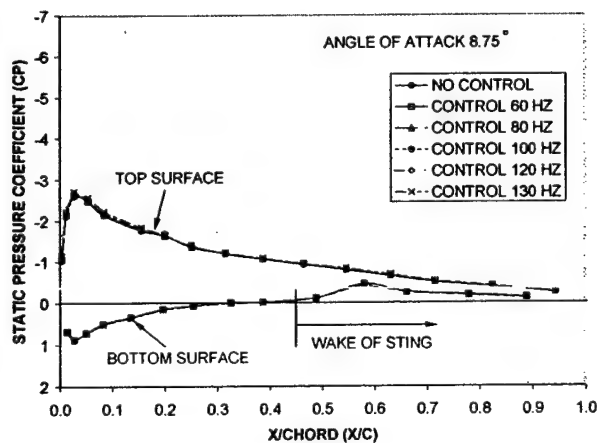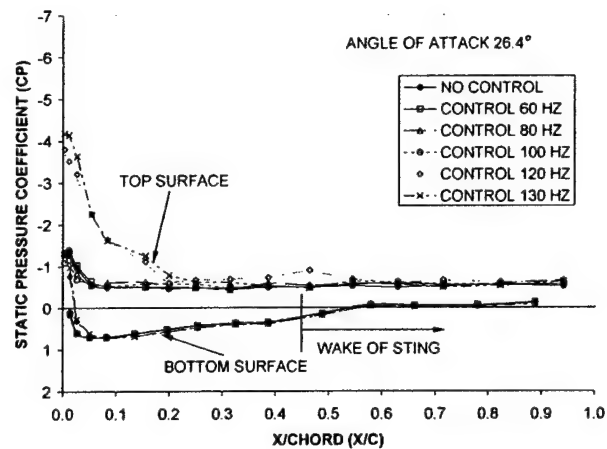Figure 4.50: Surface static pressure distribution for $\alpha = 26.4$ degrees and $U_\infty = 35$ m/s.
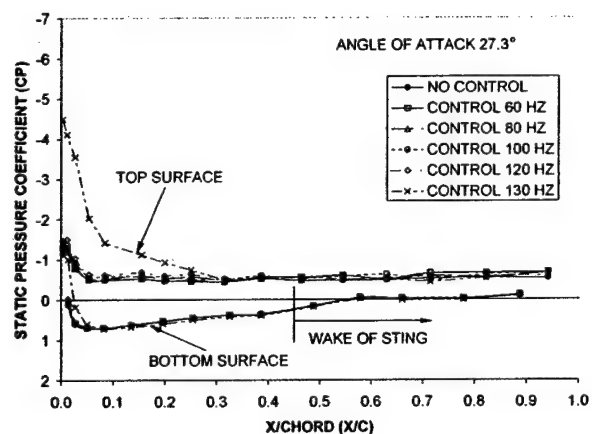
Figure 4.51: Surface static pressure distribution for $\alpha = 27.3$ degrees and $U_\infty = 35$ m/s.
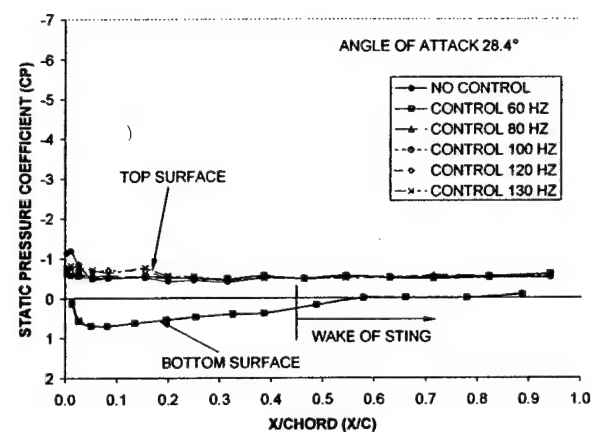
Figure 4.52: Surface static pressure distribution for $\alpha = 28.4$ degrees and $U_\infty = 35$ m/s.
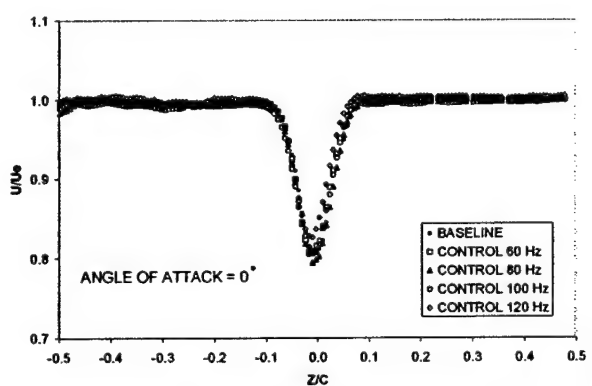
Figure 4.53: Wake survey of test wing at $\alpha = 0.0$ degrees and $U_\infty = 35$ m/s.

61

Figure 4.54: Wake survey of test wing at α = 8.0 degrees and U_∞ = 35 m/s.

Figure 4.55: Wake survey of test wing at α = 12.0 degrees and U_∞ = 35 m/s.

Figure 4.56: Wake survey of test wing at α = 16.0 degrees and U_∞ = 35 m/s.
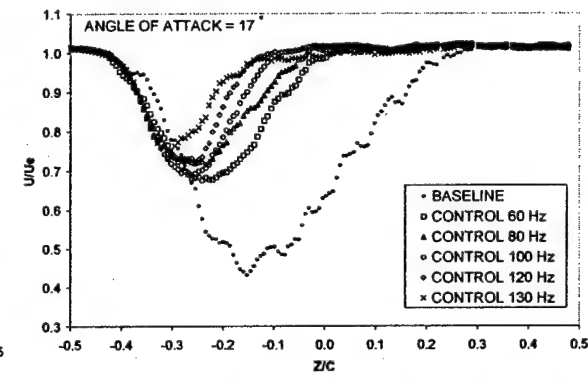
Figure 4.57: Wake survey of test wing at α = 17.0 degrees and U_∞ = 35 m/s.
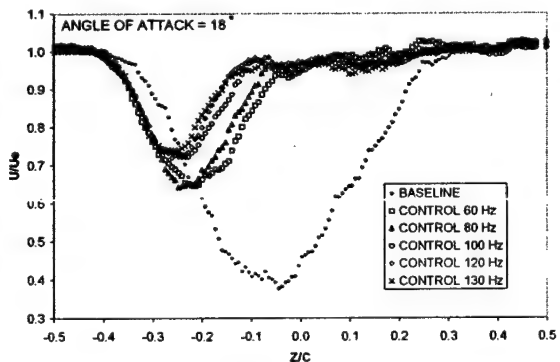
Figure 4.58: Wake survey of test wing at α = 18.0 degrees and U_∞ = 35 m/s.
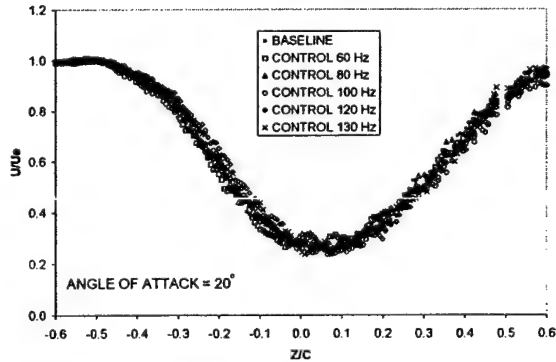
Figure 4.59: Wake survey of test wing at α = 20.0 degrees and U_∞ = 35 m/s.

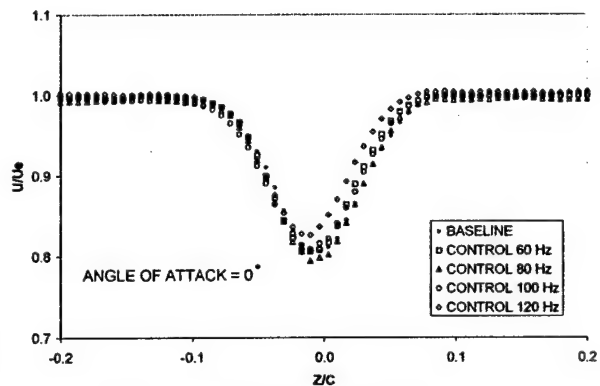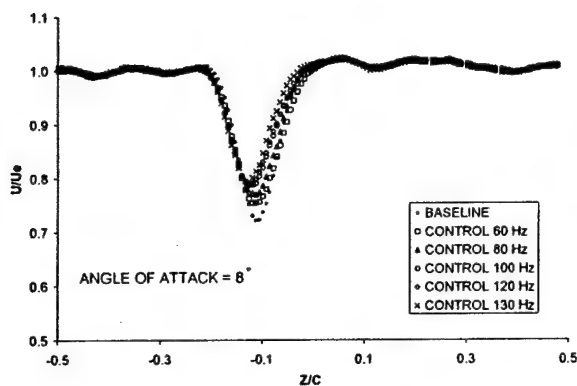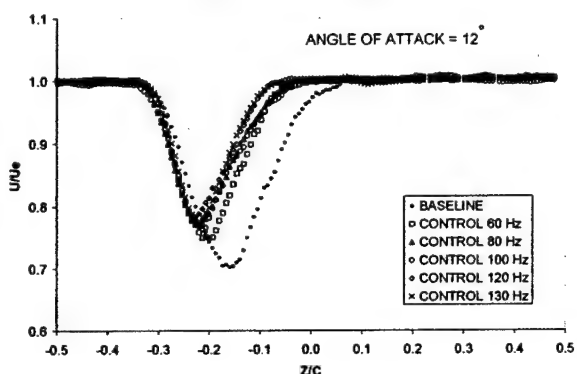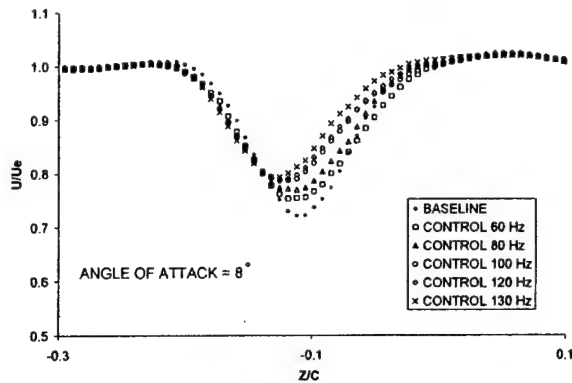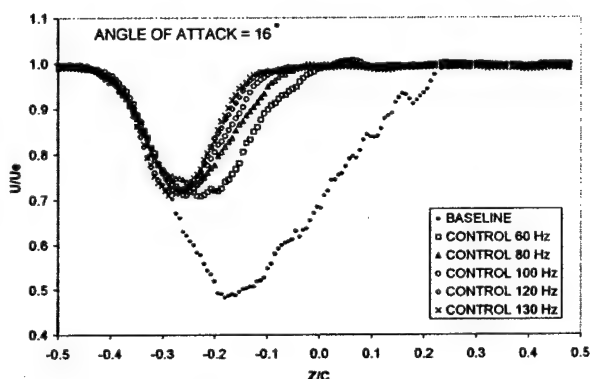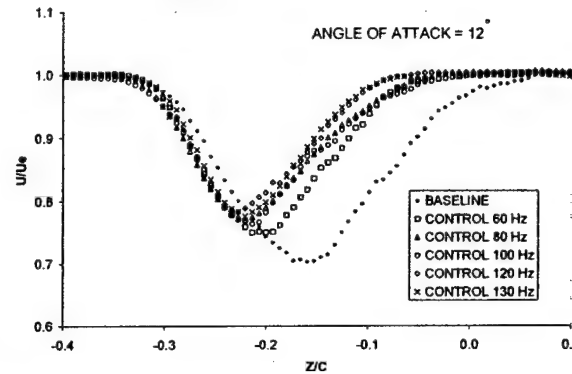# 5. DISCUSSION OF ACTUATOR CHARACTERIZATION AND STEADY WIND TUNNEL TEST RESULTS

General

This section contains discussion of the results from the investigation of the effects of a synthetic jet actuator on the performance of a test wing.

The data is presented in the following way:
- Bench Tests: Data used to characterize the flowfield at the exit of the SJA is shown.
- Force Balance: Data is presented showing the effect of the synthetic jet actuators on lift, drag, pitching moment and the location of the wing's aerodynamic center.
- On-Surface Flow Visualization: Limiting streamlines patterns, determined using titanium dioxide suspended in kerosene are presented for the wing placed at several angles of attack. Tufts are also used to provide a second means of surface flow visualization.
- Off-Surface Flow Visualization: Flow visualization by the injection of smoke upstream of the wing is presented.
- Surface Pressure: Surface pressures were recorded close to the mid-span of the wing, at 32 locations distributed on the top and bottom surfaces. The effect of the SJA on chordwise distribution of the surface pressure is presented for several angles of attack.
- Wake Surveys: Plots showing the effect of the SJA on the wake generated by the test wing are included for various angles of attack.

Bench Tests

Figures 4.1 and 4.2 present the maximum velocity magnitude, inside the exit slot and in the middle of its width, for the two different slot configurations that were tested for the single piston actuator prototype. In each plot, the theoretically calculated maximum velocity (from the incompressible continuity equation) is also shown. The difference between the theoretical and measured curves provides a measure of the magnitude of the compressibility effects within the actuator. Several observations can be made. First, for the displacement volume and slot widths, exit velocities as high as 90 m/sec can be achieved. As it should be intuitively expected, compressibility effects are more pronounced for the narrow slot (0.8 mm) and for the higher actuation frequencies. For low frequencies the two curves are in good agreement. For the narrow slot, the curves start diverging from each other sooner (at around 80 Hz) than the wider slot (at around 110 Hz). So, it is interesting to note that at the high frequency end (around 250 Hz), the measured velocities only differ by 50% (60m/sec and 90m/sec, for the wide and narrow slots, respectively), while their theoretical values differ by 100% (65m/sec and 130m/sec, for the wide and narrow slots, respectively).

Figure 4.3 through 4.4 present the maximum velocity magnitude, measured at the exit of each one of the piston exit slots in the middle of its width, for the second generation synthetic jet array as a function of actuator frequency. Figure 4.3 shows a comparison between the hotwire measurements and the theoretical value calculated using the incompressible continuity equation. As may be seen in the figure, the measured values and the theoretical predictions agree quite well despite the simplicity of the model. This is due to the fact that the exit slot was designed to be wide enough to minimize compressibility effects inside the piston chambers. Also of interest is the fact that velocities up to 90 m/sec were obtained for an actuator frequency of 130 Hz. The differences between the curves corresponding to measurements made for each one of the pistons may be due to several factors discussed below.

Although care was taken during the machining of the curved surfaces of the exit slots and during the assembly of the actuator components, small differences in the slot width for different pistons or uneven wear between the piston rings and the cylinder lining may account for a significant difference in the exit velocity measured at each piston. Also, considering that the slot has a width of 2 mm, any misalignment between the traverse mechanism that moves the measuring probe (hotwire or fast response probe) and the exit slot of the actuator may affect the measurements dramatically.

Figure 4.4 shows a comparison between the measurements of the maximum slot exit velocity made with a hotwire and with a fast response pressure probe. Individual plots are included for each one of the pistons. As may be seen in the figures the agreement between the measurements is good.

Figure 4.5 shows the jet momentum coefficient ($C\mu$) as a function of actuator frequency for each one of the pistons. These values were calculated using the maximum exit velocity of the slot measured experimentally and shown in figures 4.3 and 4.4. For the type of actuator presented here (for a given freestream velocity) the jet momentum coefficient is a function of slot width (which is fixed) and actuator frequency. Consequently the jet momentum coefficient and the actuator frequency may not be varied independently. This is a drawback of the developed system, which is associated with the use of pistons with a fixed stroke length. Evaluations are currently underway to develop a slot with a variable geometry.

Figure 4.6 shows the spanwise distribution of the maximum slot exit velocity for an actuator frequency of 120 Hz. The figures show the data corresponding to measurements performed before and after the installation of the separating walls in the slot. As may be seen in the figure, for the case of the measurements performed before the installation of the separating walls, the minimum exit velocity was achieved for pistons 2 and 5. This is because for these pistons both of the neighboring pistons are out of phase. On the other hand, piston 1 and 6 present the highest exit velocity, as they only have one neighboring piston, which is out of phase. Finally pistons 3 and 4 present an intermediate value as these pistons have one out of phase piston on one side and one in-phase piston on the other side. As may be seen in the figure, this strong interaction between the out-of-phase pistons was greatly reduced after the installation of the separating walls within the slot. However for this configuration the wake of the walls is now evident.

Figure 4.7 presents the power consumption of the synthetic jet actuator as a function of its operating frequency. As it may be seen, the actuator requires a power of almost 1200 W to operate at 150 Hz, while operation at 100 Hz requires less than half of that power. For the results presented here, the frequency of the SJA array never exceeded 130 Hz due to limitations of the available power supply.

Force Balance

Figures 4.8 to 4.10 show the results from three tests conducted on the basic wing (without actuation) at the same wind tunnel operating conditions ($U_\infty = 35$ m/s) to verify the repeatability of the data measured by the pyramidal balance. As may be seen in the figures, the repeatability of the results is very good for both pre and post-stall conditions. Figure 4.11 to 4.13 show the results corresponding to tests performed on the basic wing for three different freestream velocities in order to investigate the effects of Reynolds number on the aerodynamic forces measured on the wing. The wing was tested at freestream velocities (U_∞) of 30, 35 and 40 m/s, which corresponded to Reynolds numbers of 7.68×10^5, 8.96×10^5 and 1.02×10^6 respectively. Tests were not performed at higher velocities due to the limitations of the pyramidal balance. As may be seen in the figures, the agreement between the different tests is good; hence the effect of Reynolds number on the measurements was small (for the tested Reynolds number range). Figure 4.14 through 4.21 present the effect of operation of a SJA on the aerodynamic performance of the test wing. These force measurements were performed at a freestream velocity U_∞ of 35 m/s, which corresponded to a Reynolds number of 8.96×10^5.

Effect of SJA on Lift Coefficient

As may be seen in figure 4.14, at angles of attack (α) below 10 degrees, an increase in the actuator frequency causes a slight increase in the lift curve slope ($CL\alpha$). This effect may be seen more clearly in figure 4.15, which presents the lift coefficient as a function of angle of attack in radians for a range of angles of attack between 0 and 10 degrees (0 and 0.18 radians respectively). As may be seen in this figure, the effect of the actuator in this range of angle of attack is to rotate the lift curve by increasing its slope. Figure 4.16 shows the variation of the lift curve slope ($CL\alpha$) as a function of actuator frequency. For actuator frequencies between 60 and 130 Hz, the increase in the lift curve slope scales linearly with actuator operating frequency.

The use of synthetic jet actuators causes a dramatic increase in the value of CL_{max} (80%) (figure 4.14). This is also shown in figure 4.17, which presents the increase in lift coefficient (ΔCL) vs. angle of

attack. The operation of the SJA extends the range of angles of attack for which the wing may be operated without stalling. The angle of attack for which stall occurs was increased from 12 degrees on the clean (or basic) wing to 18 degrees for the case of SJA actuation. As shown in figure 4.18, in the range of operating frequencies that were tested, the frequency of actuation does not seem to have a significant effect on the magnitude of CL_{max}. For these tests CL_{max} had a low value due to the fact that the Reynolds number of the tests is relatively low (Traub, 1992).

Figure 4.14 also shows that the basic wing has a very docile stall, which is typical of aft stall, which is also referred to as trailing edge stall. This type of stall mechanism is typical for thick airfoils and is characterized by the gradual upstream movement of the separated flow region from the trailing edge, as the angle of attack increases. With SJA actuation, the stall mechanism is more similar to that of medium thickness airfoils which is called leading edge short bubble stall, and is characterized by flow separation taking place rather abruptly over the entire top surface of the airfoil when the bubble bursts, with the origin of this separation occurring close to the leading edge. As may be seen in the figure, the lift curve presents a sharp peak close to CL_{max}, and decreases rapidly above the stall angle, this behavior is very similar to the one presented by the leading edge stall mechanism. It may be said then that application of synthetic jet actuators delays the occurrence of trailing edge stall until a point at which the mechanism of separation behaves more like a leading edge short bubble separation.

For $\alpha > 18$ degrees, once massive stall has occurred on both airfoil configurations (basic and actuated), the operation of the synthetic jets still provides a small amount of lift augmentation, however the effects of the actuator is relatively small. It may be seen that for angles of attack larger than 25 degrees (post-stall), a large frequency of actuation is required to produce any noticeable effects, i.e. only actuation at frequencies above 100 Hz seem to produce any appreciable lift augmentation.

Effects of SJA on Drag Coefficient

Figure 4.19 shows that the use of the synthetic jet actuator produces a drag reduction on the wing at high CL. This was further verified by inspection of the wake surveys that will be discussed later. For lift coefficients below 1.0 ($\alpha < 10$ degrees), the use of the SJA does not seem to have any effect over the drag coefficient. The decrease in drag at angles of attack between 10 and 18 degrees (CL between 1.0 and 1.4 respectively) is due to the suppression of the separated region over the wing, with its resulting reduction of the form or pressure drag. For the case of the post-stall region, the SJA produces a small reduction of the drag force. The improvements obtained are not only a consequence of reattaching the flow but also eliminating a large wake region

Effects of SJA on Pitching Moment Coefficient and Aerodynamic Center Location

Figure 4.20 shows the effect of the synthetic jet actuators on the pitching moment of the airfoil. The slight slope of the pitching moment curve is due to the fact that the pitching moment coefficient was calculated at the quarter chord position measured from the leading edge ($x = \frac{1}{4} C$), which is the theoretical position of the aerodynamic center for NACA symmetrical profiles. As may be seen in figure 4.21, the location of the aerodynamic center for the test wing is at 30 % of the chord. It is suspected that this difference is caused by the relatively large thickness of the trailing edge of the airfoil. Summers and Page (1950) experimentally showed that as the trailing edge thickness of their test wing was increased, more lift was carried over the rear portion of the airfoil section, with an increase in the slope of the pitching moment curves. This would explain a rearwards shift in the aerodynamic center of the wing. Furthermore, asymmetry in the construction of the wing halves may also be a contributing factor in this shift.

Returning to figure 4.20, it may be seen that stall is characterized by a strong nose down pitching moment. The effects of the SJA are to delay stall, hence the occurrence of the strong nose-down pitching moment is delayed for the actuated case. Note that for lift coefficients lower than 1.0 (i.e. before the basic wing stalls), higher actuation frequencies result in a larger nose-down pitching moment. This is due to the fact that wing loading moves further aft, see figure 4.21. At lift coefficients between 1.0 and 1.2 the frequency of actuation does not seem to have any effect over the pitching moment, however as the lift coefficient increases beyond this value, the higher frequencies of actuation delay the occurrence of stall to higher lift coefficient values.

On-Surface Flow Visualization

For these tests two methods of on-surface flow visualization were used. The first one consisted of the use of oil, kerosene and titanium dioxide, while the second one was based on the use of tufts.

Oil Surface Flow Visualization

Figure 4.22 shows the limiting streamlines formed at the exit of the synthetic jet actuator slot. These images were taken for the actuator operating at a frequency of 120 Hz with no freestream imposed on the wing, i.e. the wind tunnel was off. Note that for this case, there are five distinct flow regions clearly visible in the pictures. Notice that the center region encompasses the exit of the two center slots, which are in phase. The other four regions correspond to the exit of each one of the other pistons, which are out of phase with the pistons located on either side. The curvature of the surface streamlines suggest the possibility of the presence of streamwise vortices, at the edge of each individual jet, which may be produced as a result of the strong shear layer caused by the difference in the phasing of the pistons. No evidence of such structures was encountered in the rest of the tests performed on the wing with the presence of a freestream. Figure 4.23 through 4.27 show images of the limiting surface streamlines for the tests performed at a freestream velocity (U_∞) of 35 m/s, which corresponds to a Reynolds number of 8.9×10^5. These images include pictures of the limiting streamlines with and without actuation at 120 Hz, for angles of attack (α) of 8, 12, 16, 18 and 20 degrees.

At $\alpha = 8$ degrees (figure 4.23) the flow was fully attached, hence images of the controlled case were not included. As may be seen in the figure, the surface streamlines are parallel to the freestream, with no evidence of three dimensionality of the flowfield over the wing. This supports the assumption that the sideplates installed on the wings were keeping the flow two-dimensional, which eliminates any aspect ratio effects on the measurements.

At $\alpha = 12$ degrees (figure 4.24), for the case of the flow without actuation, images (a) and (b) show a clear evidence of the presence of trailing edge separation, with two very distinct counter-rotating open recirculation regions close to the trailing edge of the wing. For the actuated case, images (c) and (d) show that the synthetic jet actuators have completely reattached the flow, eliminating the trailing edge separation.

Figure (4.25) shows the limiting streamlines for the wing at $\alpha = 16$ degrees. For this case, images (a) and (b) show that for no actuation, the flow is almost completely separated from the surface, i.e. the extent of the separated region almost reaches as far upstream as 20% of the chord (measured from the leading edge). Note that there are two recirculating regions, one large one close to the center of the wing and a smaller one close to the top edge of image (a) (left side of the wing when seen from behind). For the actuated case, images (c) and (d) show that the synthetic jet actuator has kept most of the flow attached over the center span of the wing, however there is still a sizeable recirculation region on the right hand side of image (c), and a smaller one on the left hand side of image (c). The presence of these separated regions may be due to the fact that the SJA does not cover the entire span of the wing; hence it has no control authority over these regions that are close to the sideplates.

At $\alpha = 18$ degrees (figure 4.26) for the case of no control, it may be seen in figures (a) and (b) that the separation region has now reached the location of the synthetic jet actuator (close to 10% of the chord), and it probably extends further upstream, however that is not visible by the oil. Notice how the two counter-rotating recirculation regions have moved further upstream. For this case the video that was taken during the tests showed that the flow close to the surface moved towards the leading edge of the wing from the trailing edge. Evidence of this is shown by the large oil deposit shown in the middle of image (b). For the case of the controlled flowfield, image (c) and (d) show that the synthetic jets were capable of keeping the flow attached over the whole chord line for the left half of the wing. The flow still remained separated on the right half of the wing.

At $\alpha = 20$ degrees (figure 4.27) for the case of no control, it may be seen that the flow is now completely separated and that the velocity of the flow close to the surface has a strong upstream component, evidenced by the large oil deposits close to the actuator exit. The controlled case showed that for this angle of attack, the synthetic jet actuator was able to keep the flow attached over the whole chord

line for half of the wing. It is of particular interest to mention that if the actuators were turned on after the freestream had reached its value of 35 m/s, the flow separated over the left half of the wing, on the other hand, if the actuator was turned on before the wind tunnel, then the flow separated on the right half of the wing.

Tufts Surface Flow Visualization

Figures 4.28 through 4.31, show the results obtained by the use of tufts as a surface visualization device. The use of tufts permitted the observation of the flowfield characteristics in "real-time", and the effects of having or not having SJA control on the wing were clearly visible without having to change the operating conditions of the wind tunnel as in the case of oil surface flow visualization.

For these tests, the freestream velocity (U_∞) had a value of 35 m/s, which corresponds to a Reynolds number of 8.9×10^5. Data were taken at angles of attack of 8, 12, 16 and 18 degrees.

For $\alpha = 8$ degrees, figure 4.28 shows that the flowfield is attached over the whole surface of the wing. Images (a) and (b) correspond to the case with no control and images (c) and (d) correspond to the controlled case. For this angle, there is no apparent difference between the controlled and the uncontrolled case, however close inspection of images (c) and (d), reveal that the tufts that are located close to the SJA exit show a behavior similar to that over a separated/unsteady region. This may be due to the oscillating nature of the flowfield close to the actuator exit.

For the case of $\alpha = 12$ degrees (figure 4.29), the tufts show the existence of trailing edge separation that covers about the last 40% of the chord. In the image it seems that the separated region covers more of the wing (about 60%) but this is due to the fact that the wing is viewed at an angle from the back. For the actuated case, images (c) and (d) show that the flow has been kept attached, however the unsteady region close to the actuator exit is evident.

Figure 4.30 shows the flowfield over the wing for $\alpha = 16$ degrees. Images (a) and (b) show that for the non-controlled case, the separated flow reaches the position of the synthetic jet (about 12% of the chord). Close inspection of the tufts close to the trailing edge shows that the tufts are pointing in the upstream direction, which coincides with the observation made with the oil surface flow visualization. Image (c) and (d) show that the flow has been kept attached for the actuated case. The unsteady pocket close to the actuator exit is also visible in the images.

Finally, for the case of $\alpha = 18$ degrees (figure 4.31), the non-controlled images (a) and (b) show that the flow is separated from a position upstream of the actuator. For the actuated case, the flow is seen to be attached. Note however that in image (c), the flow on the lower row of tufts seems to indicate the presence of a separated region close to the trailing edge. This corresponds to the separated region observed in the oil flow visualizations.

For all of the angles of attack that were tested with tufts, the results agree very well with the results obtained with the oil flow visualization technique.

Off-Surface Smoke Flow Visualizations

Figure 4.32 through 4.35 show the flow visualizations obtained by the injection of smoke upstream of the wing, for a freestream velocity of 35 m/s. Figure 4.36 shows the results for a freestream velocity of 30 m/s.

Figure 4.32 shows the results for the wing at an angle of attack of 8 degrees. For this case there is no noticeable difference between the flow without (top) and with (bottom) actuation. For an angle of attack of 12 degrees (figure 4.33), it can be seen that the downward deflection of the streak-line (line of smoke) corresponding to the actuated case (bottom image) is slightly larger than for the case with no actuation. Figure 4.34 shows that for an angle of attack of 16 degrees, for the case of no actuation (top) the smoke injected upstream of the wing is captured in the separated region of the flow (wake) and there is not a visible streak-line leaving the wing. On the other hand, for the actuated case (bottom) the streak-line is clearly defined in the image and the smoke has not diffused into the wake. For $\alpha = 18$ degrees (figure 4.35), the top image (no actuation) shows that the separated wake of the wing is quite large and the smoke has clearly been entrained in this separated region. For the actuated case, the streak-line is clearly visible in the bottom image and it seems to be attached to the wing surface. Finally, 4.36 shows

the flow without (top) and with (bottom) actuation for an angle of attack of 25 degrees and a freestream velocity of 30 m/s. Without actuation the flow separates close to the leading edge and the wing is in the post-stall region. With actuation, the flow remains attached over the whole wing chord.

Surface Pressure Measurements

Figures 4.37 through 4.52 show the surface pressure measurements from the wing at a freestream velocity of 35 m/s and several angles of attack. The pressure tappings on the upper and lower surfaces were placed close to the mid-span of the wing, hence for the case of the ones on the pressure surface (bottom half) of the wing, their location was such that the pressure that was measured by them was affected by the wake of the sting that supported the wing. The area of the flowfield that was affected by the wake of the sting is clearly marked in the figures.

Figures 4.37 and 4.38 show the pressure distribution for angles of attack of −1.20 and 0.6 degrees respectively. These two figures clearly show that the test wing is not completely symmetric. Figures 4.39 through 4.42 show the pressure distribution for the wing at angles of attack of 4.85, 6.75, 8.75 and 10.0 respectively. Note that for these figures actuation of the SJA only has an effect on the pressure distribution over the first 25% of the upper surface of the wing, that is, the effect of the actuator is limited to a small area close to the leading edge of the wing. For these figures it can be seen that the magnitude of the suction peak increases as the angle of attack is increased. The pressure distribution on the bottom surface is unaffected by the SJA. Notice also that for figures 4.39 and 4.40, at the location signaled by the arrow that marks the top surface, the flat pressure distribution suggests the presence of a localized separation bubble.

For the case of α = 12.6 degrees (figure 4.43), comparing the pressure distribution of the basic wing and the one generated with actuation of the SJA, it is evident that the synthetic jet has now a global effect over the pressure distribution on the suction surface of the wing. The pressure distribution for the actuated cases match the inviscid flowfield more closely as separation is suppressed, while for the basic wing trailing edge separation is now visible and extends to a position of about 60% of the chord, that is 40% of the chord presents separation. For this angle, the pressure surface of the wing also shows to be affected slightly by the SJA.

Increase of the angle of attack produced further increase of the suction peak for the actuated case. The pressure also increased on the windward (pressure) side of the wing with the SJA compared to the basic wing. Upper surface suction decreased significantly for the basic wing due to large trailing edge flow separation extending over approximately 80% of the chord (see figures 4.44 and 4.45). The suction peak for the actuated cases reaches a maximum at an angle of attack of 17.6 degrees (figure 4.46). In this range, the frequency of actuation has a small effect on the pressure distribution over the wing. This is important because for the case of DC motor driven SJAs the power input to the actuator increases for an increase in actuator frequency (figure 4.7), hence a lower required actuation frequency would require less power.

Figure 4.47 shows the pressure distribution for α = 18.6 degrees. It is interesting to note that in just 1 degree, the suction peak (for the actuated cases) has decreased drastically and 70% of the airfoil suction is lost due to trailing edge separation. This indicates a violent stall, and although there is no doubt that for this case the separation mechanism is a trailing edge stall, its characteristics are more similar to the case of leading edge stall. Further increase of the angle of attack to 19.4 degrees continues to reduce the suction peak for the actuated case with concomitant massive separation over the top half of the wing. On the other hand, the suction peak of the basic wing has increased, and the pressure on the bottom surface of the wing no longer seems affected by the SJA.

For the case of 25.4 degrees, the basic wing is totally stalled (there is no suction peak), while for the actuated case the suction peak near the leading edge is still maintained. As the angle of attack increases, only actuation at higher frequencies is able to sustain a suction peak on the upper surface of the wing. For example at α = 26.4 (figure 4.50) only the curves for 120 and 130 Hz produce a suction peak over the upper surface of the wing, while at 27.3 degrees, only the peak at 130 Hz is visible. Finally at 28.4 degrees the SJA looses all control authority and the wing is stalled for both actuated and non-actuated cases. Analysis of the surface pressure distribution plots shows that the SJA effect is not to generate more lift but to actually augment the available lift by reducing the separation losses.

Wake Surveys

Figures 4.53 through 4.59 show the results corresponding to wake surveys of the flowfield at a location of $x/C = 1.2$ downstream of the wing. For these plots, the freestream velocity was 35 m/s. Figure 4.53 shows the wake of the airfoil for an angle of attack (α) of 0 degrees. For this case the wake is very narrow and the effects of the SJA are very small. At $\alpha = 8$ degrees, the wake becomes wider and the peak velocity deficit is higher. The effects of the SJA are now noticeable, and although the flow for the basic wing is completely attached, the SJA narrowed the wake and reduced the velocity deficit, suggesting a reduction in profile drag. For the range of angles of attack between 12 and 18 (figures 4.55 to 4. 58) the flow for the basic wing shows signs of separation as the wake becomes wider with increasing α and the magnitude of the velocity deficit increases. For the actuated case, the trend seems to be that higher frequencies of actuation produce narrower wakes and a lower velocity deficit. Finally for an angle of attack of 20 degrees, the wake widens dramatically due to massive separation, and the actuator seems to have no control authority over the characteristics of the wake.

6. EFFECTS OF SYNTHETIC JET ACTUATION ON A RAMPING NACA 0015

An experimental investigation was undertaken to evaluate the effectiveness of a Synthetic Jet Actuator (SJA) for flow control on a pitching airfoil. A NACA 0015 profiled wing was pitched up at various rates with concomitant surface pressure acquisition. A self-contained synthetic jet actuator was positioned in the interior of the wing. Synthetic jet actuation parameters included actuator frequency, exit width and rate of change of the exit width. The behavior of the surface pressures is investigated as well as their integrated properties. The data suggests that the effect of the SJA is to delay the onset of the dynamic stall vortex formation to higher incidence, and in some cases, for the parameters and incidence range investigated, suppress it totally. However, in the instances when formed, the synthetic jet appears to increase the loading induced by the stall vortex. At low ramp rates, the synthetic jet forcing causes the formation of a stall vortex where the unforced data showed a pseudo-static stall type behavior. Hot wire anemometer surveys of the jet exit showed that compressibility effects would manifest for small slot exit areas, and increased with frequency. Variation of the SJA driving frequency showed the ability to control the flow from massively separated to fully attached at 25 degrees instantaneous angle of attack.

A characteristic of a stalled airfoil is a pronounced negative pitching moment, induced by the lack of pressure recovery over the aft airfoil section. As SJAs can control the extent of flow separation, the significant pitching moment induced by the movement of the airfoil's center of pressure, as the flow separates, presents itself as a natural mechanism to generate moments for hinge-less pitch control at high angles of attack. Existing static pitch data indicates that this methodology would be effective, however, effectiveness for a dynamically pitched wing has not been ascertained. When a wing is ramped beyond the static stall angle, the motion maintains the inviscid nature of the flow delaying the forward progression of the trailing edge stall (for moderate to thick airfoils), with boundary layer development aided through the "leading edge jet effect". At higher incidence, viscous effects manifest causing stall. However, if the ramp rate is sufficiently high, and depending on aerofoil and freestream parameters, a collision of reversed flow near the leading edge (caused by the significant adverse pressure gradient aft of the leading edge suction peak) with the oncoming air stream can cause boundary layer lift off with formation of a so called dynamic stall vortex. The vortex, in turn, causes a secondary boundary layer eruption. Interaction of this ejected vorticity and the D.S.V. feeding sheet causes detachment; this is a similar interaction mechanism to that of the secondary vortices and primary vortex feeding sheet over a delta wing with freestream disturbances (Shih and Ding, 2002). As this vortex advects rearward over the surface, it causes significant pitching moment fluctuations. The stall vortex forms closer towards the wing leading edge on a two-dimensional than three-dimensional wing (Ferrecchia et al., 1999). Greenblatt and Wygnanski (2001) have shown that a SJA can reduce dynamic effects and moment excursions on a pitch-oscillating wing.

In this section, an experimental investigation into the effects of the actuator on the pressures, forces and moments recorded over a pitching wing are explored. The ability of a SJA to generate pitching moments suitable for control at high incidence during ramp type motions is also evaluated. Presented data includes: surface pressures, SJA exit slot velocity measurements, upper surface instantaneous boundary layer profiles and integrated loads and moments.

Experimental Equipment and Procedure

The SJA driving mechanism consists of a DC motor with its shaft connected eccentrically to a crank, which is in turn connected to the piston of the SJA. Due to the eccentricity, the rotary motion of the motor is translated to linear motion of the SJA membrane/piston. This design offers benefits over, piezoceramic driving mechanisms, since it can achieve membrane/piston oscillation amplitudes at least an order of magnitude higher; it eliminates the dependence of oscillation amplitude on the oscillation frequency which can be problematic for piezoceramic mechanisms; with available state-of-the-art, high power-density electric motors it can match and exceed the power densities of piezoceramic mechanisms; it requires significantly smaller driving voltages. At present the actuator can operate at frequencies up to

about 120Hz. Consequently, for practical freestream velocities, the actuator is limited to non-dimensional frequencies, F^+, of ≈ 1.5. This value is significantly lower then that achieved using piezoelectric actuators[12]. Their study showed that large F^+ values, $O(10)$, showed continuing performance improvement compared to frequencies $O(1)$. However, this effect appeared to saturate, such that for $F^+ > 10$ it was frequency independent such that higher values of F^+ showed no benefit. Similarly, data taken prior, on a similar wing setup[10], showed lift saturation (or frequency independence) for actuator frequencies above 60Hz. Consequently, the limitation on F^+ for the present actuator design is not viewed as a significant hindrance.

For the present SJA, as shown in Fig. 6.1, electric motors drive a series of "off the shelf" small gasoline engines which are used as reciprocating compressors. The cylinder head of each of these engines is perforated and attached to a plenum, which is closed on all sides except for a slot machined on one of the walls. The change in the cavity volume of the plenum causes the pressure inside the cavity to fluctuate, creating the synthetic jet. The use of the available engine technology reduces the effort to manufacture pistons with no leakage, thus simplifying the design and construction of the SJA. As shown in Fig. 6.1, the present SJA array is composed of 6 reciprocating compressors (pistons), which are driven by two DC motors. Each piston has a diameter of 27.7 mm and a peak-to-peak piston stroke of 22 mm. Each DC motor measured 69.8 mm in length and 41.1 mm in diameter, had a maximum power of 800 W and weighed 0.34 kg. The exit slot of the plenum is curved in order to permit the jet to exit tangentially to the surface of the wing, taking advantage of the Coanda effect. It should be noted that the cylinders had to be properly phased in order to reduce array vibration. This phasing in turn required the compartmentalization of the plenum, as it is obvious that if the plenum was not divided into six individual compartments, each one corresponding to each of the six cylinders, the engine phasing would result in zero net volume change in the plenum during an operation cycle and thus no synthetic jet effect. The plenum and exit slot in the actuator were designed such that the exit area was dynamically adjustable, through the use of a rotating cam (details shown in Fig. 6.2). The exit width could be varied from 0 to 1.3mm. The length of slot over each piston chamber was 41mm.

The wind tunnel model, presented in Figures 6.3 and 6.4, was machined in two halves using a CNC mill. The wing's profile was that of a NACA 0015. The upper wing half was made from Plexiglas®. The lower surface was machined from Aluminum. The wing chord was 420mm. Tests were undertaken at a freestream velocity of 20m/s giving a chord based Reynolds number of 0.57×10^6. Boundary layer transition was enforced using trip strips located at approximately 5% of the chord on the upper and lower surfaces. Surface flow visualization indicated that the trips where successful in promoting transition. No wind tunnel wall interference or blockage corrections were applied to the data, as their application for dynamic motions is uncertain at best. Also, the current tests are comparative and as such all data would contain similar wind tunnel wall effects. The wing contained the synthetic jet actuator described earlier. All instrumentation was self-contained in the wing and will be described subsequently. The SJA exit slot was located at 12% of the chord. This location was dictated by geometric considerations.

The performance of the SJA actuator is documented in Figs. 6.5-6.7. Measurements were performed using a TSI model 1054 hot wire anemometer, with the sensor located as shown. Prior to performing the measurements, the stability and damping of the anemometer where set to maximize frequency response for the highest expected SJA exit velocity. The hot wire was then calibrated; a quadratic equation was used to relate measured velocity to bridge voltage. Figure 6.5 shows normalized time and velocity for four data sets. Time was normalized using the period of one cycle. The presented data was de-rectified to show the correct sign of the velocity throughout the cycle. As may be seen, the exit/inlet velocities are, generally, sinusoidal, with little effect due to frequency or slot exit width apparent. Figure 6.6 investigates effects of compressibility. The parameter K (determined from the Continuity equation) should be a constant for a given piston and stroke combination if the flow behaves as incompressible. As may be seen, for a 1.2mm slot, the flow is incompressible. Reducing the slot width shows significant compressibility effects. An SJA frequency of 100Hz shows greater compressibility effects than 54Hz. SJA performance, quantified in terms of exit velocity, is presented in Figs. 6.7a, 6.7b. For a 1.2mm slot exit, exit velocity is seen to vary essentially linearly with actuator frequency, reflecting the marginal effect of compressibility for this geometry. The maximum velocity measured at the slot exit is also indicated for slot widths of 0.4 and 0.8mm. Although the sparse nature of the data mitigates

establishment of characteristic trends, the form of the data suggests a somewhat linear dependence of velocity on frequency in this range. Maximum jet exit velocity as a function of slot exit width for two driving frequencies is detailed in Fig. 6.7b. As Continuity considerations may infer, reducing the slot exit width increases jet exit velocity, however, compressibility effects lessen the relative increase in velocity. Nonetheless, for a 0.4mm slot exit, an exit velocity of 124m/s (peak) was recorded (f=100Hz).
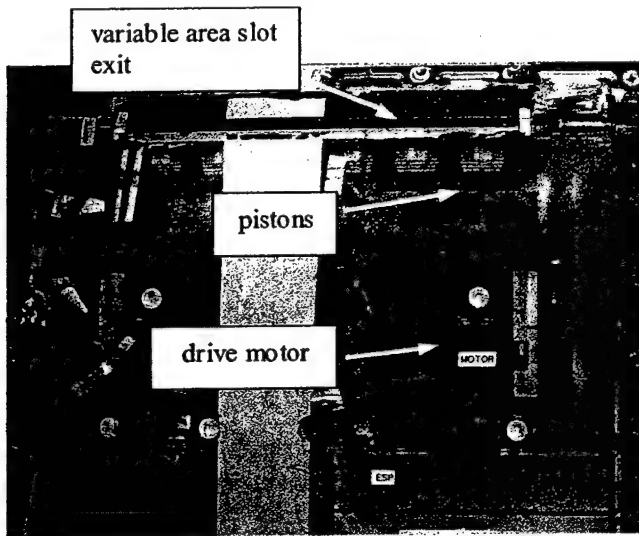

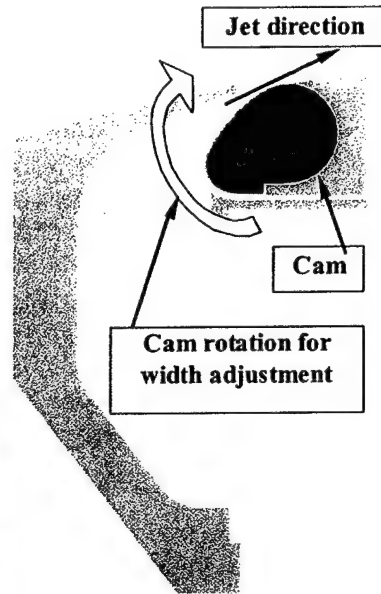Fig. 6.1 Synthetic jet actuator mounted in wing.

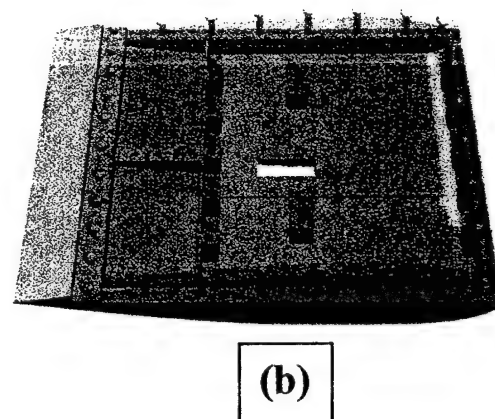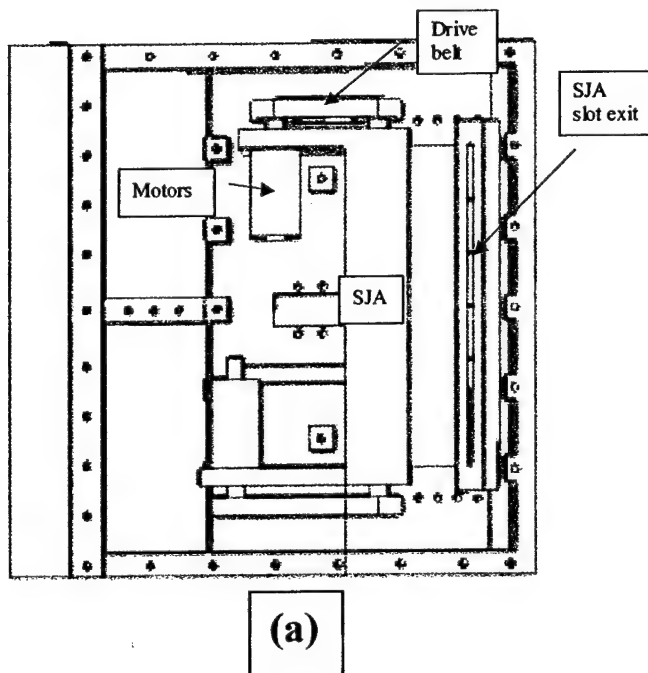Fig. 6.2 SJA exit cross section showing slot design details.

Fig. 6.3 Wind tunnel model details: (a) internal structure, (b) assembled Plexiglas (top) and aluminum (bottom) halves.
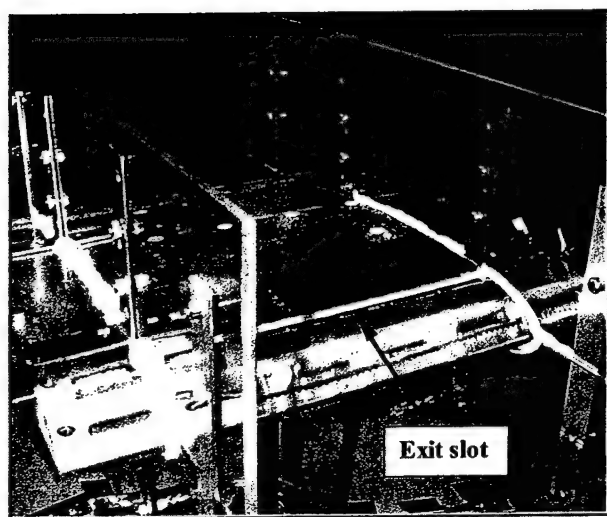
Fig. 6.4 Assembled wing installed in wind tunnel.
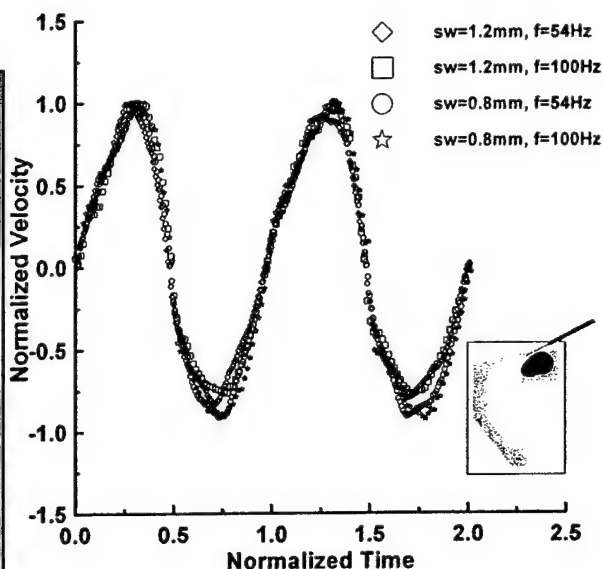
Fig. 6.5 Effect of SJA frequency and slot width on normalized SJA exit velocity.
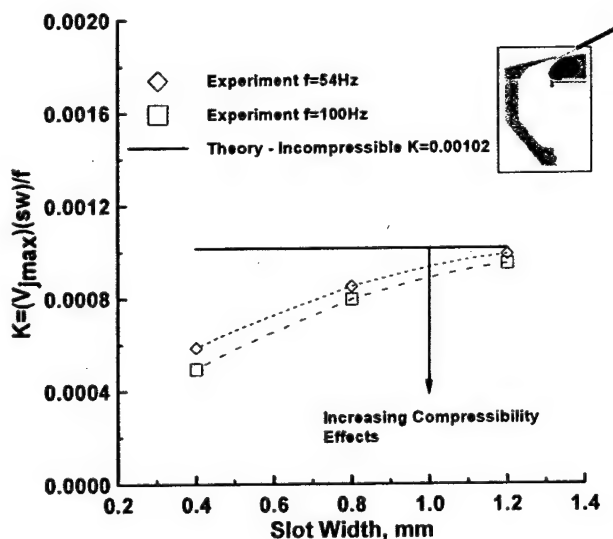
Fig. 6.6 Effect of compressibility on parameter K.
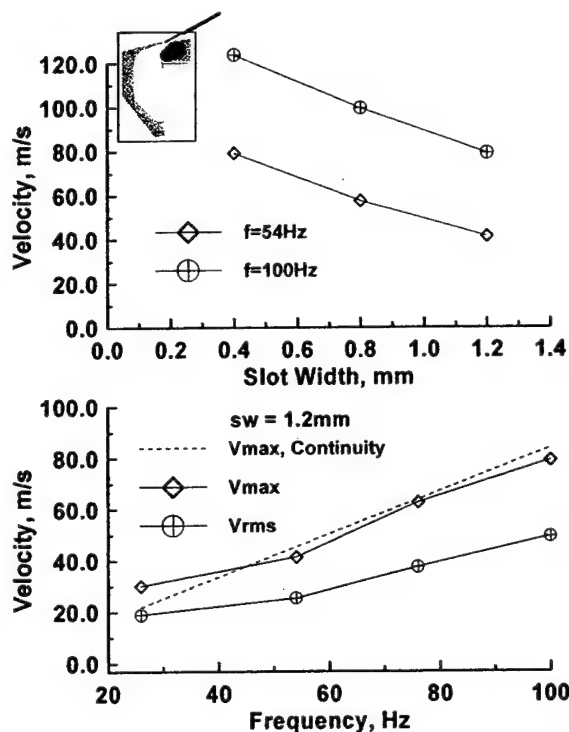
Fig. 6.7 Effect of frequency and slot width on SJA exit velocity: (a) velocity dependence on frequency, sw = 1.2mm, (b) maximum SJA exit velocity as a function of slot width.

Surface pressures where measured over the wing using a 32-channel ESP pressure scanner. The ranges of the 32 embedded transducers was ±10inH$_2$O (±2.49kPa). Location of the ports is shown in Fig. 6.8. Prior to use, the ESP was calibrated using an Edwards's barocel as a reference. Sequential checks of the validity of the calibration indicated pressure deviations of no more then 0.3% of the calibration values.

To account for acoustic effects, the transfer function for the tubing connecting the surface pressure tappings to the ESP was determined using an acoustic test facility (Johansen, 2001). The results indicated that the tubing was over damped. Consequently, the instantaneous pressures were corrected for lag effects using the method of Wildhack (1937) as this method is simple to apply, but is only applicable for over damped systems. To ensure quasi-two-dimensional behavior, side plates were mounted on the wing, as shown in Fig. 6.4. Subsequent data presentation will suggest that the small size of the end plates did not allow the achievement of two dimensional flow. However, mechanical pitching considerations eliminated the use of large plates, and using separate supported side plates can cause problems due to the gap, which has to be small, which in turn can cause alignment problems in concert with a dynamic system. Forces and moments were calculated through integration of the pressure distribution around the wing. The upper and lower surface pressure traces were fitted using cubic splines. The splines were then integrated to yield forces and moments. Presented moment coefficients are about the quarter chord.

A schematic of the experimental set-up is presented in Fig. 6.9. The wing pitching motion was controlled using a stepper motor (SLO-SYN) controlled by a microlynx^{TM} stepper motor controller. During a pitch test, wing position was recorded using an encoder mounted on the stepper shaft. Data from the ESP was digitized using a 16-bit Computer Boards A/D board. Each presented data set is comprised of 30 ensemble averages runs. Uncertainty in the measured angle of attack was estimated through repeated ramp motions in addition to static checks as well. The ramp motions indicated an uncertainty in the instantaneous angle of attack of 0.2 deg. Static checks indicated angular positioning capability within 0.1 deg. Comparison of similar data runs containing 5, 10 and 30 ensemble averages indicated that the instantaneous pressure distributions had low noise and were highly repeatable. As mentioned above, the estimated uncertainty in the indicated pressure was approximately 0.3%.
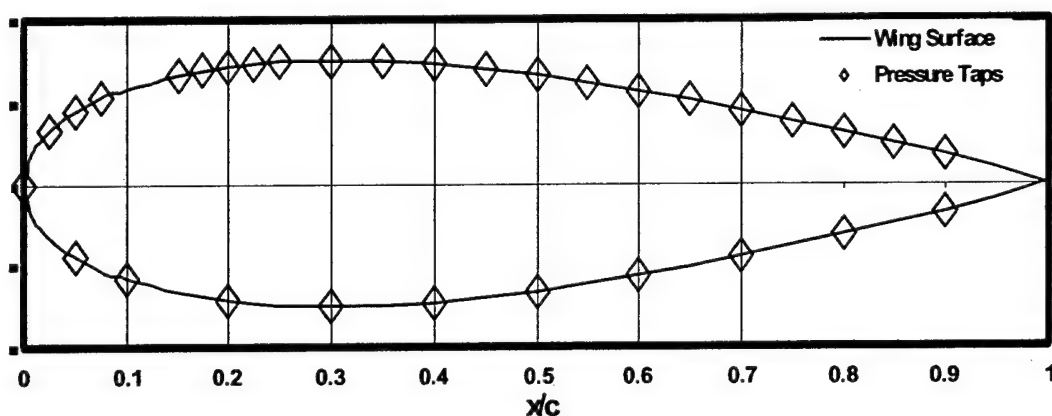

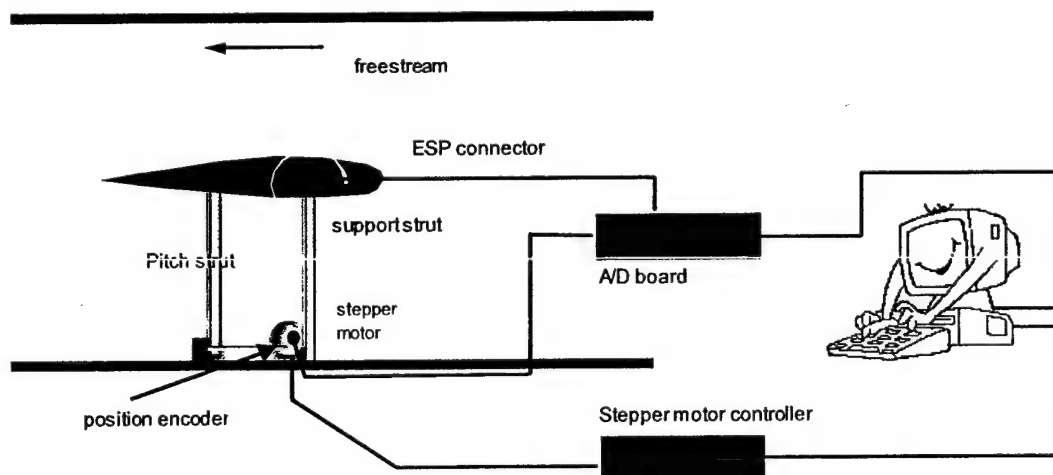Fig. 6.8 Location of surface pressure tappings.

Fig. 6.9 Schematic of experimental set-up.

74

Results and Discussion

In all experiments, the wing was ramped at a constant angular velocity from 0 deg to 27 deg. Data is presented detailing the effects of the SJA on surface pressure, force and moments. Only upper surface pressures are shown, as the data indicated marginal effects on the windward surface for all tested configurations. The SJA exit slot width was 1.2mm unless mentioned otherwise.

Table 1 presents a summary of the jet momentum coefficients for the experimental data. The jet momentum coefficient indicates the momentum content of the jet, levels of lift augmentation may also indicate how effectively it's used. The jet momentum coefficient may be defined as

$$C\mu = \frac{2V_{rms}^2 sw}{U^2 c} \tag{6.1}$$

The root mean square of the jet exit velocity was calculated using the aforementioned hot wire anemometer data. Note that decreasing the slot width to 0.4mm from 0.8mm does not increase the jet momentum due to compressibility effects lessening the exit velocity.

Table 1 Jet Momentum Coefficient Summary

sw, mm	Cμ	F+
0.4	0.013	1
0.6	0.012	1
0.8	0.013	1
1.2	0.009	1
1.2	0.019	1.4
1.2	0.0048	0.66
1.2	0.0023	0.33

The effects of actuator frequency, F+, on the calculated lift and pitching moment are presented in Fig. 6.10. Values of F^+ from 0 to 1.4 are presented. The slot exit width, sw, was set to 1.2mm. Prior studies[20] have suggested that depending on the SJA configuration and requirement, a value of $F^+ \approx 1$ is optimal as it corresponds to the presence of approximately 2-4 convecting vortical structures over the upper surface. The wing was pitched linearly at a non-dimensional rate of 0.009 (corresponding to pitching the wing through 27 deg in 1s). Measurements of the lift curve slopes give values of $\approx 0.8\pi$, indicating that the end plates were not totally successful in achieving 2D flow. However, as mentioned earlier, this is not significant due to the comparative nature of this investigation. The data indicates the formation of a D.S.V. for all values of F+ presented. D.S.V. formation is also associated with a significant nose down pitching moment due to the streamwise advection of the vortex and its associated induced localized loading. Fluidic actuation significantly delays the onset of D.S.V. formation by approximately 6 deg incidence. The data shows that the initial "rounding" of the Cl – angle of attack curve, indicating trailing edge boundary layer thickening and separation is lessened with actuation. When formed, the strength of the D.S.V. appears to be enhanced compared to the F+ = 0 case. This may be due to the ability of the SJA to effectively organize the separated shear layer into a coherent structure and keep it in closer proximity to the wing surface. Comparing F+ = 1.4 to F+ = 1 shows only a marginal delay in D.S.V. formation (inferences are clearer from the Cm data). The strength of the D.S.V. also appears attenuated compared to the F+ = 1 case (i.e. the lift augmentation is less). This may be due to forcing at other then the optimal receptivity frequency range for the shear layer[20]. Also note that from Table 1, Cμ = 0.009 (F+ = 1) and Cμ = 0.019 (F+ = 1.4). However, the data in Fig. 6.10 shows that although Cμ doubles in increasing F+ from 1 to 1.4, this is not reflected in any obvious performance increase, showing the

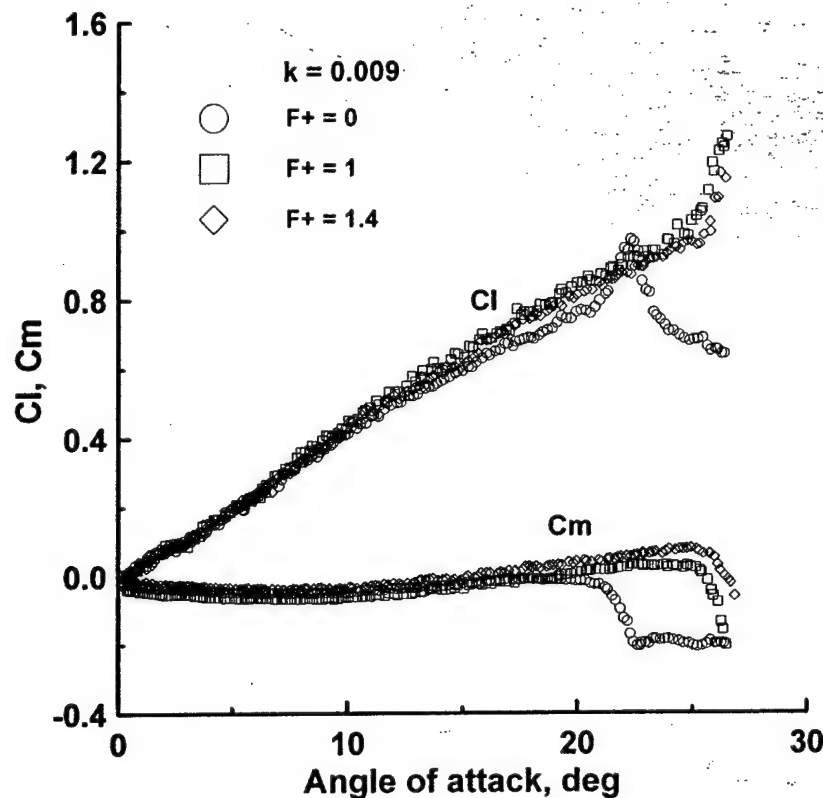importance of forcing in the correct frequency range.

Fig. 6.10 Comparison of unforced (F+ = 0) and forced (F+ ≠ 0) effects on integrated lift and pitching moment coefficient.

For greater presentational clarity, systematic variations of F+ are explored in Fig. 6.11a. Increasing F+ in this range is seen to delay D.S.V. formation. It may be seen that the D.S.V. induced surface loading is greater for F+ = 0.33 and 0.66 then 1.4, despite a four fold increase in Cμ, see Table 1. As mentioned prior, this may be due to the lower F+ values corresponding to the optimum shear layer receptivity range. Figure 6.11b shows a "snapshot" of the instantaneous upper surface pressure distribution when the wing incidence equaled 25 deg. Clearly, the no actuation case, F+ = 0, shows massive upper surface flow separation with an essentially flat pressure distribution. A similar distribution is seen for F+ = 0.33, where the D.S.V. has already advected off the wing as may be inferred from the loading presented in Fig. 6.11a. Higher values of F+ show the presence of a leading edge suction peak, with F+ = 1.4 showing the highest overall leading edge suction levels. Figure 6.11c shows the systematic evolution of the upper surface pressure distribution as a function of incidence for F+ = 0. Although not blatantly obvious the effect of the D.S.V. is seen as a localized "hump" in the pressure distribution that advects downstream. Its influence diminishes as it moves downstream due to greater wing-vortex proximity as well as vorticity diffusion. The presence of the D.S.V. is also indicated by a significant reduction if not elimination of the leading edge suction peak. Figure 6.11d presents similar data with SJA actuation, F+ − 0.33. Similar characteristics to those detailed in Fig. 6.11c are seen, except the D.S.V. peak is somewhat larger. The effect of the actuation frequency on the D.S.V formation incidence is presented in Fig. 6.11e. These angles were determined from examination of the lift and pitching moment data. As such, they do not necessarily represent the exact angle at which the vortex started formation, but rather that at which its effect on Cl and Cm became noticeable. The plot suggests that within the limitations of the sparse data set, the delay in D.S.V. inception with increasing F+ is roughly linear for F+ < 0.8.

76

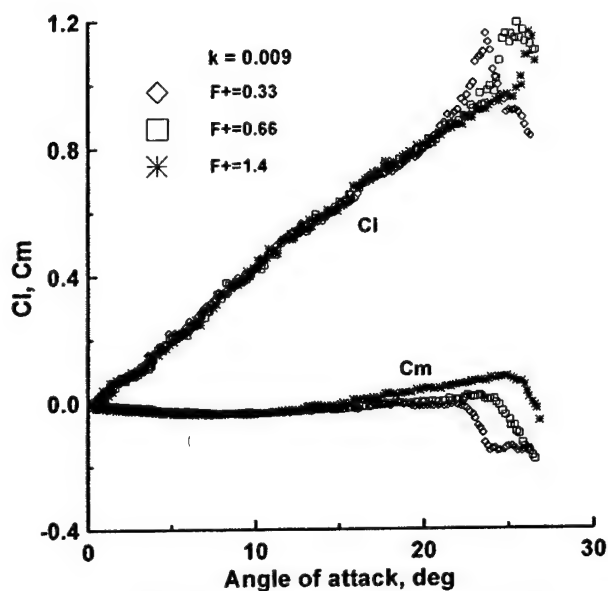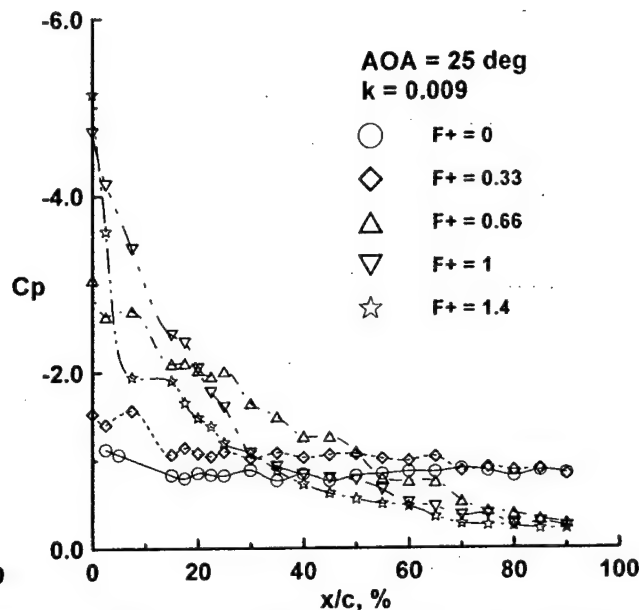Fig. 6.11a Systematic effects of SJA frequency (F+) on integrated lift and pitching moment coefficient.

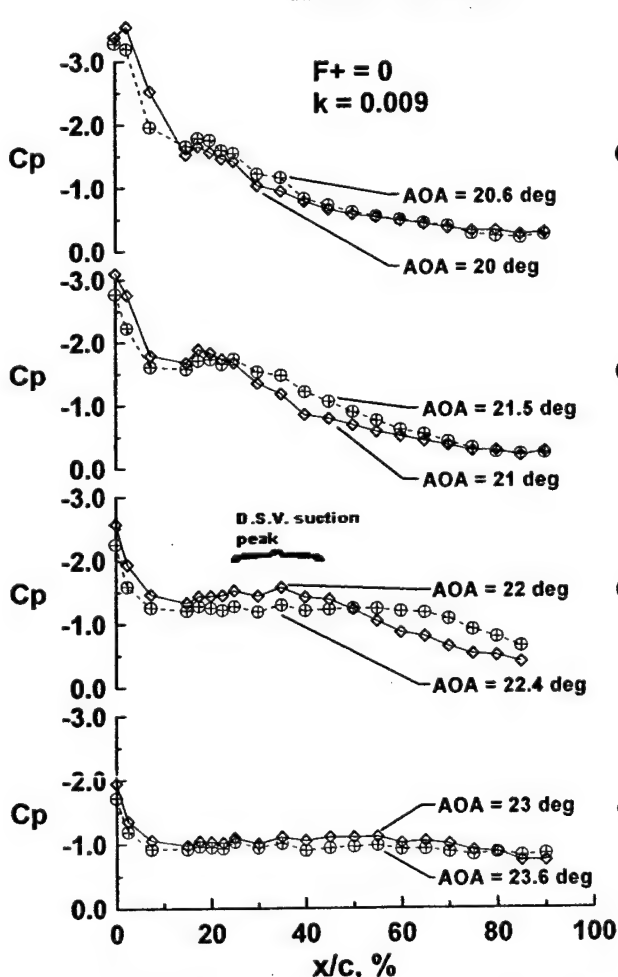Fig. 6.11b Effect of SJA frequency (F+) on measured upper surface pressures.

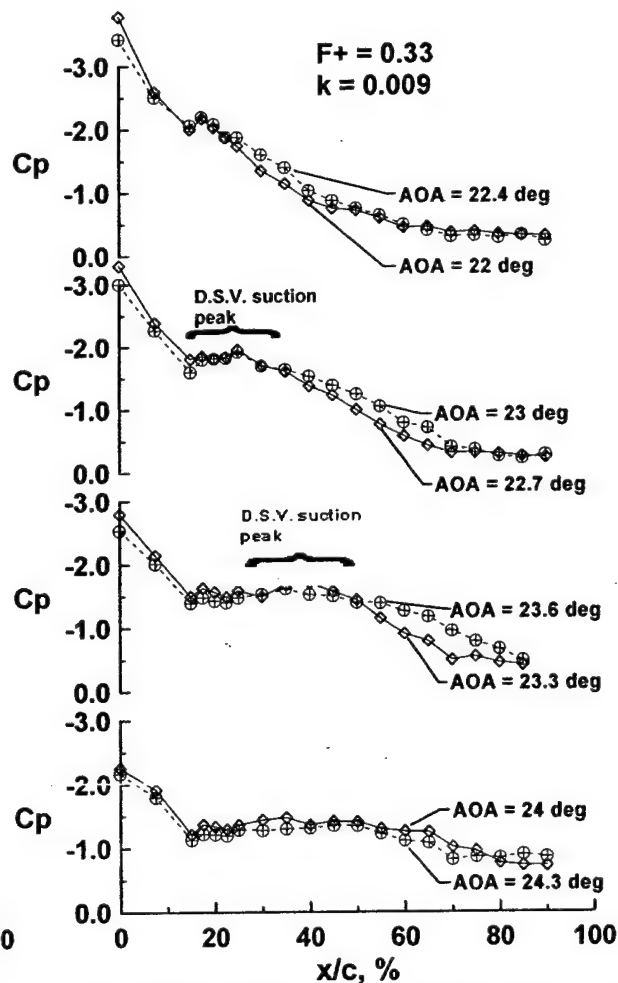Fig. 6.11c Effects of wing incidence on upper surface pressure trace evolution, F+ = 0.

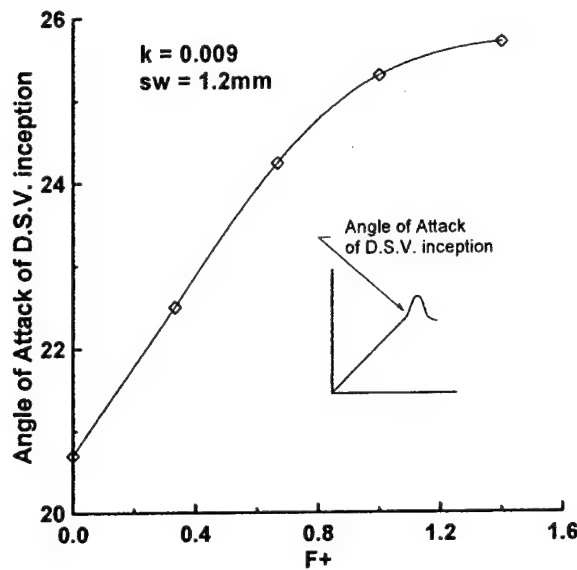Fig. 6.11d Effects of wing incidence on upper surface pressure trace evolution, F+ = 0.33.

Fig. 6.11e Effect of F+ on D.S.V. formation incidence.

The effect of the non-dimensional pitch rate, k, is explored in Figs. 6.12a-6.12b, with and without actuation. Pitch rates of k = 0.005 (27 deg in 2s), 0.009 (27 deg in 1s) and 0.019 (27 deg in 0.5s) are presented. The data in Fig. 6.12a (F+ = 0) displays the expected effects of pitch rate. As k increases, the linear portion of the lift curve is extended, reflecting the delayed boundary layer development. For the lowest pitch rate, k = 0.005, the data does not show clear evidence of a D.S.V. formation. Increasing k to 0.009 shows the formation of a D.S.V. at approximately 21 deg incidence. A marked nose down moment is indicated at the D.S.V. onset. The highest pitch rate, k = 0.019, shows an extension of the lift curve slope to 27 deg (corresponding to the highest achievable incidence, equipment limitations precluding higher incidences). Notice the form of the pitching moment break for k = 0.005 and 0.009. The plot for the higher pitch rate shows a small moment reversal corresponding to the incidence at which the lift data suggests that the D.S.V. has passed off the wing, approximately 22.5 deg.

Figure 6.12b shows the effects of SJA actuation for the same ramp motions as presented in Fig. 6.12a. The data shows that actuation causes D.S.V. formation for k = 0.005, which was not present without actuation, see Fig. 6.12a. This is most likely due to the SJA forcing causing the separating shear layer to roll-up into a coherent vortical structure or D.S.V. Without actuation, for this pitch rate, the flow separates and the wing stalls in a psuedo-steady manner. As seen and documented prior for higher pitch rates the SJA has the effect of delaying D.S.V. formation to higher incidence.

Figure 6.13a shows the effects of slot width on calculated Cl and Cm for F+ = 1 and k = 0.009. Also shown is data for a variable slot. For the variable slot case, the slot width was 0.4mm at the start of the motion (incidence = 0 deg) and was linearly increased to 1.2mm by the end of the ramp motion. The effect of the variable slot width does not appear to be significant within the resolution of the experiment. Notice that for the data presented, the sw does have a small effect on the wing incidence angle at which the D.S.V. forms (as may be inferred off the Cm plot). Figure 6.13b shows a "snapshot" of the upper surface pressures at a wing incidence of 25 deg for fixed slot widths of 0.4, 0.8 and 1.2mm. The largest slot width, 1.2mm, shows the largest suction peak but diminished loading over the mid chord of the airfoil compared to slot widths of 0.4mm and 0.8mm.
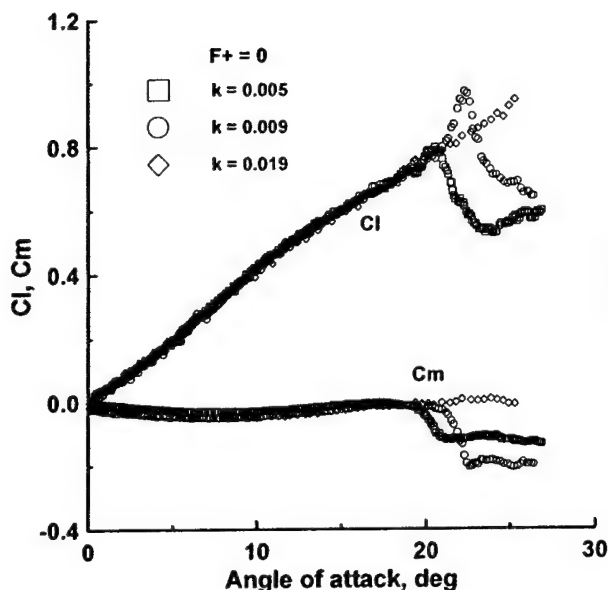
78

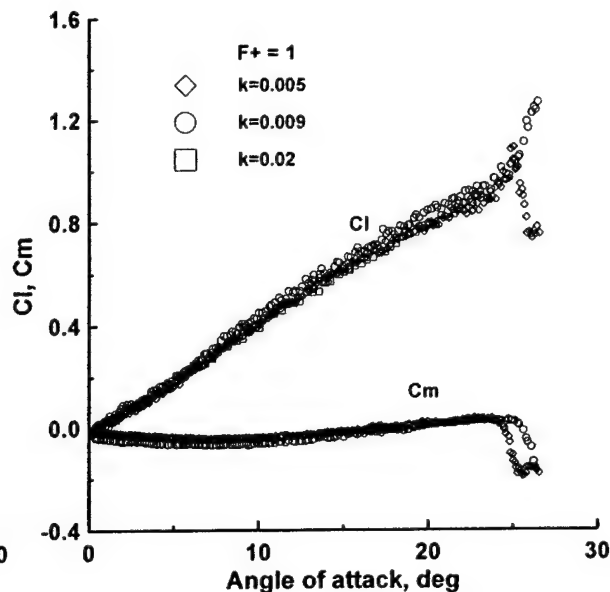Fig. 6.12a Effects of wing pitch rate (k) on integrated lift and pitching moment coefficient, F+ = 0.

Fig. 6.12b Effects of wing pitch rate (k) on integrated lift and pitching moment coefficient, F+ = 1.
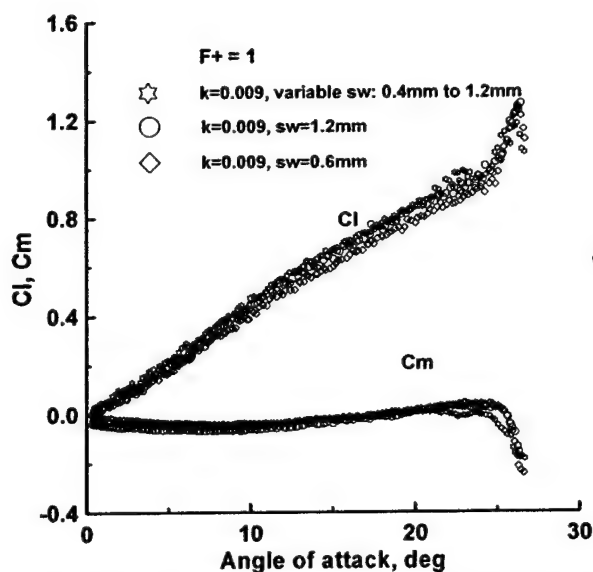
Fig. 6.13a Effects of slot width (sw) on integrated lift and pitching moment coefficient, F+ = 1.
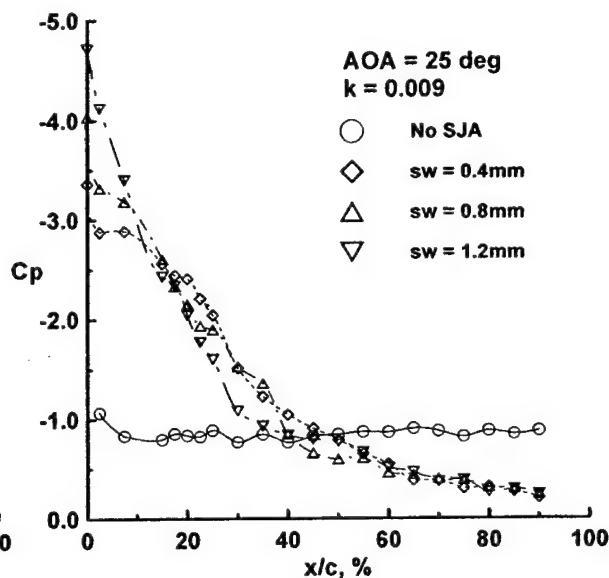
Fig. 6.13b Effect of slot width (sw) on measured upper surface pressures.

To gain an insight into the flow physics associated with the fluidic actuation, a hot wire anemometer survey was conducted over the wing. The flow adjacent to the upper wing surface was traversed, with the probe displacement perpendicular to the surface. A cosine point spacing was used, with the traverse containing 25 points in the Znormal direction. At each point, approximately 8000 readings were collected at 8kHz. Temporal phasing was achieved using an encoder signal connected to the motor shaft. The quantity of data collected facilitated phase averaging; each set represents 25 averages. The survey was conducted with the probe located axially at 32% of the chord (when at the closest position to the wing surface) and the wing at a fixed 20 deg incidence. Data from these surveys is summarized in Fig. 6.14. Plots are presented showing the instantaneous phase averaged velocity profiles at successive time instants throughout one cycle of the SJA. The data clearly shows the direct boundary

layer injection of momentum due to actuation. During the mid-cycle, t=0.5T, the boundary layer profile is seen to be significantly "filled" out, whereas at the beginning and towards the end of the stroke cycle (t=0T and t=0.875T), there is a velocity deficit towards the surface associated with a conventional boundary layer profile. Further away from the wing surface, Znormal/c > 0.03, the velocity is seen to be approximately uniform and similar for all time instants.

The Hot Wire data shown in Fig. 6.7 indicates that for the SJA operating conditions presented in Fig. 6.14, Vrms ≈ 25m/s (Vrms/U = 1.25) and Vmax ≈ 41m/s (Vrms/U = 2.05). These jet exit velocities were measured in the absence of a freestream, but it would be expected that the impact of a freestream, and thus reduced exit pressures, would be to increase the exit velocities during the ejection cycle, and decrease them during the inflow cycle. The data in Fig. 6.14 shows no apparent "jetting" in the near surface boundary layer, although the jet velocity ratios mentioned above suggest that the exit velocities are of sufficient magnitude for temporal jetting to be present. The Hot Wire measurement plane was 20% (84mm) behind the SJA exit and indicates the rapid attenuation of the jet due to viscosity and spreading.
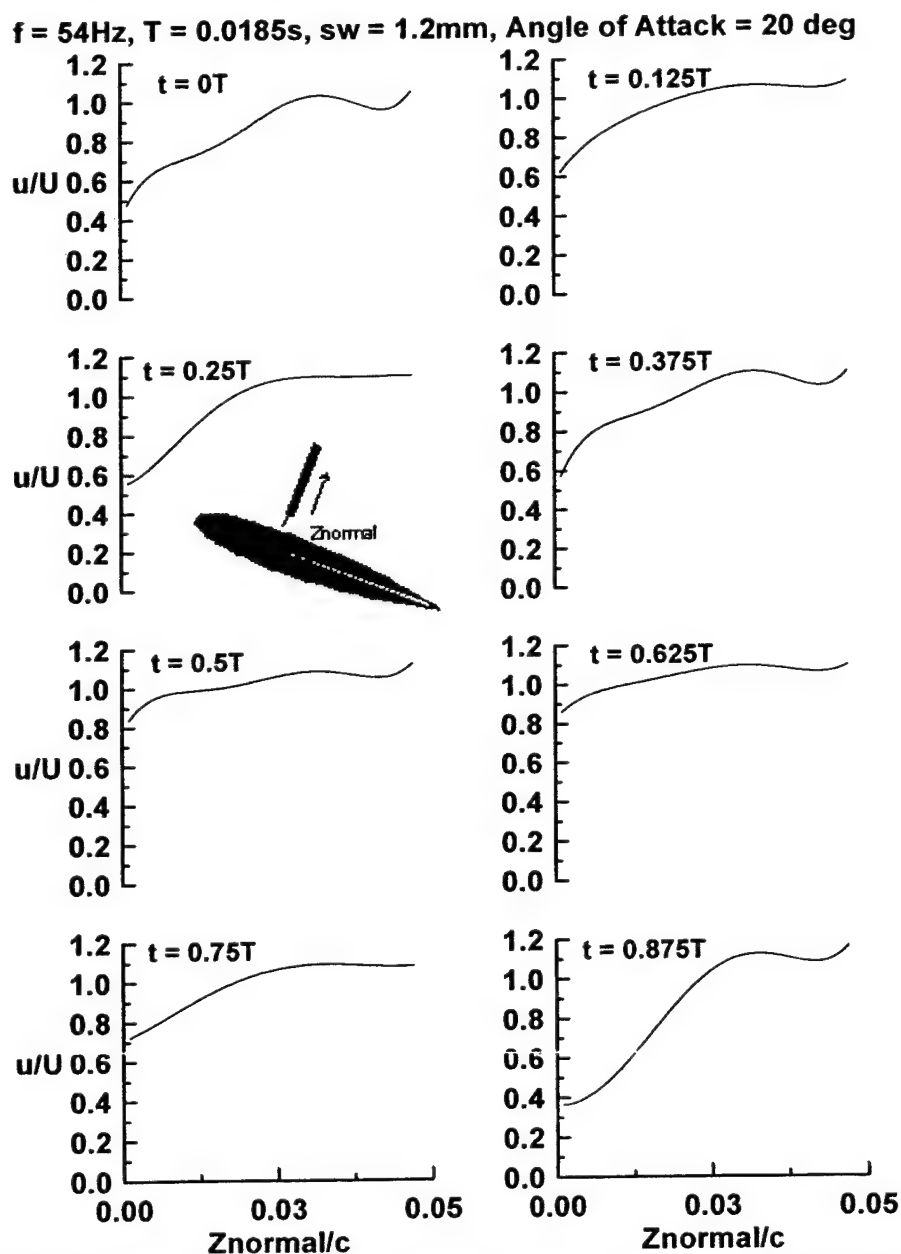

Fig. 6.14 Instantaneous temporally phase averaged velocities measured aft of the SJA, F+ = 1.

The preceding results indicate that in the tested flow regime, upper surface pressures may be independently manipulated though SJA drive frequency, and to a lesser extent slot width variations. This is explored more thoroughly in Figs. 6.15 and 16 that present the location of the section's center of pressure and quarter chord pitching moment as a function of F^+ respectively. For these figures the slot width was 1.2mm with k = 0.009. Variation of the actuator frequency (from 0.33 to 1.4) is seen to cause significant movement of the center of pressure (as increasing F^+ results in more complete flow re-attachment such that the c.p. location approaches the theoretical potential flow location, i.e. Xc.p./c = 0.25). Locations indicating massively separated flow (F^+ = 0.33, Xc.p./c = 0.42) to fully attached (F^+ = 1.4, Xc.p./c = 0.25) are indicated. The effects of these large changes in the center of pressure are quantified in Fig. 6.15. For reference, the figure also displays predicted pitching moments that deflection of a 10% trailing edge flap would generate. These estimates were calculated using a Smith-Hess panel method. The data clearly shows that nose down pitching moments, comparable in magnitude to that achievable through a conventional trailing edge control device can be generated through control of the extent of flow separation. Naturally, this form of fluidic control would only be of value at high angles of attack, alternative flow control methods would have to be found to achieve hinge-less control in attached flow regimes.
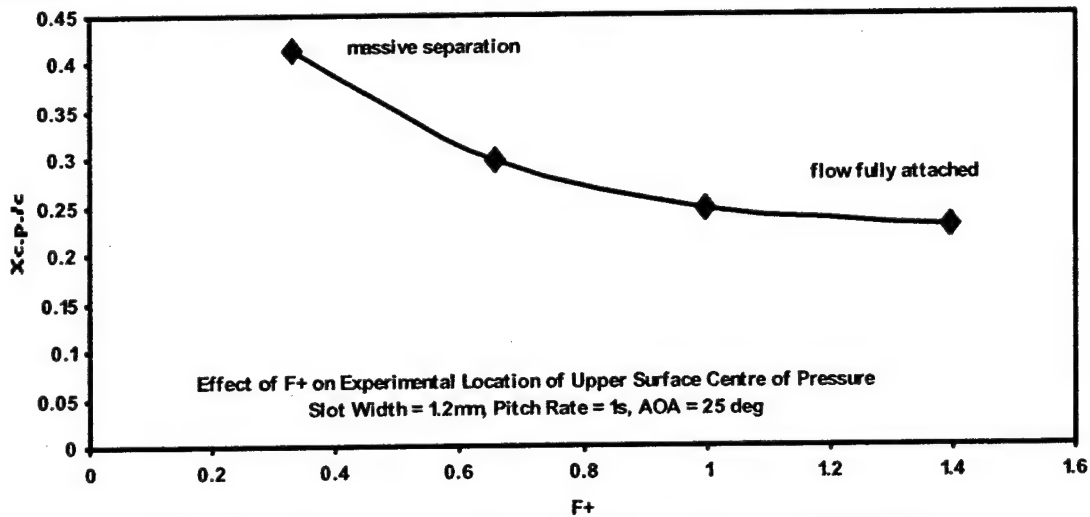

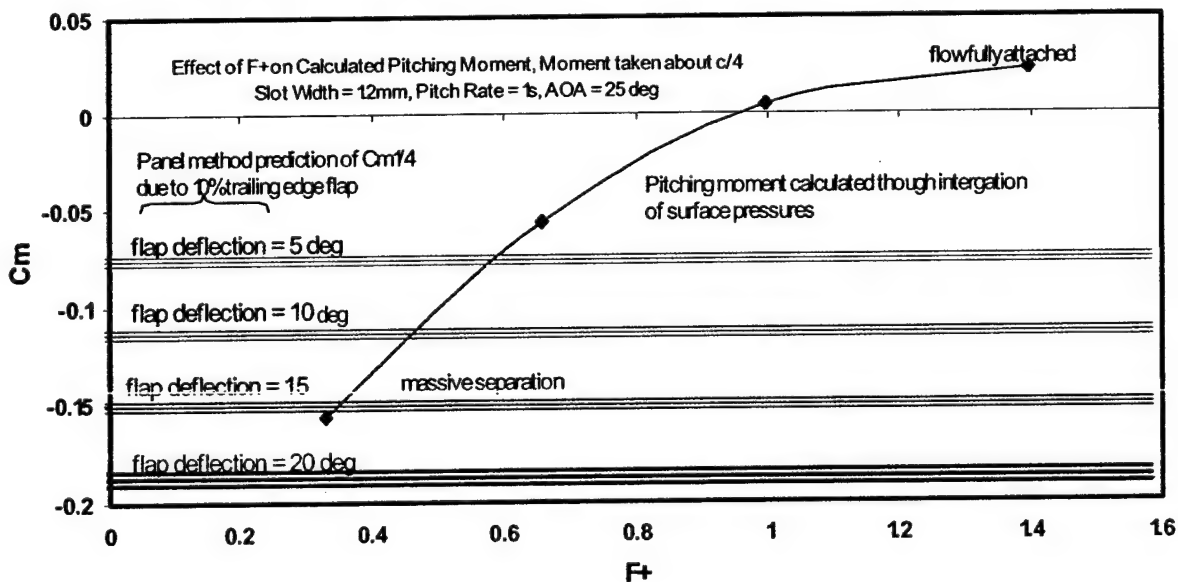Fig. 6.15 Effect of F^+ on location of upper surface center of pressure.

Fig. 6.16 Effect of F^+ on calculated quarter chord pitching moment.

81

7. EFFECTS OF SYNTHETIC JET ACTUATION ON LARGE AMPLITUDE SINUSOIDAL PITCH MOTIONS

In this part of the work, a low speed wind tunnel investigation was conducted to determine the effects of Synthetic Jet Actuators (SJAs) on a sinusoidally pitching wing. Experiments were performed in a low speed 3' by 4' wind tunnel. During the dynamic motion, pressures were recorded around the wing using a high-speed pressure scanner connected to thirty-two tappings. Integration of these pressures yielded instantaneous lift and pitching moment. The motion consisted of a 12.5 deg excursion around a 12.5 deg mean. Pitch frequencies of 0.2Hz to 2.0Hz were evaluated. The data showed that during the upstroke, at low pitch frequencies, the SJA delayed stall. As the frequency increased, the effect of the SJA compared to the unforced case diminished as the dynamic motion itself delayed the onset of stall. During the downstroke, the SJA caused a more rapid flow re-attachment, resulting in considerably smaller hysterisis loops. For the highest pitch frequency evaluated, the hysterisis loop was eliminated.

As already previously discussed, rapid airfoil motions, caused by either rapid pitching during maneuvering or the cyclic pitching of a rotor-craft blade can cause significant changes in the aerodynamic characteristics compared to the static (equivalent incidence) case. The lift curve slope may be significantly extended beyond the static stall due to boundary layer improvement effects (i.e. leading edge jet and moving wall effects). Depending on the pitch rate, this linear extension may either terminate in a conventional quasi-static type stall or a significant non-linear lift overshoot, caused by the formation of a Dynamic Stall Vortex (DSV). This vortex is a large scale coherent vortical structure that typically forms near the quarter chord of the wing. As this structure advects rearwards, loading increases until it reaches the mid chord, from where it reduces. Vortex passage is also indicated by large moment excursions, reaching a maximum with vortex location over the trailing edge. Research has suggested that the formation of the DSV may be due to: 1) bursting of the leading edge laminar separation bubble, 2) transonic flow near the leading edge, 3) separation of the turbulent flow following closure of the laminar separation bubble, and 4) reverse flow near the leading edge stemming from an upstream penetrating reverse layer associated with trailing edge stall.

Expanding on formation mechanism 4) above, if the ramp rate is sufficiently high, and depending on aerofoil and freestream parameters, a collision of the reversed flow near the leading edge (caused by the significant adverse pressure gradient aft of the leading edge suction peak) with the oncoming air stream can cause boundary layer lift off with formation of the DSV. The vortex, in turn, causes a secondary boundary layer eruption. Interaction of this ejected vorticity and the DSV feeding sheet causes detachment; this is a similar interaction mechanism to that of the secondary vortices and primary vortex feeding sheet over a delta wing with freestream disturbances. As this vortex advects rearward over the surface, it causes significant pitching moment fluctuations and excursions. The effects of DSV formation are seen as undesirable due to these moment excursions and possible fatigue of oscillatory loaded surfaces. The DSV affects the performance of helicopter rotors (causing fatigue and limiting the cruise speed), wind turbines and turbo-machinery. Methods to attenuate their impact include active flow control methodologies such as pulsed vortex generators, slot suction and blowing. Structural modifications include slats, leading edge droop as well as shape variable airfoils. Greenblatt and Wygnanski (2001) have performed experiments showing the effect of fluidic actuation on a NACA 0015 airfoil performing oscillations. The airfoil excursion angle was 5 deg around the mean. Their data showed that for the test parameters, excitation attenuated the moment excursions and increased the lift to drag ratio. In this section, an experimental investigation into the effects of large amplitude sinusoidal pitching under SJA control, on calculated lift and pitching moment is presented. The study was conducted to increase the available data base on the effects of fluidic oscillation for sinusoidal pitch motions as well as present data that may be used for CFD validation. Presented forces and moments are calculated through pressure integration. Data with and without fluidic actuation is presented to reveal the effects of active flow manipulation for these dynamic motions.

Experimental Equipment and Procedures

The wind tunnel model and the SJA actuator has been presented and discussed in Section 6 and Figures 6.1 through 6.8. A schematic of the experimental electronic hardware set-up is presented in Fig. 7.1. The hardware was designed and assembled specifically for this application. The wing was pitched using a

maxon DC motor connected to the wing's pitch strut through a 43:1 maxon reduction gearbox. During a pitch test, wing position was recorded using an encoder mounted on the motor shaft. Data from the ESP was digitized using a 12-bit A/D chip incorporated into the electronic hardware. Each presented data set is comprised of 10 ensemble averages runs. Uncertainty in the measured angle of attack was estimated through repeated ramp motions in addition to static checks as well. The ramp motions indicated an uncertainty in the instantaneous angle of attack of 0.2 deg. Static checks indicated angular positioning capability within 0.1 deg. Comparison of similar data runs containing 5, 10 and 30 ensemble averages indicated that the instantaneous pressure distributions had low noise and were highly repeatable. As mentioned above, the estimated uncertainty in the indicated pressure was approximately 0.3%.

Results and Discussion

In all experiments, the wing was pitched in a sinusoidal fashion through a target amplitude of 12.5 deg, yielding a sinusoidal pitch motion with an excursion of 12.5 deg around a mean setting incidence of 12.5 deg. As the SJA frequency was much larger then the pitch rate, a phase relationship was unnecessary. As the data will show, there is a small variation in the angular excursion for pitch frequencies over 1Hz due to the target motion not exactly tracking that commanded. However, as the data is comparative in nature (effects with and without actuation) this has little significance in the identification of trends. The controller and hardware have a bandwidth of about 2Hz, although for signals above 1Hz, phase and amplitude differences between the reference and achieved angle-of-attack signals exist. However, even for the frequencies that exhibit phase differences, the angle-of-attack response is very repeatable and thus ensemble-averaging techniques can be applied. For the experimental data presented, the jet momentum coefficient, defined as:

$$C\mu = \frac{2V_{rms}^2 sw}{U^2 c} \tag{7.1}$$

has a value of 0.009. The uncertainty in $C\mu$ is estimated as approximately 2%. The root mean square of the jet exit velocity was calculated using data from a hot wire anemometer survey of the jet exit. The SJA actuator non-dimensional frequency, $F+$, was set to 1. Prior studies have suggested that depending on the SJA configuration and requirement, a value of $F^+ \approx 1$ is optimal as it corresponds to the presence of approximately 2-4 convecting vortical structures over the upper surface. Measurements of the lift curve slopes of the data to be presented gives values of $\approx 0.9\pi$, suggesting that the end plates were not totally successful in achieving 2D flow. However, as mentioned earlier, this is not significant due to the comparative nature of this investigation. Data will be presented showing the systematic effect of pitch rate on the integrated lift and pitching moment coefficient with and without actuation. Subsequent data comparisons will explore the effects of the SJA for a specific pitch rate. Additionally, data summarizing observed trends will be presented and discussed.

Figure 7.2 shows the effect pitch rate for $F+ = 0$. The data shows that increasing the ramp rate delays the onset of stall, until the stall coincides with the maximum pitch angle, i.e. 25 deg, for a pitch rate of 1Hz (k = 0.021). The delay of stall is affected as a linear extension of the lift curve, until viscous effects manifest causing boundary layer separation. Due to the comparatively low ramp rates, a dynamic stall vortex does not form. As the pitch rate increases, the hysterisis effects seen during the down stroke increase, indicating that boundary layer re-attachment is delayed. Thus, larger pitch rates lead to larger hysterisis loops, a result noted by Lee and Petrakis (2000).

Figure 7.3 comprised the same motions as in Fig. 7.2, except that the SJA was active. The data shows that the systematic delay in stall onset shown in Figure 7.2 as f increases is not as apparent. For f > 0.2Hz, increasing the ramp rate has little effect on the shown data, i.e. it becomes somewhat independent of the dynamic motion. This indicates that for these experimental conditions, the SJA maintains attached flow over the upper wing surface essentially up until the termination of the upstroke. Similarly, the size and dispersion of the downstroke's hysterisis loops are also decreased. A similar effect was observed in the numerical results of the effect of a pulsating jet flow on an oscillating NACA 0015 airfoil (Ekaterinaris, 2002). Specifics will be quantified later in this section.

The following discussion will clarify the observed trends associated with operation of the SJA for different pitch rates. Data is presented showing the systematic effects of increasing f from 0.2Hz to 2Hz. Figure 7.4 presents the lift and pitching moment coefficient as a function of incidence for f = 0.2Hz with and without excitation. The effect of the actuation is to delay the onset of stall approximately 4 deg until just prior

to the maximum incidence angle, i.e. 25 deg. The size of the hysterisis loop is observed to be smaller for F+ = 1 then F+ = 0. In addition, the re-attachment of the upper surface boundary layer appears to occur more rapidly as may be inferred from the slope of the return leg of the hysterisis loop (i.e. the incidence range over which the lift increases from its maximum post stall value to equal the pre-stall value during the upstroke decreases). Pitching moment coefficient excursions are seen to be roughly comparable in magnitude for both cases.

Figure 7.5 presents similar data for f = 0.4Hz. For this pitch rate, maximum lift for F+ = 1 corresponds to the maximum incidence of the oscillations. The dynamic motion is seen to delay stall significantly for the unforced case. Comparisons of the return leg of the hysterisis loop, i.e. during the downward portion of the motion, show that fluidic actuation significantly reduces the size of the loop. Unlike the f = 0.2Hz case, actuation does reduce the magnitude of the nose down moment excursion associated with the onset of large-scale upper surface flow separation. A reduction in the maximum moment excursion was also seen in Ekaterinaris' numerical results (2002) modeling a pulsating jet on a oscillating airfoil.

Similar results to those cited for f = 0.4Hz are seen for f = 0.6Hz, see Fig. 7.6. Notice, however, that increasing the pitch frequency causes an increase in the size of the hysterisis loop indicating greater delay in the re-attachment of the upper surface boundary layer during the downstroke. The negative moment break associated with stall is seen to be significantly more severe for the unforced case. Similar trends are in evidence for a pitch frequency of 0.8Hz (Fig. 7.7).

Increasing the pitch frequency to 1Hz, as presented in Fig. 7.8, shows the dynamic pitching motion delaying stall comparably to that achieved using forced flow control at lower pitch rates. Although increasing the pitch rate steadily delays the upper surface re-attachment for F+ = 0, fluidic forcing reduces the dependency of the re-attachment process during the downstroke on the frequency of the motion, as the SJA itself re-attached the flow. For this frequency, the negative moment break associated with stall is seen to be severe (F+ = 0).

Increasing the pitch frequency to 1.2Hz and greater (Figs. 7.9 to 7.13) shows the formation of a DSV at the termination of the upstroke, indicated by the non-linear lift augmentation. Notice the data for these pitch rates (1.2Hz to 2Hz) suggests that the SJA actuation has a marginal impact on formation of the DSV. Our results of Section 6 showed a delay in the onset of the DSV due to actuation for a ramp and hold motion over a similar wing. It was also found that the SJA could cause DSV formation at low ramp rates when this was not in evidence in the unforced case. Additionally, when formed, the stall vortex appeared stronger in the forced case then the unforced case. Notice that the size of the forced case hysterisis loop increases to a maximum for f = 1.6Hz, Fig. 7.11. However increasing the pitch frequency then shows a reduction in the hysterisis loop size until it is eliminated for f = 2Hz. For the unforced case, at the higher pitch frequencies, the data suggests that the flow is essentially separated for the entire pitch down motion.

Salient features of the prior data sets are summarized in Figs. 7.14 to 7.16. Figure 7.14 presents the angle of attack of the observed flow re-attachment angle as a fraction of the maximum angle. Presenting the data in this format eliminates effects due to small variations in the pitch amplitude angle. The data in Figure 7.14 shows that the effect of flow control is essentially to promote earlier re-attachment during the downstroke, effected as an approximately constant offset for all tested pitch frequencies. Actuation reduces the angle of attack decrement required for re-attachment by about 20%. The data shows that the delay in re-attachment with increasing f is approximately linear for f < 0.8Hz. This appears to be followed by a localized plateau for 0.8 < f < 1.2Hz (within the density of presented data), and then a resumption of the pseudo-linear delay in re-attachment angle as f increases further. The apparent cause for this behavior was not clearly established.

Figure 7.15 shows the angle of attack at which the maximum lift coefficient was recorded for the unforced case reduced by the forced case, and is essentially a quantification of the effect of the dynamic motion to the forced actuation as means to suppress upper surface flow separation. As may be seen, the effect of the dynamic motion becomes comparable to the fluidic forcing for f > 1Hz. Generally, increasing the pitch rate has an analogous effect that of forcing, although the mechanisms through which flow separation is prevented are vastly different. Figure 7.16 shows the angle of attack for the maximum lift coefficient reduced by the angle of attack of the excursion. As may be seen, for the frequency range of pitch motions, these two angles are coincident for F+ = 1, indicating that maximum lift was achieved at the termination of the upstroke, and that the flow was still potentially attached. For the unforced case, the airfoil stalls prior to the maximum angle of attack for f < 1Hz. As the frequency of the oscillations reaches 1, the dynamic effects of the motion

84

(leading edge jet effect with concomitant boundary layer energizing/improvement) delay stall such that the maximum measured lift is coincident with the angle of attack of the motion.
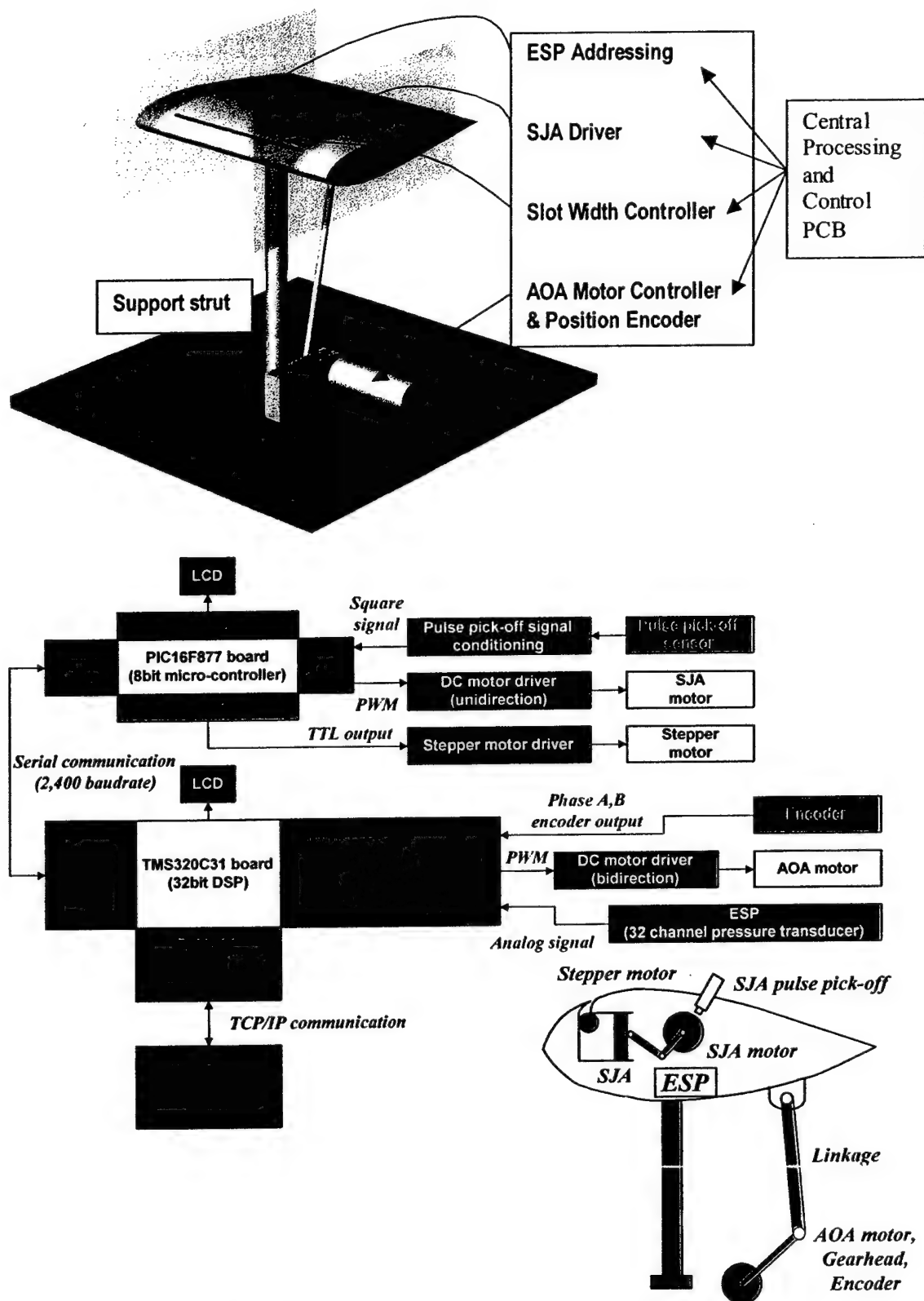

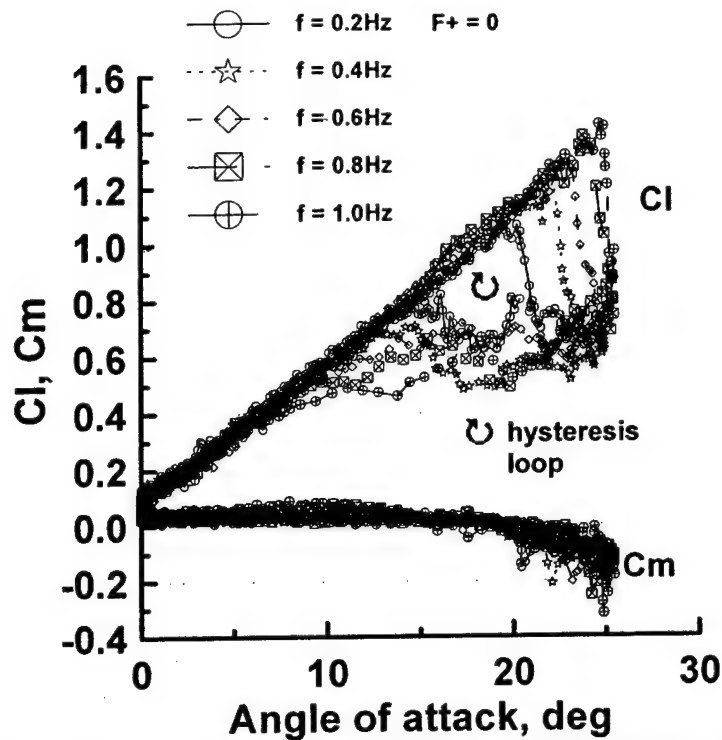Fig. 7.1. Experimental electronics hardware setup.

Fig. 7.2 Effect of pitch frequency (f) on calculated lift and pitching moment coefficient, F+ = 0.

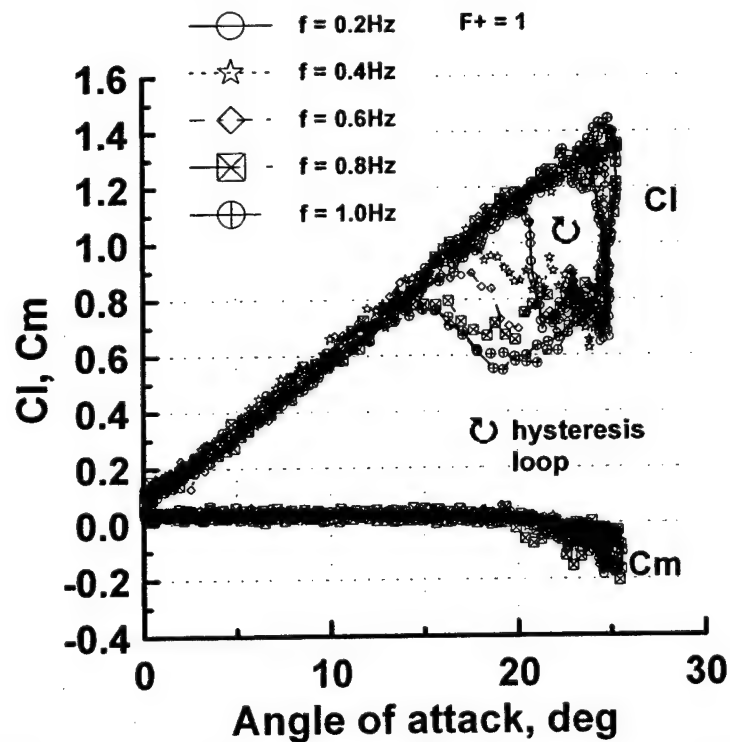Fig. 7.3 Effect of pitch frequency (f) on calculated lift and pitching moment coefficient, F+ = 1.
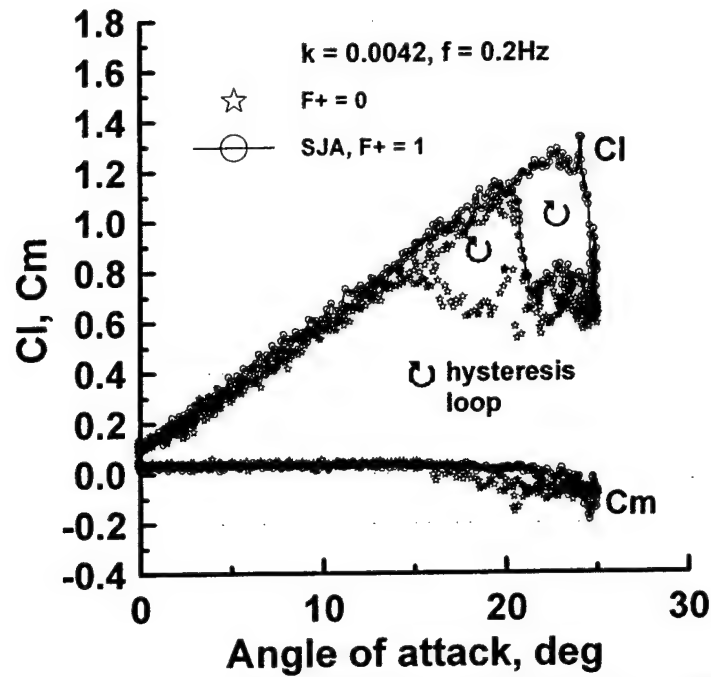
Fig. 7.4 Effect of fluidic actuation on calculated lift and pitching moment coefficient, f = 0.2Hz.

Fig. 7.5 Effect of fluidic actuation on calculated lift and pitching moment coefficient, f = 0.4Hz.

Fig. 7.6 Effect of fluidic actuation on calculated lift and pitching moment coefficient, f = 0.6Hz.

Fig. 7.7 Effect of fluidic actuation on calculated lift and pitching moment coefficient, f = 0.8Hz.

Fig. 7.8 Effect of fluidic actuation on calculated lift and pitching moment coefficient, f = 1.0Hz.

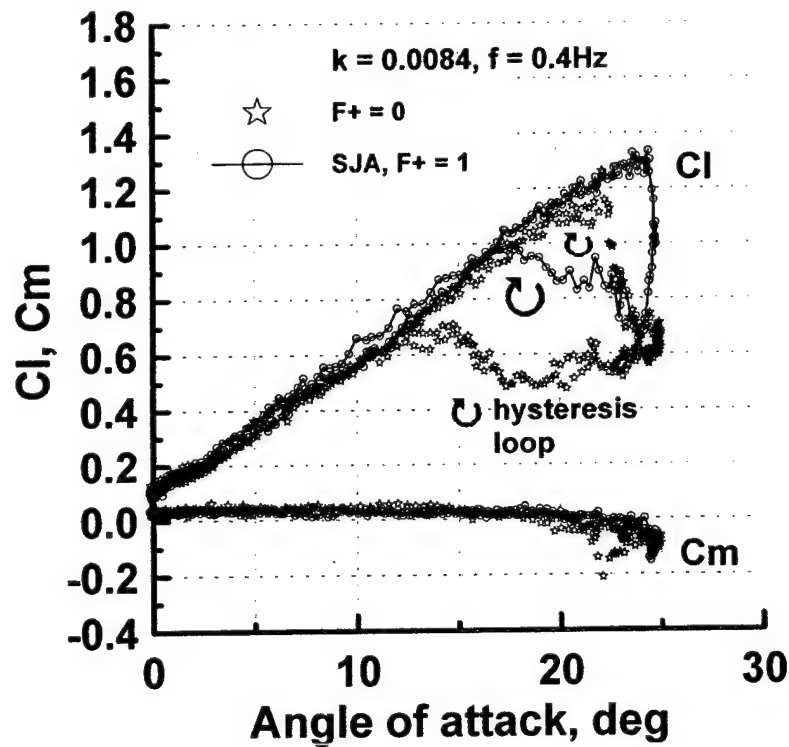Fig. 7.9 Effect of fluidic actuation on calculated lift and pitching moment coefficient, f – 1.2Hz.

89

Fig. 7.10 Effect of fluidic actuation on calculated lift and pitching moment coefficient, f = 1.4Hz.

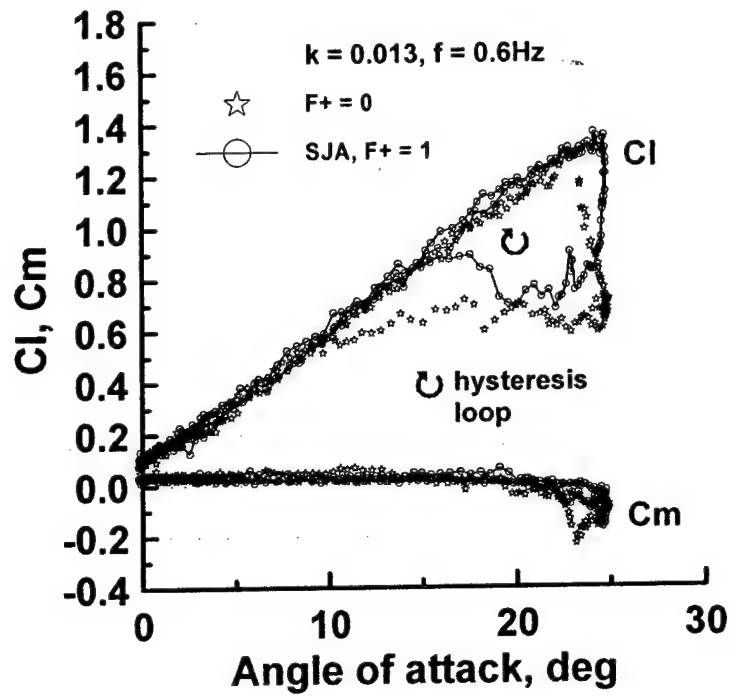Fig. 7.11 Effect of fluidic actuation on calculated lift and pitching moment coefficient, f = 1.6Hz.

Fig. 7.12 Effect of fluidic actuation on calculated lift and pitching moment coefficient, f = 1.8Hz.
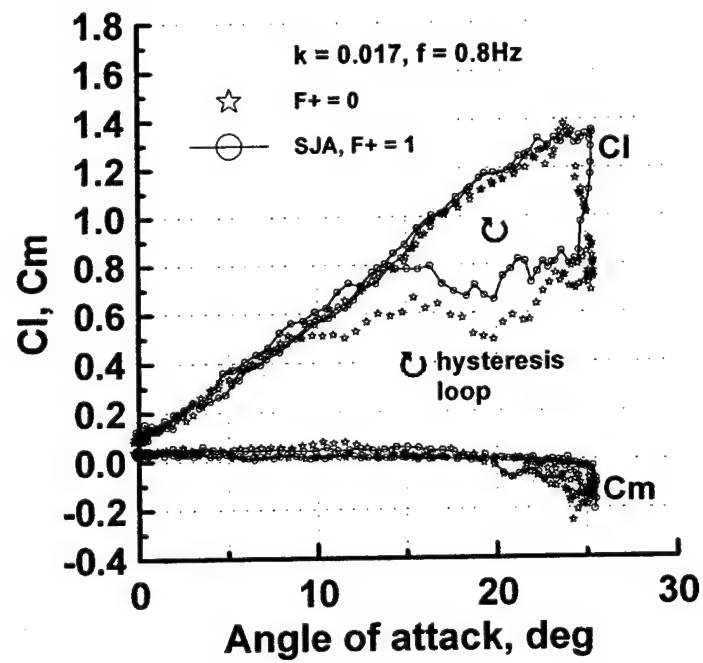

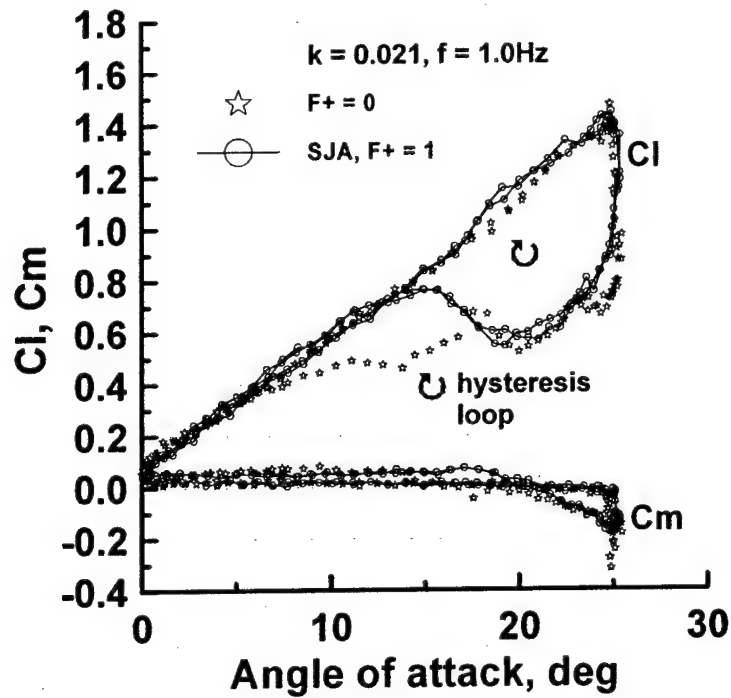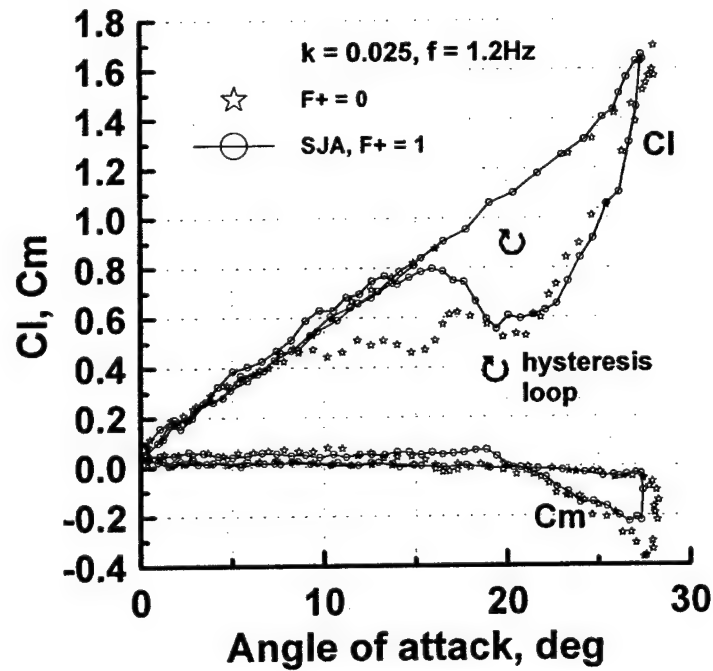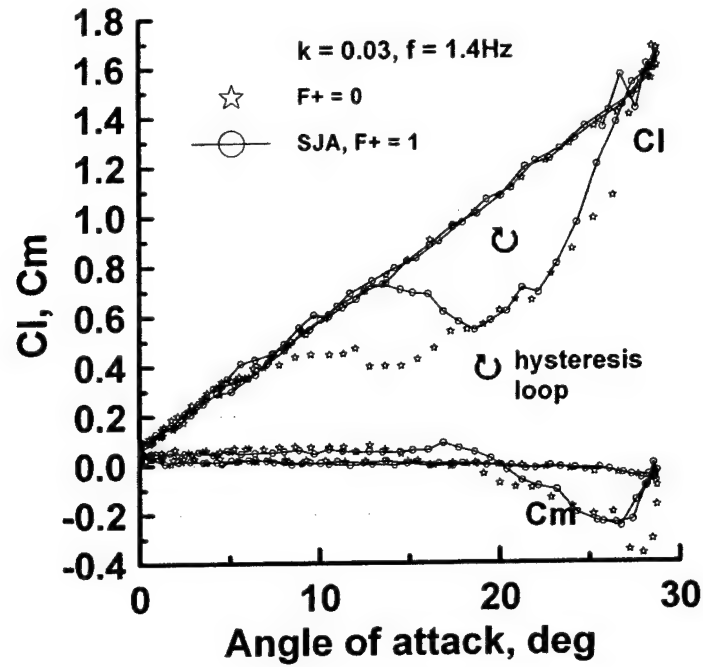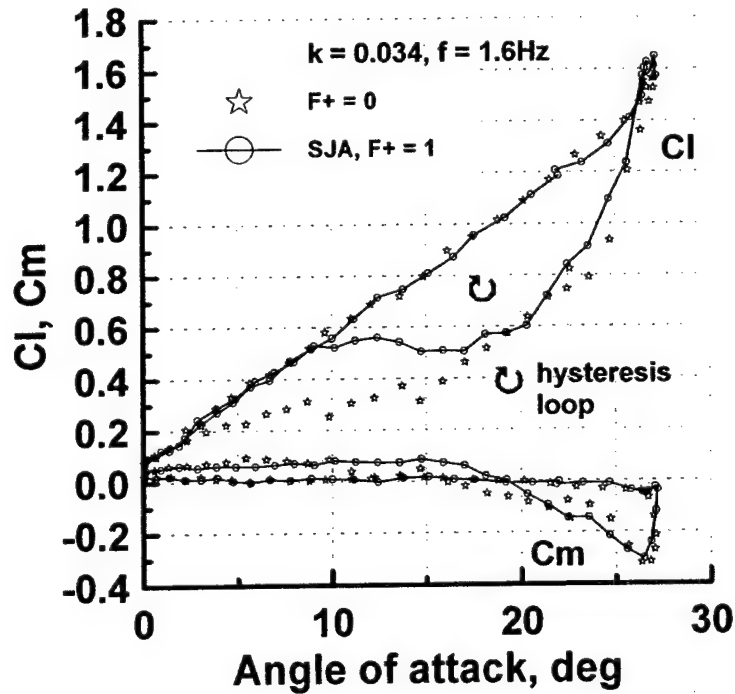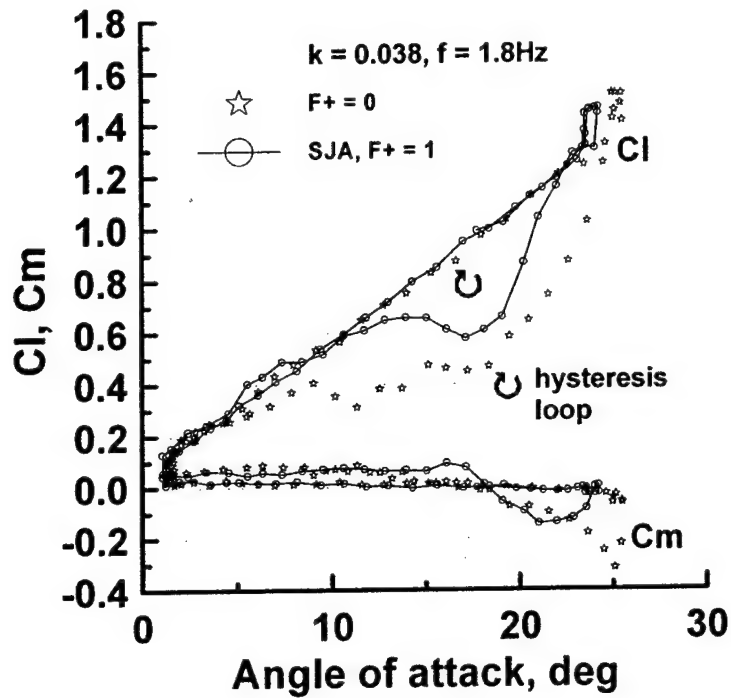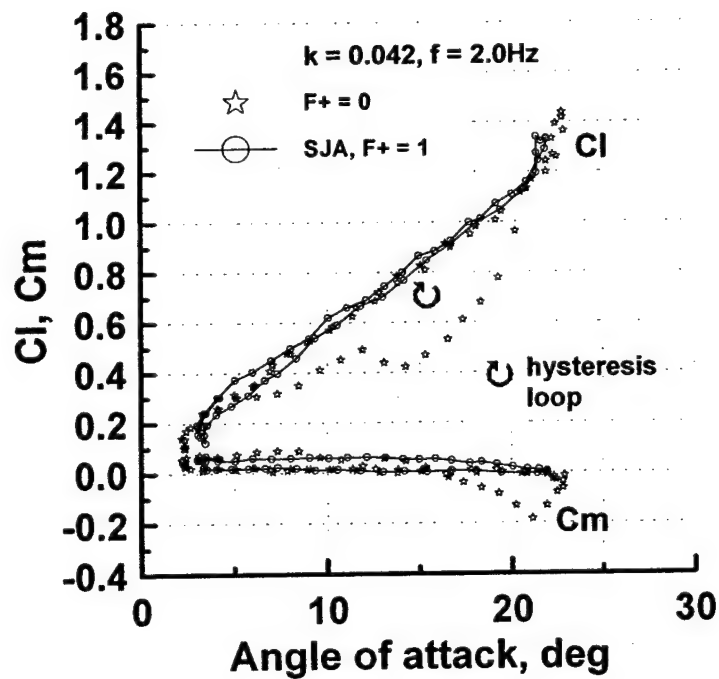Fig. 7.13 Effect of fluidic actuation on calculated lift and pitching moment coefficient, f = 2.0Hz.
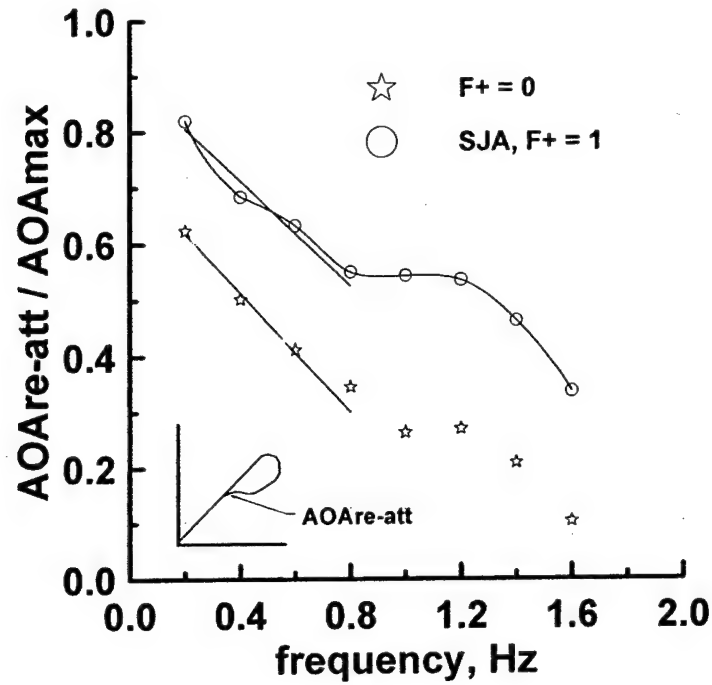
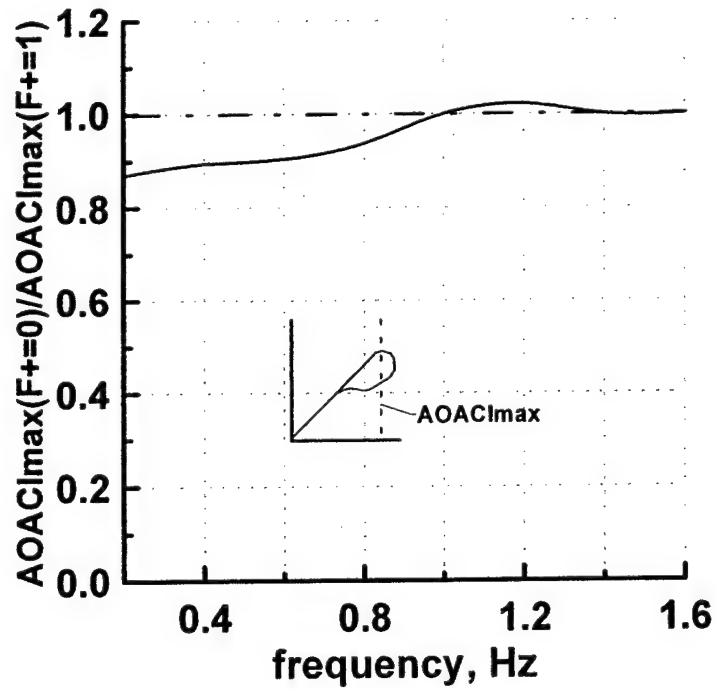Fig. 7.14 Effect of fluidic actuation and pitch frequency on downstroke boundary layer re-attachment incidence.

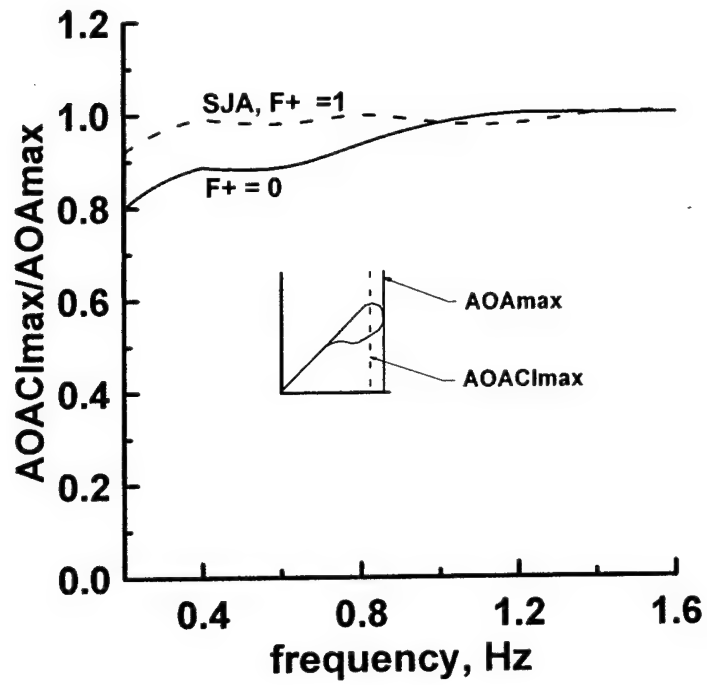Fig. 7.15 Ratio of the incidence at which the Clmax occurs with and without SJA actuation.

Fig. 7.16 Effect of forcing on the incidence at which the maximum lift coefficient occurs.

8. MODELING AND CONTROL OF SYNTHETIC JET ACTUATOR

MODELING OF THE ACTUATOR DYNAMICS

This section presents the modeling and control of the SJA developed and described in Section 2. The motor was supplied with the input voltage profile generated by dSPACE, as shown in Figure 8.1lower. This input consists of superimposed sinusoidal and square signals of different frequencies, so that all the dynamic modes of the motor are excited for correct model identification. Figure 8.1upper shows the response of the motor and the scaled input is superimposed on the output to indicate that there is no phase lag in the response. This experimental data is fed to an Observer Kalman Identification Algorithm (OKID) which identifies a linear model with 'Voltage' as the input and 'SJA Motor Frequency' as the output. The discrete linear model obtained is as follows:

$$x_{k+1} = 0.98877x_k + 0.58386u_k \qquad (8.1)$$

$$y = 0.43745x_k + 6.7999u_k \qquad (8.2)$$

where x_k is the state at the kth step, u_k is the control (Voltage) and y_k is the output (SJA Motor Frequency) and the sampling time for the discrete model is $T = 0.0015sec$. The corresponding continuous linear model is:

$$\dot{x} = -7.5324x + 391.44u \qquad (8.3)$$

$$y = 0.43745x + 6.7999u \qquad (8.4)$$

Figure 8.2 shows the comparison between the experimental data and the best fit as predicted by the linear model. Note that the predicted output does not match the actual measured output, for values below 60Hz and above 90Hz (the increase in the number of modes in the model does not increase the accuracy of the prediction). This leads us to guess that the SJA Motor Frequency does not depend linearly on Voltage 'V', but might have some dependence of the form V^α where α is a constant. This possibility is investigated later. Also determining the steady state relationship between the input and the output is achieved by setting $\dot{x} = 0$:

$$y = [-\frac{BC}{A} + D]u \qquad (8.5)$$

for a model in the standard state space form

$$\dot{x} = Ax + Bu \qquad (8.6)$$

$$y = Cx + Du \qquad (8.7)$$

For the identified model the relationship between the input and the steady state output y_{ss} is $y_{ss} = 29.7533u$, and is shown in Figure 8.3.
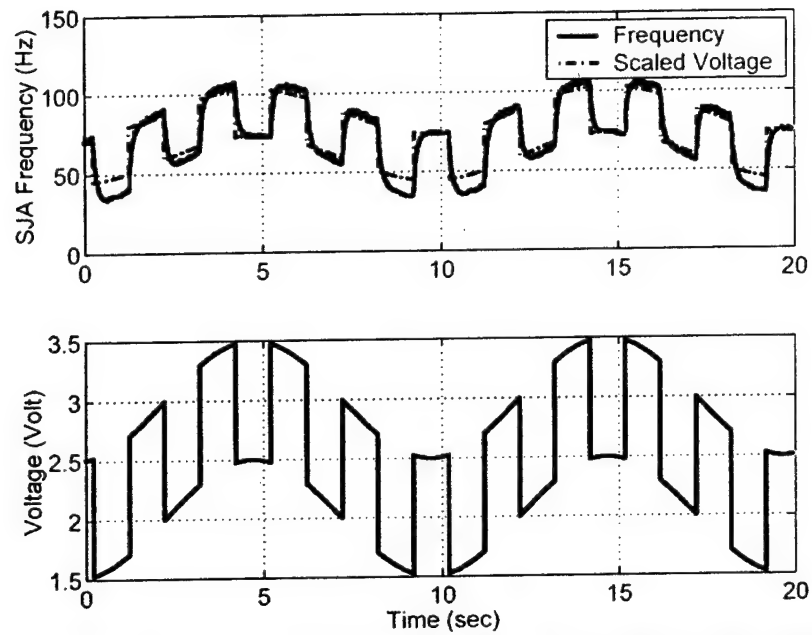
Fig. 8.1. Upper: Motor response and scaled input voltage; Lower: Input voltage profile.
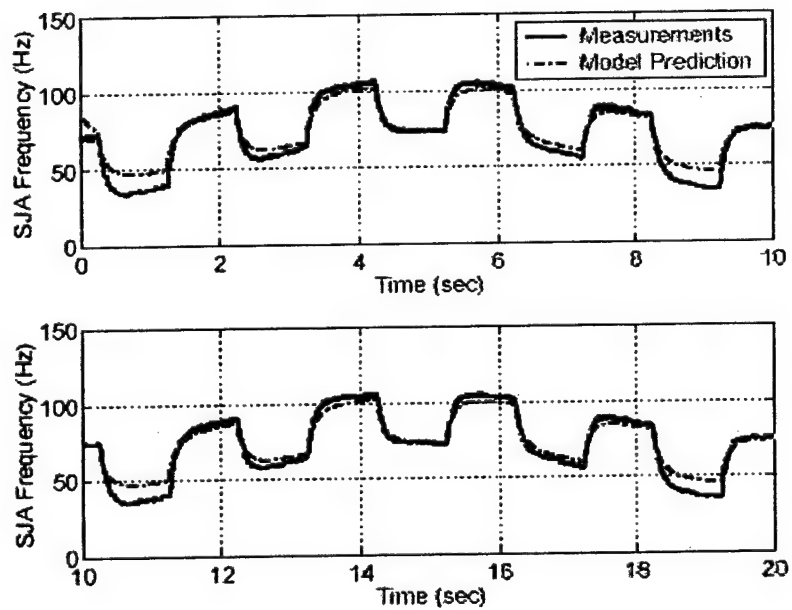
Fig. 8.2. Comparison between the experimental data and the best fit as predicted by the linear model.
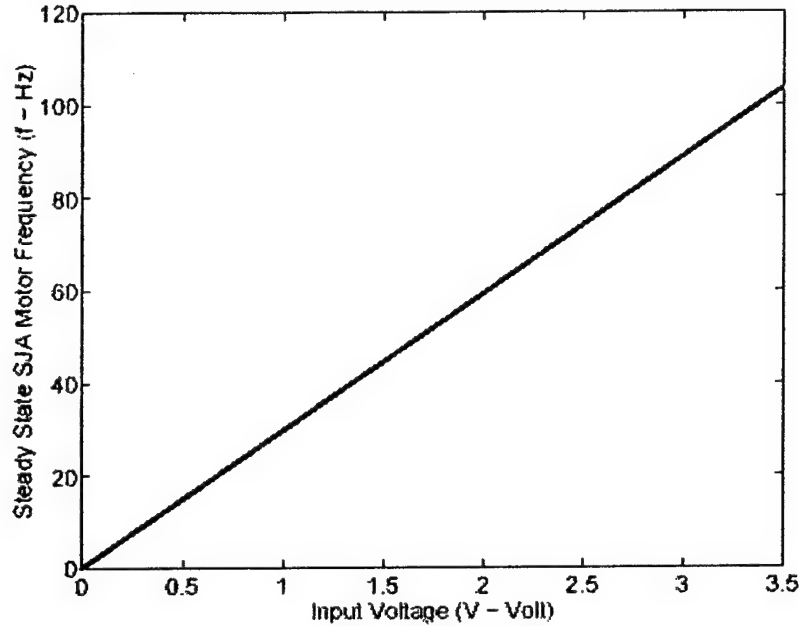
Fig. 8.3. Steady state SJA frequency versus input voltage for linear model.

The input measurements of Voltage 'V' are transformed by a nonlinear transformation V^α and this is considered as the new modified input. Various values of α are considered and $\alpha = 1.3$ gives the best results. The discrete model identified for $\alpha = 1.3$ is:

$$x_{k+1} = 0.98686x_k + 0.58497u_k \qquad (8.8)$$
$$y = 0.4123x_k + 3.4325u_k \qquad (8.9)$$

and the corresponding continuous version is:

$$\dot{x} = -8.8195x + 392.57u \qquad (8.10)$$
$$y = 0.4123x + 3.4325u \qquad (8.11)$$

Figure 8.4 shows that the predictions made by the Pseudo-Linear Model are very close to the actual measured SJA Motor Frequencies. For the identified psuedo-linear model the relationship between the input and the steady state output y_{ss} is $y_{ss} = 21.784u$. Figure 8.5 shows a comparison between the steady state predictions for both the models. Thus the pseudo-linear model shows predictions much better than the linear model.

The identified pseudo-linear model was then verified by two sets of experimental data. For the first set, the input voltage is applied as sinusoids, square waves and saw-tooth profiles with varying frequencies, in order to verify the performance of the identified model at different frequencies (Figure 8.6). For the second set of the verification data, the phenomenon of 'beats' is used to generate a sinusoidal signal of varying amplitude and this is added to a saw-tooth signal to span the entire operating range (Figure 8.7). As seen in both figures, the model does a very good job at predicting the output for both cases.

96
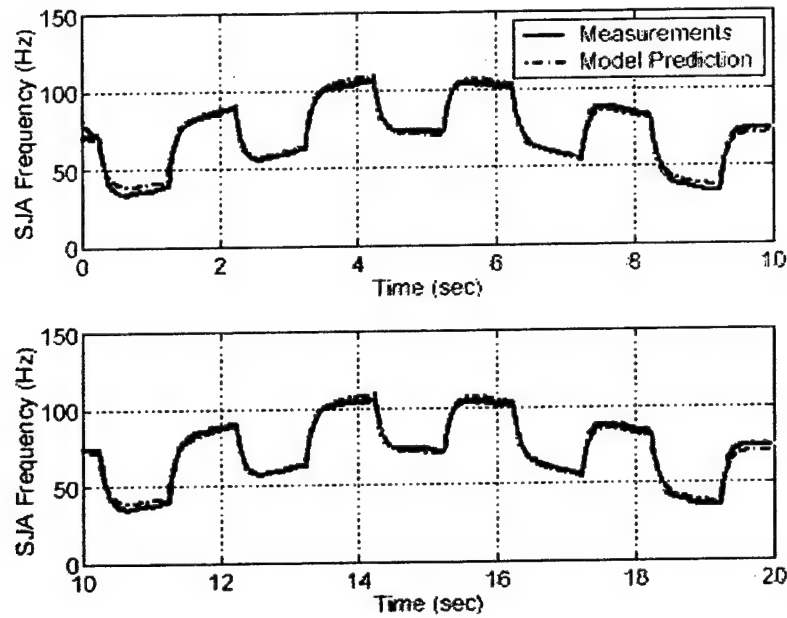
Fig. 8.4. Comparison between the experimental data and the best fit as predicted by the pseudo-linear model with transformed input.
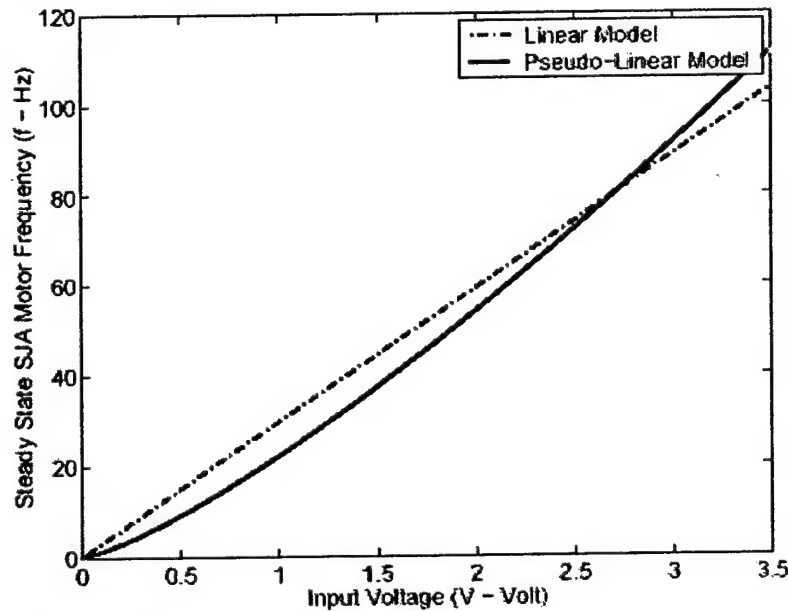
Fig. 8.5. Comparison between the steady state SJA frequency versus input voltage for the two identified models.

Subsequently, we went on to design the SJA controller. The designed control has a feedforward and a proportional feedback component (Figure 8.8). The feedforward component is the inverse mapping of the voltage V to steady state SJA frequency f mapping. Thus it is the inverse mapping of the graph shown in Figure 8.5, for the pseudo-linear model. Since this mapping is obtained with $V^{1.3}$ as the input, the inverse mapped signal u is raised to the power $\frac{1}{1.3}$ to get the actual applied voltage. The map between u and V exists and is unique for all positive values of voltage (the operating range is from 0.5 to 3.5

Volt). A feedback component with gain K is also added to compensate for the modeling errors and the transient dynamics. The value of K obtained by experiment is 0.1. This control law was implemented with the rapid control prototyping software of dSPACE. The control law was then tested with 4 test trajectories and the results are shown in Figures 8.9 to 8.15. As seen from these figures, the controller is performing very well.
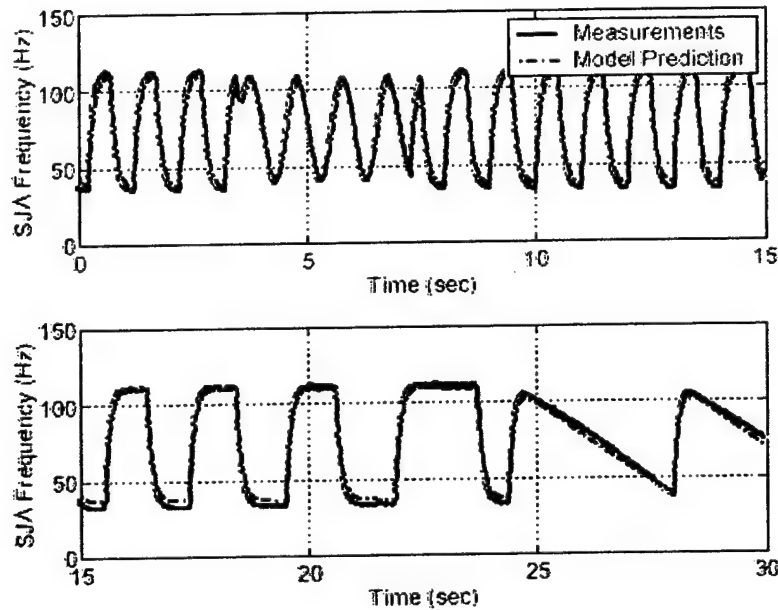
Fig. 8.6. Comparison between the verification experimental data#1 and the best fit as predicted by the pseudo-linear model with transformed input.
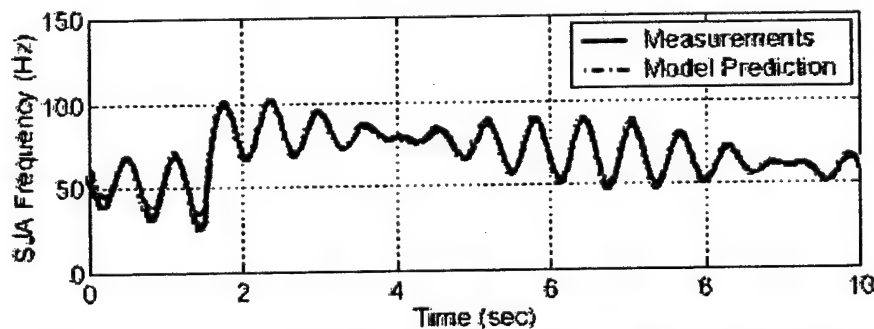
Fig. 8.7. Comparison between the verification experimental data#2 and the best fit as predicted by the pseudo-linear model with transformed input.
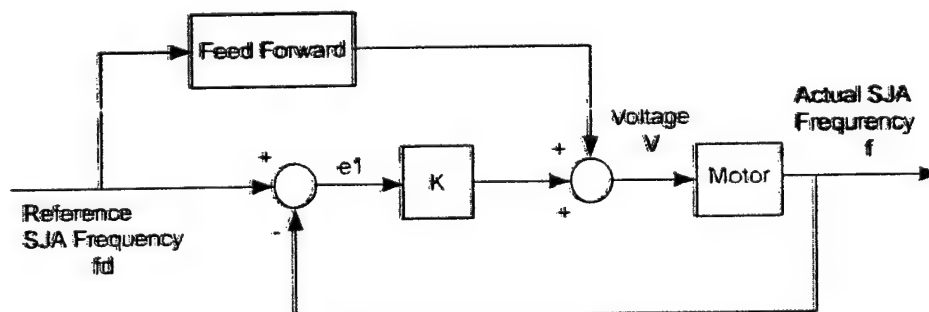
Fig. 8.8. Inner control loop (SJA control loop) architecture.

98
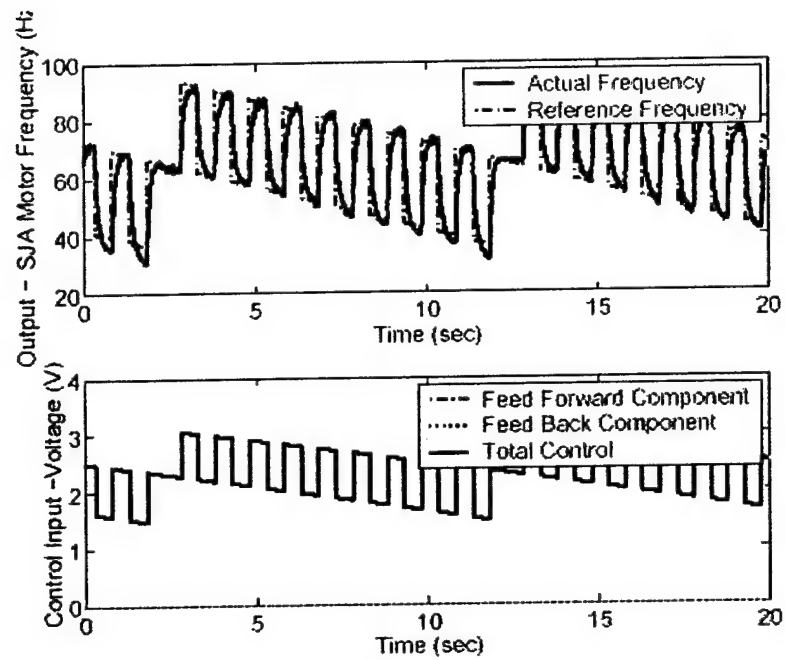
Fig. 8.9. Tracking signal#1 with no feedback.
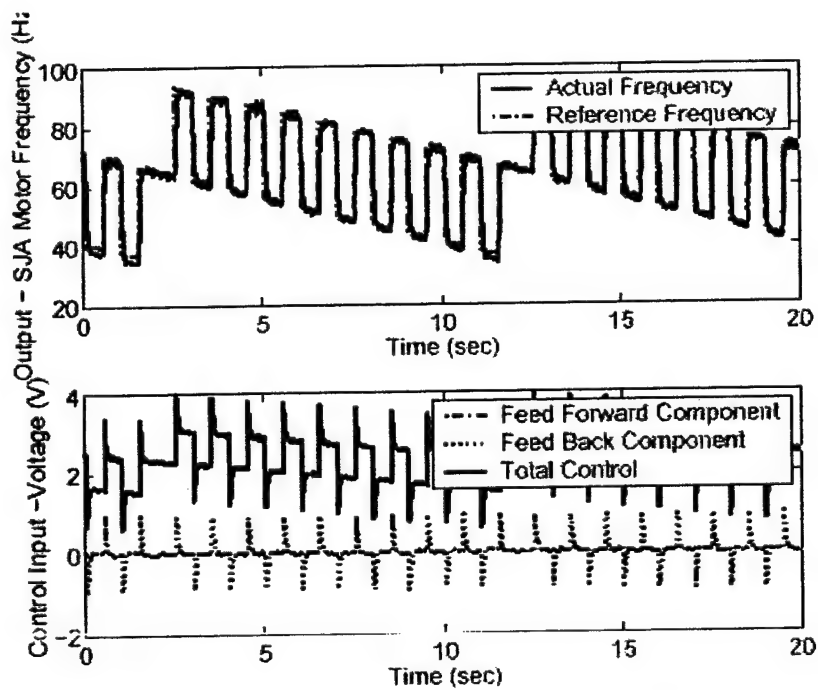
Fig. 8.10. Tracking signal#1 with feedback & feedforward.

99
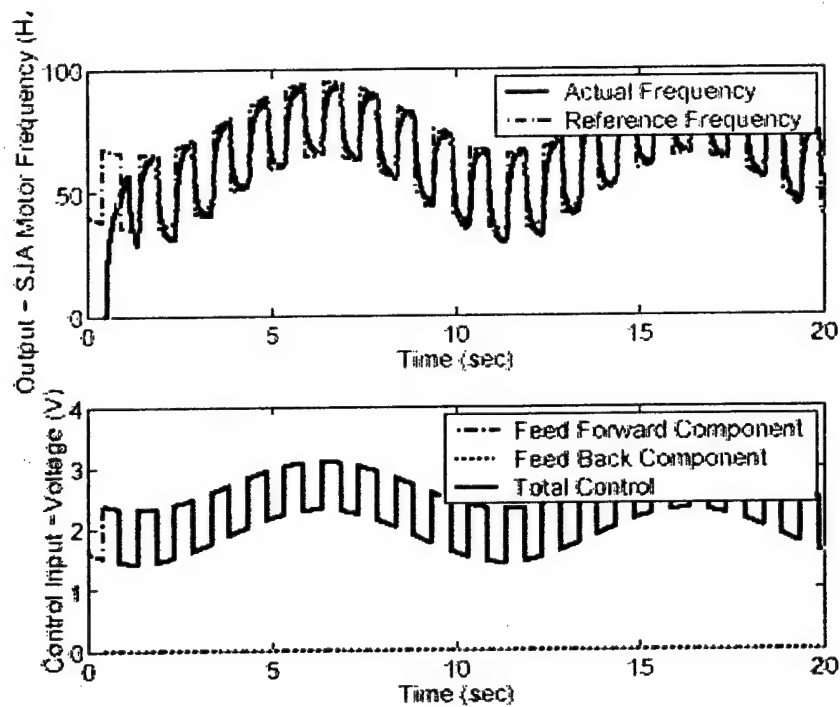
Fig. 8.11. Tracking signal#2 with no feedback.
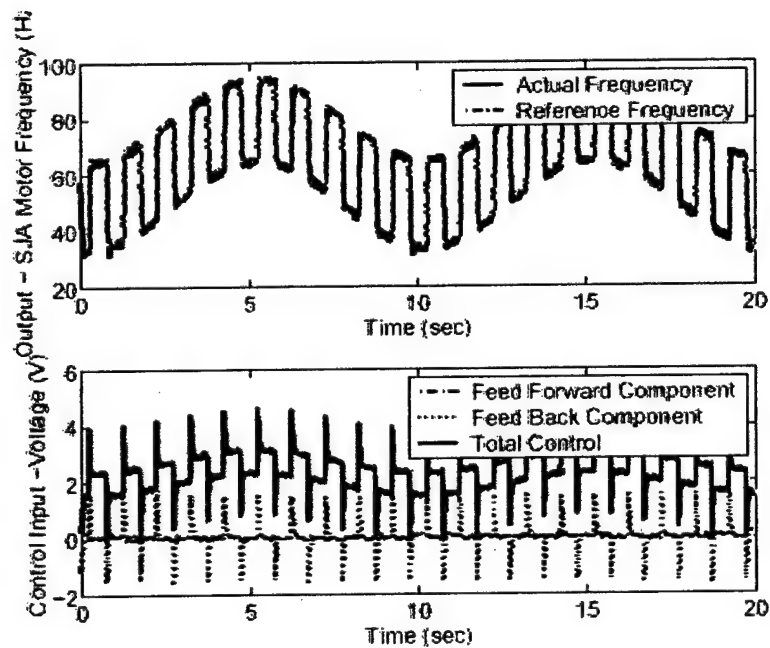
Fig. 8.12. Tracking signal#2 with feedback & feedforward.

100
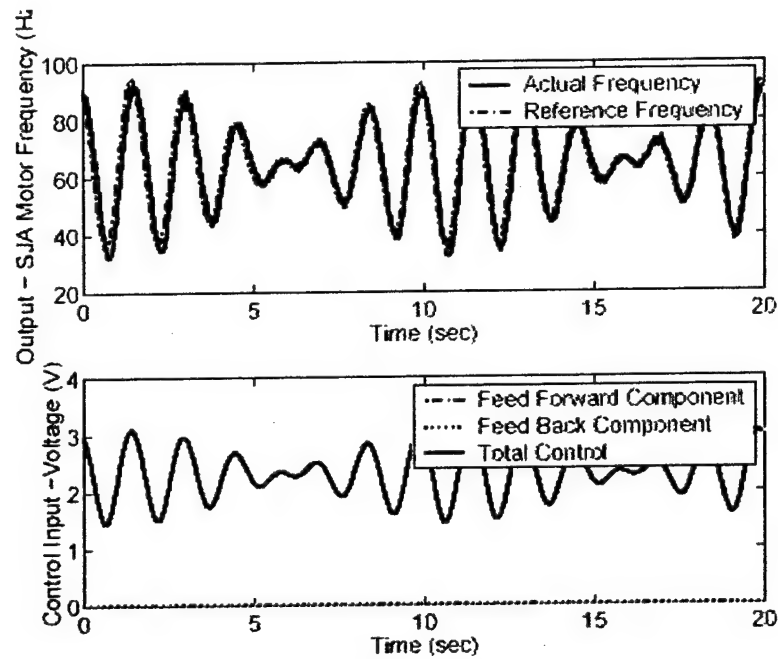
Fig. 8.13. Tracking signal#3 with no feedback.
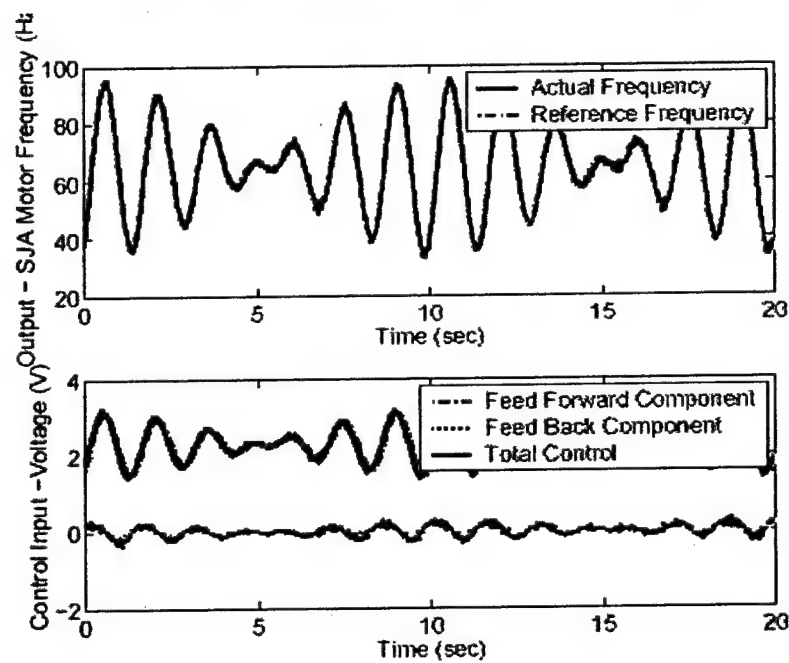
Fig. 8.14. Tracking signal#3 with feedback & feedforward.

101
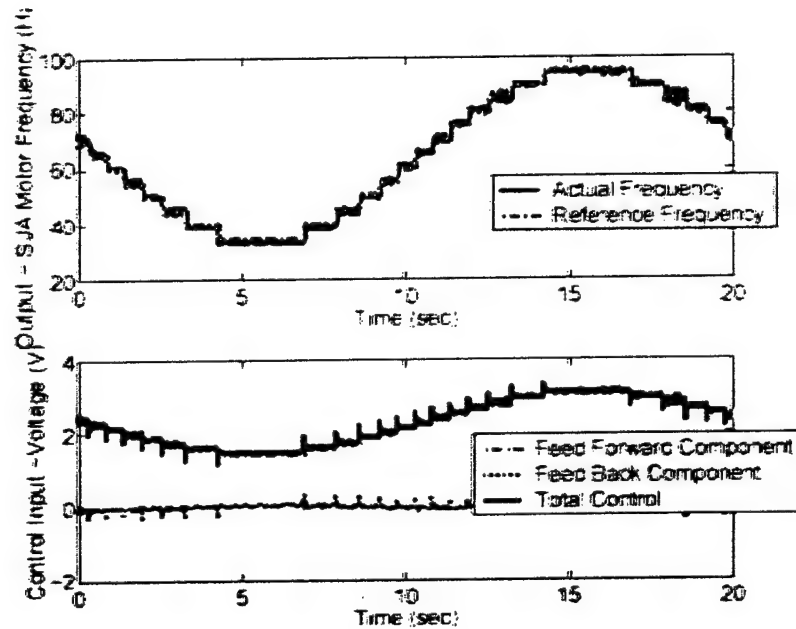
Fig. 8.15. Tracking signal#4 with feedback & feedforward.

MODELING OF THE ACTUATOR FLUID MECHANICS

This section discusses the modeling of the SJA fluid mechanics, i.e. the development of an actuator model that accepts as its input the actuator frequency and outputs the actuator velocity at its exit. For validating the model, the flow velocity measurements were done using a constant-temperature hot wire anemometer. The velocity was measured at the center of the exit slot of the SJA. Because of the very small width of the slot, it was not possible to identify the center of the slot precisely. Hence, the exit velocity was measured at four different points along the slot width and the maximum of these velocities is taken as the velocity at the center of the slot. The frequency of the motor is varied from 0 to around 150 Hz and exit velocities as high as 120 m/s are measured using this hot wire anemometry system. An overheat ratio of 1.4 is used for the hot wire anemometer experiments. Different actuator parameters were modeled and tested. Major emphasis in this analysis has been given to the effects of frequency of oscillation, exit slot width and cavity volumes on the SJA performance.

Model Without Accounting For Friction Losses At Exit
Figure 8.16 shows a schematic of a typical synthetic jet actuator.
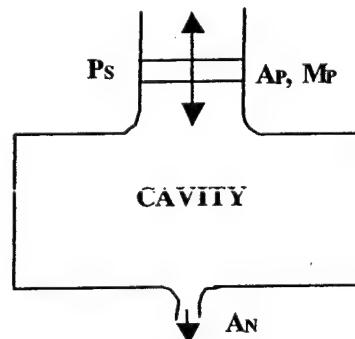
Fig. 8.16. General schematic of a synthetic jet actuator.

The following analysis presents a theoretical model to predict the compressibility effects of the jet at the exit. The displacement and velocity of the piston oscillations at any instant of time are expressed as

$$x = A.[1 - \cos(2.\pi.f.t)] \qquad (8.12)$$

$$\dot{x} = 2.A.\pi.f.\sin(2.\pi.f.t) \qquad (8.13)$$

A is the amplitude of the piston oscillation, which is one half the stroke of the piston. Volume of air inside the cavity $= V_O - A_P.x$. We consider both the suction and blowing cycle for this analysis. During the suction part of the cycle, mass is added to the system and during the blowing part of the cycle, mass is removed from the system. Hence, the mass flow rate through the system is positive during the suction cycle and negative during the blowing cycle.

$$\frac{dm}{dt} = -\rho.A_S.U \qquad (8.14)$$

Mass of air in the system $= \rho.(V_O - A_P.x)$. Differentiating this and equating it to the mass flow rate,

$$-\rho.A_S.U = \frac{d}{dt}[\rho.(V_O - A_P.x)] \qquad (8.15)$$

$$-\rho.A_S.U = -\rho.A_P.\dot{x} + \dot{\rho}.(V_O - A_P.x) \qquad (8.16)$$

Rearranging this,

$$\frac{\dot{\rho}}{\rho} = \frac{A_P.\dot{x}}{(V_O - A_P.x)} - \frac{A_S}{(V_O - A_P.x)}.U \qquad (8.17)$$

We introduce the constants c1 and c2 as

$$c1 = \frac{A_P.\dot{x}}{(V_O - A_P.x)} \qquad (8.18)$$

$$c2 = \frac{A_S}{(V_O - A_P.x)} \qquad (8.19)$$

Hence,

$$\frac{\dot{\rho}}{\rho} = c1 - c2.U \qquad (8.20)$$

When the flow is incompressible, $\dot{\rho} = 0$. Hence the jet exit velocity equation for incompressible flow simplifies to

$$U = \frac{c1}{c2} = \frac{A_p}{A_s}.\dot{x} \qquad (8.21)$$

The above equation suggests that for incompressible flow, the jet exit velocity is a linear function of the motor frequency as expected. At higher frequencies of operation though, the flow is not incompressible and also smaller slot widths make the flow more compressible and hence a comprehensive study of the compressibility effects would help optimize the design to minimize the compressibility effects. As derived earlier, for compressible flow

$$\frac{\dot{\rho}}{\rho} = c1 - c2.U \qquad (8.22)$$

Now we assume that the air has zero velocity at the center of the cavity. The air inside the cavity has very low momentum. Applying the unsteady Bernoulli's equation between the center of the cavity and the exit slot,

$$\nabla(\dot{\phi} + \frac{p}{\rho} + \frac{U^2}{2}) = 0 \qquad (8.23)$$

which upon expansion between the center of the cavity and the exit slot yields,

$$p_c - p_o = \frac{1}{2}.\rho.U^2 + \rho.(\dot{\phi}_o - \dot{\phi}_c) \qquad (8.24)$$

The subscript "o" represents exit slot terms and the subscript "c" represents cavity terms. The exit slot is open to the atmosphere and hence it is at ambient pressure. The velocity potential at the exit slot can be evaluated from the following expression.

$$\phi_o = \phi_c + \int(\frac{d\phi}{dx}).dx = \phi_c + U.l \qquad (8.25)$$

where l is the acceleration length of the exit slot. We assume the acceleration length is a multiple of the slot width, hence,

$$\dot{\phi}_o - \dot{\phi}_c = \dot{U}.l \qquad (8.26)$$

Substituting equation (8.26) in equation (8.24), we get

$$p_c = p_o + \frac{1}{2}.\rho.U^2 + \rho.\dot{U}.l \qquad (8.27)$$

During the blowing part of the cycle, $1/2\rho U^2$ is positive and during the suction part of the cycle it is negative. Hence to account for both blowing and suction,

$$\frac{1}{2}.\rho.U^2 = \frac{1}{2}.\rho.U.|U| \qquad (8.28)$$

which gives

$$p_c = p_o + \frac{1}{2}.\rho.U.|U| + \rho.\dot{U}.l \qquad (8.29)$$

Assuming the air inside the cavity to be isothermal, we get

$$p_c = \rho.R.T$$
$$\dot{p}_c = \dot{\rho}.R.T \qquad (8.30)$$

Differentiating equation (8.29) and substituting for $\dot{p}_c$ from (8.30) yields

$$\dot{\rho}.R.T = \frac{1}{2}.\rho.\frac{d}{dt}(U.|U|) + \rho.\ddot{U}.l + \dot{\rho}.\dot{U}.l + \dot{\rho}.\frac{U.|U|}{2} \qquad (8.31)$$

104

Dividing by ρ and substituting for $\dfrac{\dot{\rho}}{\rho}$ from (8.22), we get

$$c1.(R.T - \frac{U.|U|}{2} - \dot{U}l) - c2.(U.R.T - \frac{U^2.|U|}{2} + U.\dot{U}l) - \ddot{U}l - \frac{1}{2}.\frac{d}{dt}(U.|U|) = 0 \quad (8.32)$$

Equation (8.32) represents the jet exit velocity equation for compressible flow without accounting for friction losses and separation effects at the exit slot. This equation is solved using finite difference method for different frequencies of the motor. The initial boundary conditions used are: at $t = 0$, jet exit velocity = 0 and velocity acceleration at exit = 0. The jet exit velocity is also a periodic function of time. We are interested only in the maximum velocity generated. Hence, the amplitude of the jet exit velocity is plotted as a function of the actuator frequency for both compressible and incompressible flow for different slot geometries and different cavity volumes. The effect of the acceleration length, l, on the flow is also studied. The jet exit velocity is plotted for different motor frequencies. Table 8.1 gives a list of the different slot geometries and the cavity volumes that were tested using this analysis.

Piston Diameter (inches)	Piston Stroke (inches)	Exit Slot Width (inches)	Exit Slot Length (inches)	Cavity Width (inches)
0.906	0.811	0.032	2.5	0.3
0.906	0.811	0.032	2.5	0.4
0.906	0.811	0.032	2.5	0.5
0.906	0.811	0.064	2.5	0.3
0.906	0.811	0.064	2.5	0.4
0.906	0.811	0.064	2.5	0.5

TABLE 8.1. Different geometric parameters of SJAs tested for compressibility effects.

Figures 8.17 and 8.18 represent the design of the exit slot and the cavity of the SJAs that were analyzed.
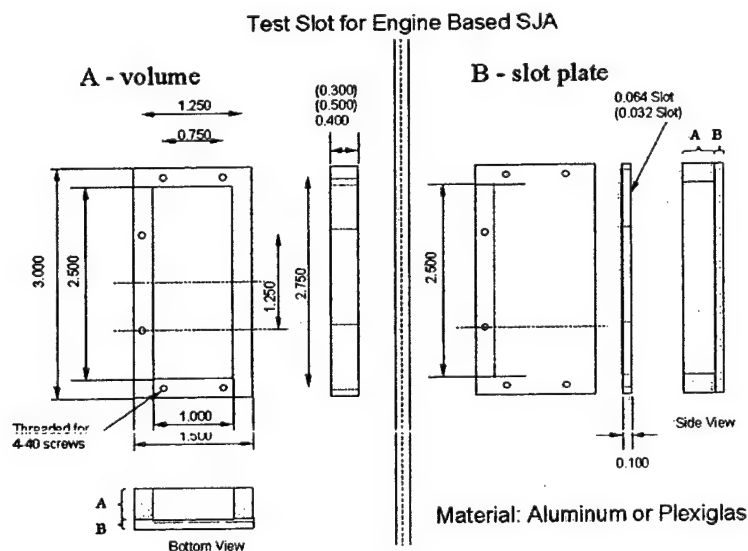
Fig. 8.17. Design of SJA exit slot / cavity.

"Slot Plate"

(not to scale)
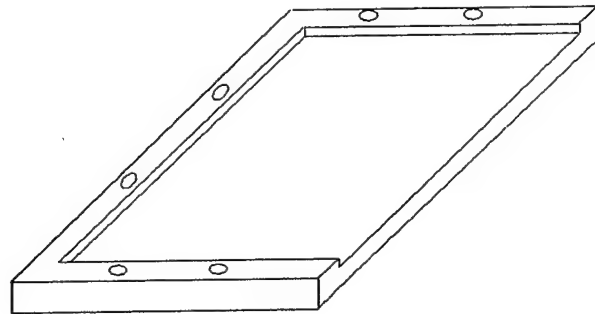
Fig. 8.18. Design of exit slot plate.
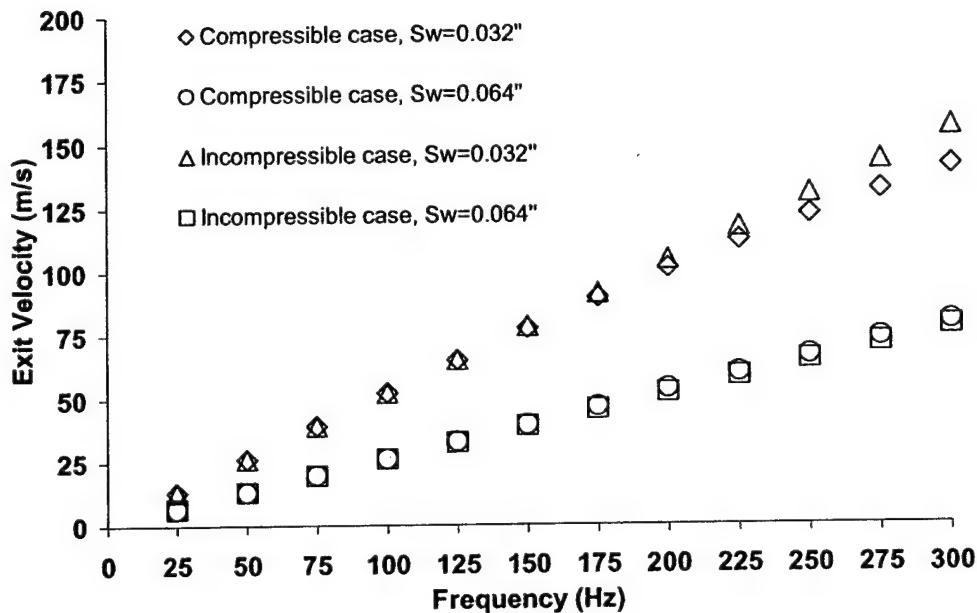
Fig. 8.19. Jet exit velocity comparison for incompressible and compressible flow.

Figure 8.19 represents the comparison between the theoretical compressible and incompressible jet exit velocity for both slot widths. Figure 8.19 shows that as expected, the compressible case velocity is lesser than the incompressible case for both slot widths and also the smaller slot width has a higher velocity (both incompressible and compressible case) than the larger slot width, which is also expected. Also this plot shows that compressibility effects are more predominant at larger frequencies and the flow tends to be more incompressible at smaller frequencies. Hence, the study of compressibility effects on the performance of the SJA is very important at higher frequencies and helps formulate an appropriate model to optimize the design of the SJA. Figure 8.20 shows the variation of exit velocity with acceleration length for both theoretical compressible and incompressible flow for a slot width of 0.032 inches. Figure 8.20 shows that the acceleration length does not have much of an effect on the jet exit velocity at lower frequencies, and at higher frequencies the jet exit velocity increases with increase in acceleration length. Based on the previous plot, the compressibility effects are more dominant at higher frequencies thus

106

reducing the jet exit velocity and hence the lower acceleration length of $3*S_W$ is assumed hereafter for this model.
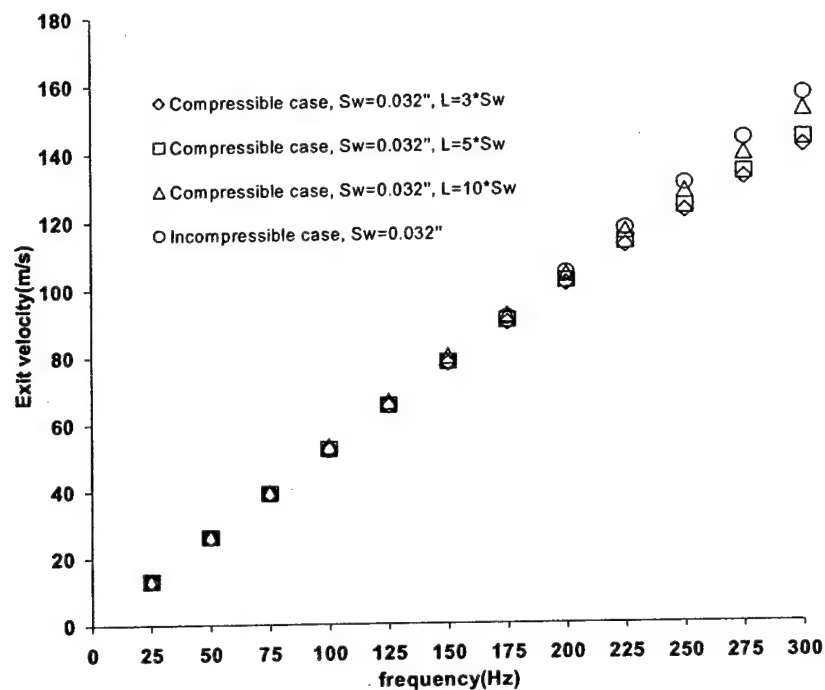
Fig. 8.20. Exit velocity comparison between compressible and incompressible flow for different acceleration lengths.
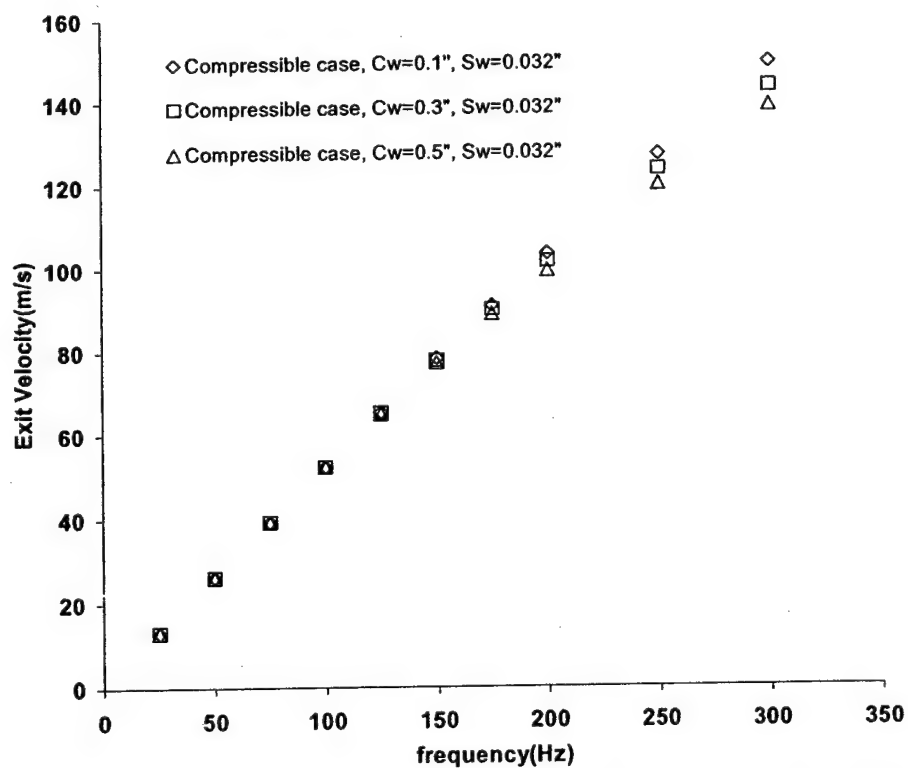
Fig. 8.21. Variation of jet exit velocity with cavity volume for slot width 0.032".

107
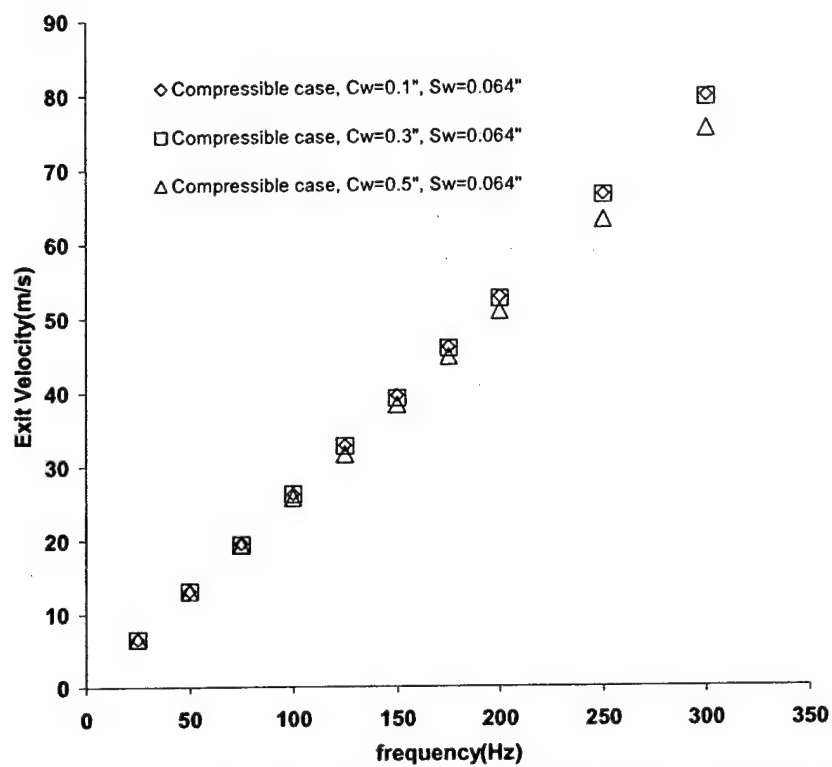
Fig. 8.22. Variation of jet exit velocity with cavity volume for slot width 0.064".
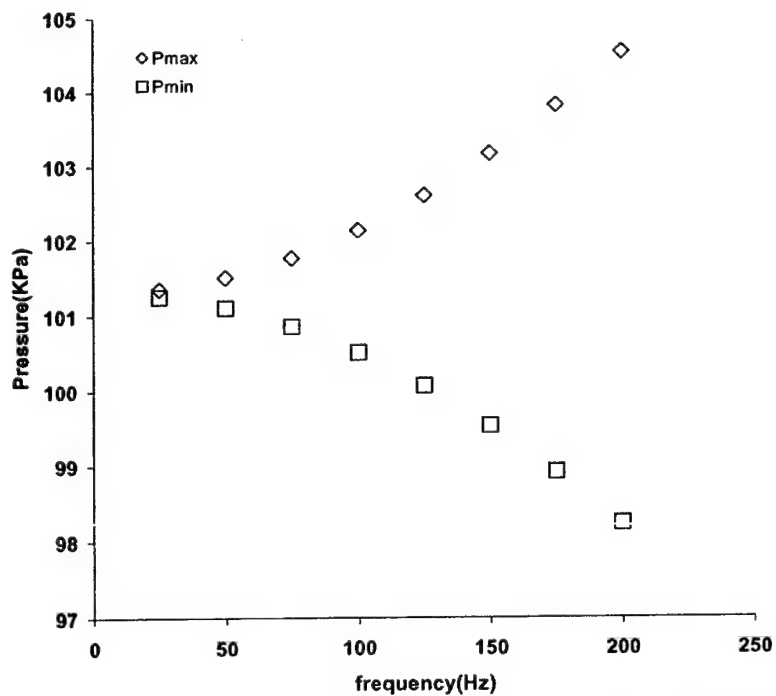
Fig. 8.23. Variation of maximum and minimum pressure at the center of the cavity.

Figures 8.21 and 8.22 represent variation of the exit velocity with cavity volume for both slot widths.Based on Figures 8.21 and 8.22, we can conclude that the cavity volumes tested do not change the jet exit velocity too much. More drastic cavity volume changes are necessary to see a more prominent change in the velocity. It is however observed that the jet exit velocity decreases marginally with the increase in cavity volume at higher frequencies for both slots. Figure 8.23 represents the maximum and minimum pressure distribution at the center of the cavity.

This model is also used to analyze the performance of the developed six-cylinder SJA. The volume of the cavity is reduced due to the curvature on the corners of each of the six cavities in this case. This reduction is calculated and subtracted from the total cavity volume using integration with the geometry of the curvature being known. Two DC motors are used to run this six-cylinder SJA. Table 8.2 lists the parameters of this new six-cylinder SJA that was tested using this model. Figure 8.24 compares the compressible jet exit velocity and the incompressible case.

Piston Diameter (Inches)	Piston Stroke (Inches)	Slot Length (Inches)	Slot Width (Inches)
1.091	0.866	1.61	0.075

TABLE 8.2. Geometric parameters of six-cylinders SJA tested with model.
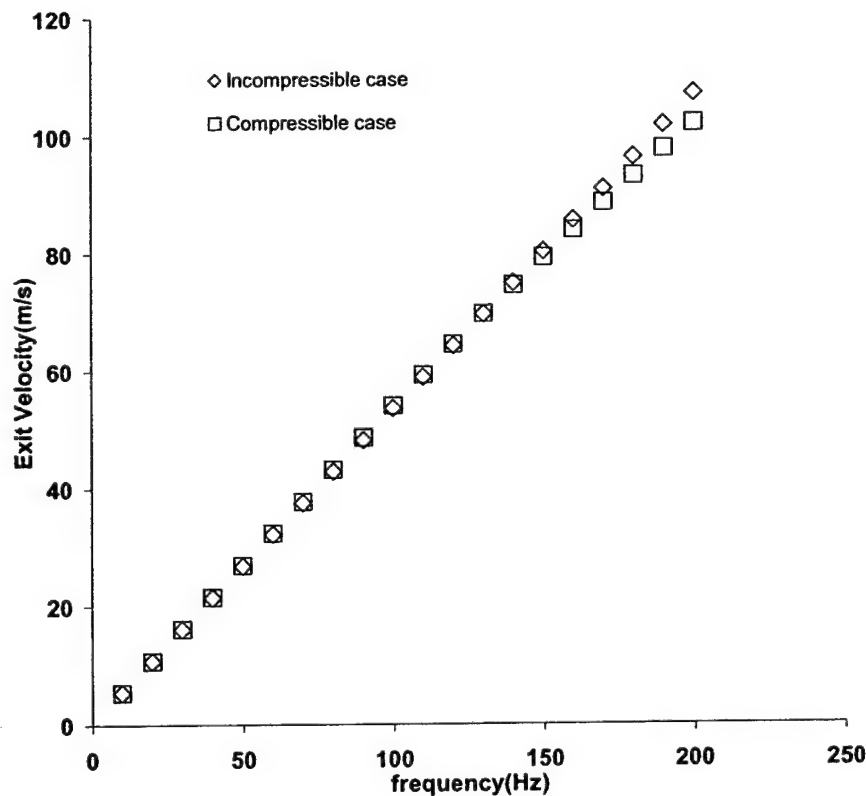
FIG. 8.24. Jet exit velocity comparison between compressible and incompressible case for six-cylinders SJA.

As observed earlier, the compressible velocity is less than the incompressible velocity and also the compressibility effects are more predominant at higher frequencies. Figure 8.25 represents the variation of exit velocity for compressible case with the cavity volume for the six cylinders SJA. The cavity volume is increased 10, 20 and 30% of its original value to generate these plots.

109
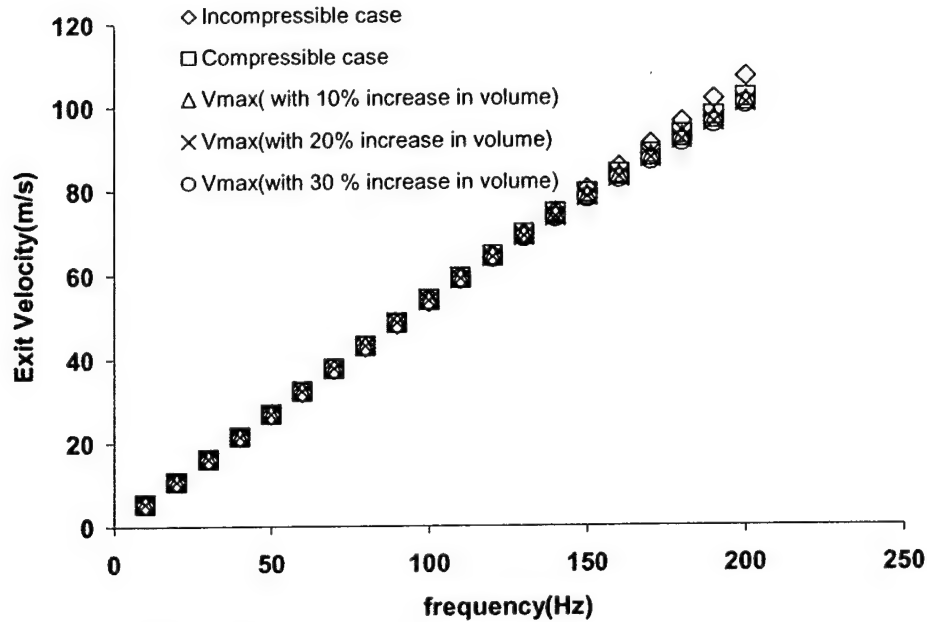
FIG. 8.25. Variation of exit velocity with 10, 20 and 30 % increase in cavity volume for six-cylinders SJA.

Figure 8.25 shows that a higher cavity volume shows more compressibility effects compared to a smaller volume. The same phenomenon was also observed in the cavity volumes tested with the single-cylinder SJA and this new model with increased cavity volumes seems to produce the same behavior of the jet exit velocity variation thus reiterating the conclusion that reducing the cavity volume would decrease compressibility effects and produce a larger velocity of the jet. Also, it can be seen that at smaller frequencies, the cavity volume does not have too much of an effect on the jet velocity as observed with the single-cylinder SJA. Figure 8.26 represents the variation of jet exit velocity with cavity volume with the cavity volume decreased 10, 20 and 30% of its original value.
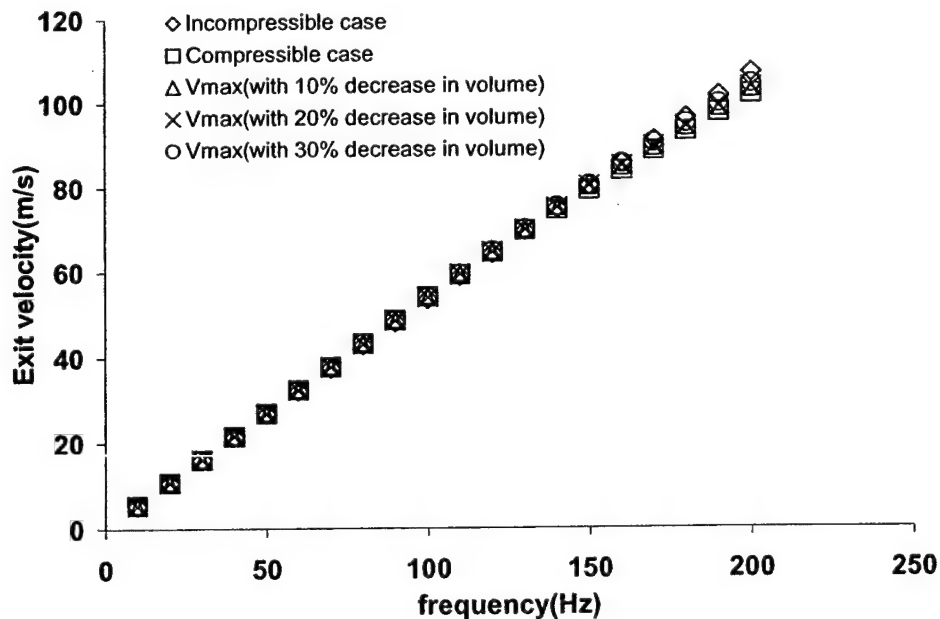
FIG. 8.26. Variation of jet exit velocity with 10, 20 and 30 % decrease in cavity volume for six-cylinders SJA.

110

The same trend as the previous case with the increase in cavity volume is observed here, with the higher cavity volume tending to be more compressible than the lower cavity volume. It should however be noted that with 30% decrease in volume, the jet exit velocity approaches incompressible flow. The optimal design of the cavity would hence suggest that a smaller cavity volume would result in larger jet exit velocities. Figure 8.27 represents the maximum and minimum pressure at the center of the cavity for this six-cylinder SJA case. It should be noted here, however, that this model does not account for any viscous losses that occur at the exit slot and also any separation effects that might reduce the velocity. The next section discusses the model accounting for both the viscous losses and the separation effects.
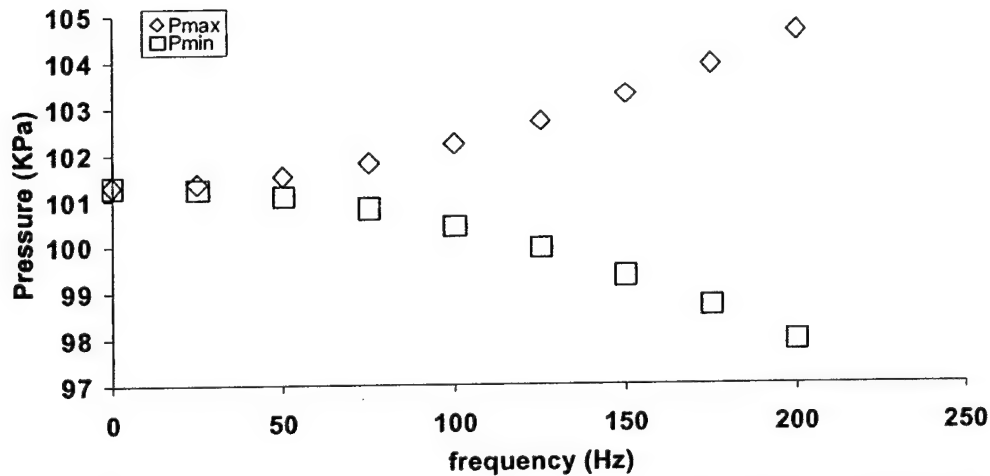
FIG. 8.27. Maximum and minimum pressure at center of cavity.

Model accounting for friction losses and separation effects at exit

This section presents a theoretical model to predict the jet exit velocity with viscous losses and flow separation effects at the exit slot plane taken into account. Friction losses in the throat and flow separation at the exit plane of the slot cause damping. The line integral of the momentum equation along a streamline relates the exit velocity to the pressure inside the cavity. Boundary layer separation occurs at the exit slot plane where the flow curves around the cavity edge to enter the slot. The line integral is evaluated between the cavity and the exit plane of the slot and the resulting equation is:

$$\rho . \frac{d}{dt} (\int U.ds) + \rho . \int [\nabla (\frac{U^2}{2} + p).ds] = -\mu . \int (\nabla x \omega) ds \qquad (8.33)$$

After integrating this equation, during the blowing part of the cycle, we get

$$\frac{dU}{dt} = \frac{p}{L_e . \rho} - \frac{U^2}{2.C_d^2 . L_e} - \frac{8.\mu .U.L_v}{\rho . L_e . h_t^2} \qquad (8.34)$$

During the suction part of the cycle,

$$\frac{dU}{dt} - \frac{p}{L_e . \rho} + \frac{U^2}{2.C_d^2 . L_e} - \frac{8.\mu .U.L_v}{\rho . L_e . h_t^2} \qquad (8.35)$$

In the above equations, L_e represents the equivalent inertia length of the exit slot, L_v represents the equivalent viscous length of the slot, h_t represents the height or the width of the slot and C_d is the flow coefficient associated with the streamline curvature at exit. To account for both suction and blowing in the same equation, we can write the equation for the exit velocity as

111

$$\frac{dU}{dt} = \frac{p}{L_e \cdot \rho} - \frac{U \cdot |U|}{2 \cdot C_d^2 \cdot L_e} - \frac{8 \cdot \mu \cdot U \cdot L_v}{\rho \cdot L_e \cdot h_t^2} \qquad (8.36)$$

Here p represents the relative pressure in the cavity $= p_c - p_o$

Differentiating equation (8.36) with respect to time,

$$\ddot{U} = \frac{p_o \cdot \dot{\rho}}{L_e \cdot \rho^2} - \frac{\frac{d}{dt}(U \cdot |U|)}{2 \cdot L_e \cdot C_d^2} - \frac{8 \cdot \mu \cdot L_v \cdot \dot{U}}{\rho \cdot L_e \cdot h_t^2} + \frac{8 \cdot \mu \cdot L_v \cdot U \cdot \dot{\rho}}{\rho^2 \cdot h_t^2 \cdot L_e} \qquad (8.37)$$

We substitute $p_o = \rho \cdot R \cdot T_o$ and for $\dfrac{\dot{\rho}}{\rho}$ from (8.22) and introduce the constant c as

$$c = \frac{8 \cdot \mu \cdot L_v}{L_e \cdot h_t^2} \qquad (8.38)$$

Rearranging equation (8.37) after the above mentioned substitutions yields,

$$\ddot{U} = \frac{c1 \cdot R \cdot T_o}{L_e} - \frac{c2 \cdot R \cdot T_0 \cdot U}{L_e} - \frac{\frac{d}{dt}(U \cdot |U|)}{2 \cdot L_e \cdot C_d^2} - \frac{c \cdot R \cdot T_o \cdot \dot{U}}{p_o} + \frac{c1 \cdot c \cdot U \cdot R \cdot T_o}{p_o} - \frac{c \cdot c2 \cdot R \cdot T_o}{p_o} \qquad (8.39)$$

The above equation is solved for the jet exit velocity using finite difference method and the velocity is plotted as a function of frequency. This exit velocity is compared with the case where the friction losses are neglected and boundary layer separation has also been ignored.

Let us now try to evaluate the constant, c, which is dependent on the geometry of the SJA and the flow properties.

$$c = \frac{8 \cdot \mu \cdot L_v}{L_e \cdot h_t^2} \qquad (8.40)$$

L_e = equivalent inertia length = $L_t + (A_s \cdot \pi / 4)^{1/2}$
h_t = Resonator throat height = width of the exit slot
L_v = equivalent viscous length of the throat = Acceleration length of air in the exit

As of now, the only information we have is $L_v <= L_t$, Hence we assume $L_v = k \cdot L_t$, where $L_t = S_L$. The variation of C_d with frequency and the geometry/ dimensions of the exit slot was studied and the results of this study and its effects on this new model accounting for friction losses at the exit are presented in the following section.

Results and Discussion

The behavior of the jet exit velocity with the friction losses at the exit taken into account is studied and it is observed that C_d might be a function of the frequency of oscillation. The variation of C_d is studied and its effects on the exit velocity are observed. Figure 8.28 represents the variation of jet exit velocity between the incompressible case, the theoretical compressible model without accounting for friction losses at the exit and the model accounting for friction/viscous losses, for a slot width 0.032" inches.

112
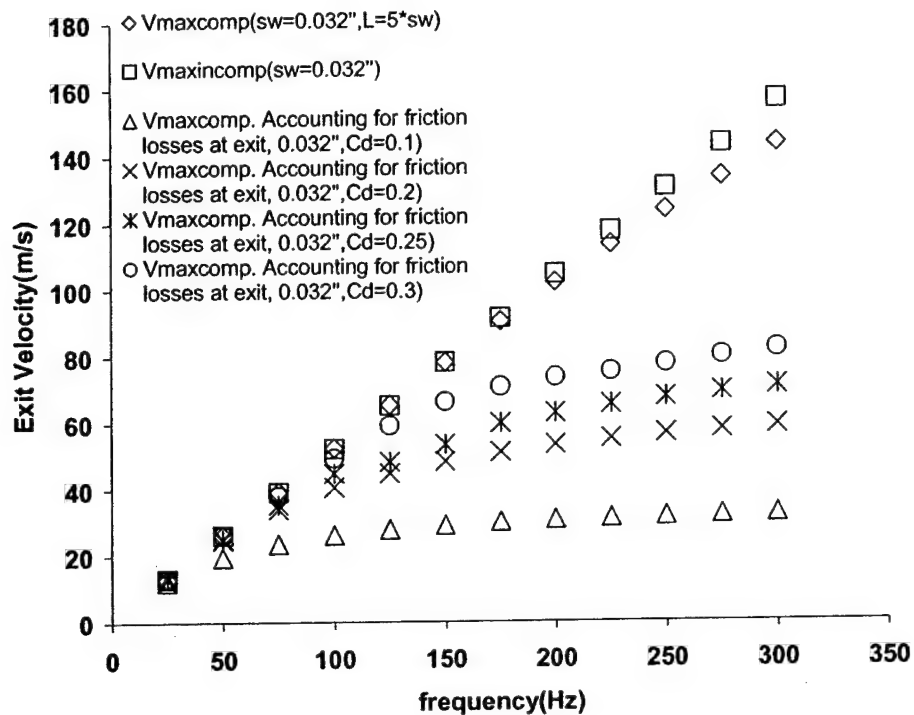
FIG. 8.28. Jet exit velocity comparison between incompressible and compressible cases with and without friction losses for slot width 0.032".
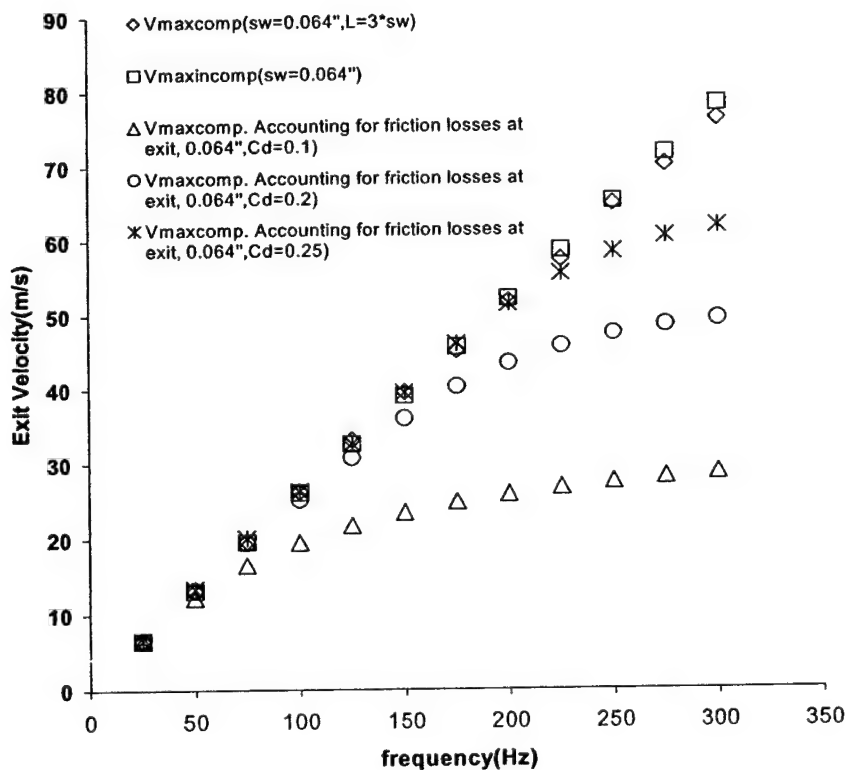
FIG. 8.29. Jet exit velocity comparison between incompressible and compressible cases with and without friction losses for slot width 0.064".

113

From the above plot, we can see that at lower frequencies, the effects of friction/viscous effects are smaller. At higher frequencies however, the viscous effects predominate and need to be considered while modeling the SJA. Also, the variation of jet exit velocity with C_d was presented above and the jet exit velocity decreased drastically with decrease in C_d at higher frequencies suggesting that lower values of C_d represent very high viscous losses and flow separation effects at the exit.

Figure 8.29 represents the variation of jet exit velocity between the incompressible case, the theoretical compressible model without accounting for friction losses and the model accounting for friction/viscous losses, a slot width 0.064" inches. As stated previously, the same observation that friction and viscous effects predominate at higher frequencies than at lower frequencies is observed in Figure 8.29. The comparison of viscous effects between the two slot widths itself is made in Figure 8.31. Also, the same trend of the jet exit velocity variation with C_d is observed with the larger slot as the smaller slot. The smaller C_d values correspond to larger viscous losses and separation effects at the exit slot plane.

Figure 8.30 represents the variation of jet exit velocity with slot width for the compressible theoretical model without accounting for friction losses and the model accounting for friction losses at the exit. This plot assumes a C_d value of 0.25. It can be seen from Figure 8.30 that the smaller slot has higher viscous losses and flow separation effects compared to the larger slot. In fact, the larger slot exhibits very little viscous effects and the exit velocity between the compressible cases with and without friction match pretty well suggesting that we should consider the large viscous/ friction effects produced by a smaller slot while optimizing the design of the SJA. Also the viscous losses and flow separation effects predominate only at higher frequencies for both slots. For the smaller slot, the viscous losses start to dominate at around 100 to 125 Hz frequency whereas for the larger slot, the viscous losses start surfacing only at frequencies as high as 200 to 225 Hz.
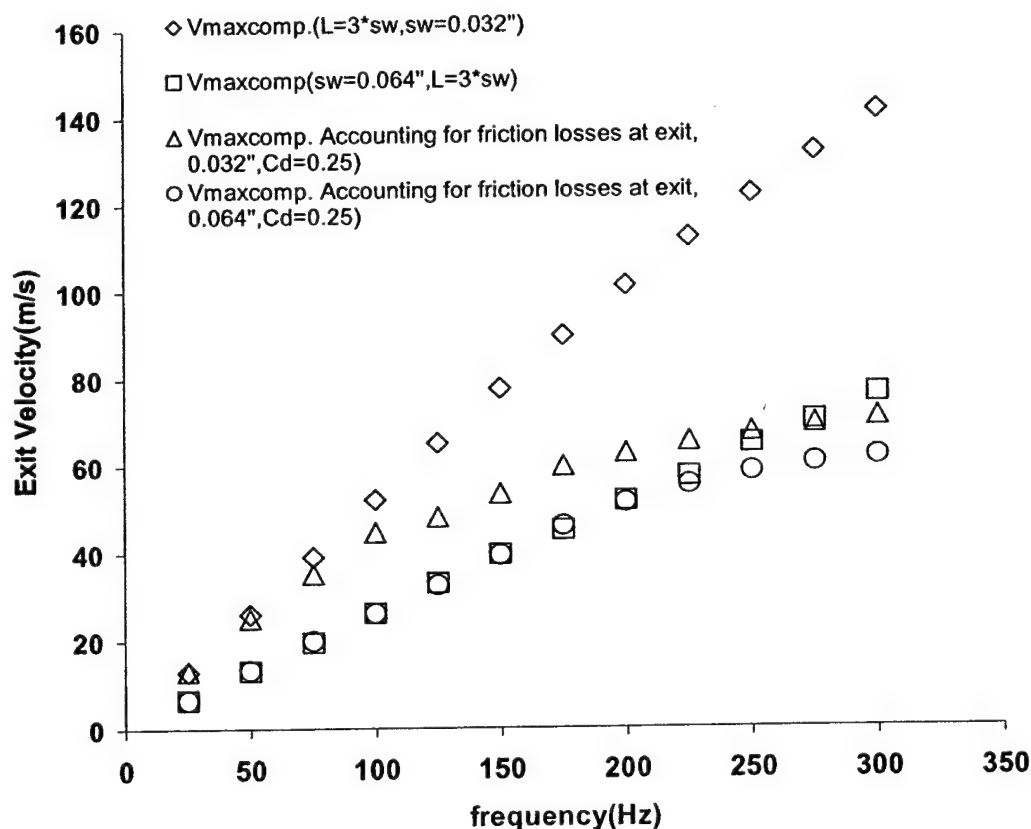
FIG. 8.30. Variation of jet exit velocity with slot width for the compressible case accounting for friction losses at exit.

114

Figure 8.31 represents the variation of exit velocity with cavity volume between the compressible case with and without accounting for friction losses, for a slot width 0.032 inches.

FIG. 8.31. Variation of jet exit velocity with cavity volume for the compressible case with and without friction for slot width 0.032".

As observed earlier, Figure 8.31 suggests that an increase in cavity volume reduces the velocity in both cases. This leads us to conclude that the viscous effects / friction effects are also more predominant in the case of a larger cavity. However, it is also observed that for the smaller slot, the cavity sizes tested do not show too much variation in jet exit velocity compared with the larger slot. Also at smaller frequencies, where the flow is more incompressible, the cavity volume does not have any effects on the jet exit velocity. These factors should be considered while designing the cavity for optimal performance of the SJA. Figure 8.32 represents the variation of jet exit velocity with cavity volume between the compressible case without accounting for friction and the compressible case accounting for friction losses, for a slot width 0.064".

As stated previously, the same trend is observed here. The larger cavity volume seems to show more viscous / friction effects. It should also be noted here that the larger slot shows more variation in jet exit velocity with cavity volume as compared to the smaller slot. A correct balance between the slot size and the cavity size needs to be made with the help of these plots that would maximize the jet exit velocity and also the flow reattachment performance using the SJA.

The influence of C_d on the jet exit velocity needs to be examined further. Currently, based on the information available, it has been concluded that a C_d value of around 0.2 seems to match the theoretical compressible case velocity well with the experimental value at a slot width of 0.032 inches and a C_d value of around 0.25 seems to match the theoretical compressible case velocity well with the experimental value at a slot width of 0.064 inches. The C_d is expected to be a function of the frequency and the geometry of the exit slot of the SJA. A more exhaustive study into the effects of the streamline curvature effects on the

115

exit slot velocity is required to understand this phenomenon thoroughly.

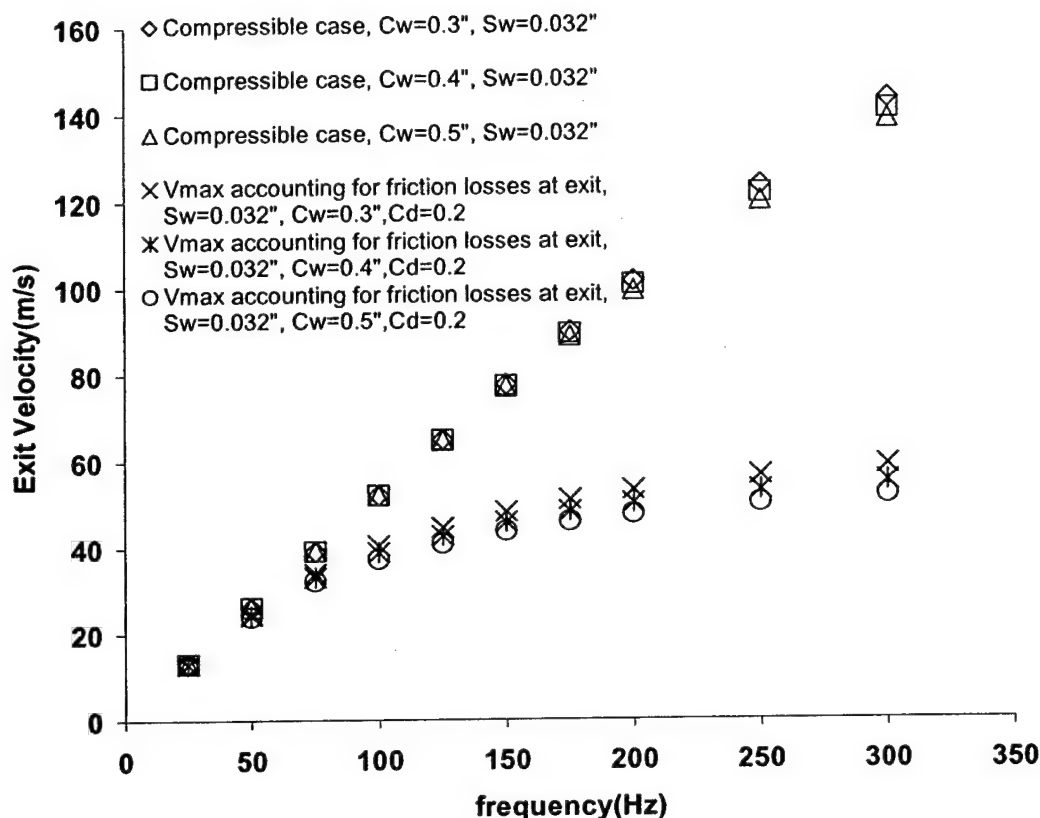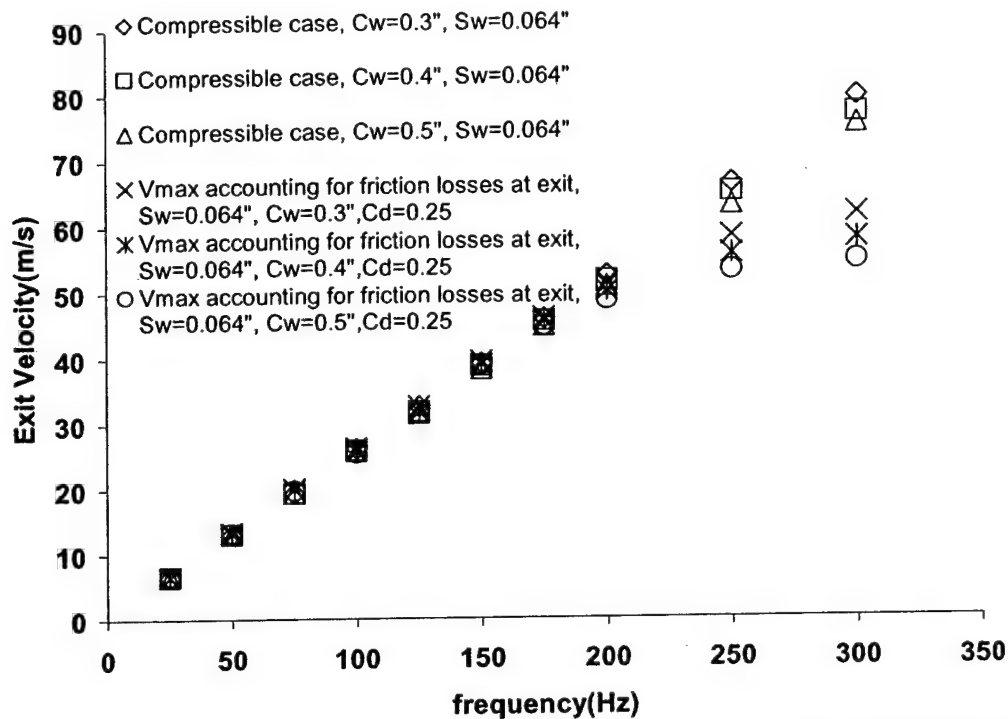FIG. 8.32. Variation of jet exit velocity with cavity volume for the compressible case with and without friction losses for slot width 0.064".

Model Validation

The theoretical models presented above provide a good insight into the effects of compressibility and viscosity at the exit slot on the performance of the SJA. The theoretical models are now validated by comparing them with hot-wire anemometer experiments performed under similar conditions. The accuracy of the current theoretical model developed in predicting the performance of any geometry/design of SJA is discussed later in this chapter.

For the purpose of validation, hot wire anemometer experiments were performed to measure the slot exit velocity under different test conditions to compare and validate with the theoretical models. A constant current hot wire anemometer setup is used to perform the experiments. The hotwire is first calibrated using a Barocell Pressure Standard calibrator. An overheat ratio of 1.7 was used for calibration.

Three different cavity volumes and two different slot widths were used for our experiments. The inside of the cavity where the air enters the slot was smoothened to minimize flow separation. Figures 2 and 3 represent the design of the cavity and exit slot respectively. Most previous researchers have used a circular orifice. This slot has a rectangular cross-section with a curved geometry at its end making the air gradually exit on to the wing surface tangentially and also this curvature minimizes separation effects at the exit slot.

The exit velocity is measured at the center of the exit slot. This is achieved by measuring the exit velocity at four different points along the slot width and the maximum of these velocities is taken as the velocity at the center of the slot. The anemometer is connected to an oscilloscope and the voltage fluctuation from the anemometer is recorded through the oscilloscope and this in turn is connected through a parallel port to the computer, where the voltage data is recorded as a function of time for different frequencies of oscillation of the motor using a data acquisition board in the computer. This voltage data is then reduced to velocity data using the calibration file generated earlier.

The frequency of the motor was varied from 0 to 150 Hz in steps of 25 Hz. The motor frequencies were not steady after 150 Hz. Hence this is the maximum frequency that was tested. The results of this experimental study are then compared with the theoretical models presented above to validate and

116

account for the compressibility effects of the jet at the exit slot. Figure 8.33 represents the comparison between experimental and theoretical incompressible and compressible case without accounting for friction at slot width 0.032 inches.
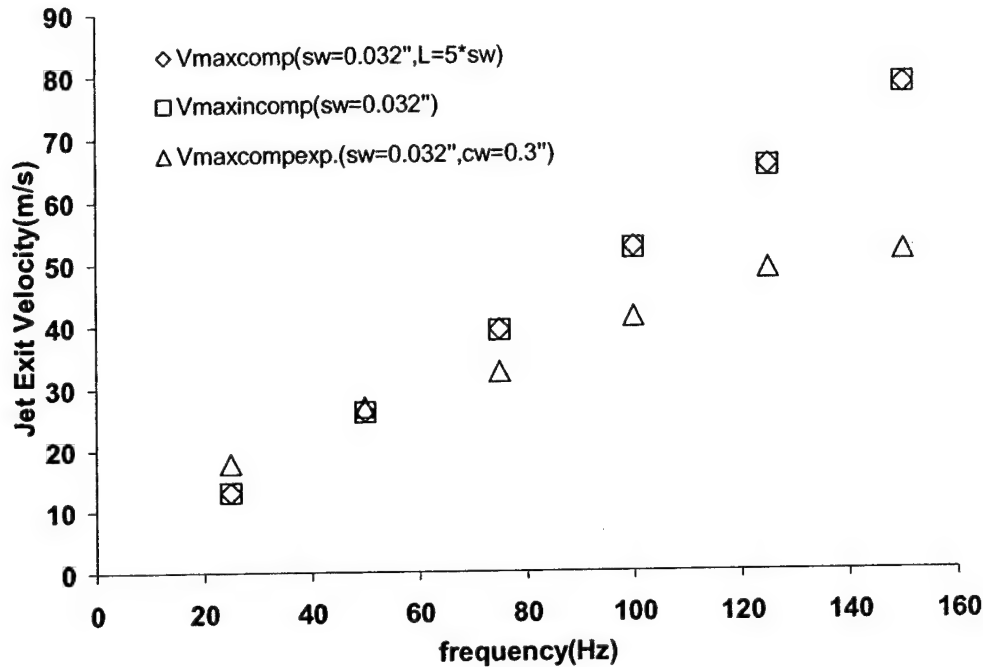
FIG. 8.33. Jet exit velocity comparison between experiment and theoretical compressible case without accounting for friction losses at slot width 0.032".

Figure 8.33 shows that the experimental jet exit velocity matches the theoretical case reasonably well at smaller frequencies as expected where the compressibility and the friction / viscous effects are negligible. At higher frequencies however, the friction effects predominate and need to be compared with the model that accounts for friction losses at the exit. Figure 8.34 represents the comparison between experimental and theoretical incompressible and compressible cases without accounting for friction at slot width 0.064 inches.

Based on Figure 8.34, it can be seen that the compressibility effects and friction loss effects are not too predominant for the larger slot width when compared to the smaller slot. The discrepancy of the experimental velocity being slightly higher than the theoretical compressible case may be attributed to errors involved while conducting the experiment. The hot-wire anemometer damping and inability to exactly measure at the center of the slot may be factors that need to be considered while conducting the experiment and accounting for the discrepancies. Figure 8.35 compares experimental results and theoretical compressible results with and without accounting for friction losses at exit for slot width 0.032 inches.
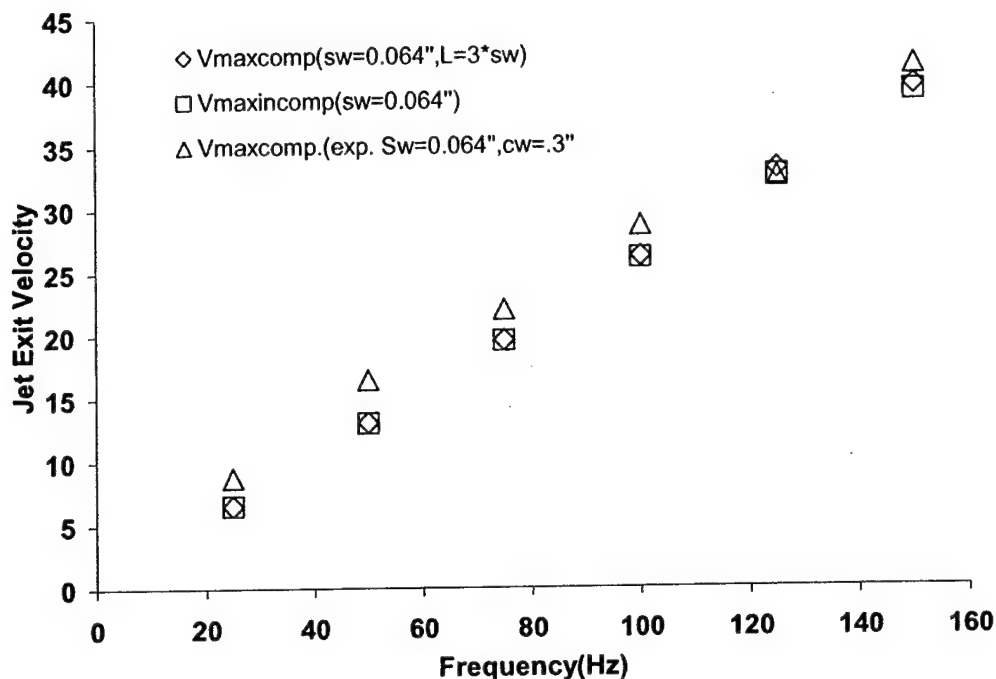
FIG. 8.34. Jet exit velocity comparison between experiment and theoretical compressible case without accounting for friction losses at slot width 0.064".
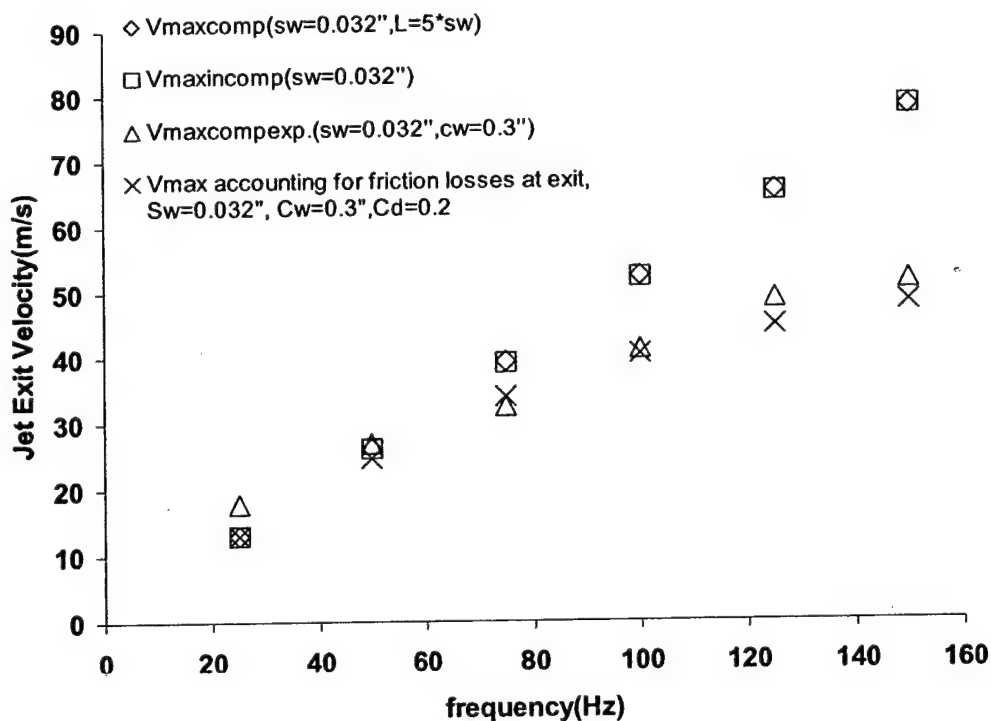
FIG. 8.35. Jet exit velocity comparison between experimental and theoretical compressible cases with and without accounting for friction losses at exit for slot width 0.032".

It can be seen from Figure 8.35 that a C_d value of 0.2 for the theoretical model accounting for friction losses at the exit seems to predict the exit velocity within a good accuracy of the experimental case. Further it is observed that this smaller slot shows more friction loss / viscous effects than the larger

118

slot, which is reproduced by the experimental results. At smaller frequencies however, the experimental jet velocity behaves similar to the incompressible velocity, as expected. Figure 8.36 compares experimental results and theoretical compressible results with and without accounting for friction losses at exit for slot width 0.064 inches.
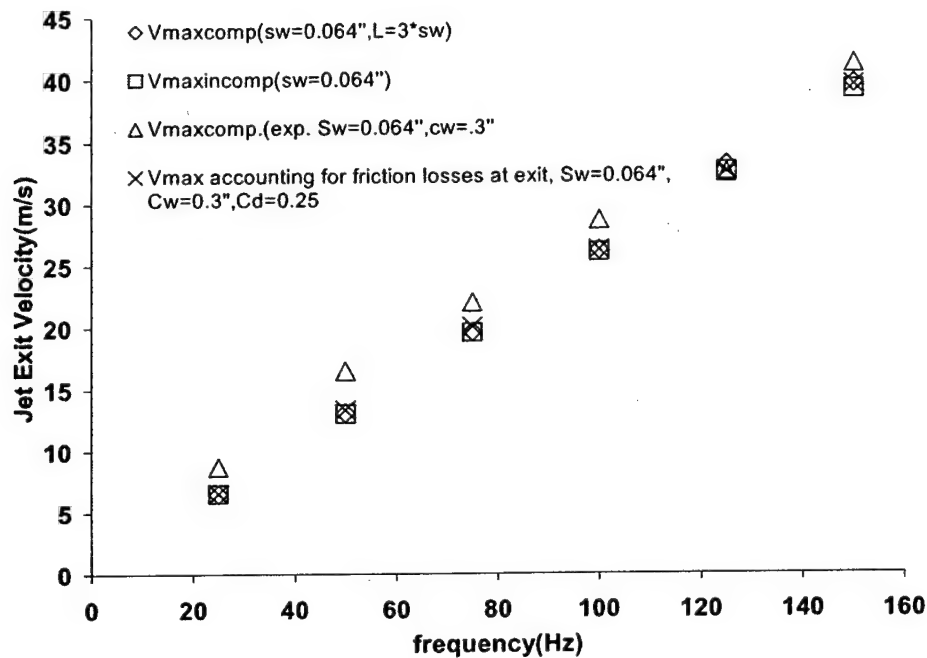
FIG. 8.36 . Jet exit velocity comparison between experimental and theoretical compressible cases with and without accounting for friction losses at exit for slot width 0.064".
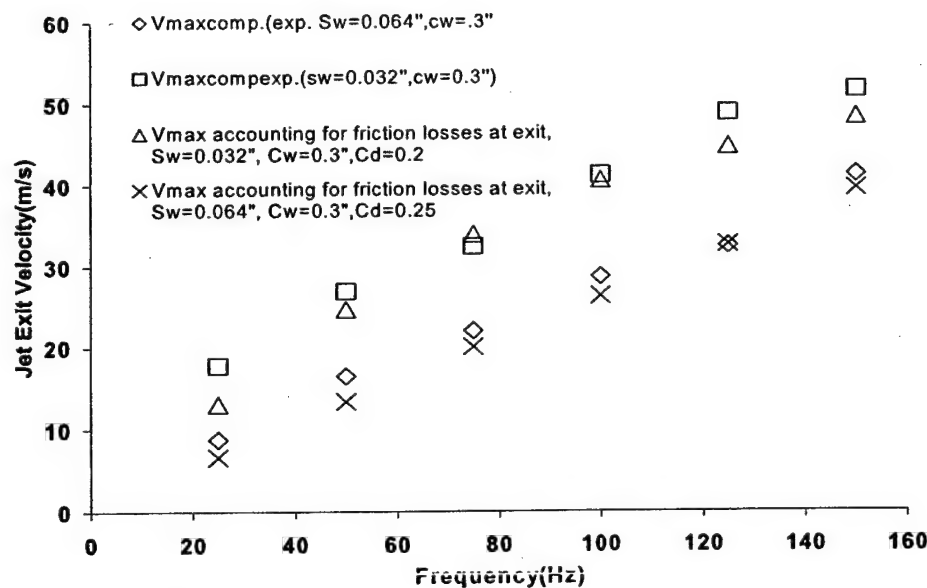
FIG. 8.37. Variation of jet exit velocity with slot width for experimental study and the theoretical compressible model accounting for friction losses.

As in the previous case, the experimental velocity is compared to the theoretical model accounting for friction losses and a C_d value of 0.25 predicts the experimental velocity to a good

119

accuracy. As stated earlier though, the compressibility and the friction losses effects are less predominant in the larger slot when compared to the smaller slot, which is proven by the experimental results too.

Figure 8.37 represents the variation of exit velocity with slot width for the experimental study and the theoretical model accounting for friction losses at exit. Figure 8.37 shows that, as expected, both the theoretical and experimental models predict the larger slot to have a smaller velocity. Also, the smaller slot seems to exhibit more friction losses and compressibility effects when compared to the larger slot. At smaller frequencies however, both the slot widths behave very close to the incompressible case. These factors have to be considered while designing the slot geometry/size of the SJA.

Figure 8.38 represents the variation of exit velocity with cavity volume for both the experimental study and the theoretical compressible model accounting for friction losses at the exit for slot width 0.032 inches. Based on Figure 8.38, it is seen that as predicted by the theoretical model, the higher cavity volume produces the smaller jet velocity and hence shows more compressibility effects and also shows more friction loss / viscous effects compared to the smaller cavities. This needs to be considered while designing the cavity of the SJA. At lower frequencies however, as stated earlier, the cavity volumes tested do not have much of an effect on the jet exit velocity. It should however be noted here that with the current DC motor-driven actuator, the SJA can be operated at higher frequencies producing a higher velocity of the jet thus necessitating the need for study of cavity volume effects on the performance of the SJA.
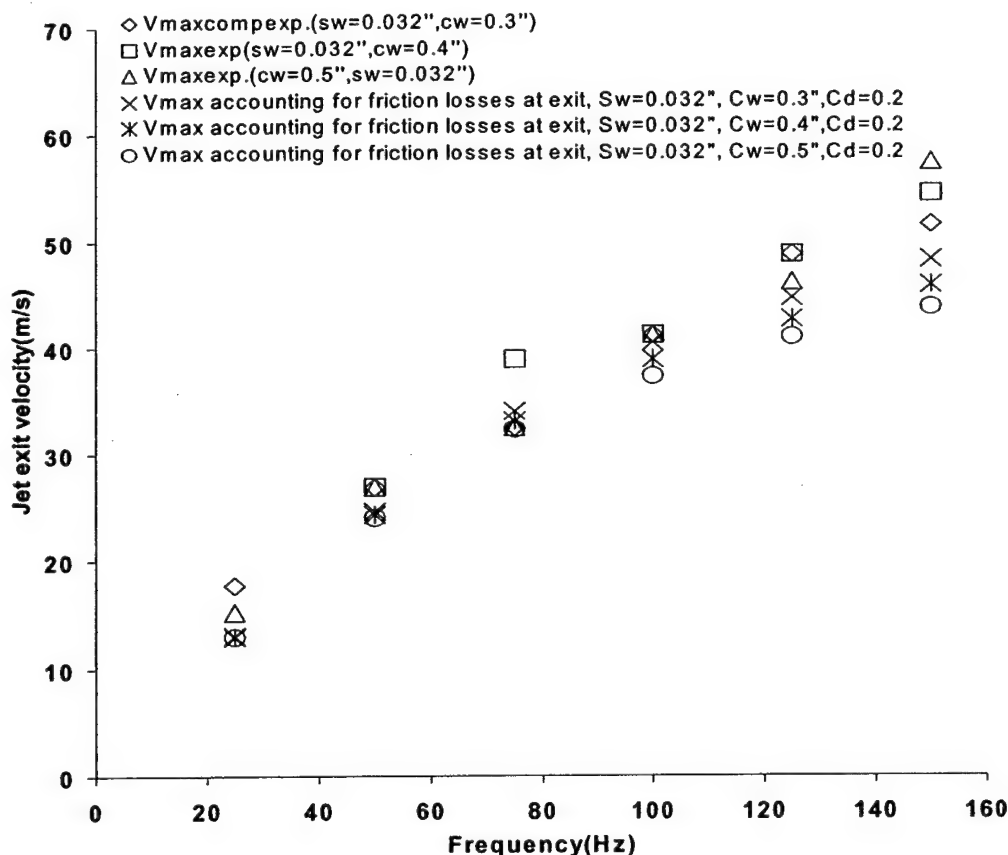
FIG. 8.38. Variation of exit velocity with cavity volume for the experimental study and the theoretical compressible model accounting for friction losses for slot width 0.032".
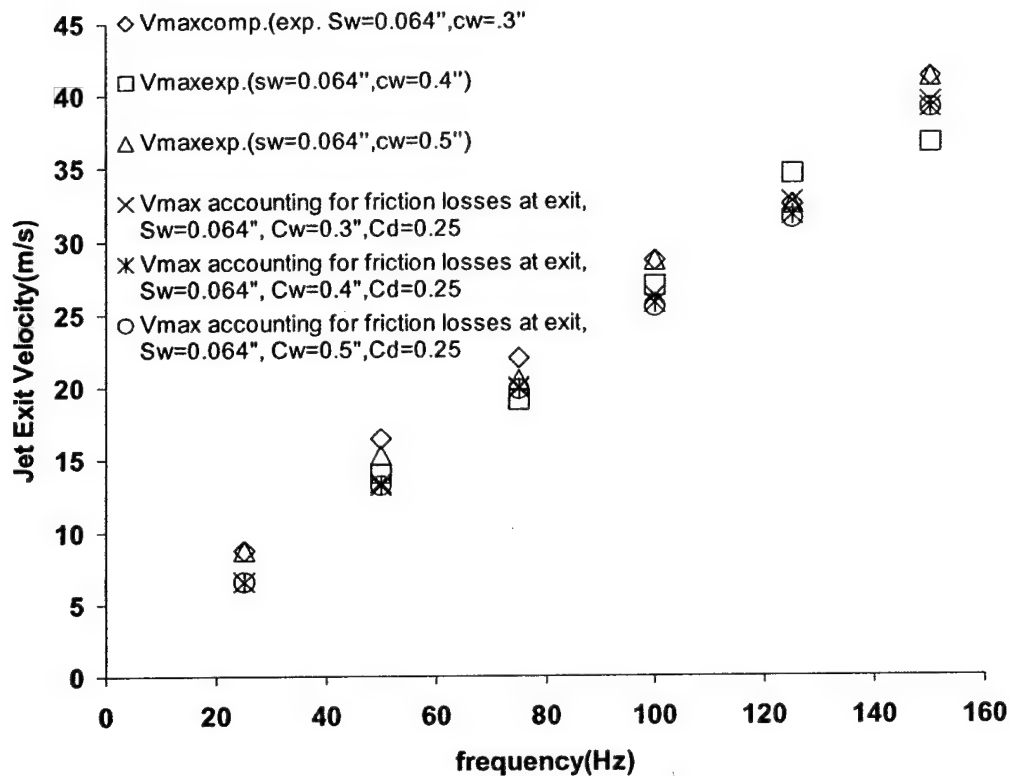
FIG. 8.39. Variation of exit velocity with cavity volume for experimental study and theoretical compressible model accounting for friction for slot width 0.064".

Figure 8.39 represents the exit velocity variation with cavity volume between the experimental case and the theoretical compressible case accounting for friction for slot width 0.064 inches. As stated earlier, Figure 24 suggests that a larger cavity volume produces a smaller velocity as predicted by the theoretical model indicating that the smaller cavity is desirable to produce larger velocities, which achieve more efficient flow reattachment. The above analysis can also be used to optimize the design of the SJA to identify what slot width and cavity volume combination will maximize the blowing momentum coefficient to allow complete flow reattachment. Also, the geometry of the exit slot needs to be changed to see what effects different slot geometry with minimal viscous effects and separation effects would have on the exit velocity.

9. MODELING AND CONTROL OF THE AERODYMANICS

In this section, we discuss the on-going efforts in designing the control laws for hinge-less wing control. We particularly discuss the control methodologies to generate a desired pitching moment at a particular angle of attack. The main challenge in designing the control methods for the SJA wing is the unknown input-output mapping. Different methods have been discussed in the literature to model the dynamic wing motion but all of these methods are complicated and can present difficulties when incorporated with aircraft equations. In the present investigation, we use a non-parametric approach to model the unknown wing dynamics. In the last two decades, Radial Basis Function based neural networks have emerged as powerful tools for continuous function approximation as well as dynamical system approximation.

The RBFN (Radial Basis Function Network) technique consists of approximating a non-linear function as the weighted sum of a set of radial basis functions, mainly Gaussian density functions, because their response can be confined locally without altering the global mapping:

$$g(\mathbf{x}) = \sum_{k=1}^{N} w_k \phi_k + a + \mathbf{b}^T \mathbf{x} \qquad (9.1)$$

where ϕ_k is a radial basis functions with μ_k as the center of the kth radial basis function and is given by:

$$\phi_k = \exp(-\frac{1}{2}(\mathbf{x} - \mu_k)^T \mathbf{R}^{-1}(\mathbf{x} - \mu_k)) \qquad (9.2)$$

where $\mathbf{R}$ is a positive definite covariance matrix and is a measure of the spread of the function. For a Gaussian function we need to learn n parameters for μ_k, $n + \frac{n(n-1)}{2}$ for the covariance matrix $\mathbf{R}$ and 1 for its weight, for a total of $\frac{(n+2)(n+1)}{2}$ parameters for one Gaussian function.

The dimensionality of the RBFN is dictated by the total number of parameters required to approximate the given input-output data. The total number of parameters required is directly proportional to the size of the network. Different learning algorithms have been developed in the literature (Musavi et al., 1992; Tao, 1993) to learn these parameters. While all these methodologies are very effective, most of them suffer from the drawback of potential explosion in the number of basis functions needed to approximate the function behavior. The reason for this stems from the fact that, almost always, the radial basis functions are chosen to be circular. To overcome this problem, recently an "Intelligent" scheme known as *Directed Connectivity Graph Approach* (Singla et al., 2004) has been developed, that sequentially learns the orientation of the dataset in real time and changes the orientation of the basis functions themselves, along with the centers and widths of the basis functions. More details on the Directed Connectivity Graph Approach can be found in Singla et al. (2004).

To develop control laws for closed loop synthetic jet actuation, static experiments were first conducted to model the pitching moment coefficient of the wing section. Further, this model was then utilized to design control laws for set point tracking of the angle of attack. In the coming sections, we will present the formulation of two different control laws for synthetic jet actuation pitch control. The first formulation involves the design of a PID controller for set point tracking that is easy to implement and useful in gaining sufficient insight into the control related issues. The second formulation involves the design of model-error control synthesis (Nelson, 1997) based controller that could resolve the limitations faced with the PID controller. Before going into the details of control law formulation, we first present the results for static data modeling using the Directed Connectivity Graph approach.

Aerodynamic Model

For a fixed value of angle of attack and free stream velocity (20m/s), we varied the jet frequency from $30Hz$ to $100Hz$ in intervals of $10Hz$. Then keeping the free stream velocity constant, we varied the angle of attack from $17°$ to $23°$, in intervals of $2°$ and measured the pitching moment using the pyramidal force balance. Figure 9.1 shows the static pitching moment (in Nm) versus angle of attack (in degrees) for different SJA frequencies. As the available experimental data corresponds to static experiments, we model the pitching moment coefficient as a function of angle of attack and jet frequency:

$$C_M = g(\alpha, f)$$

The Directed Connectivity Graph algorithm mentioned earlier was used to approximate the static pitching moment data. The method introduces a network of locally valid approximations of the output variables (in our case C_M) in the space of the input variables (in our case α, f). The result is a global family of locally valid least square approximations that are averaged in such a way that global piecewise continuity results. Details can be found in Singla et al. (2004). To invoke the directed connectivity graph approach, we divide the input space into a 2×2 grid and finally pick up **8 basis functions** to approximate the experimental data.

Figure 9.2 shows the variation of modeled and experimental moment data for various actuation frequencies. From these figures it is clear that we were able to model the static pitching moment data $(M/2/U^2)$ within experimental error tolerances. It is important to mention that we required only **8 Gaussian functions** to model the static pitching moment data although very few data points (total 36) were available for modeling. As needed, better modeling accuracy can be achieved by increasing the number of functions. We can use this RBFN model to compute the slopes of pitching moment with respect to angle of attack and SJA frequency at different operating points thereby enabling us to perform quasi-steady control of the SJA wing.
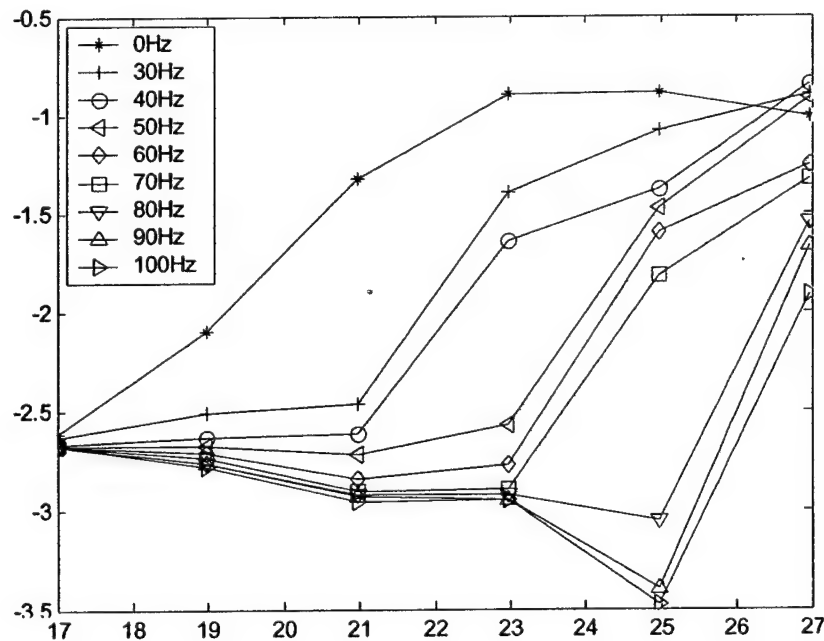
Fig. 9.1. Static pitching moment (in Nm) versus angle of attack (in degrees) for different SJA frequencies.

123

Control Law Formulation: PID Controller

The equation of motion for a leading-edge SJA controlled, free-to-pitch wing can be represented as:

$$I\ddot{\alpha} = M(\alpha, f) - M_0 \qquad (9.3)$$

where I is the moment of inertia of the wing about the pivot point, α is the angle of attack f is the SJA frequency and M_0 is the static moment acting due to the offset between the center of gravity of the wing and the pivot point. The nonlinear moment function $M(\alpha, f)$ is unknown and is modeled by RBFN as described in the previous section using static experimental data. However, the control variable f appears in a non-affine way that makes the control problem more difficult. To be able to characterize these and other nonlinear control effects better, we first investigate the efficacy of simple PID based fixed/scheduled gain controllers for quasi-steady control of the SJA wing in the wind tunnel. So, initially, the moment function is approximated by first order Taylor series expansion:

$$M(\alpha, f) \approx \bar{M} + C_{m_\alpha}\alpha + C_{m_f}f \qquad (9.4)$$

where, C_{m_α} and C_{m_f} represent the pitching moment slopes with respect to angle of attack, α and jet frequency, f, respectively. Approximate values for these slopes can be obtained from the RBFN fit of the data.

124
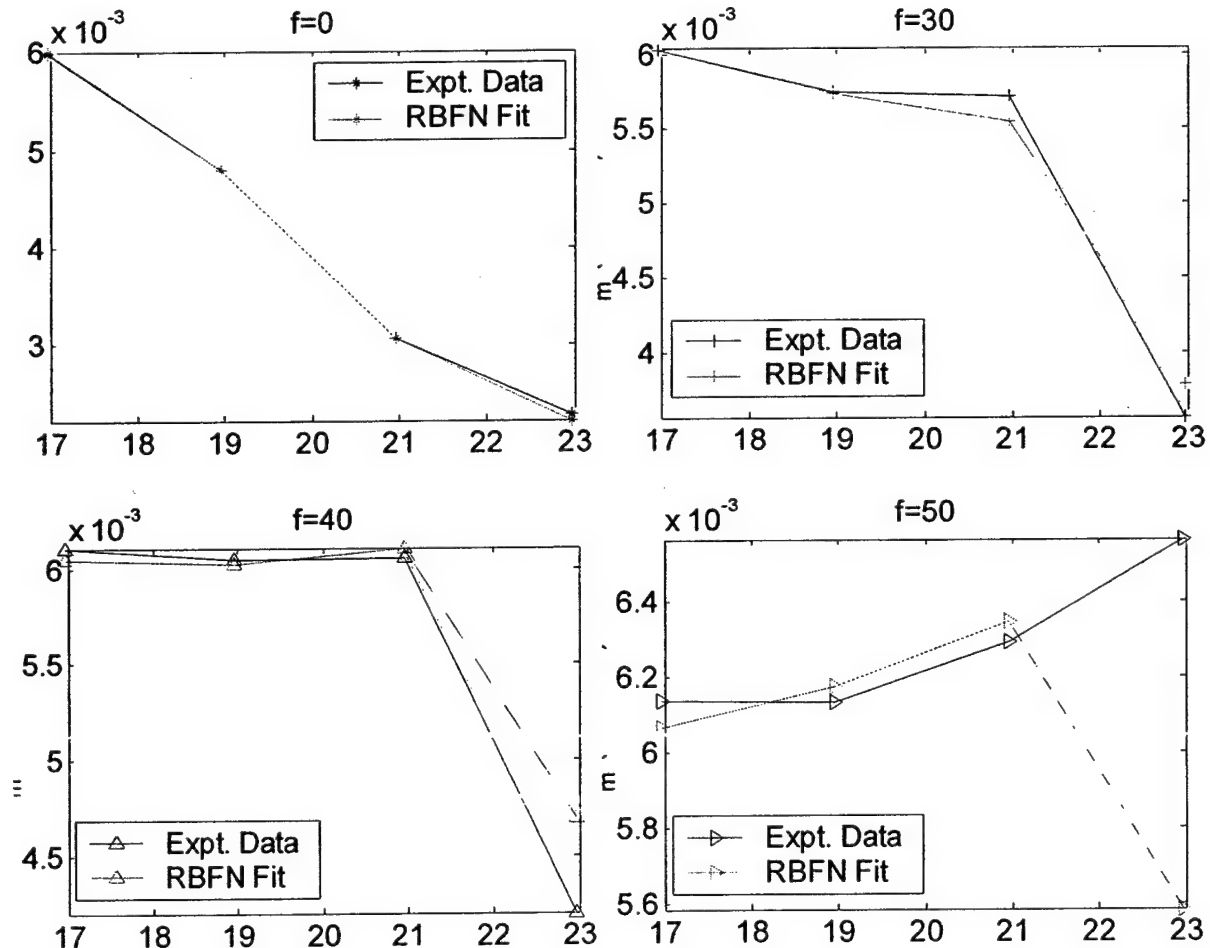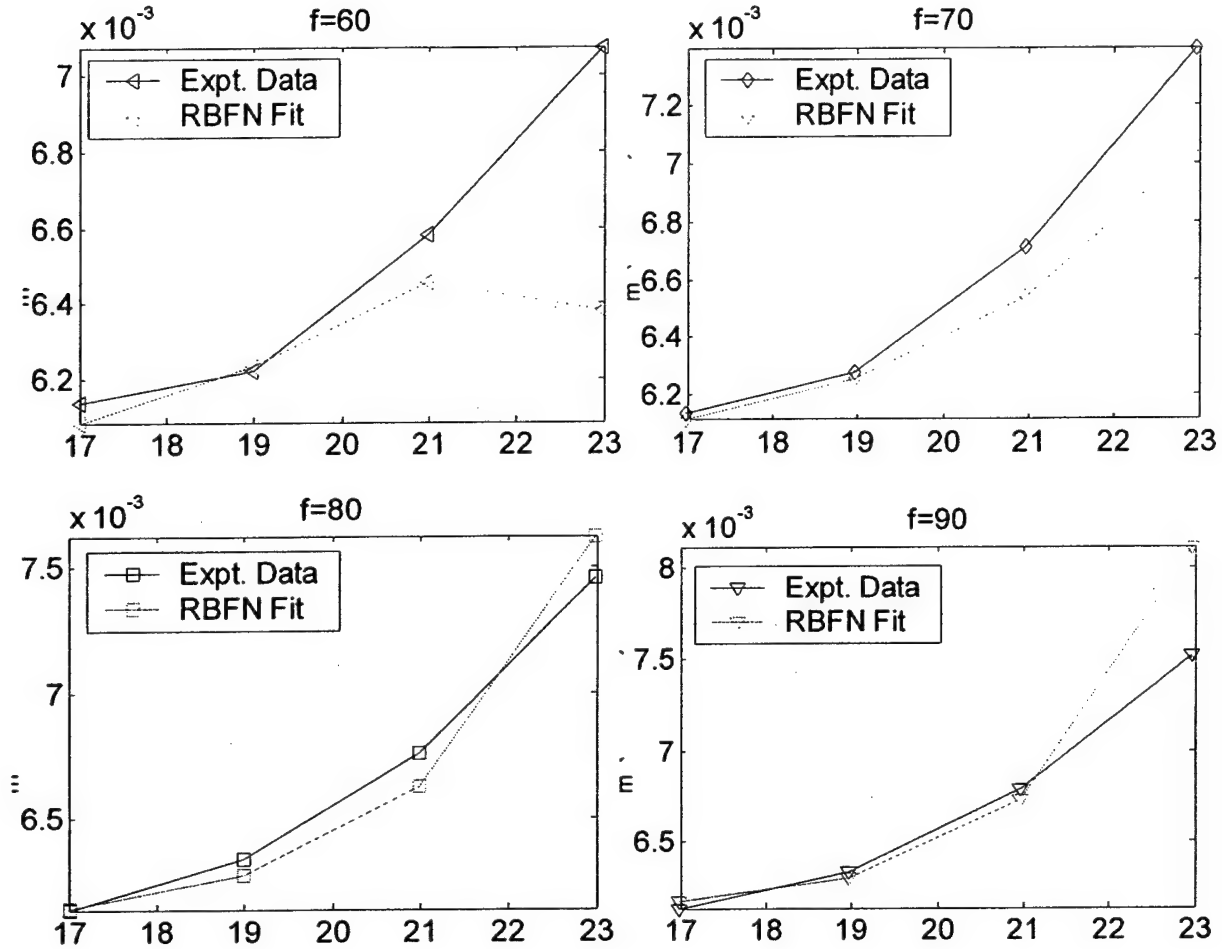
Fig. 9.2. Static pitching moment ($M/2/U^2$) versus angle of attack (in degrees) for different actuation frequencies (in Hz).

Now, substitution of equation (9.4) into (9.3) yields:

$$I\ddot{\alpha} = C_{m_\alpha}\alpha + C_{m_f}f - M_0 \qquad (9.5)$$

It is important to mention that M_0 in the above equation also includes the effect of the $\bar{M}$ term (pitching moment when $\alpha = f = 0$).

Now, the main control objective is to track a reference trajectory in terms of α_r which is at least twice differentiable with respect to time (so $\dot{\alpha}_r, \ddot{\alpha}_r$ can be determined). The reference trajectory can be designed as a step function from one angle of attack value to another or a smooth 5th order polynomial, so that any "jerking" is minimized.

Let us define e as the error between the actual and the reference angle of attack:

$$e = \alpha - \alpha_r \qquad (9.6)$$

Now, differentiating twice equation (9.6) and further substituting for $\ddot{\alpha}$ from equation (9.5) yields the following equation for the error dynamics:

$$\ddot{e} = \frac{C_{m_\alpha}}{I}\alpha + \frac{C_{m_f}}{I}f - \frac{M_0}{I} - \ddot{\alpha}_r \qquad (9.7)$$

Adding and subtracting $\dfrac{C_{m_\alpha}}{I}\alpha_r$ to the right hand side, we get:

$$\ddot{e} = \frac{C_{m_\alpha}}{I}e + \frac{C_{m_f}}{I}f + \left(\frac{C_{m_\alpha}}{I}\alpha_r - \frac{M_0}{I} - \ddot{\alpha}_r\right) \qquad (9.8)$$

Now, we write the commanding actuation frequency signal as a summation of two components, $f = f_1 + f_2$ where the first component performs PID control on the tracking error:

$$f_1 = -K_1\int e\,dt - K_2 e - K_3\dot{e} \qquad (9.9)$$

and the second component of the control performs dynamic inversion to cancel the known nonlinear terms $\left(\dfrac{C_{m_\alpha}}{I}\alpha_r - \dfrac{M_0}{I} - \alpha_r\right)$,

$$f_2 = -\left(\frac{C_{m_\alpha}}{C_{m_f}}\alpha_r - \frac{M_0}{C_{m_f}} - \frac{I}{C_{m_f}}\ddot{\alpha}_r\right) \qquad (9.10)$$

Substitution for f in equation (9.8) yields the following expression for the closed-loop error dynamics:

$$\ddot{e} + \left(\frac{C_{m_f}K_3}{I}\right)\dot{e} + \left(\frac{C_{m_f}K_2}{I} - \frac{C_{m_\alpha}}{I}\right)e$$
$$+ \left(\frac{C_{m_f}K_1}{I}\int e\,dt\right) = 0 \qquad (9.11)$$

Further, introducing the new state variables $z_1 = \int e\,dt, z_2 = e$ and $z_3 = \dot{e}$, we can re-write equation (9.11) as:

$$\dot{z} = Az \qquad (9.12)$$

where,

$$\mathbf{z} = \{z_1 \quad z_2 \quad z_3\}^T$$

$$\mathbf{A} = \begin{bmatrix} 0 & 1 & 0 \\ 0 & 0 & 1 \\ -\dfrac{C_{m_f} K_1}{I} & \left(-\dfrac{C_{m_f} K_2}{I} + \dfrac{C_{m_\alpha}}{I}\right) & -\dfrac{C_{m_f} K_3}{I} \end{bmatrix} \quad (9.13)$$

The asymptotic stability of the closed loop system corresponds to having the eigenvalues of matrix $\mathbf{A}$ (given by equation 9.13) in the left half-plane. Further, using the Routh-crieteria, the following conditions can be easily obtained, in order for the eigenvalues of $\mathbf{A}$ to lie in the left half-plane:

$$C_{m_f} K_1 > 0, \quad \left(C_{m_f} K_2 - C_{m_\alpha}\right) > 0, \quad C_{m_f} K_3 > 0$$

$$K_2 C_{m_f} - C_{m_\alpha} - \frac{K_1}{K_3} > . \qquad (9.14)$$

Since $C_{m_f} > 0$ (moment increases with the jet frequency), K_1, K_3 should be greater than zero and $K_2 > \dfrac{C_{m_\alpha}}{C_{m_f}}$. Thus, by making a judicious choice for the various gains, asymptotic tracking of the reference trajectory could be achieved.

The above control law assumes that C_{m_α} and C_{m_f} are known accurately so that the dynamic inversion component of the control law can cancel out the terms $\left(\dfrac{C_{m_\alpha}}{I}\alpha_r - \dfrac{M_0}{I} - \ddot{\alpha}_r\right)$. But that is not the case in reality and hence to handle any disturbance due to modeling errors we can design indirect adaptation laws for C_{mD} and C_{m_f} as discussed in Subbarao (2001). Further, from Figures 9.1, 9.2 it is apparent that C_{mD} itself is a function of angle of attack, α, and jet actuation frequency, f. To deal with that we need to schedule the gains, i.e. we need to choose different values of controller gains depending upon the value, particularly the sign, of C_{mD} as it is difficult to meet the conditions listed in equation (25) for different values of C_{mD}. However, scheduling of gains for different values of C_{mD} corresponds to switching to different controller, which is difficult to do as we do not know in advance how many times we will need to perform the switching. Beside all this, a PID controller requires the knowledge of the rates of angle of attack, which are not being directly measured in the current set up. To obtain estimates of the rate of change of angle of attack, we need to use a first order lead filter or a first/second order difference of the filtered angle of attack measurements as discussed in Singla et al. (2004) which may cause system instability if the values of the gains are not robust enough to take care of measurement errors.

Control Law Formulation: Model Error Control Synthesis

In the previous section, we discussed the PID controller design for the synthetic jet actuation by generating a linear model from the nonlinear model learnt by RBFN. But this procedure did not work as the pitching moment slope, C_{mD} not only changes with angle of attack but its sign also changes due to flow separation at low actuation frequencies (Figure 9.1), which the linear model was not able to capture.

127

So it becomes necessary to use a model which can capture the points where the flow separate. Secondly the model learnt by RBFN is actually not a dynamical model so it becomes difficult to come up with a range of stabilizing gains. Therefore, we need to concentrate on the nonlinear control system design problem, which can also deal with large uncertainties in the model dynamics. So we decided to adopt a model error control synthesis (MECS) approach (Crassidis, 1999), which can take care of large model errors too. The approach presented in this section is not a new control scheme but is a combination of some existing control techniques.

Again, the equation of motion for a SJA controlled, free to pitch wing can be represented as:

$$I\ddot{\alpha} = M(\alpha, \omega) - M_0 \qquad (9.15)$$

where I is the moment of inertia of the wing about the pivot point, α is the angle of attack, is the SJA frequency and M_0 is the static moment acting due to the offset between the center of gravity of the wing and the pivot point.

The nonlinear moment function $M(\alpha, \omega)$ is unknown and can be learnt online/off-line by RBFN as described in the previous sections. However, the main problem in RBFN modeling is that now the control variable appears in a non-affine way which makes the control problem more difficult. We can use the sliding mode predictive controller for non-affine control system design, but due to lack of literature on non-affine control system design we first decided to make the control variable affine. Therefore, we approximate the static moment data by the following nonlinear model instead by RBFN:

$$I\ddot{\alpha} = \left(f(\alpha) + g(\alpha)\omega\right)V^2 - Wl\cos(\alpha) \quad (9.16)$$

where, $f(\alpha)$ and $g(\alpha)$ are third order polynomials (given by equation (9.17)) of the angle of attack, W is the weight of the wing and l is the distance between c.g. and pivot point:

$$f(\alpha) = a_0 + a_1\alpha + a_2\alpha^2 + a_3\alpha^3$$
$$g(\alpha) = b_0 + b_1\alpha + b_2\alpha^2 + b_3\alpha^3 \qquad (9.17)$$

Further, we use the method of Gaussian Least squares to determine the various coefficients of $f(\alpha)$ and $g(\alpha)$. Figure 9.3 shows the variation of modeled (by polynomials and RBFN) and experimental moment data for various actuation frequencies. From this figure it is clear that even though the polynomial fit is able to capture the flow separation points (where the sign of $C_{m\alpha}$ changes), RBFN capture the behavior with higher accuracy.

128
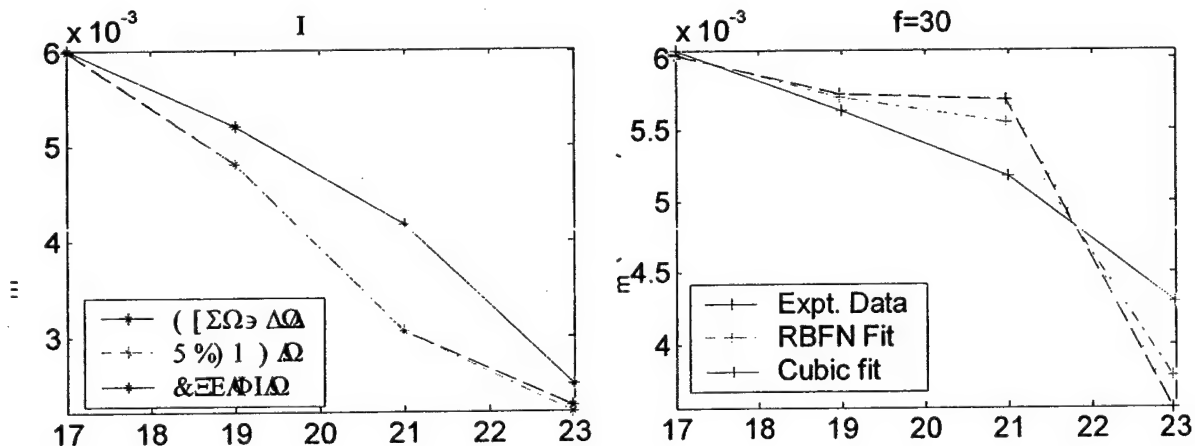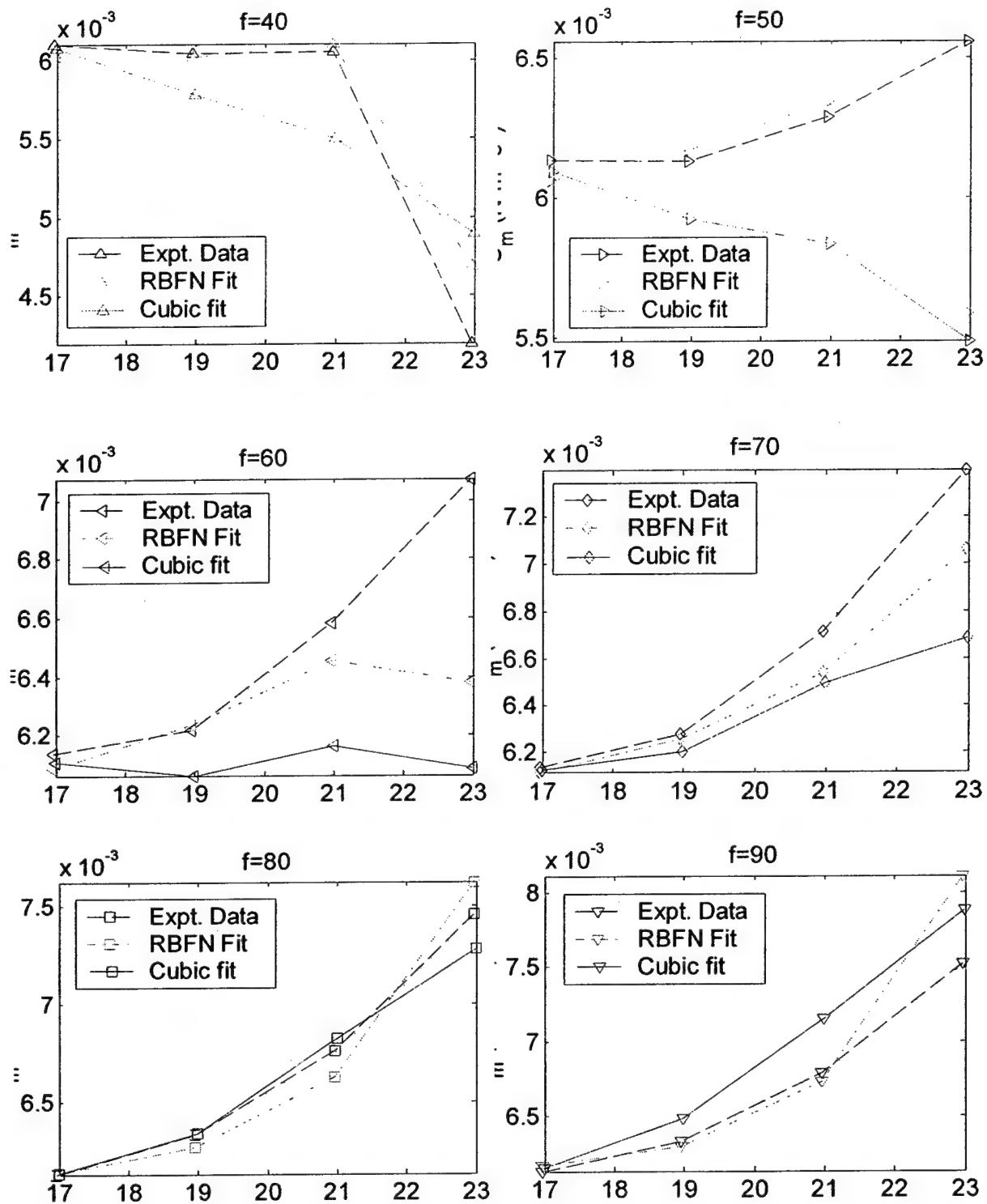
Fig. 9.3. Static pitching moment Coefficient versus angle of attack (in degrees) for different actuation frequencies.

The first step in the MECS approach is to find the value of nominal control based upon the best-known model. We will use the sliding mode concept to come up with the value of nominal controller as sliding mode control methodology itself can take care of small model errors. So first we define the error sliding surface as:

$$s \left(\frac{d}{dt} \; \lambda \right) e \qquad (9.18)$$

where, $e = \alpha - \alpha_r$ is the tracking error. Now, we choose the nominal value for jet actuation frequency, $\bar{\omega}$ so that:

$$\dot{s} = -\eta s, \qquad \eta > 0 \qquad (9.19)$$

After carrying out some mathematical manipulations, we come up with the following value for $\mathcal{Z}$:

$$\bar{\omega} = \frac{I}{V^2 g(\alpha)} \; [-\frac{V^2}{} f(\alpha) + \frac{Wl}{I} \cos \alpha$$
$$- \lambda \dot{e} + \ddot{\alpha}_r - \eta sat \left\{ \frac{s}{\rho} \right\} \qquad (9.20)$$

where *sat* is a saturation function given by:

$$sat(y) = y \qquad \text{if } \|y\| \le 1$$
$$sat(y) = \frac{y}{\|y\|} \qquad \text{otherwise} \qquad (9.21)$$

Further, parameter U dictates how much tracking error we can tolerate. This parameter is very useful in the presence of model error. It should be also noticed that $(1 + \lambda)$ acts as a damping parameter and $\eta \lambda$ is a kind of proportional gain.

The second step in controller design is to find the value of jet actuation frequency ($\Delta \omega$) to take care of nominal model error which we do by minimizing the error between available measurement i.e. $\tilde{\alpha}$ (t) and predicted measurement by nominal model i.e. $\alpha(t)$:

$$J = \frac{1}{2} \left[\tilde{\alpha}(t + \Delta t) - \alpha(t + \Delta t) \right]^2 \qquad (9.22)$$

However, this function gives rise to a nonlinear optimization problem which can be converted to a linear optimization problem by writing the Taylor series expansion for $\alpha(t + \Delta t)$ up to second order.

$$\alpha(t + \Delta t) \approx \alpha(t) + \dot{\alpha}(t) \Delta t + \ddot{\alpha} \frac{\Delta t^2}{2} \qquad (9.23)$$

where $\ddot{\alpha}$ is given by equation (9.16). Now, making use of the necessary condition for minimizing the loss function J, i.e. $\frac{\partial J}{\partial \Delta \omega} = 0$, we find the following expression for $\Delta \omega$:

$$\Delta\omega(t) = \frac{2I}{g(\alpha)V^2\Delta t^2}[\tilde{\alpha}(t+\Delta t) - \alpha(t) - \dot{\alpha}(t) -$$
$$\frac{V^2\Delta t^2}{2I}(f(\alpha) + g(\alpha)\bar{\omega}) + \frac{Wl\Delta t^2}{2I}\cos\alpha] \qquad (9.24)$$

Therefore our total command signal for the actuation frequency at time t can be written as:

$$\omega(t) = \bar{\omega}(t) + \Delta\omega(t) \qquad (9.25)$$

But the value of $\Delta\omega(t)$ depends upon $\tilde{\alpha}(t+\Delta t)$ which is not available at time t. So for implementation's sake we introduce a delay in $\Delta\omega(t)$

$$\omega(t) = \bar{\omega}(t) + \Delta\omega(t-\Delta t) \qquad (9.26)$$

The stability proof for this control law can be found in Crassidis (1999). Further it is shown in the same reference that deliberate time delay introduced in equation (9.25) provides extra robustness. The main advantage of the update law given by equation (9.24) is that the system parameters need not be updated since their effects on the nominal system are used to update the nominal control value.

To test the control law we performed some computer simulations with our RBFN and polynomial learnt model. The control objective is to make $= 25^0$ the set point. Initially, the wing is assumed to be balanced at $= 17^0$. To make the simulations more realistic we use the RBFN learnt model as the true plant model and the polynomial model as the nominal known plant model. Beside this, we also constrained the jet actuation frequency to lie between 0 and 120 Hz. Figure 9.4 shows the plots of achieved and reference angle of attack, while Figures 9.5 and 9.6 show the rate of change of angle of attack and commanded jet frequency, respectively.
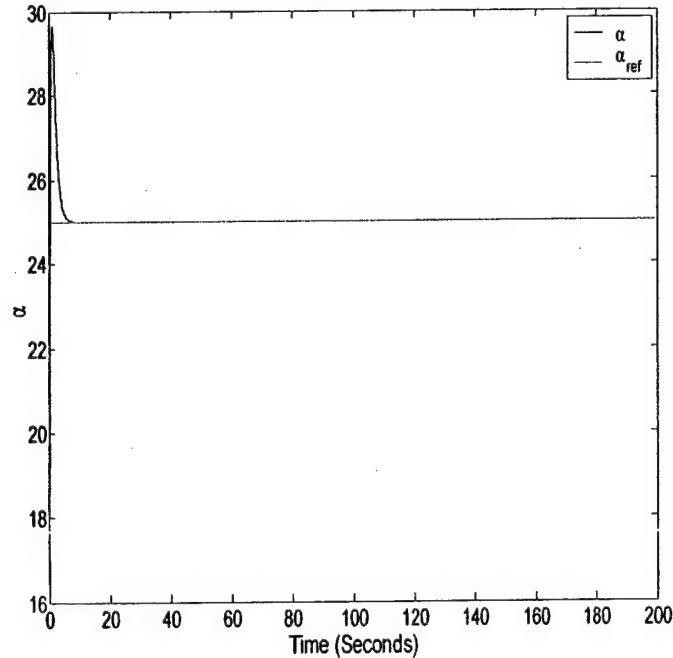
Fig. 9.4. Achieved and commanded angle of attack (in degrees) versus time (in sec).

131
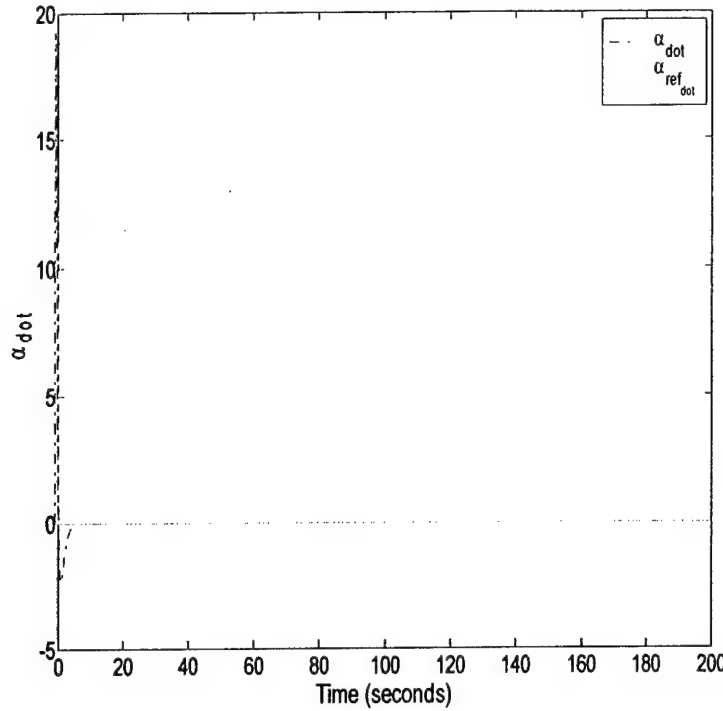
Fig. 9.5. Achieved and commanded angle of attack rate (in deg. per second) versus time (in sec).

From the figures it is clear that even in the presence of model error we were able to achieve the commanded angle of attack signal perfectly within 10 seconds.

Further, to make the simulations more realistic we put the following constraint on jet frequency due to hardware constraints:

$$\omega_{motor} = 0 \qquad if \ \omega \leq 10Hz$$
$$\omega_{motor} = 30 \qquad if \ 10 < \omega \leq 30Hz$$
$$\omega_{motor} = 120 \qquad if \ \omega \geq 120Hz$$
$$\omega_{motor} = \omega \qquad otherwise$$

Figure 9.7 shows the plots of achieved and reference angle of attack while Figures 9.8 and 9.9 show the rate of change of angle of attack and commanded jet frequency, respectively. From these plots it is clear that we are able to achieve the commanded angle of attack signal within a 0.5^0 error even in the presence of large model errors and constraints on jet actuation motor.

We finally mention that these simulation results form the basis for optimism but we are still facing some difficulties in implementing the control law in the wind tunnel. We should mention here that we heuristically demonstrated dynamic hingeless pitch control of the wing in the wind tunnel. We demonstrated control of two types of motion: (a) sinusoidal wing pitching of predetermined amplitude and (b) incremental, ramp-like changes of angle of attack from a current angle of attack to a different angle of attack. Since it was heuristic and not well documented, we are not presenting any data herein, but in the paper presentation we will show the video that illustrates the pitch control.

132

Fig. 9.6. Commanded actuation frequency (in Hz) versus time (in sec).

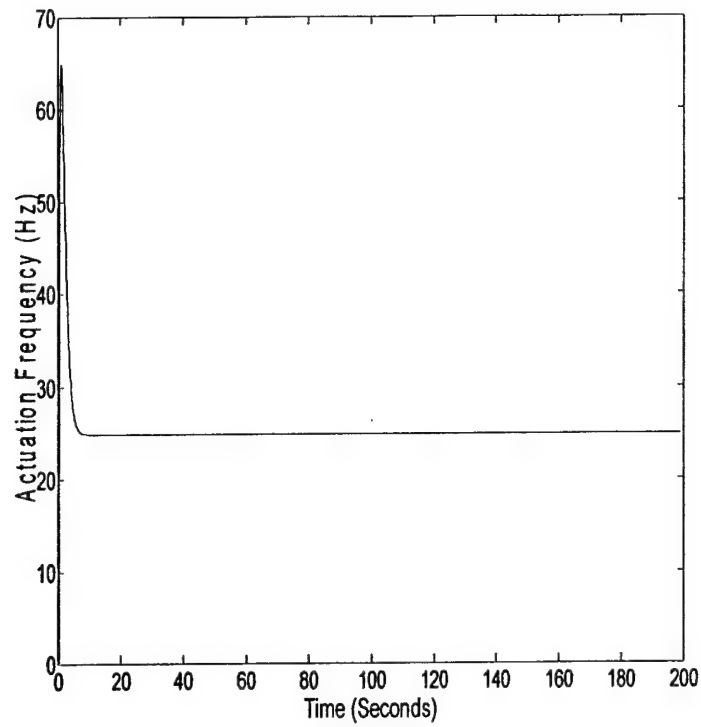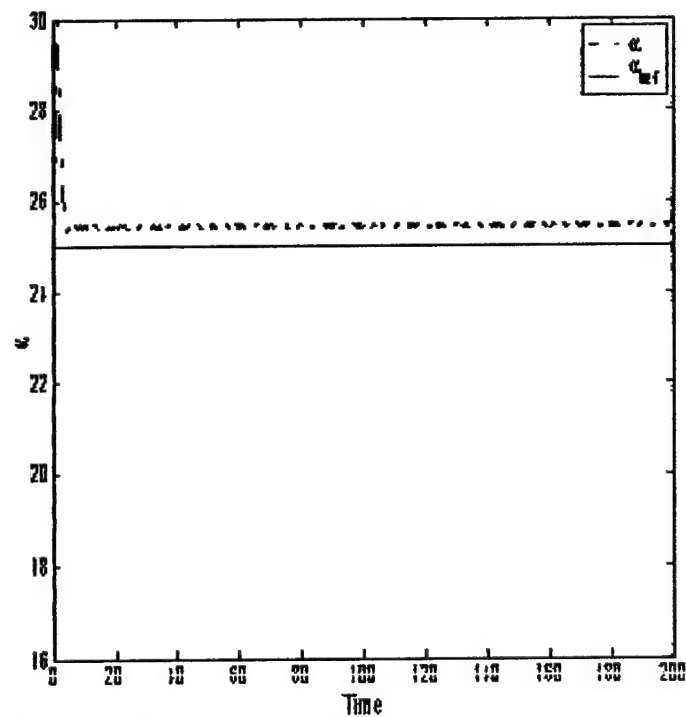Fig. 9.7. Achieved and commanded angle of attack (in degrees) versus time (in sec), with SJA motor constraints.
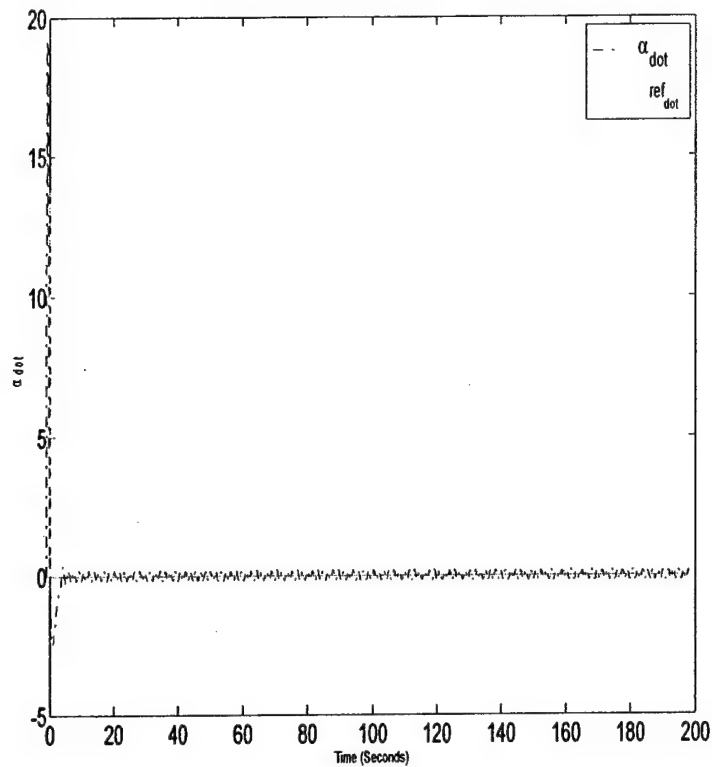
133

Fig. 9.8. Achieved and commanded angle of attack rate (in deg. per second) versus time (in sec), with sja motor constraints.
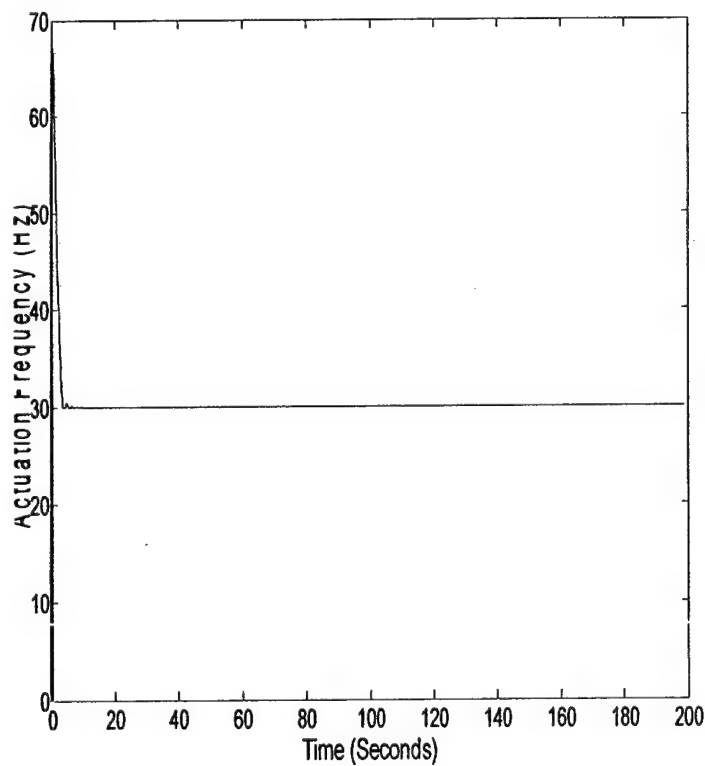

Fig. 9.9. Achieved SJA actuation frequency (in Hz) versus time (in sec), with SJA motor constraints.

134

10. SUMMARY AND CONCLUSION

This work presents an investigation of synthetic jet actuation for separation control over wings/airfoils, in steady and unsteady flows, the development of high-power, compact synthetic jet actuators (SJA) for flow separation control, the modeling and control of such actuators and the modeling and control of the resulting SJA-controlled aerodynamics and wing/airfoil, respectively.

The new developed actuator has oscillation amplitudes at least two orders of magnitude higher that those achieved by piezoceramics, and may be operated within a large frequency range without suffering deterioration of performance. The developed actuator is compact enough to fit in the interior of a NACA0015 wing with a chord of 0.375 m. Test bench experiments showed that the multi-piston actuator array was capable of producing exit velocities of up to 90 m/s for an actuator frequency of 130 Hz. The available power supply limited the operation of the actuator to a maximum frequency of 130 Hz. An increase in the available power would permit operation at frequencies with higher exit velocities. Hot-wire measurements at the exit of the initial design of the SJA plenum showed the existence of a strong interaction between the jets produced by the pistons due to the fact that they are out-of-phase. Extension of the walls separating the exits of each individual piston dramatically reduced this interaction. It was shown that the compressibility effects are also important for this type of actuators. These effects are higher as the actuator frequency increases, the exit slot width decreases and the combined plenum-cylinder internal volume increases.

The actuator was placed in a NACA 0015 wing and tested in a wind tunnel. An experimental investigation into the effects of a synthetic jet actuator on the performance of the wing was described. Emphasis was placed on the capabilities of the actuator to control the separation of the flow over the wing at high angles of attack. The investigation included the use of: force balance measurements, on-surface flow visualization with oil and tufts, off-surface flow visualizations with smoke, surface pressure distribution measurements and wake surveys. Most of the tests were performed at a freestream velocity of 35 m/s, corresponding to a Reynolds number of 8.96×10^5. The angle of attack (α) was varied from -2.0 to 29 degrees. For the tests presented here, at $\alpha < 10$ degrees the actuator tends to increase the lift curve slope as the actuation frequency is increased. For this range of α, static pressure distribution measurements showed that the SJA only affected the flow over the first 25% of the chord. At higher angles of attack, the SJA extends the range of α for which the wing may be operated without stalling. The use of the actuator causes an 80% increase in the value of CL_{max}, and the angle at which stall occurs is increased from 12 to 18 degrees. In this range of α, the effects of the SJA are global, i.e. the actuator affects the flow over the whole wing, including the flow over the pressure surface. The actuation frequency has a small effect over the pressure distribution in this range of α. For $\alpha > 18$ degrees, once massive stall has occurred over the wing, the operation of the SJA still provides a small amount of lift augmentation. At $\alpha > 25$ degrees, a large frequency of actuation is required to produce any noticeable effects. For this range of α, it was shown that the effect of the actuator once again became localized, affecting only the first 25% of the chord.

The operation of the SJA does not produce additional potential flow type lift; it only augments the available lift by delaying the occurrence of separation with its associated losses. The drag on the wing is decreased as a consequence of SJA actuation, this was verified with the force balance measurements and by analysis of the wake surveys. The basic wing showed a very docile stall, typical of thick airfoils with trailing edge separation, however, although its was shown that the stall mechanism for the wing with actuation was still a trailing edge stall, the characteristics of the stall mechanism was more similar to that of medium thickness airfoils, in which separation occurs rather abruptly. On-surface flow visualization performed at the exit of the actuator during operation without a freestream, showed evidence of the formation of streamwise vortices at the sides of each jet. No further evidence of these structures was found during operation of the actuators while the wind tunnel was on.

Subsequently a low speed wind tunnel investigation has been undertaken to determine the effect of Synthetic Jet Actuation on a airfoil performing a linear ramping motion. An instrumented NACA 0015 wing was ramped from zero to twenty seven degrees at various pitch rates during which surface pressures were recorded. The actuators frequency, slot exit width and rate of change of slot exit width were varied. Presented data included surface pressures as well as integrated parameters. The instantaneous behavior of

the synthetic jet was characterized using a Hot Wire Anemometer. The data indicated that small slot exit widths were prone to compressibility effects (reduced exit velocities), with driving frequency having a smaller, yet similar deleterious effect. The data shows that fluidic oscillation delays the onset of the dynamic stall vortex formation to higher wing incidence angles. When formed, the stall vortex appears to induce higher loading then in the unforced case. For low ramp rates with no synthetic jet actuation, a stall vortex was not observed. For the same motion, forcing caused stall vortex formation, presumably due to the ability of the forcing to control and structure the separating shear layer. Instantaneous velocities measured above the wing surface showed that for the SJA tested, the effect of the actuator was to directly inject momentum into the boundary layer.

Then an investigation was conducted to determine the effects of Synthetic Jet Actuators (SJAs) on a sinusoidally pitching wing. Experiments were performed in a low speed 3' by 4' wind tunnel at a chord Reynolds number of 0.57×10^6. The pitch motion consisted of a 12.5 deg amplitude centered around a 12.5 deg mean, yielding a sinusoidal pitch with a 25 deg peak to trough excursion angle. Pitch frequencies from 0.2 to 2.0 Hz were tested. During the dynamic motion, pressures were recorded around the wing using a high-speed pressure scanner connected to thirty-two tappings. Integration of these pressures yielded instantaneous lift and pitching moment. From the experimental data, the following conclusions are drawn. During the upstroke, at low pitch frequencies, the SJA delayed stall. As the frequency increased, the effect of the SJA compared to the unforced case diminished as the dynamic motion itself delayed the onset of stall. During the downstroke, the SJA significantly increased the angle of attack at which flow re-attachment was indicated, resulting in considerably smaller hysterisis loops. For the highest pitch frequency evaluated, the hysterisis loop was eliminated.

Subsequently modeling and control methodologies, for both controlling the DC motors driving the SJA as well as controlling the wing in free-to-pitch motions were developed. The leading-edge SJA was successfully modeled and controlled. Its response proved to be quite fast and sufficient for our purposes. A theoretical study of the compressibility effects and the viscous losses and flow separation effects on the jet exit velocity of the DC motor-driven SJA was presented. The effects of geometry/dimensions of cavity and exit slot and other actuator parameters like the motor driving frequency on the jet exit velocity were studied using the theoretical models. The actuator models were validated with experimental measurements. We then developed the aerodynamic model for the wing with a leading-edge-embedded SJA and develop the control algorithms for hinge-lessly controlling the wing in pitch at high angles of attack. For the aerodynamic modeling a novel Directed Connectivity Graph Approach, based on Radial Basis Function Networks, was developed and used to generate the aerodynamic model from experimental data. Subsequently, two different controllers were developed to control the wing in pitch. The first, a PID controller, proved inadequate. A Model Error Control Synthesis approach was developed and in simulations proved to be successful in controlling the wing in pitch.

11. REFERENCES

Alvarez-Calderon, A., 1964, "Rotating Cylinder Flaps of V/STOL Aircraft", Aircraft Engineering. Vol. 36, pp. 304-309.

Amitay M., Smith B. L. and Glezer A.,1998, "Aerodynamic Flow Control Using Synthetic Jet Technology," AIAA Paper No. 98-0208.

Bae, J., Breuer, K. S. and Tan, C. S., 2000,"Control of Tip Clearance Flows in Axial Compressors", AIAA Paper No. 2000-2233.

Bar-Sever, A., 1989, "Separation Control on an Airfoil by Periodic Forcing", AIAA Journal, Vol. 27, pp.820-821.

Chang, P. K., 1976, "Control of Flow Separation", Hemisphere Publishing, Washington, D.C., pp.1-84, 154-412.

Crassidis, J.L., "Robust Control of Nonlinear Systems Using Model Error Control Synthesis," AIAA Journal of Guidance, Control, and Dynamics, Vol. 22, No. 4, July-Aug. 1999, pp. 595-601.

Davis, S. A., and Glezer, A., 2000, "The Manipulation of Large and Small-Scales in Coaxial Jets Using Synthetic Jet Actuators", AIAA Paper No. 2000-0403.

De Silva, C. W., 1999, "Vibration: Fundamentals and Practice", CRC Press, New York, pp. 762-771.

Donovan, J. F., Kral, L. D., and Cary, A. W., 1998, "Active Flow Control Applied to an Airfoil", AIAA Paper No. 98-0210.

Ekaterinaris, J. A., "Numerical Investigations of Dynamic Stall Active Flow Control for Incompressible and Compressible Flows," Journal of Aircraft, Vol. 39, Jan.-Feb. 2002, pp. 71-78.

Englar, R. J., 1975, "Circulation Control for High-Lift and Drag Generation on STOL Aircraft", Journal of Aircraft, Vol. 7, pp.457-464

Englar, R. J., 2000, "Circulation Control Pneumatic Aerodynamics: Blown Force and Moment Augmentation and Modification; Past, Present and Future", AIAA Paper No. 2000-2541.

Ferrecchia, A, Coton, F. N., and Gailbraith, R. A., "An examination of dynamic stall vortex inception on a finite wing and on a NACA 0015 aerofoil," AIAA Applied Aerodynamics Conference, 17th, Norfolk, VA, June 28-July 1, 1999, Collection of Technical Papers (A99-33352 08-02).

Gad-el-Hak, M., 1990, "Control of Low-Speed Airfoil Aerodynamics", AIAA Journal, Vol. 28, pp.1537-1552.

Gad-el-Hak, M., 2000, "Flow Control: Passive, Active, and Reactive Flow Management", Cambridge University Press, New York, pp. 150-188

Gad-el-Hak, M. and Bushnell, D., 1991, "Separation Control: Review", ASME Journal of Fluids Engineering, Vol. 113, pp. 5-30.

Gilarranz, J. L., 1998, "Development of a High-Frame-Rate High-resolution Particle Image Velocimetry System and Application to the Characterization of Synthetic Jet Actuators", M.S. Thesis, Texas A&M University, Texas.

Gilarranz, J. L., and Rediniotis, O.K., 2001a, "Compact High-Power Synthetic Jets for Flow Separation Control", AIAA Paper No. 2001-0737.

Gilarranz, J. L., and Rediniotis, O.K., 2001b, "Compact, High-Power Synthetic Jets for Flow Separation Control, Proceedings of the Sixth National Congress on Mechanics, Thessaloniki, Greece, pp. 371-378.

Gilarranz, J. L., Yue, X. and Rediniotis, O., 1998, "PIV Measurements and Modeling of Synthetic Jet Actuators for Flow Control", Proceedings of FEDSM'98,1998 ASME Fluids Engineering Division Summer Meeting, Washington, D.C.

Goodmanson, L. T., and Gratzer, L. B., 1973, "Recent Advances in Aerodynamics for Transport Aircraft – Part 1", Astronautics and Aeronautics, Vol.11, pp. 30-45.

Goodmanson, L. T., and Gratzer, L. B., 1974, "Recent Advances in Aerodynamics for Transport Aircraft – Part 2", Astronautics and. Aeronautics, Vol.12, pp. 52-60.

Greenblatt, D. and Wygnanski, I., 1998, "Dynamic Stall Control by Oscillatory Forcing", AIAA Paper No. 98-0676.

Greenblatt, D., and Wygnanski, I., "Dynamic Stall Control by Periodic Excitation, Part 1: NACA 0015 Parametric Study", Journal of Aircraft, Vol. 38, No. 3, 2001, pp. 430-438.

Greenblatt, D., Darabi, A., Nishri, B., and Wygnanski, I., 1998, "Separation Control By Periodic Addition of Momentum with Particular Emphasis on Dynamic Stall," Proceedings Heli Japan 98, Paper T3-4, American Helicopter Society.

Hassan, A., and Munts, E. A., 2000, "Transverse and Near-Tangential Synthetic Jets for Aerodynamic Flow Control", AIAA Paper No. 2000-4334.

He, Y., and Kral, L., 2000, "Post-Stall Control on an Airfoil Using Localized Jet Actuators", AIAA Paper No. 2000-0408.

He, Y., Cary, A. W. and Peters, D. A., 2001, "Parametric and Dynamic Modeling for Synthetic Jet Control of a Post-Stall Airfoil", AIAA Paper No. 2001-0733.

Holman, J.P., 1994, "Experimental Methods for Engineers", McGraw-Hill, New York, pp.229-259.

Honohan, A. M., Amitay, M., and Glezer, A., 2000, "Aerodynamic Control Using Synthetic Jets", AIAA Paper No. 2000-2401.

Hsiao, F. B., Liu, C. F., and Shyu, J. Y., 1990, "Control of Wall Separated Flow by Internal Acoustic Excitation", AIAA Journal, Vol. 28, pp.1440-1446.

Huang, L. S., Maestrello, L., and Briant, T. D., 1987, "Separation Control Over an Airfoil at High Angles of Attack by Sound Emanating From the Surface", AIAA Paper No. 87-1261.

Ingard, U., 1953,"On the Theory and Design of Acoustic Resonators," Journal of the Acoustical Society of America, Vol. 25, pp.1037-1061.

Johnson, W. S., Tennant, J. S., and Stamps, R. E., 1975, "Leading-Edge Rotating Cylinder for Boundary Layer Control on Lifting Surfaces", Journal of. Hydronautics, Vol. 9, pp.76-78.

Johansen, E. S., "Development of a fast-response multi-hole probe for unsteady and turbulent flowfields," Ph.D. Dissertation, Aerospace Engineering Department, Texas A&M University, College Station, Dec. 2001.

Joshi, S. S., Speyer, J. L. and Kim, J., 1997, "A Systems Theory Approach to the Feedback Stabilization of Infinitesimal and Finite-Amplitude Disturbances in Plane Poiseuille Flow", Journal of Fluid Mechanics, Vol. 332, pp. 157-184.

Koga, D. J., Reisenthel, P., and Nagib, H. M., 1984, "Control of Separated Flowfields Using Forced Unsteadiness", Fluids and Heat Transfer Report No. R-84-1, Illinois Institute of Technology, Chicago, Illinois.

Kral, L. D., Donovan, J. F., Cain, A. B. and Cary, A. W., 1997, "Numerical Simulation of Synthetic Jet Actuators", AIAA Paper No. 97-1824.

Lee, T., and Petrakis, G. "Boundary-layer transition, separation and reattachment on an oscillating airfoil model." Journal of Aircraft, Vol. 37, Dec. 2000, pp. 360-365.

Lachman, G. V., 1961, "Boundary Layer and Flow Control", Vols. 1 and 2, Pergamon Press, Oxford, Great Britain.

Lin, J. C., Robinson, S. K., Mc.Ghee, R. J., and Valarezo, W. O., 1992, "Separation Control on High Reynolds Number Multi-Element Airfoils", AIAA Paper No. 92-2636.

Mallison, S. G., Reizes, J. A., and Hong, G., 2001, "An Experimental and Numerical Study of Synthetic Jet Flow", The Aeronautical Journal, Vol. 105, pp.41-49.

Maskell, E. C., 1955, "Flow Separation in Three Dimensions", RAE Report Aero. 2565, Royal Aircraft Establishment, Farnborough, Great Britain

McCormick, D., 2000, "Boundary Layer Separation Control with Directed Synthetic Jets", AIAA Paper 2000-0519

McManus, K., and Magil, J., 1997, "Airfoil Performance Enhancement Using Pulsed Jet Separation Control", AIAA Paper No. 97-1971.

McManus, K., Ducharme, A., Goldey, C., and Magil, J., 1996, "Pulsed Jet Actuators for Suppressing Flow Separation", AIAA Paper No. 96-0442.

Modi, V. J., Mokhtarian, F., Fernando, M., and Yokomizo, T., 1989, "Moving Surface Boundary Layer Control as Applied to 2-D Airfoils", AIAA Paper No. 89-0296.

Mokhtarian, F., and Modi, V. J., 1988, "Fluid Dynamics of Airfoils with Moving Surface Boundary-Layer Control", Journal of Aircraft, Vol. 25, pp.163-169.

Moore, F. K., 1958, "On the Separation of the Unsteady Laminar Boundary Layer", Boundary Layer Research, Editor. H. Görtler, Springer-Verlag, Berlin, pp. 296-310.

Müller, M., Bernal, L., Moran, R., Washabaugh, P., Parviz, B. and Najafi, K., 2000, "Micromachined Acoustic Resonators for Microjet Propulsion", AIAA Paper 2000-0547.

Musavi, M., W. Ahmed, K. Chan, K. Faris and D. Hummels, "On training of radial basis function classifiers,"Neural Networks, vol. 5, 1992, pp. 595—603.

Nelson, R.C., "Flight Stability and Automatic Control," Mc-Graw Hill, 1997.

Pack, L., and Seifert, A., 1999, "Periodic Excitation for Jet Vectoring and Enhanced Spreading", AIAA Paper No. 99-0672.

Pack, L., and Seifert, A., 2000, "Dynamics of Active Separation Control at High Reynolds Numbers", AIAA Paper No. 2000-0409.

Panton, R. L., 1996, "Incompressible Flow", Wiley, New York, pp.113 –115.

Parekh, D. E., and Glezer, A., 2000, "AVIA: Adaptive Virtual Aerosurface", AIAA Paper No. 2000-2474.

Prandtl, L., 1904, "Über Flüssigkeitsbewegugng bei sehr kleiner Reibung", Proceedings of the Third International Mathematics Congress, Heidelberg, Germany, pp.484-491.

Rae, W., and Pope, A., 1984, "Low Speed Wind Tunnel Testing", Wiley, New York, pp. 199-208, 362-424.

Rao, P. Gilarranz, J. L., Ko, J. Strganac, T. and Rediniotis, O. K., 2000, "Flow Separation Control Via Synthetic Jet Actuation", AIAA Paper 2000-0407.

Rathnasingham, R. and Breuer, K. 1997, "Coupled Fluid-Structural Characteristics of Actuators for Flow Control," AIAA Journal, Vol. 35, pp. 832-837.

Ritchie, B. D., and Seitzman, J. M., 2000, "Controlled Fuel-Air Mixing Using a Synthetic Jet Array", AIAA Paper No. 2000-3465.

Rizzetta, D., Visbal, M. and Stanek, M., 1999, "Numerical Investigations of Synthetic-Jet Flow Fields", AIAA Journal, Vol. 37, pp. 919-927.

Rott, N., 1956, "Unsteady Viscous Flow in the Vicinity of a Stagnation Point", Quarterly of Applied Mathematics, Vol. 13, pp.444-451.

Sears, W. R., 1956, "Some Recent Developments in Airfoil Theory", Journal of the Aeronautical Sciences, Vol. 23, pp. 490-499.

Seifert, A., and Pack, L., 1999a, "Oscillatory Control of Separation at High Reynolds Numbers", AIAA Journal, Vol. 37, pp. 1062-1071.

Seifert, A., and Pack, L., 1999b, "Oscillatory Excitation of Unsteady Compressible Flows Over Airfoils at Flight Reynolds Number", AIAA Paper No. 99-0925.

Seifert, A., and Pack, L., 2000, "Separation Control at Flight Reynolds Numbers: Lessons Learned and Future Directions", AIAA Paper No. 2000-2542.

Seifert A., Bachat T., Koss D., Shepshelovich M., Wygnanski I., 1993, "Oscillatory Blowing: A Tool to Delay Boundary-Layer Separation", AIAA Journal, Vol. 31, pp. 2052-2060.

Seifert, A., Darabi, A., and Wygnanski, I., 1996, "On the delay of Airfoil Stall by Periodic Excitation", Journal of Aircraft, Vol. 33, pp. 691-699.

Seifert A, Eliahu S, Greenblatt D, Wygnanski I, 1998, "On the Use of Piezoelectric Actuators for Airfoil Separation Control", AIAA Journal, Vol. 36, pp.1535-1537.

Shih, C. and Ding, Z., "Vortex Interaction of a Delta-Wing Flowfield," AIAA Journal 41, 2002, 314-316.

Singla, P., K. Subbarao, J.L. Junkins and O.K. Rediniotis, "Intelligent Multi-Resolution Modelling: Application to Synthetic-Jet Actuation and Flow Control," AIAA Paper 2004-0774, Jan. 2004

Smith, A. M. O., 1975, "High-Lift Aerodynamics", Journal of Aircraft, Vol. 12, pp. 501-530.

Smith, B. L., and Glezer, A., 1997, "Vectoring and Small-Scale Motions Effected in Free Shear Flows Using Synthetic Jet Actuators", AIAA Paper No. 97-0213.

Smith, B. L., and Glezer, A., 1998, "The Formation and Evolution of Synthetic Jets", Physics of Fluids, Vol. 10, pp. 2281-2297.

Smith, B. L., Trautman, M. A., and Glezer, A., 1999, "Controlled Interactions of Adjacent Synthetic Jets", AIAA Paper No. 99-0669.

Smith, D., Amitay M., Kibens V., Parekh D. and Glezer A., 1998, "Modifications of Lifting Body Aerodynamics Using Synthetic Jet Actuators," AIAA Paper No. 98-0209.

Subbarao K., "Structured Adaptive Model Inversion: Theory and Applications to Trajectory Tracking for Non-Linear Dynamical Systems," Ph.D Dissertation, Aerospace Engineering Dept., Texas A&M University, August 2001.

Sultanian, B. K., Nagao, S. and Sakamoto, T., 1999, "Experimental and Three-Dimensional CFD Investigation in a Gas Turbine Exhaust System", Journal of Engineering for Gas Turbines and Power, Vol. 121, pp. 364-374.

Summers, J. L., and Page, W. A., 1950, "Lift and Moment Characteristics at Subsonic Mach Numbers of Four 10-Percent-Thick Airfoil Sections of Varying Trailing-Edge Thickness, NACA R. M. A50J09, NACA, Washington D.C.

Tao, K., "A closer look at the radial basis function networks," Conference record of 27th Asilomar Conference on signals, system and computers, Pacific Grove, CA, USA, pp 401—405, 1993.17.

Traub, L. W., 1992, "A Subsonic Wind-Tunnel Investigation of the Effect of Sharp Edged Sheared Tips on a Moderate Aspect Ratio Flat Plate Wing", M.S. Thesis, University of the Witwatersrand, Johannesburg, South Africa.

Traub, L. W., 1999, "Effects of Spanwise Camber on Delta Wing Aerodynamics: A Theoretical and Experimental Investigation", Ph.D. Dissertation, Texas A&M University, Texas.

Wildhack, W.A., "Pressure drop in tubing in aircraft instrument installations," NACA TN-593 , 1937, pp. 30.

United Sensor, 1983, "United Sensor Pitot-Static Pressure Probe Catalog", Bulletin 2, Watertown, Massachusetts.